Improving the Efficiency, Stability, and Flexibility of Perovskite Solar Cells

A Thesis Submitted to the College of

Graduate and Postdoctoral Studies

In Partial Fulfillment of the Requirements

For the Degree of Doctor of Philosophy

In the Department of Chemistry

University of Saskatchewan

Saskatoon

By

Kianoosh Poorkazem

PERMISSION TO USE

In presenting this thesis/dissertation in partial fulfillment of the requirements for a Postgraduate degree from the University of Saskatchewan, I agree that the Libraries of this University may make it freely available for inspection. I further agree that permission for copying of this thesis/ dissertation in any manner, in whole or in part, for scholarly purposes may be granted by the professor Timothy L. Kelly, who supervised my thesis/dissertation work or, in their absence, by the Head of the Department or the Dean of the College in which my thesis work was done. It is understood that any copying or publication or use of this thesis/dissertation or parts thereof for financial gain shall not be allowed without my written permission. It is also understood that due recognition shall be given to me and to the University of Saskatchewan in any scholarly use which may be made of any material in my thesis/dissertation.

Requests for permission to copy or to make other uses of materials in this thesis/dissertation in whole or part should be addressed to:

Head of the Department of Chemistry
University of Saskatchewan
Saskatoon, Saskatchewan
S7N 5C9, Canada

OR

Dean
College of Graduate and Postdoctoral Studies
University of Saskatchewan
107 Administration Place
Saskatoon, Saskatchewan S7N 5A2, Canada

ACKNOWLEDGEMENT

I am grateful to people who made enormous contributions to this thesis. I thank Dr. Tim Kelly for all I learned from him. I am grateful to Dr. Dianyi Liu for sharing his knowledge and experience with me. I thank Ms. Amelia Hesketh and Mr. Kyle Fransishyn for great collaboration.

During my PhD studies, I have benefited from the support of several individuals. I would like to thank my friends, particularly Dr. Hessam Younesi, Mr. Adel Panahi, and Dr. Hiwa Salimi. I would like to express my gratitude to Mr. Kris Kembel and Ms. Joanne Horsley, as I had the honor of being a member of the Momentum Martial Arts family for five years. I would like to express my appreciation to Dr. Ron Steer for helpful discussions. I am grateful to Dr. Valerie MacKenzie for providing a constructive environment to teach effectively. I thank Dr. Alexandra Bartole-Scott for developing my teaching skills. I thank Ms. Leah Hildebrandt for all the assistance. I thank the Kelly group, especially Mr. Phil Boutin, Dr. Mahesh Gangishetty, and Mr. Nick Randell. I appreciate the help from Dr. Matthew Paige for using AFM. I am grateful to Dr. Eiko Kawamura for help in using the SEM. I am thankful to Mr. Garth Perry for helping me with experimental setups. I appreciate work done by Physics Machine Shop staff, especially Mr. Ted Toporowski. I appreciate the useful feedback by Drs. Lee Wilson, Robert Scott, and Qiaoqin Yang. I thank Dr. Andrew Grosvenor and Mr. Tom Bonli for permission to use the pXRD diffractometer.

I am thankful for supports from different organizations: I thank Western College of Veterinary Medicine Image Center for permission to use the SEM. I am thankful for financial supports from the Natural Sciences and Engineering Research Council of Canada (NSERC), the University of Saskatchewan, Canada Research Chair program, the Inorganic Chemistry Exchange (ICE) program, Government of Saskatchewan, and Canada foundation for innovation.

DEDICATION

I dedicate this thesis to my parents: Marzieh and Ali. Your unconditional love and support have been the most valuable things in my life.

ABSTRACT

Solar cells are a renewable, clean alternative to fossil fuels. Silicon solar cells are used in about 90% of commercial modules. Despite having high efficiency and stability, silicon solar cells are costly and rigid. To produce an efficient, stable, cost-effective, and flexible module, different strategies have been explored. One strategy is photon upconversion, where multiple sub-bandgap photons can be converted into a single photon of higher energy, allowing it to be absorbed by the semiconductor of a solar cell. Another strategy is the cost-effective fabrication of efficient perovskite solar cells, composed of CH_3NH_3I and PbI_2. Unlike silicon, the perovskite can be fabricated on top of flexible plastic substrates coated with transparent conductive metal oxide electrodes; however, the limit of its flexibility needs to be explored and improved for real-world applications. More importantly, the major barrier to the commercialization of perovskite solar cells is their instability when exposed to either high humidity or O_2 and sunlight. Therefore, improving stability, while not sacrificing efficiency, is extremely important.

In this thesis, different strategies are developed to fabricate such a multi-faceted solar cell. Plasmonics are used to enhance the quantum yield of the photon upconversion process. As another strategy, the inflexible metal oxide electrodes of perovskite devices are replaced by flexible polymer-based ones. Then, the intrinsic flexibility of the $CH_3NH_3PbI_3$ layer is assessed by comparing the results of bending tests performed on a perovskite device and on a highly-flexible organic solar cell. Furthermore, the results of compositional engineering are shown, where partially replacing the $CH_3NH_3^+$ cation with formamidinium is shown to improve the stability of the perovskite film. Following this, the possibility of completely eliminating $CH_3NH_3^+$ from state-of-the-art devices is shown, resulting in improved stability and similar efficiencies.

TABLE OF CONTENTS

LIST OF TABLES

LIST OF FIGURES

LIST OF ABBREVIATIONS

AFM	atomic force microscopy
AgNP	Ag nanoplates
AM0	air-mass zero
AM1.5G	air-mass 1.5 global
ANOVA	analysis of variance
AgNA	Ag nanoprism arrays
AuNP	Au nanoprisms
CFCs	chlorofluorocarbons
DMF	*N*,*N*-dimethylformamide
DMSO	dimethylsulfoxide
DPA	9,10-diphenylanthracene
DPBF	1,3-diphenylisobenzofuran
DSSCs	dye-sensitized solar cells
EA	ethylammonium
EET	electronic energy transfer
E_g	bandgap energy
ETA	extremely-thin absorbers
FA	formamidinium
FCM-IB	$FA_{(1-x-y)}Cs_xMA_yPbI_{(3-z)}Br_z$
FC-I	$FA_{(1-x)}Cs_xPbI_3$
FF	fill factor
FTO	fluorine-doped tin oxide
FCG-I	$(GA)FA_{(1-x)}Cs_xPbI_3$
FWHM	full width at half maximum
GA	guanidinium
HC-PEDOT	highly-conductive poly(3,4-ethylenedioxythiophene):poly(styrenesulphonate)

IPCE	incident photon-to-current efficiency
ISC	inter-system crossing
ITO	indium tin oxide
IVR	intramolecular vibrational redistribution
J_{mp}	maximum-power current density
J_{sc}	short-circuit current density
J-V curves	current-voltage curves
K_{sp}	solubility product constant
Li-TFSI	lithium-bis(trifluoromethanesulfonyl)imide
LSPR	localized surface-plasmon resonance
MA	methylammonium
M-In_2O_3	metallized In_2O_3
MSSC	meso-superstructured solar cell
NCs	nanocrystals
NREL	national renewable energy laboratory
O.D.	optical density
ODP-Weighted	ozone depletion potential-weighted
OSCs	organic solar cells
OTR	oxygen transmission rate
P3HT	poly(3-hexylthiophene)
$PC_{61}BM$	(6,6)-phenyl-C_{61}-butyric acid methyl ester
PCE	power conversion efficiency
PdOEP	palladium octaethylporphyrin
PEDOT:PSS	poly(3,4-ethylenedioxythiophene):poly(styrenesulphonate)
PET	polyethylene terephthalate
P_{in}	incident power
PL	photoluminescence
P_{max}	maximum power

PMMA	poly(methyl methacrylate)
PSCs	perovskite solar cells
PtOEP	Platinum(II) octaethylporphyrin
PVDF	polyvinylidene difluoride
pXRD	powder X-ray diffraction
R2R	roll-to-roll
RB	Rose Bengal
RH	relative humidity
R_s	series resistance
R_{sh}	shunt resistance
S_0	ground state singlet
S_1	first excited singlet state
SCLC	space-charge limited conduction
SC-PEDOT	semiconducting poly(3,4-ethylenedioxythiophene):poly(styrenesulphonate)
SEM	scanning electron microscopy
Spiro-OMeTAD	2,2′,7,7′-tetrakis-(*N*,*N*-di-*p*-methoxyphenylamine)-9,9′-bifluorene
SPP	surface-plasmon polariton
ssDSSC	solid-state dye-sensitized solar cells
T_1	first excited triplet state
t_f	Goldschmidt tolerance factor
TTA	triplet-triplet annihilation
V_{oc}	open-circuit voltage
V_{mp}	maximum-power voltage
V_{TFL}	trap-filled limit voltage

Chapter 1. INTRODUCTION

Exploring renewable and environmentally friendly alternatives to fossil fuels is one of the most important objectives in energy production. The amount of fossil fuels is limited, an issue that becomes more serious when one looks at the growth of population on Earth. In addition, there are many disadvantages regarding the extraction, transportation, and consumption of fossil fuels. Their extraction needs workers to go to dangerous areas and work in hard conditions. As easily-extracted fossil fuels are consumed, their continued production requires working in deeper mines or deeper off-shore reservoirs, which adds to the level of risk. Fossil fuels must also be transported, and accidental spills during transport can cause serious environmental problems. In addition, the consumption of fossil fuels has several environmental impacts. The presence of atmospheric gases, such as H_2O and CO_2, produced by fossil fuel consumption is the major cause of global warming (**Figure 1.1a**). These gases are transparent to visible-region solar photons, allowing them to reach the surface of the Earth. But when the energy of sunlight is downconverted by absorption and emission on the surface of the Earth, the gases absorb the now lower-energy photons. This process results in an increase in the temperature of the Earth's surface. In addition, fossil fuel combustion is one of the main causes of N_2O emission. Although the amounts of produced chlorofluorocarbons (CFCs) have been controlled after the 1987 Montreal protocol, the production of N_2O is now considered the main reason of ozone layer depletion (Figure 1.1b).[1] Another disadvantage of fossil fuel consumption is gaseous products, which result in acid rain and health problems, such as asthma. Therefore, renewable and clean sources of energy should be used to help address these issues.

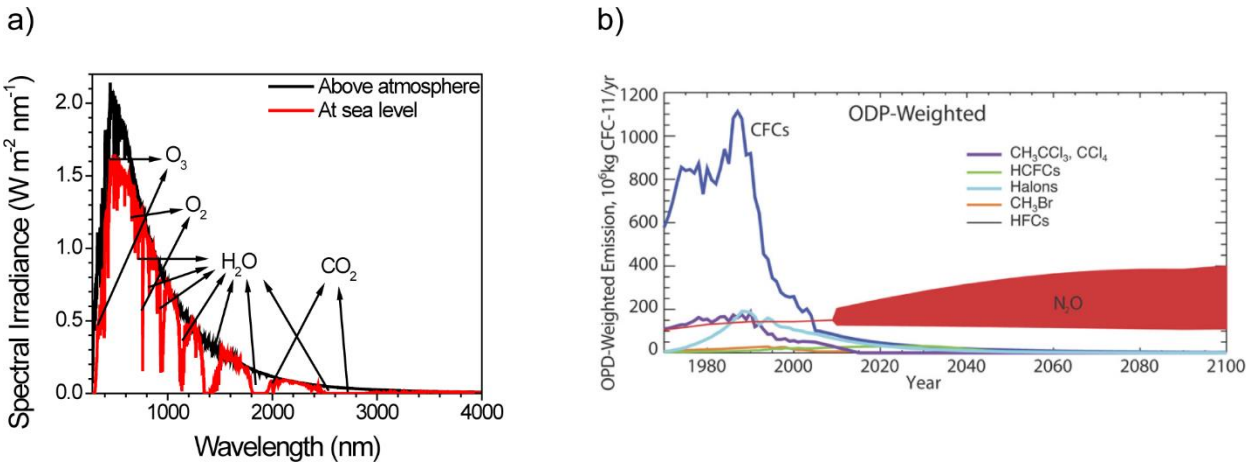

Figure 1.1. (a) Spectral irradiance of the sunlight above the atmosphere (air-mass zero – denoted by AM0) and at sea level (air-mass 1.5 global – denoted by AM1.5G). (b) A comparison of ozone depletion potential-weighted emission for different gasses in the near past and future. The red band shows calculation uncertainties. Reprinted with permission from AAAS.[1]

1.1 Solar Cells

1.1.1 Need for a Clean Type of Renewable Energy

Sunlight is the source of almost all types of renewable energy (geothermal energy is a key exception). The energy of sunlight can be directly used via solar cells or solar thermal collectors, and can be indirectly used via wind power plants, hydroelectric power plants, biofuels, and biomass. However, compared to the use of solar cells, there are more formidable barriers to the use of other types of renewable energy: solar thermal collectors are not effective in winter, and usually use copious amount of water (or other expensive fluids) for cooling and heating systems; geothermal power plants may trigger earthquakes by stimulating underground reservoirs,[2] and can be built only in specific regions; wind power plants are noisy (and hence stressful),[3] and kill birds; hydroelectric power plants use dams that have negative impacts on ecosystems; and biofuels and

biomass need large land areas and copious amount of water. In contrast, solar cells are free of these drawbacks and considered, to a great extent, a renewable and clean source of energy.

1.1.2 Challenges of Different Types of Solar Cells

To commercially compete with fossil fuels, solar cells need to meet demanding requirements, including high efficiency, low cost, and long-term stability. Among different types of single-junction solar cells (which have either one *p*-*n* junction or one excitonic active layer), GaAs and silicon devices have achieved the highest efficiencies during the last 40 years of research (**Figure 1.2**). Between these two, silicon devices are more cost effective, as silicon is more abundant and their manufacturing process has already been scaled up. In addition to high efficiency, silicon devices have long-term stability (that helps companies provide a 25-year warranty).[4] As a result, they represent 90% of solar cells on the market. However, high-temperature furnaces are used to fabricate silicon single crystals. As a result, the final price of silicon solar cells is still not cost effective enough to compete with fossil fuels (albeit this is not the case for all regions of the world).

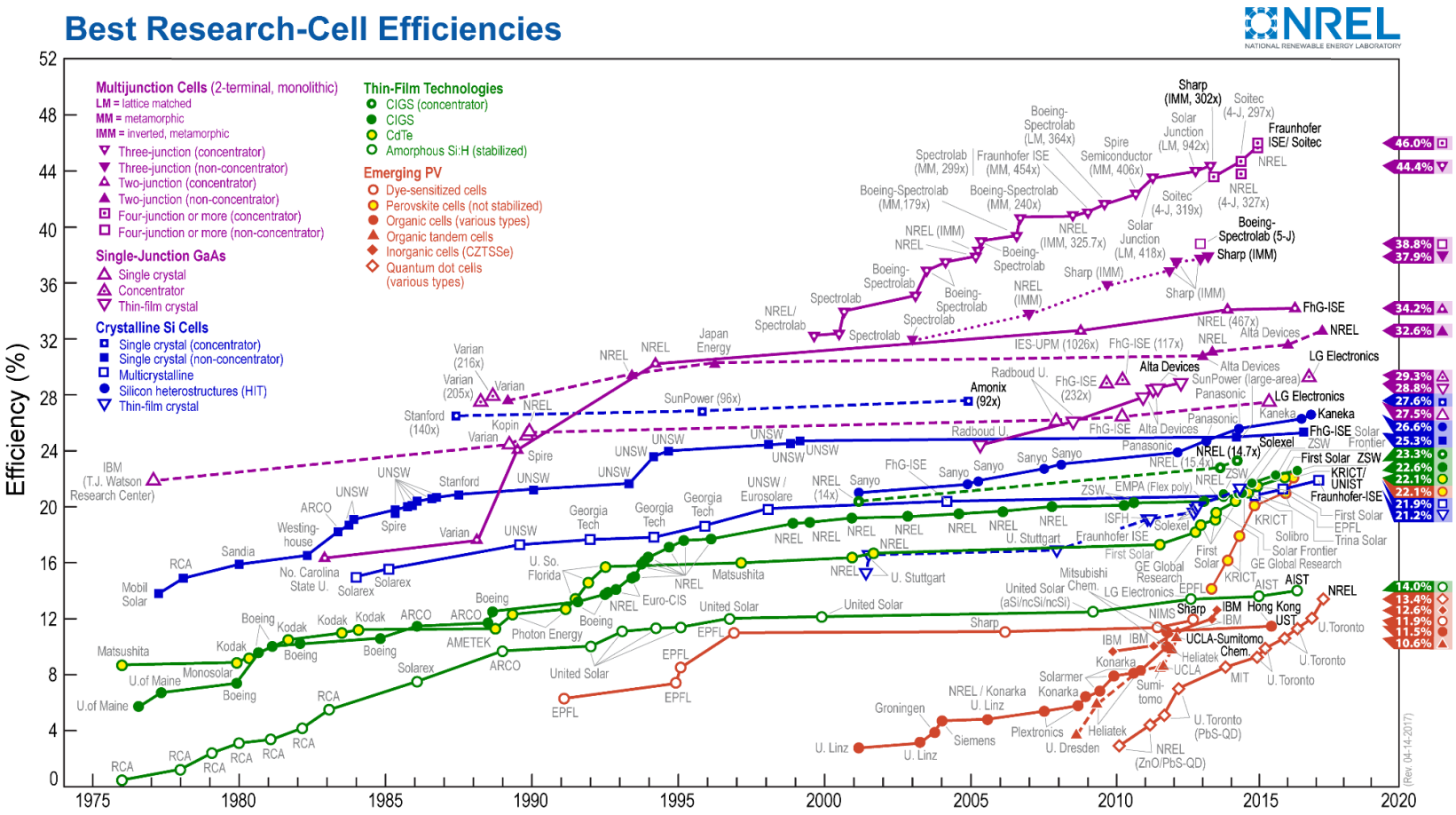

Figure 1.2. A plot of the certified record-setting efficiency for different types of solar cells as a function of year, https://www.nrel.gov, date accessed: July 2017.

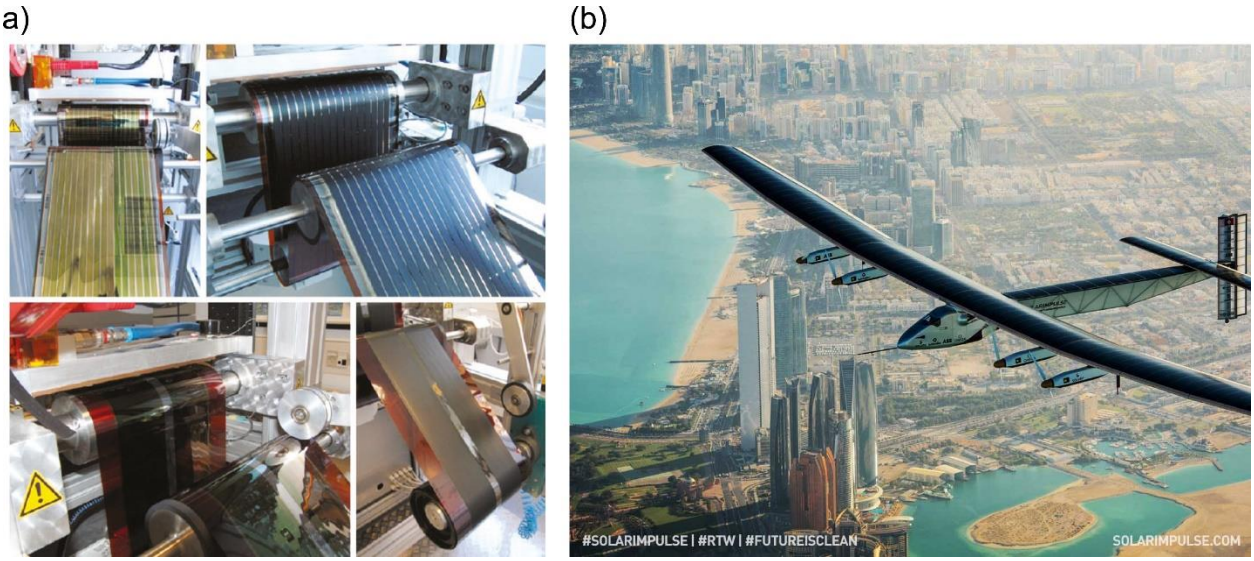

Figure 1.3. Examples of (a) flexible and (b) light-weight solar cells. (a) Reprinted by permission from Macmillan Publishers Ltd: Nature Photonics, copyright 2011.[5] (b) Image courtesy of Solar Impulse, date accessed: September 2016.

Other than cost and efficiency, flexibility and light weight are important for certain applications. One application is the use of roll-to-roll (R2R) fabrication processes for flexible thin-film solar cells; this is a fast, easy, and high-throughput type of manufacturing (**Figure 1.3a**). Another is the use of lighter weight solar cells, which could help projects such as "Solar Impulse", in which a multi-city flight was achieved around the planet using a solar cell-equipped airplane and no fossil fuels (Figure 1.3b). Although silicon solar cells were used in such applications, they cannot be extremely flexible and light. Silicon has an indirect bandgap, resulting in a low attenuation coefficient. Hence, a thick layer of it is required to absorb enough sunlight. This makes silicon solar cells more expensive, rigid, and heavy. In comparison, organic solar cells (OSCs) are flexible and lightweight, and in addition, have more tunable bandgaps. However, their efficiency is low, despite much effort having gone into improving their efficiency (Figure 1.2). Therefore, it

has been a challenge for the photovoltaics community to find a single type of solar cell that meets all of these demanding requirements.

In this thesis, two general approaches are developed to improve solar cell technology. One is plasmon-enhanced photon upconversion, which can in theory be used to increase the photocurrent and efficiency of any kind of solar cell (section 1.2 and chapter 2). The other is the use of perovskite solar cells (PSCs), which are efficient (Figure 1.3), lightweight, somewhat flexible, and made from cost-effective starting materials (section 1.3). However, their stability needs to be improved in order for them to be suitable for commercialization. Therefore, this thesis develops various methods to improve flexibility (section 1.4 and chapter 3), stability (section 1.5 and chapter 4), or both stability and efficiency of perovskite solar cells (section 1.6 and chapter 5). In addition, a discussion section is provided to link these different approaches (section 1.7).

1.2 Plasmonics in Upconversion

1.2.1 Shockley-Queisser Limit and Photon Upconversion

The efficiency of a single-junction solar cell is limited. Shockley and Queisser theoretically calculated the highest possible efficiency to be 44% (which differs if calculated using different incident photon fluxes), a limit dependent on the bandgap of the active-layer semiconductor (**Figure 1.4a**).[6] Based on the quantum characteristics of light absorption, if a photon has energy higher that that of the bandgap, the energy difference is lost via a thermalization process. If a photon has lower energy than the bandgap, it will not be absorbed (Figure 1.4b). Hence, there is an optimum value for the bandgap of a semiconductor, which is 1.1 eV, about the same as that of

silicon. Accordingly, a large portion of low-energy sunlight may not be absorbed even with the optimum semiconductor bandgap.

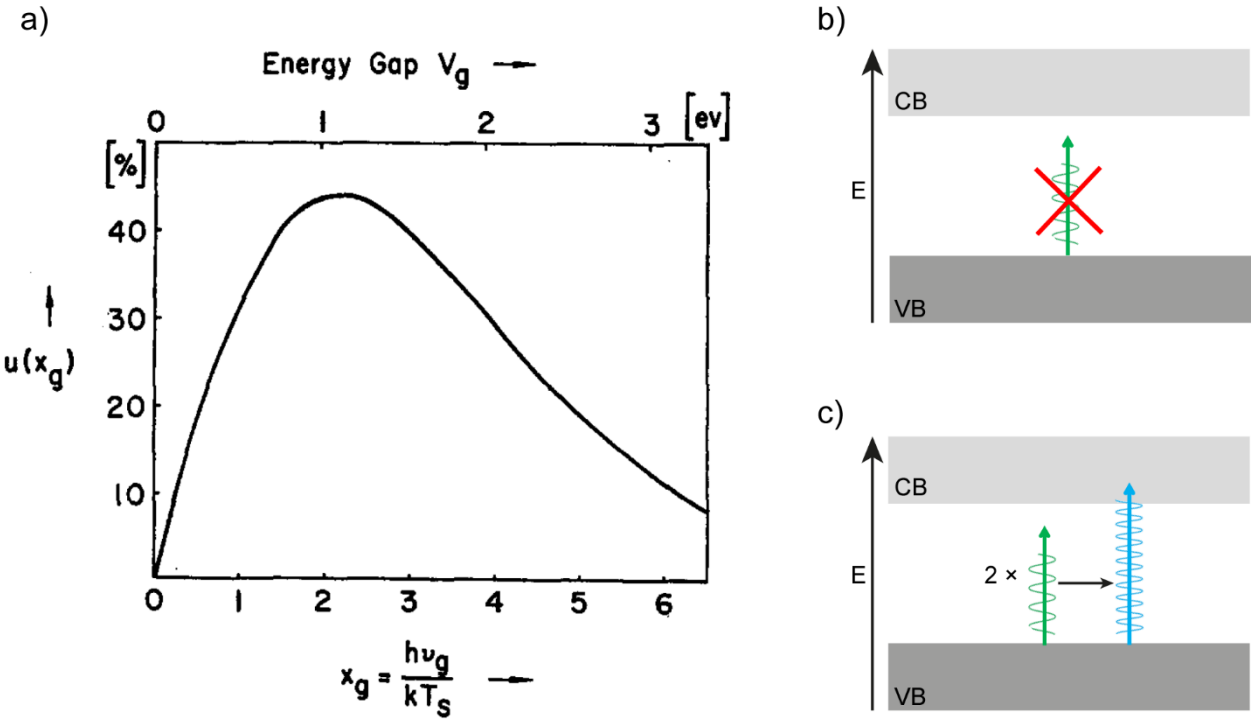

Figure 1.4. (a) A plot of maximum PCE vs the bandgap of the semiconductor. Reprinted with the permission of AIP Publishing.[6] (b, c) Schematics of a photon upconversion advantage. In (b), a sub-bandgap photon is not absorbed; in (c), two sub-bandgap photons are upconverted and the upconverted photon can be absorbed.

To circumvent the Shockley-Queisser limit and absorb a larger portion of the sunlight, a photon upconversion process can be used. In this process, a high-energy photon is produced from two (or more) low-energy photons, which is then absorbable by a large-bandgap semiconductor (Figure 1.4c). As a general strategy, this process can increase the current density and efficiency of any type of solar cell. It is especially beneficial for OSCs and dye-sensitized solar cells (DSSCs), which typically use semiconductors with bandgaps larger than 1.1 eV. Decreasing the bandgap of

organic semiconductors usually does not result in a significant increase in power conversion efficiency.[7] This is because of their high exciton binding energy (several hundred meV),[8-11] which must be overcome by a thermodynamic driving force. This is provided in two ways: (i) having a higher LUMO energy than the electron-acceptor material, (ii) having a lower HOMO energy than the hole-acceptor material. These energy difference requirements are not compatible with very low bandgap organic semiconductors. Therefore, a key advantage of upconversion systems, rather than other efficiency-enhancing strategies, is that they are not highly dependent on the bandgap energy of the semiconductor in a solar cell.

1.2.2 Triplet-Triplet Annihilation: a Bimolecular Upconversion System

Two common upconversion systems are based on either lanthanide ions or organic chromophores.[12] Lanthanide-based systems have a low quantum efficiency, resulting mainly from very narrow absorption bands in the near IR region.[13, 14] These narrow bands limit their usefulness in solar applications. However, the absorption bands of organic chromophores can be tuned to absorb photons with lower energy than that of the semiconductor's bandgap. These photons will then be upconverted, and become absorbable by the semiconductor. Among organic-based upconversion systems, one of the most efficient systems is triplet-triplet annihilation (TTA), a bimolecular process including a photosensitizer and an emitter,[15-21] e.g. Palladium octaethylporphyrin (PdOEP) and 9,10-diphenylanthracene (DPA), respectively.[20, 22, 23] An example of this system in solution can be observed in a photograph, showing a green-to-blue upconversion. (**Figure 1.5a**).[24]

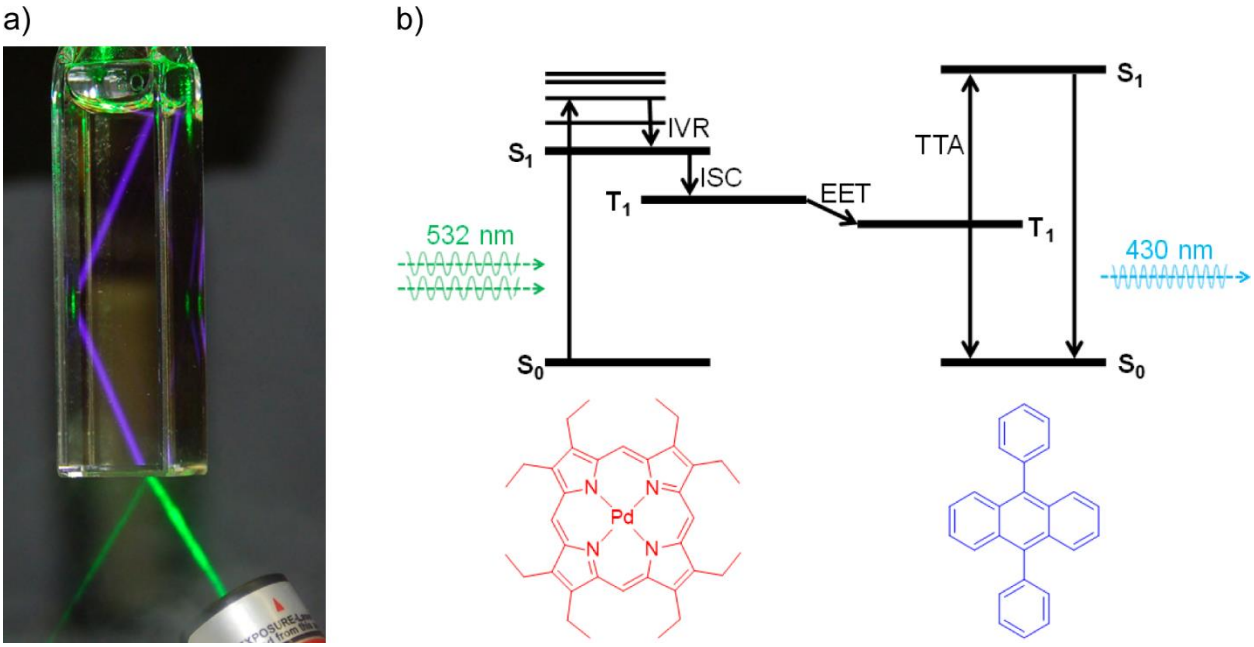

Figure 1.5. (a) A photograph of TTA in a toluene solution of tris(4,4'-Dimethyl-2,2'-bipyridine)ruthenium(II) and DPA, as the sensitizer and emitter, respectively using a 532 nm laser. Reprinted, Copyright 2010, with permission from Elsevier.[24] (b) The mechanism of a green-to-blue TTA process used in this thesis, including PdOEP and DPA as the sensitizer and emitter, respectively.

1.2.2.1 Mechanism

To have a workable TTA system, the sensitizers and emitters need to be compatible. In this system, a sensitizer absorbs light and is promoted to its first excited singlet state (S_1), after a possible intramolecular vibrational redistribution (IVR) process (Figure 1.5b). A requirement of the sensitizer is that it must have a triplet state (T_1) below S_1, which can be accessed via an inter-system crossing (ISC) process. Porphyrins with heavy metals have a high ISC quantum efficiency, resulting from strong spin-orbit coupling. Then, an electronic energy transfer (EET) process occurs to excite the T_1 state of the emitter. When two T_1-excited emitters meet each other, bimolecular TTA happens, returning one of them to its ground state (S_0) and promoting the other to S_1. Assuming the S_1-excited emitter has a high fluorescence quantum efficiency, it radiates an

upconverted photon. Two T_1-excited sensitizers can also undergo the TTA process. This occurs when: (i) the emitter does not have an appropriate T_1 state below the T_1 of the sensitizer, and (ii) the sensitizer has an excited singlet state (S_n) with energy lower than that of the sum of the two T_1 states (Equation 1.1).[16, 22]

$$E_{S_n} - E_{S_0} \leq 2\,(E_{T_1} - E_{S_0}) \qquad (1.1)$$

The result of TTA is a sensitizer in the S_n state. The energy is transferred to the emitter, exciting it to its S_1 state, which in turn, produces an upconverted photon. This additional pathway contributes to the efficiency of TTA, especially when the efficiency is controlled by the diffusion of chromophores. However, the use of an strong emitter with appropriate T_1 energy reinforces the process, through increasing the yield of T_1.

1.2.2.2 Need for quantum efficiency enhancement

The bimolecular nature of TTA presents a major barrier to its real-world application. Although the overall quantum efficiency of TTA-based upconversion is high in solution (20-45%),[25-27] it is very low (<1%) in the solid state,[28] as required for solar cell applications. This low efficiency is because two T_1 emitters need to meet each other before they can undergo the TTA process, otherwise they are quenched through a unimolecular process. This demands high diffusion rates of the emitters, but diffusion is relatively slow in the solid state.

A method of measuring the unimolecular rather than the bimolecular (TTA) quenching is based on the power dependency of the process (**Figure 1.6a** and 1.6b).[29] Power dependency is measured by monitoring the intensity of the upconverted light as a function of increasing the power density. Since two photons are required to form the two triplet states required for TTA, there is a quadratic power dependence of the TTA quantum yield on the incident power in the so called

"low-power regime", where unimolecular quenching is the dominant mechanism. However, this dependency gradually becomes linear at increasing power densities, eventually reaching the "high-power regime", where TTA is now more dominant. These are the conditions for the maximum possible efficiency of TTA. As a result, by carrying out power dependency measurements, one can comment on: (i) how high the efficiency of the TTA at a measured power density is compared to its maximum possible value at power densities required for the linear dependency, and (ii) if the solar power density of 100 mW·cm^{-2} (based on AM1.5G spectrum) lies in the high-power regime for a particular upconversion system (i.e. if that TTA system is efficient enough to improve the current density of a solar cell).

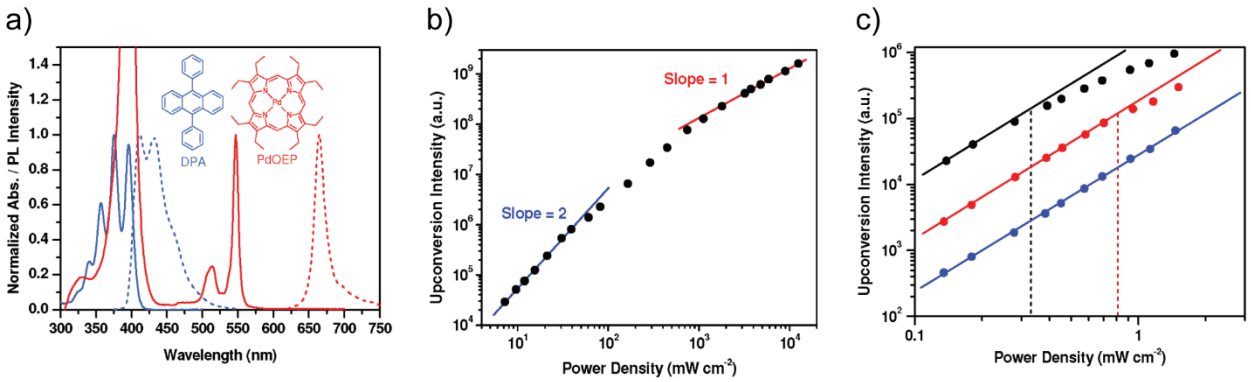

Figure 1.6. A TTA system in vacuum-degassed toluene. Reprinted with permission.[29] (a) Absorption (solid lines) and emission (dashed lines) spectra of PdOEP and DPA. (b) A plot of upconverted emission intensity against excitation power. It shows both quadratic and linear regions. (c) Power dependency for wavelengths with different optical density: 515 (red), 530 (blue), and 545 (black) nm. The solid and dashed lines show the quadratic dependency and the approximate power density at which the TTA starts to deviate from quadratic power dependency, respectively.

To have practical applications, the densities of the triplet states play an important role. In a study on the PdOEP/DPA system, the density of the triplet states was changed based on the

optical density of PdOEP at different wavelengths, using a noncoherent excitation source.[29] The triplet density was increased by going from 530 nm (in between the two Q bands of PdOEP- Figure 1.6a) to 515 nm (low optical-density Q band), and to 545 nm (high optical-density Q band). When the power dependency was measured using this order of the wavelengths, the deviation point from the quadratic dependency is pushed to lower power densities (Figure 1.6c). This implies that a larger density of triplet states is helpful to push the high-power regime of a TTA system closer to solar power densities. Therefore, to compensate for the low diffusion rates of the TTA emitters in the solid state, an effective strategy is to have a strongly absorbing TTA sensitizer.

1.2.3 Plasmonics

Plasmonics have been used to improve both the absorption cross-section and emission quantum yield of materials. The surface electron cloud of a metal nanoparticle can oscillate at a specific natural frequency; when this frequency is equal to the electric-field frequency of incident light, a resonance occurs, called a localized surface-plasmon resonance (LSPR - **Figure 1.7a**).[30] The LSPR of metal nanoparticles enhances the absorption in a medium through two mechanisms.[31] One is by increasing the effective optical path length through the medium via scattering the light, which increases absorbance based on the Beer-Lambert law. The other is by creating a strong local electrical field near the surface (approximately 10 nm) of the nanoparticles, known as the near-field effect. This local electric field can be in resonance with the electric-field oscillation of incoming or outgoing light, and enhances the absorption or emission of the surrounding material, respectively.

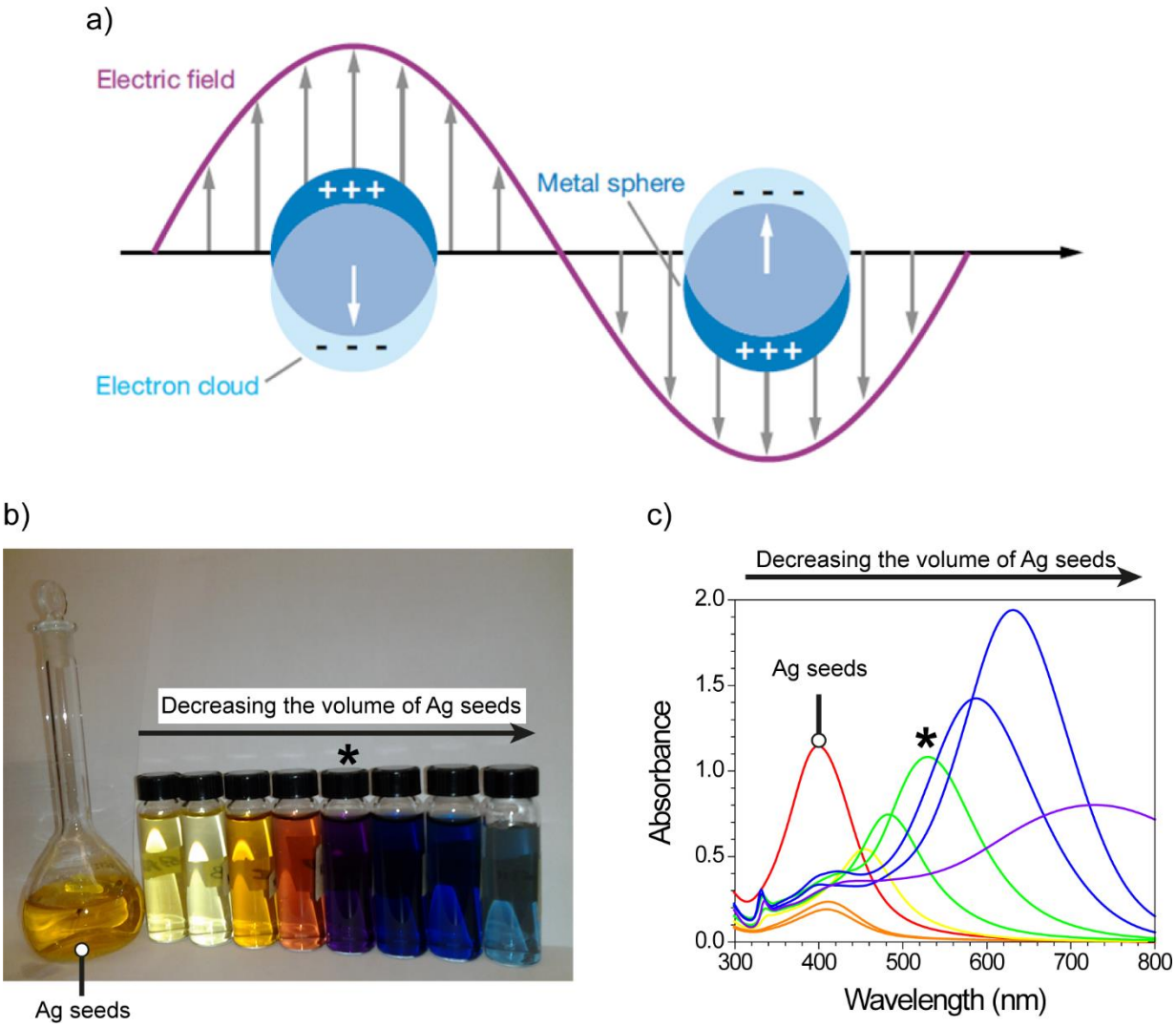

Figure 1.7. (a) Schematics of LSPR. Reprinted with permission.[30] (b) The solutions and (c) absorption spectra of Ag nanoprisms with different LSPR wavelengths. A solution with the right LSPR wavelength (530 nm) to overlap with the Q band of PdOEP is shown with an asterisk.

1.2.3.1 Size and shape dependency

Scattering and near-field effects are highly dependent on the size and shape of the metal nanoparticles. The larger the particles, the less absorption (less optical loss) and the more scattering that will occur.[32] On the other hand, very small nanoparticles (5-20 nm) have strong near-field effects. This is because of having low albedo (the ratio of the light reflected from a surface to the

light coming to it) and effective dipole moments.[31] In addition, this near-field effect is significantly stronger at the sharp corners and edges of anisotropic nanoparticles.[33] Metal nanoprisms are an example of plasmonic particles to provide a strong near-field effect. These are good indications of the need for size and shape tuning.

1.2.3.2 Metal-enhanced fluorescence

Metal-enhanced fluorescence (MEF) is one application of plasmonics. It works by matching the surface plasmon resonance of metal nanoparticles with the absorption or emission band of a chromophore, to finally improve its fluorescence intensity. To carefully match the two, one requires a facile method to tune the surface plasmon resonance. For instance, Ag nanoprisms can be synthesized by adding a fixed volume of $AgNO_3$ to different volumes of already-synthesized Ag seeds (the details of these Ag nanoprism synthesis are described in chapter 2). This results in two-dimensional anisotropic growth of the seeds to form nanoprisms with different side lengths.[34] Hence, it provides a variety of solutions with different colors and LSPRs (Figures 1.7b and 1.7c). As a general example of MEF, a 30-fold increase in the fluorescence of CdSe/ZnS nanocrystals (NCs) was achieved when they were surface plasmon coupled (SP-coupled), by coating them on top of Au nanoprisms (**Figures 1.8a** and 1.8b). This improved fluorescence can directly improve the efficiency of optoelectronic devices, such as light-emitting diodes.

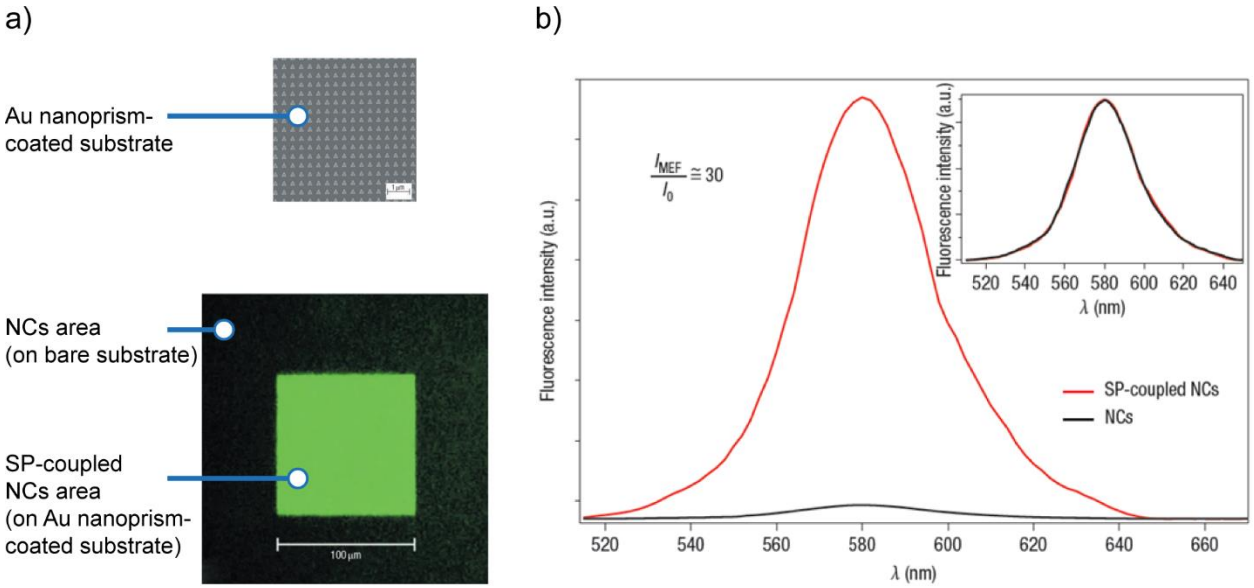

Figure 1.8. An example of metal- enhanced fluorescence. Adapted and reprinted by permission from Macmillan Publishers Ltd: Nature Nanotechnology, copyright 2006.[35] (a) SEM image of a substrate coated with Au nanoprisms (the size bar is 1 μm) and a photoluminescence map including SP-coupled CdSe/ZnS NCs and NCs areas. (b) Emission spectra of the two regions specified in (a). Inset shows normalized spectra.

1.2.4 Plasmon-Enhanced Triplet-Triplet Annihilation

Plasmonics could hypothetically enhance the efficiency of TTA. Both scattering and near-field effects of MEF can increase the density of triplet states needed for the TTA enhancement. A previous study used a 50 nm flat layer of Ag to improve the efficiency of TTA.[15] However, a prism was required to couple the incoming light to plasmon modes, and the layer could not provide either the scattering effect of nanoparticles or the strong near-field effect of anisotropic particles. Another study showed enhanced upconversion in a TTA materials/Ag nanocrescent core/shell structure using computational techniques,[36] a result which needs to be experimentally confirmed. Therefore, before our work (chapter 2), the surface plasmonic effects of any kind of metal nanaoparticle on TTA had not been experimentally explored.

1.3 Perovskite Solar Cells

1.3.1 Basic Solar Measurements

To measure the efficiency of a solar cell, the current density of a device is obtained as a function of applied voltage, resulting in a *JV* curve (**Figure 1.9a**). Such a curve provides the parameters required to calculate efficiency:

$$\eta = \frac{P_{\text{out}}}{P_{\text{in}}} = \frac{J_{\text{sc}} V_{\text{oc}} \text{FF}}{P_{\text{in}}} \tag{1.2}$$

Where η is efficiency, P_{out} is the output power of a device, P_{in} the input power of the incident light, J_{sc} is the short-circuit current density (when there is no voltage applied on the device), V_{oc} is the open-circuit voltage (when there is no current going through the device), and FF is a fill factor, defined as:

$$\text{FF} = \frac{J_{\text{mp}} V_{\text{mp}}}{J_{\text{sc}} V_{\text{oc}}} \tag{1.3}$$

where J_{mp}, and V_{mp} are the current density and voltage of the device at its maximum power point, where the value of $J \times V$ is at its maximum in the *JV* curve. Therefore, to design a high-efficiency solar cell, one may aim to improve either the J_{sc}, V_{oc}, or FF.

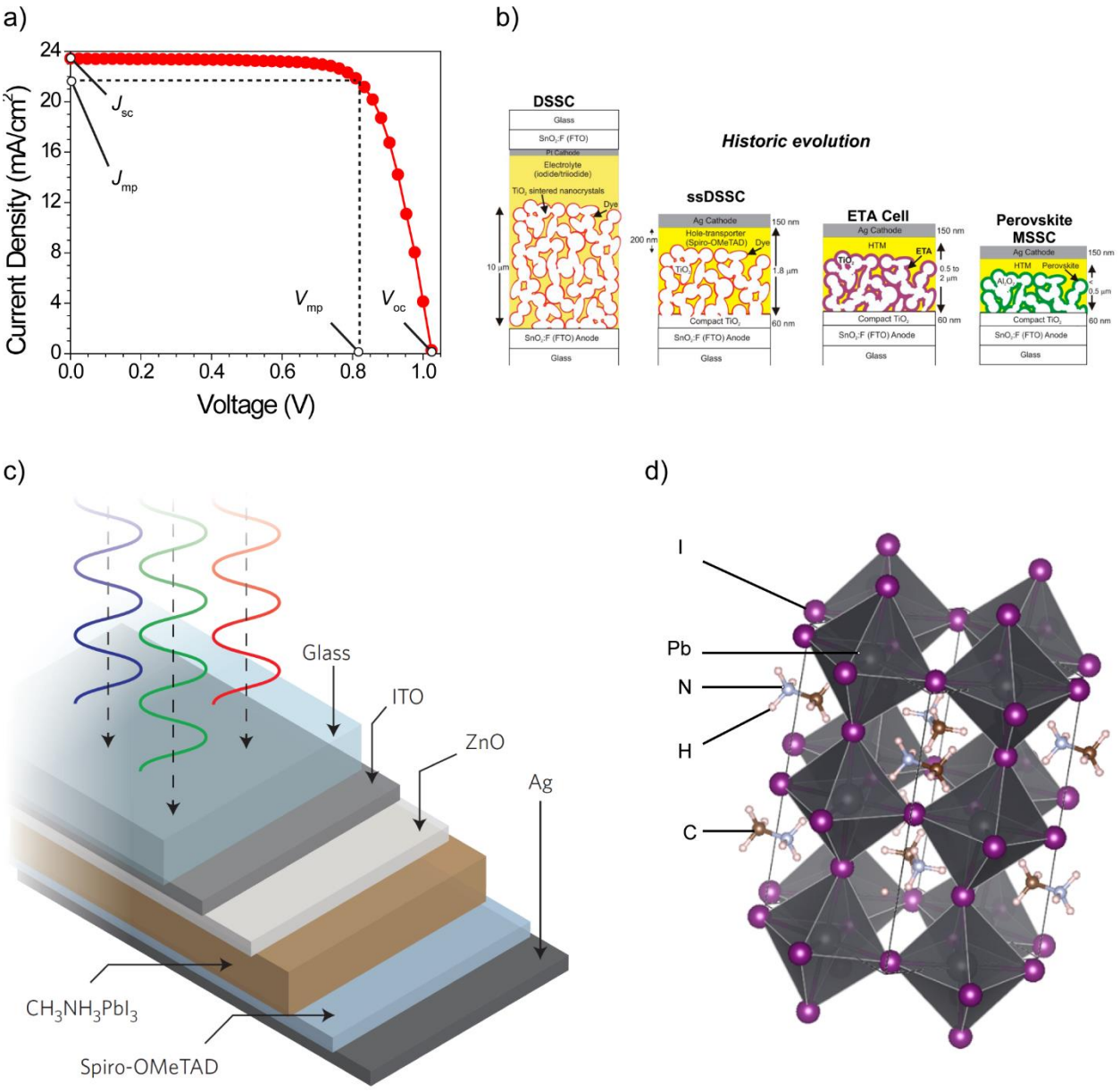

Figure 1.9. (a) A typical *JV* curve showing the current density and voltage at open-circuit or maximum-power conditions. (b) Schematics of device evolution from DSSCs to PSCs. Reprinted with permission.[37] (c) An example of a *n-i-p* and planar-heterojunction perovskite device architecture, fabricated using low-temperature techniques. Reprinted by permission from Macmillan Publishers Ltd: Nature Photonics, copyright 2013.[38] (d) The tetragonal crystal structure of $MAPbI_3$.

1.3.2 Thin-Film Excitonic Solar Cells

An important factor in solar cell design is the thickness of the active layer. The probability of light absorption is augmented by using a thicker active layer; however, thicker layers do not necessarily result in more efficient solar cells. In the process of absorbing light in excitonic solar cells, excitons (bound electrons and holes) are produced, which need to be transferred to separate electrodes without recombination. This transfer becomes less likely as the active layer thickness increases, resulting in a decrease in both J_{sc} and the internal quantum efficiency of a device. Hence, thin-film excitonic solar cells are used for multiple purposes: to minimize the required diffusion length of the excitons, to reduce the dark current (flowing electric current when there is no light), and to decrease materials costs. However, the active layer of a thin-film solar cell must therefore possess both strong light absorption and effective charge transport properties.

1.3.3 Lead Trihalide Perovskites

Lead trihalide perovskites have recently attracted the attention of researchers. They possess a high extinction coefficient and a low exciton binding energy of 2-12 meV at room temperature.[39-44] This energy is lower than the k_BT (where k_B is the Boltzmann constant and T is temperature) thermal energy of ~26 meV accessible to excitons at room temperature. Therefore, the excitons are almost completely dissociated within the perovskite layer, and the free charge carriers can diffuse independently.

1.3.3.1 Device development and the mechanism of operation

The first perovskite solar cells were developed based on designs used for DSSCs (Figure 1.9b).[37] DSSCs used a liquid electrolyte solution to reduce the photo-oxidized dye. Replacement of this solution by a solid-state hole-transport layer was a key change in PSCs (Figure 1.9b). As another change, the low binding energy of the perovskite allowed it to be used in planar-heterojunction

solar cells. DSSCs used an organic chromophore with a large exciton binding energy. Therefore, to provide effective charge separation, they needed a mesoporous TiO_2 electron-transport layer with a large surface area. In contrast, the low exciton binding energy of the perovskites removed such a need. This was found through a study showing comparable efficiencies when the mesoporous TiO_2 layer was replaced by an insulating mesoporous Al_2O_3 layer (Figure 1.9b).[37, 45] This finding indicated that the perovskite itself was capable of transporting both electrons and holes to the charge-extraction interfaces. Hence, a planar interface between the perovskite and the TiO_2 electron-transport layer was enough for effective charge extraction, and the mesoporous interface did not play an important role. Both changes allowed PSCs to be fabricated in either *n*-*i*-*p* or *p*-*i*-*n* planar device architectures. In such structures, the intrinsic (*i*) perovskite is sandwiched between *n*-type (*n* - to extract electrons) and *p*-type (*p* - to extract holes) interfacial layers. These architectures do not necessarily need high temperatures required to fabricate a mesoporous structure (Figure 1.9c). Different interfacial layers have been used in PSCs, such as metal oxide nanoparticle or compact layers, and organic small molecules or polymer layers.[46] Low temperatures used in the fabrication of interfacial layers are consistent with low thermal tolerance of flexible PSC substrates.

1.3.3.2 ABX_3 composition

A variety of ions may be used in an ABX_3-perovskite structure. Among them, lead trihalide is the material of interest in solar cells. The first perovskite used in PSCs was methylammonium (MA) lead triiodide, in which organic MA cations occupy the void spaces in the PbI_3^- inorganic framework. It has a tetragonal crystal structure at room temperature (Figure 1.9d). Compositional engineering of the perovskite showed that other ions could be substituted into the perovskite lattice, such as formamidinium (FA) instead of MA,[47] or Br^- instead of I^-.[48, 49] PSCs with these ion

substitutions could be made with the same (or improved) efficiencies. The possibility of ion substitution is determined by the Goldschmidt tolerance factor (t_f):[50]

$$t_f = \frac{r_A + r_X}{\sqrt{2}\,(r_B + r_X)} \qquad \text{(Equation 1.4)}$$

where r is the ionic radius of the A-, B-, and X-site species. To have a compact and cubic perovskite structure, t_f is ideally in the range of 0.9-1.0. The variety of choices for the composition of the perovskite provides many pathways to improving the stability and efficiency of PSCs.

1.4 Flexibility in Perovskite Solar Cells

1.4.1 History and Demands

To produce a flexible PSC, many barriers must be overcome. Conventional silicon solar cells are not highly flexible. In contrast, PSCs have shown considerable mechanical flexibility to expand solar energy applications, which is in line with the overall goal of competing with fossil fuels. Flexible devices need to be fabricated on plastic substrates, which cannot tolerate high temperatures. Since a high temperature of 450-500 ºC is typically used to anneal the mesoporous TiO_2 layer, its elimination allowed other electron-transport layers to be used, enabling possible low-temperature fabrication methods for PSCs. This, combined with low-temperature fabrication methods for the perovskite layer itself, allowed flexible PSCs on plastic substrates to be fabricated.[38, 51, 52] Our group fabricated the first flexible PSCs with an efficiency of >10%, using a ZnO nanoparticle electron-transport layer deposited at room temperature (**Figure** 1.9c, **1.10a**).[38] This device was fabricated on metal oxide-coated polyethylene terephthalate (PET) substrates, and its power conversion efficiency (PCE) was retained after bending once with a curvature radius as

low as ~1.3 mm (Figure 1.10b). Another study used a dielectric/metal/dielectric electrode in a *p-i-n* PSC architecture (Figure 1.10c). After bending 50 times using a 5.5-mm radius of curvature, the device parameters were almost unchanged (Figure 1.10d). However, in order to comment on the level of perovskite flexibility in real-world applications, the devices should be more severely tested. For example, their maximum fatigue resistance needs to be explored by monitoring the PCE while bending the device through more than 1000 cycles. It is also unclear whether the perovskite layer or other device components (e.g., the transparent electrode) limit the flexibility.

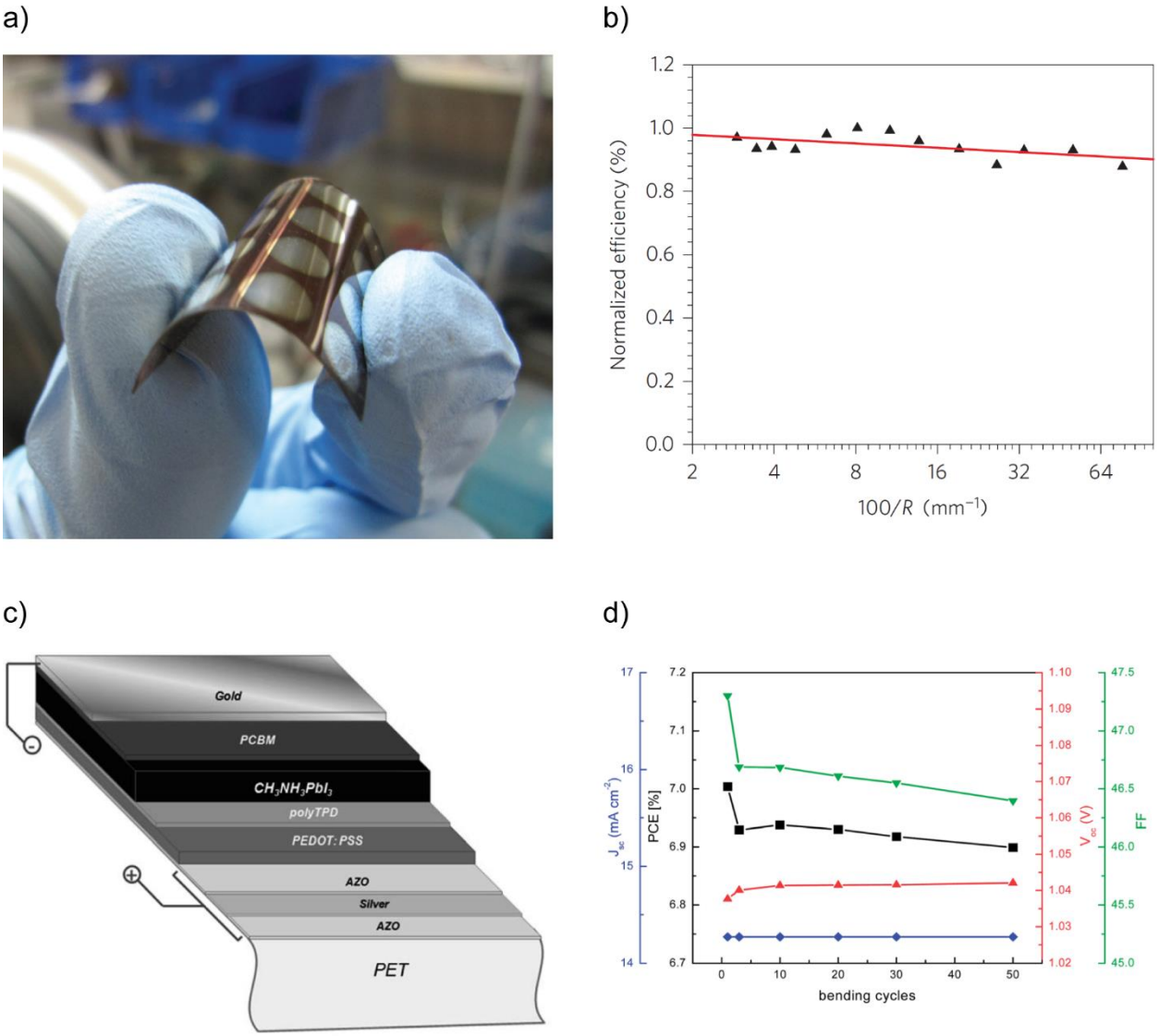

Figure 1.10. (a) A photo of a flexible PSC using the metal oxide electrodes. (b) A test for device flexibility by monitoring the efficiency, while bending the device using different radius of curvature for one time. (a, b) Reprinted by permission from Macmillan Publishers Ltd: Nature Photonics, copyright 2013.[38] (c) An ITO-free flexible perovskite device architecture. (d) A test for device flexibility by monitoring the solar parameters, while bending the device using 5.5 mm radius of curvature for different times. (c, d) Reproduced with permission of The Royal Society of Chemistry.[52]

1.4.2 Disadvantages of Metal Oxide Electrodes

The type of transparent electrode plays an important role in the price, environmental impact, and

flexibility of a solar cell. High temperatures are used to deposit fluorine-doped tin oxide (FTO), making it unsuitable for use on plastic substrates. Instead, thin layers of either indium tin oxide (ITO) or metallized indium oxide are typically used. The ITO electrode is a heavily doped (90% In_2O_3 – 10% SnO_2) n-type semiconductor, commonly used in PSCs.[38, 53] However, because of the scarcity of In, the price of ITO-coated glass has become a serious problem in photovoltaics.[5] Additionally, a life-cycle assessment of all-perovskite tandem solar cells found that the use of ITO was the most important contributor to environmental impacts. These impacts are caused by the energy-intensive sputtering methods of the ITO layer fabrication and the use of In.[54] Moreover, ITO suffers from brittleness and a tendency to crack upon bending. This limits possible flexible applications of optoelectronic devices.

1.4.3 Alternative Transparent Conductive Electrodes

To overcome the disadvantages of metal oxide electrodes, several alternatives have been explored. In a solar cell, high optical transmittance and a low sheet resistance are required in order to produce high photocurrents. Therefore, being in the top left of a graph of transmittance versus sheet resistance is favorable (**Figure 1.11a**).[55] When metal films are thick enough to have low sheet resistance, they have low transmittance as well as poor flexibility. Common methods of synthesizing graphene produce microsheets with defects and numerous boundaries (Figure 1.11b).[56] This results in limited charge transport, still far from what is expected from an ideal two-dimensional graphene sheet. As a result, when it is thin enough to have a high optical transmittance, graphene has a high sheet resistance. Silver nanowires have the best combination of transmittance and conductivity; however, nanowire and nanofiber structures have been shown to short-circuit devices by contacting the other electrode, and therefore need to be extremely flat.[57] This makes their fabrication

process difficult and gives no guarantee that the nanowire networks will maintain flat after bending. In a study, applying a mechanical pressure of 81 GPa decreased the surface roughness of Ag nanowires from 110 nm to 47 nm (Figure 1.11c), which was still unsuitable for use in LEDs and solar cells.[58] In contrast, highly-conductive poly(3,4-ethylenedioxythiophene):poly(styrenesulphonate) (PEDOT:PSS) electrodes (**Figure 1.12a**) have high transmittance even at the thicknesses required for low sheet resistance. These electrodes show enormous mechanical flexibility, and can be fabricated by easy solution-based processing.

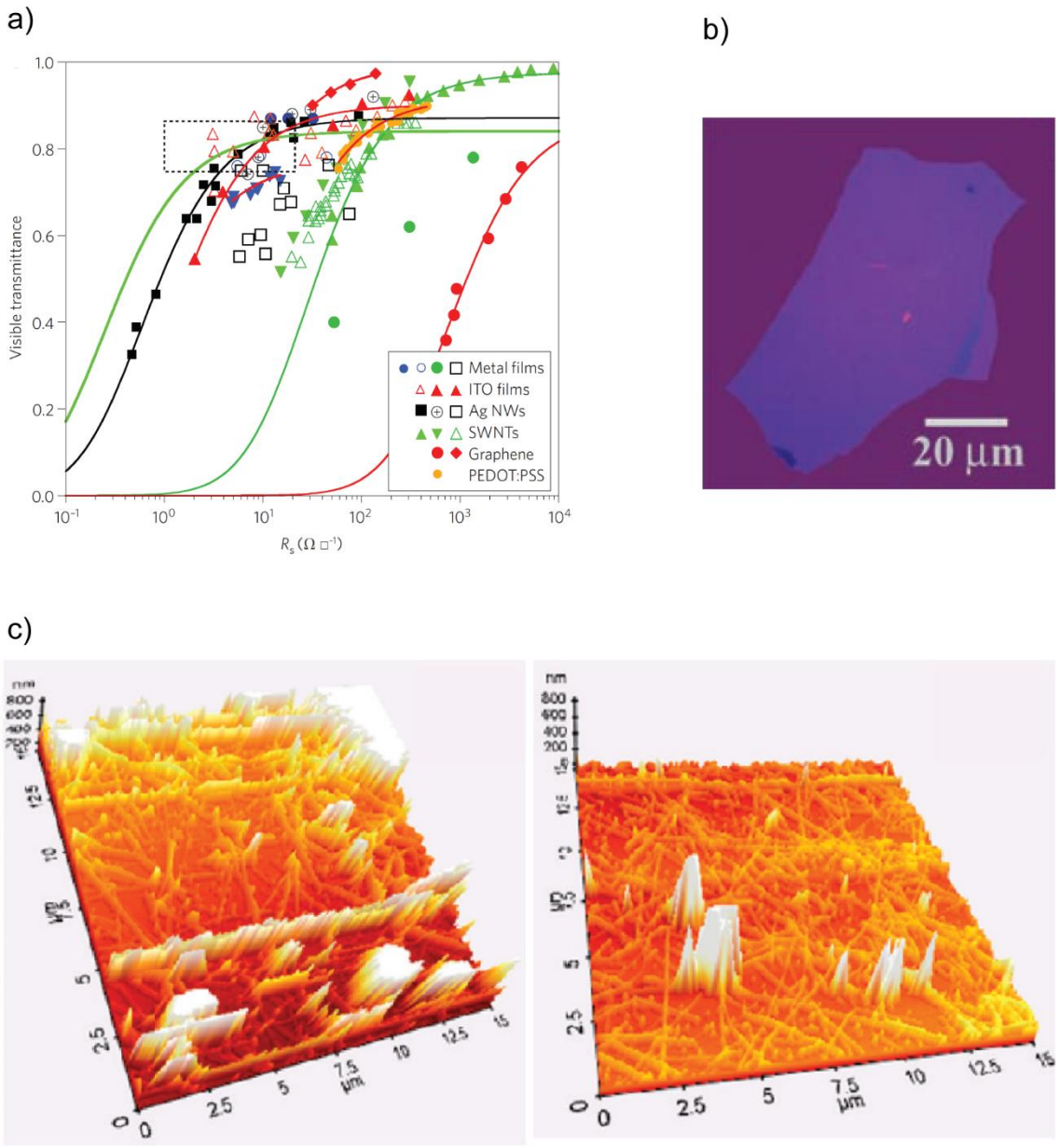

Figure 1.11. (a) Visible transmittance as a function of sheet resistance for a variety of TCEs. The rectangle's bottom and right sides suggest minimum required amounts of these two parameters for photovoltaics. The fitting lines are based on a transmittance-sheet resistance formula, Reprinted by permission from Macmillan Publishers Ltd: Nature Photonics, copyright 2012.[55] (b) A photo of a graphene microsheet. Reprinted with permission from AAAS.[56] (c) Atomic force microscopy (AFM) images of Ag nanowires (left) before and (right) after 81-GPa mechanical pressure for 50 s. Reprinted with permission.[58]

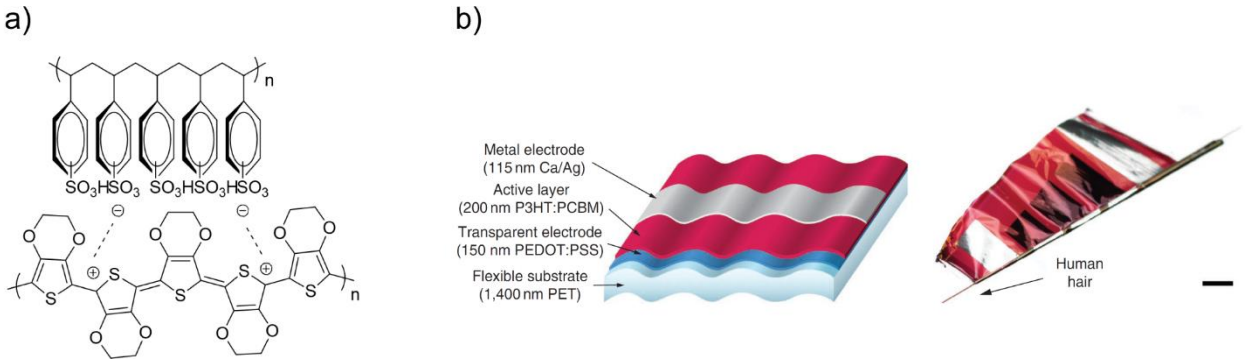

Figure 1.12. (a) Chemical structure of HC-PEDOT electrodes, as a mixture of the conductive PEDOT and insulator PSS polymers. (b) Schematics of an OSC device architecture made from a HC-PEDOT electrode, which is then bent around a piece of hair with the radius of 35 μm. Size bar is 500 μm, reprinted with permission.[59]

1.4.4 A Highly-Conductive PEDOT Electrode: an Alternative

Highly-conductive PEDOT (HC-PEDOT) electrodes have already been used in OSCs. As an example, HC-PEDOT was used to coat a 1400 nm PET substrate, onto which a bulk-heterojunction layer of poly(3-hexylthiophene) (P3HT) and (6,6)-phenyl-C_{61}-butyric acid methyl ester ($PC_{61}BM$) was then deposited.[59] The sheet resistance of the electrode was about 100 $\Omega\ \square^{-1}$. The PCE of the device was 4.2%, identical to that of devices with glass/ITO electrodes. The extremely thin substrate and the polymeric nature of the HC-PEDOT electrode made the device extremely flexible, and it could be wrapped around a piece of hair with a radius of 0.35 μm (Figure 1.12b). At the time of our publication (chapter 3), the metal oxide electrode had not been replaced by HC-PEDOT in a PSC. By comparing the fatigue resistance of a HC-PEDOT based PSC to an organic device, we hoped to gain information about the inherent flexibility and fatigue resistance of $MAPbI_3$.

1.5 Stability of Perovskite Solar Cells

Although highly-efficient, cost-effective, light-weight, and flexible, perovskite solar cells still have short device lifetimes. Expensive, heavy, and rigid silicon solar cells are nonetheless the market-leading technology, because of their high efficiency and 25-year warranty. To compete with silicon, the lifetime of PSCs needs to be substantially improved.

1.5.1 Factors Affecting the Stability

To improve the stability of perovskite solar cells, the following steps can be followed: (i) harmful environmental factors should be recognized, (ii) the mechanism by which those factors cause the degradation of a device needs to be understood, and (iii) strategies to prevent those mechanisms need to be developed. Humidity and the co-presence of O_2 and either light or electrical bias are the most significant harmful factors recognized for PSCs.[60-62]

1.5.1.1 The effect of humidity

The decomposition of $MAPbI_3$ in a humid environment occurs through the formation of hydrate phases. First, our group showed that by exposing $MAPbI_3$ to a high humidity environment, a dihydrate phase is formed.[61, 63] This eventually decomposes further, forming PbI_2 upon prolonged exposure. Further studies by Leguy *et al.* showed that before the formation of the dihydrate phase, a monohydrate phase is reversibly formed on short exposures to humidity (Figure 1.13).[60] (**Figure 1.13a**). This process is driven by the formation of hydrogen bonds between the oxygen of a H_2O molecule and the hydrogen of the MA cation, as observable in the crystal structure of the monohydrate phase (Figure 1.13b). In a longer exposure to humidity, the monohydrate phase gives place to the dihydrate phase, and can be identified by the disappearance of the monohydrate-phase peaks in a powder X-ray diffraction (pXRD) pattern.

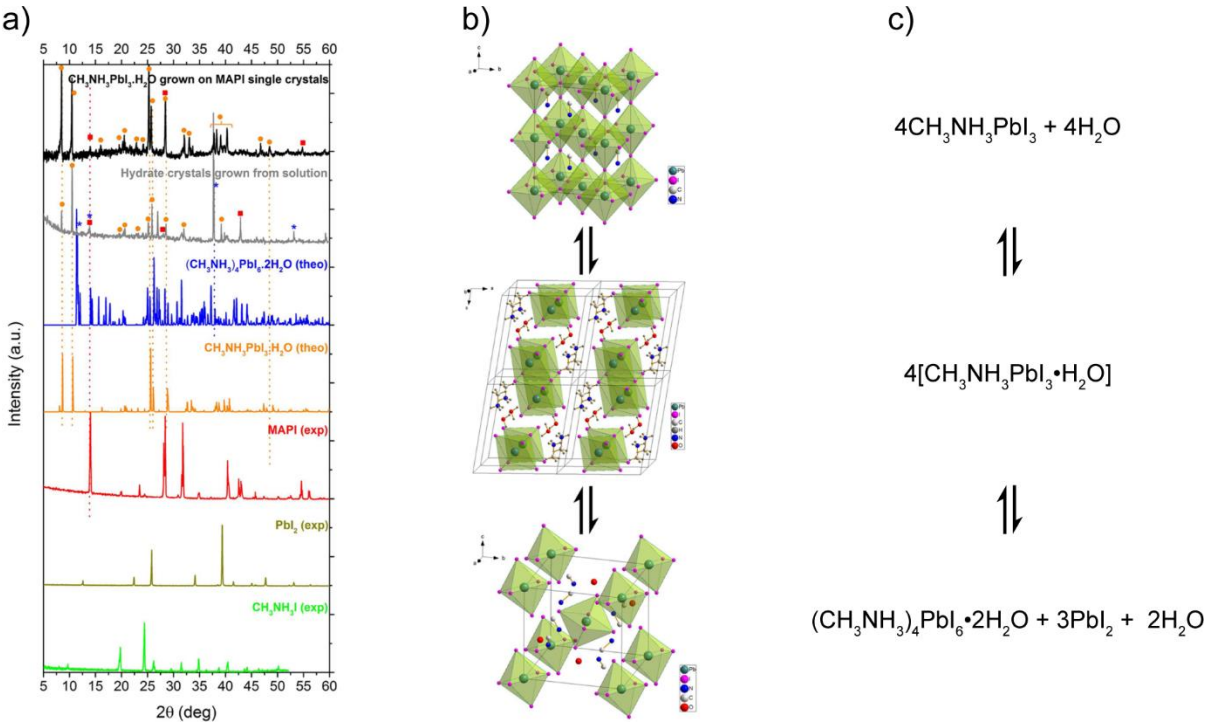

Figure 1.13. Decomposition of $MAPbI_3$ by humidity. (a) pXRD patterns, and (b) crystal structure of $MAPbI_3$ and its mono- and di-hydrate products, while exposed to humidity, reprinted with permission.[60] (c) Decomposition reaction.

1.5.1.2 The effect of O_2 and either light or bias

Despite what was initially thought, the co-presence of O_2 and conduction band electrons, produced by either light or bias, was shown to be more damaging than humidity (**Figure 1.14**).[62] This forms superoxide anions (O_2^-), by reducing O_2 molecules which are located in I^- vacancies in the crystal structure (Figure 1.14a).[64] The presence of O_2^- was evidenced by an increase in the photoluminescence intensity of a hydroethidine probe solution, after immersing the perovskite films already exposed to O_2 and light (Figure 1.14b).[62, 65] In such a solution, O_2^- oxidizes hydroethidine to a fluorescent compound.[66] After its formation, O_2^- deprotonates the MA cation of $MAPbI_3$, leading to its fast decomposition. Interestingly, when $MAPbI_3$ devices were separately

exposed to humidity, O_2, light (Figure 1.14c), or bias (Figure 1.14d), their PCE did not decrease. The synergetic effects of O_2 and conduction band electrons were stronger than the effect of each alone.

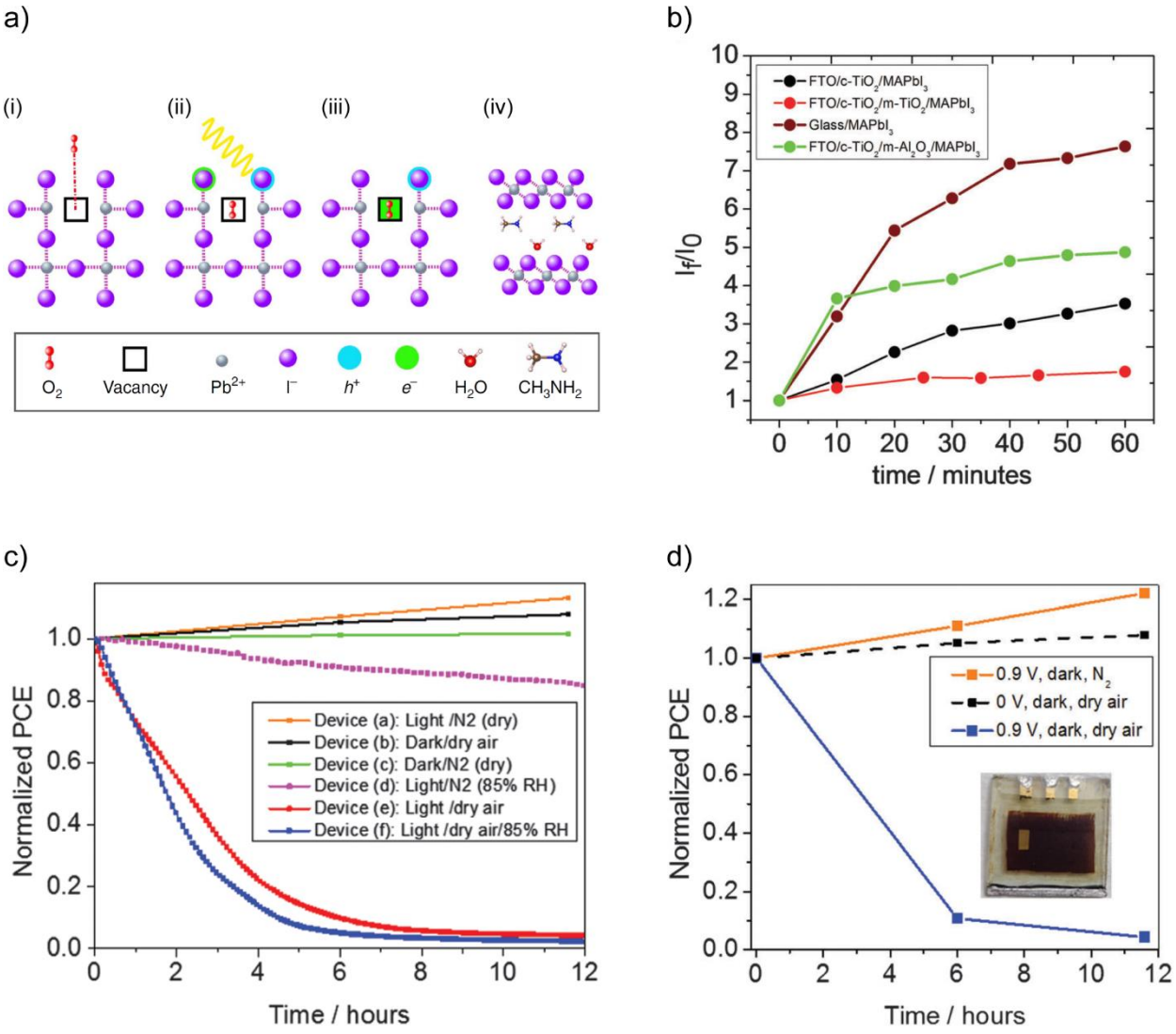

Figure 1.14. Decomposition of $MAPbI_3$ by the co-presence of O_2 and electrons. (a) Mechanism: (i) O_2 intrusion, (ii) photocarrier generation, (iii) superoxide formation, and (iv) perovskite decomposition, reprinted with permission.[64] (b) Normalized photoluminescence intensities of the perovskite films exposed to superoxide species for different time periods, and immersed in a hydroethidine probe solution. Device decomposition by (c) light or (d) bias, as the source of the electrons for superoxide formation. (b, c, and d) Reprinted with permission.[62]

1.5.2 Need for a Comprehensive Study on Perovskite Stability

To prevent the negative effects of these environmental factors, a number of different strategies have been developed. They are divided into the three main areas of interfacial-layer modification,[67-72] perovskite fabrication methods,[73-79] and perovskite compositional engineering.[80-89] As an example of interfacial-layer modification, a PEDOT:PSS hole-transport layer was replaced by a more hydrophobic layer of sulphated graphene oxide in a *p*-*i*-*n* device configuration.[70] This improved the stability when tested in either of these three conditions: in the dark under ambient conditions (15-30 ºC and 30-50% RH), under 0.5 sun light intensity and a N_2 atmosphere, and under 0.5 sun light intensity in ambient conditions. As an example of improved perovskite fabrication methods, poly(methyl methacrylate) was used in the spin-drying step of the perovskite formation process.[77] In this step, an antisolvent (in which perovskite precursors have very low solubility) is usually used to improve the crystallization of the perovskite. Using poly(methyl methacrylate) in such a solution created a template for nucleation, which resulted in a smoother layer with a higher degree of crystallinity. In addition to achieving a high PCE of 21.6%, it resulted in improved stability when devices were stored in the dark under ambient conditions. In another study, instead of reacting PbI_2 with CH_3NH_3I, PbI_2 was reacted with excess HI to produce $HPbI_3$, and then reacted with excess CH_3NH_2 to produce $CH_3NH_3PbI_3$.[76] The excess amount of the acid and base completely converted the reactants to the perovskite product with fewer vacancy defects. This resulted in improved stability when tested in ambient conditions (RH of 65 ± 5%). As an example of perovskite compositional engineering, 50% of MA was replaced by FA in $MAPb_{(1-x)}Sn_xI_3$ perovskites. This resulted in a denser perovskite layer and in resistance against oxidation, which again improved the stability when tested in ambient conditions (RH of 30-40%).[84] Looking at these studies, one has difficulty comparing the effect of different strategies,

since they were done using different tests under different environmental conditions. Different standard tests have been designed to evaluate the long-term stability of devices. For instance, to pass the standard damp-heat test of International Electrotechnical Commission, a properly encapsulated solar cell must keep its efficiency higher than 90% of its initial value, after being simultaneously exposed to 85% relative humidity (RH) and 85 ºC, for a period of 1000 h.[90] Therefore, as a basic strategy to investigate the effect of perovskite composition on the stability, each sample should be exposed to exactly the same environmental factors. Such a comprehensive study would allow valid conclusions to be drawn, leading to a better understanding of how to improve PSC technology.

1.6 Designing Stable and Efficient Perovskite Solar Cells

Although many studies have reported methods of improving the stability of perovskite solar cells, very few have not sacrificed device efficiency. A recent study conducted a life-cycle assessment of tandem solar cells, coupling commonly-used lead halide perovskites with either silicon, copper indium gallium selenide, copper zinc tin selenide, or a low-bandgap Pb-Sn mixed perovskite.[54] Promisingly, the Pb/(Pb-Sn mixed) tandem solar cell had the lowest environmental impact and energy payback time. However, the values of impact per kWh of produced electricity for all devices were 5-10 times higher than a single-junction silicon solar cell. This was attributed to the moderate efficiency of 21% and the short lifetime of 5 years calculated for the perovskite tandem solar cells, as opposed to the efficiency of 25% and the lifetime of 30 years for the single-junction silicon devices. This study highlights the importance of considering both the efficiency and stability when evaluating solar technologies.

1.6.1 Improving Efficiency by Perovskite Compositional Engineering

To optimize the efficiency of a perovskite solar cell, ion substitutions at the A-, B-, and X-sites have been explored. One important advancement was the replacement of MA by FA in the $MAPbI_3$ perovskite.[47] This shifts the bandgap from 1.53 eV[91] towards the 1.48 eV bandgap of α-$FAPbI_3$.[92] This leads to the absorption of a larger portion of the incident light and an increase in the PCE. However, pure $FAPbI_3$ has been shown to exist in a one-dimensional, non-perovskite δ phase with a large bandgap at room temperature. To stabilize the more suitable α-phase of $FAPbI_3$, it was doped with 15 mol% $MAPbBr_3$.[92] Then, a comprehensive study was carried out to optimize the efficiency of devices prepared using $FAPbI_3$ and $MAPbBr_3$ perovskite components (**Figure 1.15a**), which confirmed that a low percentage of $MAPbBr_3$ should be used.[93] Further increasing the amount of $MAPbBr_3$ resulted in a large blue shift in the bandgap, leading to a reduction in PCE. The addition of CsI to almost the same composition resulted in: (i) a reduction in the appearance of undesired phases, (ii) an increase in the reproducibility of device performance, (iii) an increase in the PCE (Figure 1.15b), and (iv) an improvement in the device stability.[88] These improvements in efficiency and stability show the high tolerance of the ABX_3 perovskite to compositional engineering.

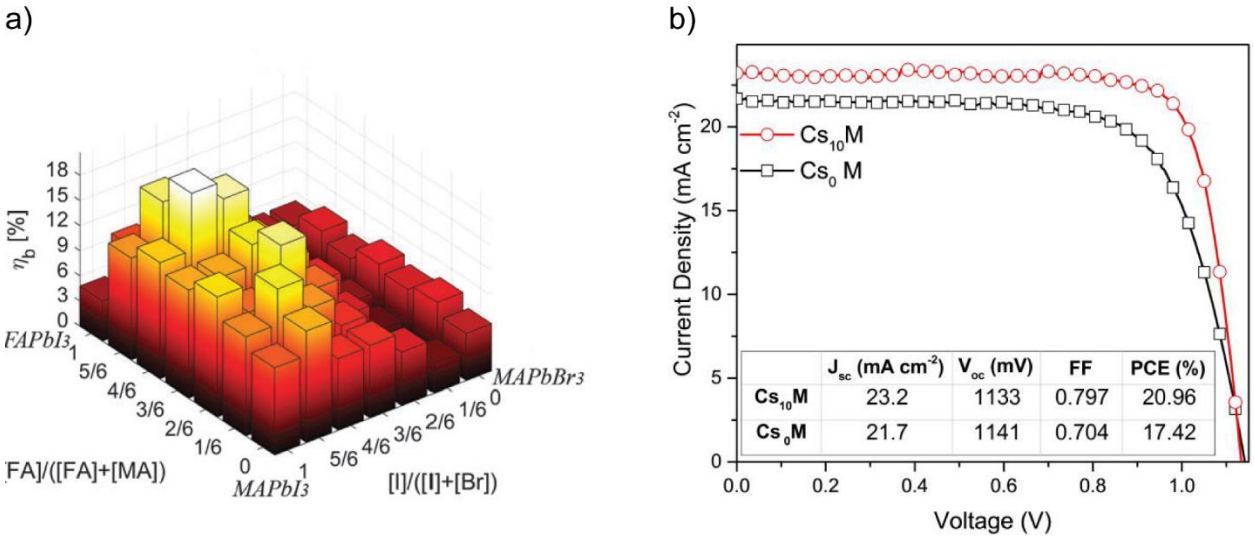

Figure 1.15. (a) Compositional engineering of perovskite to achieve the highest efficiency, Reproduced with permission of The Royal Society of Chemistry.[93] (b) Improving efficiency when 10% CsI is added to the spin-coating solution of perovskite with almost the same composition (shown as *M*) in (a), $Cs_{10}M$ rather than Cs_0M, reprinted with permission.[88]

1.6.2 Device Voltage Loss and Efficiency

The next step to improve the efficiency of perovskite solar cells should be a reduction in device voltage losses. In a recent study, the solar parameters of five literature examples of perovskite solar cells with >20% PCE were compared with their theoretical limits (**Figure 1.16a**).[94] The maximum J_{sc} was calculated by integrating the AM1.5G solar spectrum for wavelengths shorter than the bandgap of the corresponding perovskite. The maximum V_{oc} was calculated based on the Shockley-Queisser limit. In this regard, one can think about a solar cell and its surroundings in the dark and all at ambient temperature. The solar cell absorbs part of the infrared blackbody radiation of the surroundings. In an equilibrium condition, the solar cell must emit what it has absorbed. This dark emission of the solar cell determines its maximum possible V_{oc}, known as the thermodynamic radiative limit.[94] Based on this V_{oc}, the maximum FF can be calculated (the maximum FF values shown by a line and bars (Figure 1.15a) are based on direct and defective

electron-hole recombination, respectively). As observed, the experimental J_{sc} and FF values are very close to their maximum limit; however, the V_{oc} can still be increased (Figure 1.16a). Non-radiative recombination is an important contributor to a low V_{oc} value. The main cause of non-radiative recombination is the presence of trap states originating from defects, such as iodide vacancies. In line with this concept, the highest perovskite solar cell efficiency reported to date (certified 22.1%) was achieved by providing extra I^- to mitigate I^- vacancies.[95] Therefore, the focus of future research to improve device efficiency should be on decreasing the density of trap states in the perovskite.

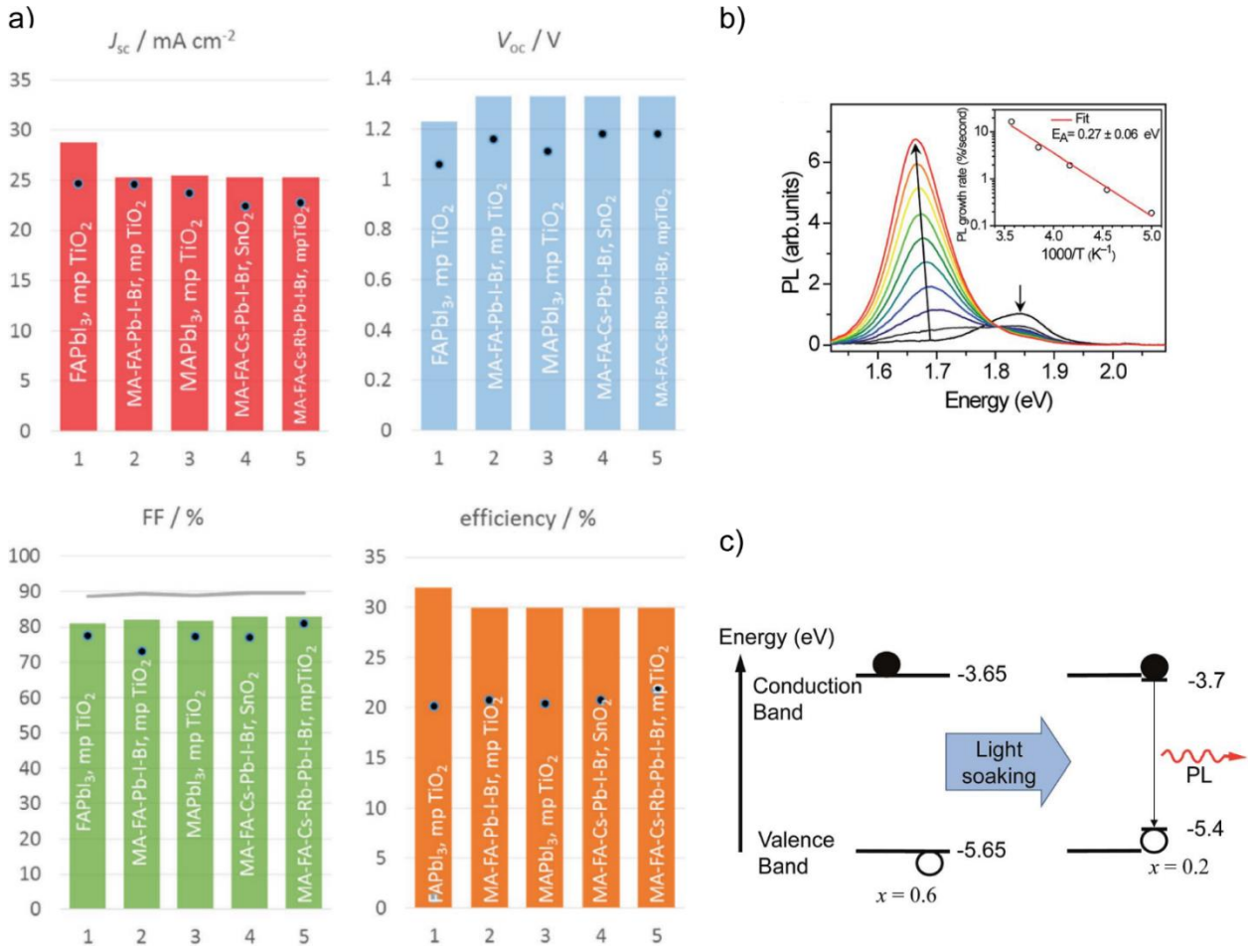

Figure 1.16. (a) The maximum theoretically-possible (bars) and currently-achieved (black dots) values of the solar parameters. The achieved values were picked from five studies reporting a >20% PCE: 1,[96] 2,[97] 3,[98] 4,[99] 5,[82] reprinted with permission.[94] (b) Changes in the photoluminescence (PL) spectra of a $MAPbI_{3-x}Br_x$ perovskite during 45 s of illumination at 15 mW/cm^2 using an Ar ion laser. Inset shows the temperature dependency of the PL growth, (c) Schematics of trap states related to I^--rich domains (here shown with -5.4 eV energy level) in between the HOMO and LUMO of $MAPbI_{3-x}Br_x$, reprinted with permission.[100]

1.6.3 Concerns over Stability

To compete with silicon solar cells in the market, one should improve the efficiency while not decreasing device lifetimes. Although compositional engineering of the perovskite layer has led to remarkable improvements in efficiency, a perovskite with that composition suffers from two important stability issues. Based on the results of our study on the stability of lead halide

perovskites (chapter 4), FA-containing perovskites decompose slower than pure $MAPbI_3$ when exposed to either humidity or oxygen and light. State-of-the-art perovskite solar cells still contain 15 mol% of MA. Therefore, one strategy to improve the stability of these devices is to eliminate MA entirely. In addition, it has been shown that $MAPbI_{3-x}Br_x$ perovskites suffer from a halide segregation phenomenon.[100] After illumination at a low intensity of 15 mW/cm^2 for a short time (45 s), the high-energy photoluminescence peak of these perovskites was replaced by a low-energy one (Figure 1.16b). The low-energy peak was attributed to the trap states of I^--rich domains (Figure 1.16c), located between the valence and conduction bands of $MAPbI_{3-x}Br_x$. In addition, the activation energy for the growth rate of the low-energy photoluminescence peak was calculated to be 0.27 ± 0.06 eV (Figure 1.16b - inset). This is consistent with the energy required for ion migration in such perovskites. Therefore, eliminating MA and Br, while not sacrificing device efficiency, may be a useful strategy to improve the stability of perovskite solar cells.

1.7 *Thesis Scope:* Our Approaches to Improve Solar Cell Technology

1.7.1 Objectives of the Research

The overall goal of this thesis is to improve solar photovoltaic technology. In order to accomplish this, four distinct approaches are investigated, and the results reported in chapters 2-5. The specific goal of the first approach is to increase the quantum efficiency of TTA using plasmonic metal nanoparticles. If the efficiency of TTA can be sufficiently increased, this photon upconversion process could be used as a general strategy to increase the photocurrent of a solar cell. The other three approaches described in this thesis are focused on improving perovskite solar cell technology. The specific goal of the second approach is to find and remove the key factor limiting

the flexibility of perovskite solar cells, and to measure the fatigue resistance of the perovskite layer. The third approach is focused on perovskite stability; the specific goal of this project is to compare the effect of various dopants on the moisture resistance and photochemical stability of perovskite films. The specific goal of the last approach is to improve the stability of state-of-the-art perovskite solar cells, without sacrificing device efficiency in the process. To do this, a perovskite composition commonly used by other researchers to fabricate highly efficient devices was studied, and its stability issues were removed. Each of these individual objectives is related to the overall theme of improving solar cells.

1.7.2 Connection between Individual Chapters

As outlined in section 1.7.1, four different approaches have been taken to improve solar cell technology, and each is discussed in a separate chapter of this thesis (chapters 2-5). This section includes a brief outline of the studies and findings, with logical explanations for transitions between each of the chapters.

In chapter 2, a step is made toward breaking the Shockley-Queisser limit. PdOEP and DPA are used as upconversion materials in a thin film of poly(methyl methacrylate). To enhance the quantum efficiency of this TTA process, the scattering and near-field effects of Ag nanoplates are used. The LSPR of these nanoparticles is tuned to match the Q band of PdOEP, which results in an increase in the absorption of PdOEP and in the density of triplet states. This, in turn, results in a more efficient TTA process and an 8.5-fold increase in the intensity of the upconverted light.

Other than TTA, which still faces formidable barriers to its use in real-world applications, other strategies are explored to improve solar cell technology. The emergence of perovskite solar cells presents exciting new opportunities for the development of solar technology. In chapter 3,

the flexibility of PSCs is improved by replacing the metal oxide electrode. First, it is shown that it is the formation of cracks in the metal oxide electrode that, propagating into the perovskite layer, limits the device flexibility. By replacing it with HC-PEDOT electrodes, the fatigue resistance of the devices is improved. This is tested by bending the devices for 2000 cycles using a 4 mm radius of curvature. Next, by comparing the fatigue resistance of the PSCs and organic solar cells, both fabricated using HC-PEDOT electrodes, the inherent flexibility of $MAPbI_3$ is studied.

Improving perovskite stability is the third strategy. By the time of completion of our study on the flexibility of PSCs, it was clear that the major barrier to the commercialization of perovskite solar cells was their instability under operational conditions. To improve the stability, different dopants were used by different research groups through different fabrication methods. In addition, device stability was measured using a variety of testing procedures, and by exposing films or devices to different environmental factors. Therefore, the effects of each dopant and each environmental factor on the stability were unknown.

In chapter 4, the effects of different dopants on the stability of $MAPbI_3$ perovskite films are compared. In addition to pure $MAPbI_3$, thin films with 20% of either bromide, chloride, EA, or FA doping are prepared. Then, they are stored in either an 85% RH environment or under one sun illumination in dry air. The FA-doped perovskite shows both great moisture resistance and photochemical stability.

In chapter 5, our findings on the stability of perovskite films is further used to improve the stability of state-of-the-art perovskite devices. The majority of devices with efficiencies >20% use a perovskite fabricated by adding $PbBr_2$ and CH_3NH_3Br to PbI_2 and formamidinium iodide. Since this composition suffers from both the relative instability of the MA-rich domains and the halide segregation phenomenon, the stability is improved in this thesis, while not sacrificing the

efficiency in the process. This is done by eliminating the $PbBr_2$ and CH_3NH_3Br components. In addition, since this results in a lower open-circuit voltage, it is shown that the voltage loss can be minimized by adding PbI_2 and guanidinium iodide to the perovskite solution. This leads to a reduction in trap state density.

Plasmon-enhanced TTA strategy can be a starting point for future research to improve the efficiency of any type of solar cell. In addition, other approaches to improve the flexibility, stability, and efficiency of perovskite solar cells are very important regarding the future of this technology.

1.8 References

1. A. R. Ravishankara, J. S. Daniel and R. W. Portmann, *Science*, 2009, **326**, 123-125.
2. C. E. Bachmann, S. Wiemer, J. Woessner and S. Hainzl, *Geophys. J. Int.*, 2011, **186**, 793-807.
3. J. M. Gohlke, S. H. Hrynkow and C. J. Portier, *Environ. Health Perspect.*, 2008, **116**, A236-A237.
4. M. Peplow, *ACS Central Science*, 2015, **1**, 159-160.
5. O. Inganas, *Nat. Photonics*, 2011, **5**, 201-202.
6. W. Shockley and H. J. Queisser, *J. Appl. Phys.*, 1961, **32**, 510-519.
7. B. Lim, G. Y. Margulis, J. H. Yum, E. L. Unger, B. E. Hardin, M. Gratzel, M. D. McGehee and A. Sellinger, *Org. Lett.*, 2013, **15**, 784-787.
8. S. Kraner, R. Scholz, C. Koerner and K. Leo, *J. Phys. Chem. C*, 2015, **119**, 22820-22825.
9. H.-W. Li, Z. Guan, Y. Cheng, T. Lui, Q. Yang, C.-S. Lee, S. Chen and S.-W. Tsang, *Adv. Electron. Mater.*, 2016, **2**, 1600200.
10. M. Knupfer, *Appl. Phys. A*, 2003, **77**, 623-626.
11. B.-G. Kim, C.-G. Zhen, E. J. Jeong, J. Kieffer and J. Kim, *Adv. Funct. Mater.*, 2012, **22**, 1606-1612.
12. J. de Wild, A. Meijerink, J. K. Rath, W. van Sark and R. E. I. Schropp, *Energy Environ. Sci.*, 2011, **4**, 4835-4848.
13. A. Bagheri, H. Arandiyan, C. Boyer and M. Lim, *Adv. Sci.*, 2016, **3**, 1500437.
14. S. Fischer, N. J. J. Johnson, J. Pichaandi, J. C. Goldschmidt and F. C. J. M. v. Veggel, *J. Appl. Phys.*, 2015, **118**, 193105.
15. S. Baluschev, F. Yu, T. Miteva, S. Ahl, A. Yasuda, G. Nelles, W. Knoll and G. Wegner, *Nano Lett.*, 2005, **5**, 2482-2484.

16. S. Baluschev, V. Yakutkin, G. Wegner, B. Minch, T. Miteva, G. Nelles and A. Yasuda, *J. Appl. Phys.*, 2007, **101**.
17. S. Baluschev, J. Jacob, Y. S. Avlasevich, P. E. Keivanidis, T. Miteva, A. Yasuda, G. Nelles, A. C. Grimsdale, K. Mullen and G. Wegner, *ChemPhysChem*, 2005, **6**, 1250-1253.
18. P. E. Keivanidis, S. Baluschev, T. Miteva, G. Nelles, U. Scherf, A. Yasuda and G. Wegner, *Adv. Mater.*, 2003, **15**, 2095-2098.
19. Y. C. Simon and C. Weder, *J. Mater. Chem.*, 2012, **22**, 20817-20830.
20. S. Sugunan, PhD thesis, University of Saskatchewan, 2012.
21. C. Zhang, J. Y. Zheng, Y. S. Zhao and J. N. Yao, *Adv. Mater.*, 2011, **23**, 1380-1384.
22. S. Baluschev, T. Miteva, V. Yakutkin, G. Nelles, A. Yasuda and G. Wegner, *Phys. Rev. Lett.*, 2006, **97**, 143903.
23. R. R. Islangulov, J. Lott, C. Weder and F. N. Castellano, *J. Am. Chem. Soc.*, 2007, **129**, 12652-12653.
24. T. N. Singh-Rachford and F. N. Castellano, *Coord. Chem. Rev.*, 2010, **254**, 2560-2573.
25. T. Ogawa, N. Yanai, A. Monguzzi and N. Kimizuka, *Sci. Rep.*, 2015, **5**, 10882.
26. F. Deng, A. J. Francis, W. W. Weare and F. N. Castellano, *Photochem. Photobiol. Sci.*, 2015, **14**, 1265-1270.
27. K. Xu, J. Zhao, D. Escudero, Z. Mahmood and D. Jacquemin, *J. Phys. Chem. C*, 2015, **119**, 23801-23812.
28. P. C. Boutin, K. P. Ghiggino, T. L. Kelly and R. P. Steer, *J. Phys. Chem. Lett.*, 2013, **4**, 4113-4118.
29. A. Haefele, J. Blumhoff, R. S. Khnayzer and F. N. Castellano, *Journal of Physical Chemistry Letters*, 2012, **3**, 299-303.
30. K. A. Willets and R. P. Van Duyne, *Annu. Rev. Phys. Chem.*, 2007, **58**, 267-297.
31. H. A. Atwater and A. Polman, *Nat. Mater.*, 2010, **9**, 865-865.
32. A. P. Kulkarni, K. M. Noone, K. Munechika, S. R. Guyer and D. S. Ginger, *Nano Lett.*, 2010, **10**, 1501-1505.
33. J. Nelayah, M. Kociak, O. Stephan, N. Geuquet, L. Henrard, F. J. G. de Abajo, I. Pastoriza-Santos, L. M. Liz-Marzan and C. Colliex, *Nano Lett.*, 2010, **10**, 902-907.
34. D. Aherne, D. M. Ledwith, M. Gara and J. M. Kelly, *Adv. Funct. Mater.*, 2008, **18**, 2005-2016.
35. P. P. Pompa, L. Martiradonna, A. D. Torre, F. D. Sala, L. Manna, M. De Vittorio, F. Calabi, R. Cingolani and R. Rinaldi, *Nat. Nanotechnol.*, 2006, **1**, 126-130.
36. A. C. Atre, A. García-Etxarri, H. Alaeian and J. A. Dionne, *J. Opt.*, 2012, **14**, 024008.
37. H. J. Snaith, *J. Phys. Chem. Lett.*, 2013, **4**, 3623-3630.
38. D. Liu and T. L. Kelly, *Nat. Photonics*, 2014, **8**, 133-138.
39. A. Miyata, A. Mitioglu, P. Plochocka, O. Portugall, J. T.-W. Wang, S. D. Stranks, H. J. Snaith and R. J. Nicholas, *Nat. Phys.*, 2015, **11**, 582-587.
40. J. Even, L. Pedesseau and C. Katan, *J. Phys. Chem. C*, 2014, **118**, 11566-11572.
41. Y. Yamada, T. Nakamura, M. Endo, A. Wakamiya and Y. Kanemitsu, *IEEE Journal of Photovoltaics*, 2015, **5**, 401-405.
42. Q. Lin, A. Armin, R. C. R. Nagiri, P. L. Burn and P. Meredith, *Nat. Photonics*, 2015, **9**, 106-112.
43. K. Galkowski, A. Mitioglu, A. Miyata, P. Plochocka, O. Portugall, G. E. Eperon, J. T.-W. Wang, T. Stergiopoulos, S. D. Stranks, H. J. Snaith and R. J. Nicholas, *Energy Environ. Sci.*, 2016, **9**, 962-970.

44. A. M. Soufiani, F. Huang, P. Reece, R. Sheng, A. Ho-Baillie and M. A. Green, *Appl. Phys. Lett.*, 2015, **107**, 231902.
45. J. M. Ball, M. M. Lee, A. Hey and H. J. Snaith, *Energy Environ. Sci.*, 2013, **6**, 1739.
46. M. Ye, X. Hong, F. Zhang and X. Liu, *J. Mater. Chem. A*, 2016, **4**, 6755-6771.
47. N. Pellet, P. Gao, G. Gregori, T.-Y. Yang, M. K. Nazeeruddin, J. Maier and M. Grätzel, *Angew. Chem. Int. Ed.*, 2014, **53**, 3151-3157.
48. K. Tanaka, T. Takahashi, T. Ban, T. Kondo, K. Uchida and N. Miura, *Solid State Commun.*, 2003, **127**, 619-623.
49. J. H. Noh, S. H. Im, J. H. Heo, T. N. Mandal and S. I. Seok, *Nano Lett.*, 2013, **13**, 1764-1769.
50. V. M. Goldschmidt, *Naturwissenschaften*, 1926, **14**, 477-485.
51. P. Docampo, J. M. Ball, M. Darwich, G. E. Eperon and H. J. Snaith, *Nat. Commun.*, 2013, **4**, 2761.
52. C. Roldán-Carmona, O. Malinkiewicz, A. Soriano, G. Mínguez Espallargas, A. Garcia, P. Reinecke, T. Kroyer, M. I. Dar, M. K. Nazeeruddin and H. J. Bolink, *Energy Environ. Sci.*, 2014, **7**, 994-997.
53. O. Malinkiewicz, A. Yella, Y. H. Lee, G. M. Espallargas, M. Graetzel, M. K. Nazeeruddin and H. J. Bolink, *Nat. Photonics*, 2014, **8**, 128-132.
54. I. celik, A. B. Phillips, Z. Song, Y. Yan, R. Ellingson, M. Heben and D. Apul, *Energy Environ. Sci.*, 2017, 10.1039/c7ee01650f.
55. K. Ellmer, *Nat. Photonics*, 2012, **6**, 809-817.
56. K. S. Novoselov, A. K. Geim, S. V. Morozov, D. Jiang, Y. Zhang, S. V. Dubonos, I. V. Grigorieva and A. A. Firsov, *Science*, 2004, **306**, 666-669.
57. S. Soltanian, R. Rahmanian, B. Gholamkhass, N. M. Kiasari, F. Ko and P. Servati, *Adv. Energy Mater.*, 2013, **3**, 1332-1337.
58. L. Hu, H. S. Kim, J.-Y. Lee, P. Peumans and Y. Cui, *ACS Nano*, 2010, **4**, 2955-2963.
59. M. Kaltenbrunner, M. S. White, E. D. Glowacki, T. Sekitani, T. Someya, N. S. Sariciftci and S. Bauer, *Nat. Commun.*, 2012, **3**, 770.
60. A. M. A. Leguy, Y. Hu, M. Campoy-Quiles, M. I. Alonso, O. J. Weber, P. Azarhoosh, M. van Schilfgaarde, M. T. Weller, T. Bein, J. Nelson, P. Docampo and P. R. F. Barnes, *Chem. Mater.*, 2015, **27**, 3397-3407.
61. J. Yang, B. D. Siempelkamp, D. Liu and T. L. Kelly, *ACS Nano*, 2015, **9**, 1955-1963.
62. D. Bryant, N. Aristidou, S. Pont, I. Sanchez-Molina, T. Chotchunangatchaval, S. Wheeler, J. R. Durrant and S. A. Haque, *Energy Environ. Sci.*, 2016, **9**, 1655-1660.
63. B. R. Vincent, K. N. Robertson, T. S. Cameron and O. Knop, *Can. J. Chem.*, 1987, **65**, 1042-1046.
64. N. Aristidou, C. Eames, I. Sanchez-Molina, X. Bu, J. Kosco, M. S. Islam and S. A. Haque, *Nat. Commun.*, 2017, **8**, 15218.
65. N. Aristidou, I. Sanchez-Molina, T. Chotchuangchutchaval, M. Brown, L. Martinez, T. Rath and S. A. Haque, *Angew. Chem. Int. Ed.*, 2015, **54**, 8208-8212.
66. A. Gomes, E. Fernandes and J. L. F. C. Lima, *J. Biochem. Biophys. Methods*, 2005, **65**, 45-80.
67. J. Yin, J. Cao, X. He, S. Yuan, S. Sun, J. Li, N. Zheng and L. Lin, *J. Mater. Chem. A*, 2015, **3**, 16860-16866.

68. A. Fakharuddin, F. Di Giacomo, A. L. Palma, F. Matteocci, I. Ahmed, S. Razza, A. D'Epifanio, S. Licoccia, J. Ismail, A. Di Carlo, T. M. Brown and R. Jose, *ACS Nano*, 2015, **9**, 8420-8429.
69. J. Yang, K. M. Fransishyn and T. L. Kelly, *Chem. Mater.*, 2016, **28**, 7344-7352.
70. H. Chen, Y. Hou, C. E. Halbig, S. Chen, H. Zhang, N. Li, F. Guo, X. Tang, N. Gasparini, I. Levchuk, S. Kahmann, C. O. Ramirez Quiroz, A. Osvet, S. Eigler and C. J. Brabec, *J. Mater. Chem. A*, 2016, **4**, 11604-11610.
71. H. Tan, A. Jain, O. Voznyy, X. Lan, F. P. García de Arquer, J. Z. Fan, R. Quintero-Bermudez, M. Yuan, B. Zhang, Y. Zhao, F. Fan, P. Li, L. N. Quan, Y. Zhao, Z.-H. Lu, Z. Yang, S. Hoogland and E. H. Sargent, *Science*, 2017, **355**, 722-726.
72. J. Lee, J. Kim, C.-L. Lee, G. Kim, T. K. Kim, H. Back, S. Jung, K. Yu, S. Hong, S. Lee, S. Kim, S. Jeong, H. Kang and K. Lee, *Adv. Energy Mater.*, 2017, 1700226.
73. Y. Zhao, J. Wei, H. Li, Y. Yan, W. Zhou, D. Yu and Q. Zhao, *Nat. Commun.*, 2016, **7**, 10228.
74. S. Masi, A. Rizzo, R. Munir, A. Listorti, A. Giuri, C. Esposito Corcione, N. D. Treat, G. Gigli, A. Amassian, N. Stingelin and S. Colella, *Adv. Energy Mater.*, 2017, 1602600.
75. J. Lu, L. Jiang, W. Li, F. Li, N. K. Pai, A. D. Scully, C.-M. Tsai, U. Bach, A. N. Simonov, Y.-B. Cheng and L. Spiccia, *Adv. Energy Mater.*, 2017, 1700444.
76. M. Long, T. Zhang, Y. Chai, C.-F. Ng, T. C. W. Mak, J. Xu and K. Yan, *Nat. Commun.*, 2016, **7**, 13503.
77. D. Bi, C. Yi, J. Luo, J.-D. Décoppet, F. Zhang, Shaik M. Zakeeruddin, X. Li, A. Hagfeldt and M. Grätzel, *Nat. Energy*, 2016, **1**, 16142.
78. C. Qin, T. Matsushima, T. Fujihara and C. Adachi, *Adv. Mater.*, 2017, **29**, 1083808.
79. Y. Sun, Y. Wu, X. Fang, L. Xu, Z. Ma, Y. Lu, W.-H. Zhang, Q. Yu, N. Yuan and J. Ding, *J. Mater. Chem. A*, 2017, **5**, 1374-1379.
80. H. Tsai, W. Nie, J.-C. Blancon, C. C. Stoumpos, R. Asadpour, B. Harutyunyan, A. J. Neukirch, R. Verduzco, J. J. Crochet, S. Tretiak, L. Pedesseau, J. Even, M. A. Alam, G. Gupta, J. Lou, P. M. Ajayan, M. J. Bedzyk, M. G. Kanatzidis and A. D. Mohite, *Nature*, 2016, **536**, 312-316.
81. M. Yang, T. Zhang, P. Schulz, Z. Li, G. Li, D. H. Kim, N. Guo, J. J. Berry, K. Zhu and Y. Zhao, *Nat. Commun.*, 2016, **7**, 12305.
82. M. Saliba, T. Matsui, K. Domanski, J.-Y. Seo, A. Ummadisingu, S. M. Zakeeruddin, J.-P. Correa-Baena, W. R. Tress, A. Abate, A. Hagfeldt and M. Grätzel, *Science*, 2016, **354**, 206-209.
83. G. E. Eperon, T. Leijtens, K. A. Bush, R. Prasanna, T. Green, J. T.-W. Wang, D. P. McMeekin, G. Volonakis, R. L. Milot, R. May, A. Palmstrom, D. J. Slotcavage, R. A. Belisle, J. B. Patel, E. S. Parrott, R. J. Sutton, W. Ma, F. Moghadam, B. Conings, A. Babayigit, H.-G. Boyen, S. Bent, F. Giustino, L. M. Herz, M. B. Johnston, M. D. McGehee and H. J. Snaith, *Science*, 2016, **354**, 861-865.
84. Z. Yang, A. Rajagopal, C.-C. Chueh, S. B. Jo, B. Liu, T. Zhao and A. K. Y. Jen, *Adv. Mater.*, 2016, **28**, 8990-8997.
85. F. Wang, W. Geng, Y. Zhou, H.-H. Fang, C.-J. Tong, M. A. Loi, L.-M. Liu and N. Zhao, *Adv. Mater.*, 2016, **28**, 9986-9992.
86. N. Li, Z. Zhu, C.-C. Chueh, H. Liu, B. Peng, A. Petrone, X. Li, L. Wang and A. K. Y. Jen, *Adv. Energy Mater.*, 2017, **7**, 1601307.

87. J. Liang, C. Wang, Y. Wang, Z. Xu, Z. Lu, Y. Ma, H. Zhu, Y. Hu, C. Xiao, X. Yi, G. Zhu, H. Lv, L. Ma, T. Chen, Z. Tie, Z. Jin and J. Liu, *J. Am. Chem. Soc.*, 2016, **138**, 15829-15832.
88. M. Saliba, T. Matsui, J.-Y. Seo, K. Domanski, J.-P. Correa-Baena, M. K. Nazeeruddin, S. M. Zakeeruddin, W. Tress, A. Abate, A. Hagfeldt and M. Gratzel, *Energy Environ. Sci.*, 2016, **9**, 1989-1997.
89. D. Bi, P. Gao, R. Scopelliti, E. Oveisi, J. Luo, M. Grätzel, A. Hagfeldt and M. K. Nazeeruddin, *Adv. Mater.*, 2016, **28**, 2910-2915.
90. K. Leo, *Nat. Nanotechnol.*, 2015, **10**, 574-575.
91. Y. Liu, Z. Yang, D. Cui, X. Ren, J. Sun, X. Liu, J. Zhang, Q. Wei, H. Fan, F. Yu, X. Zhang, C. Zhao and S. Liu, *Adv. Mater.*, 2015, **27**, 5176-5183.
92. N. J. Jeon, J. H. Noh, W. S. Yang, Y. C. Kim, S. Ryu, J. Seo and S. I. Seok, *Nature*, 2015, **517**, 476-480.
93. T. Jesper Jacobsson, J.-P. Correa-Baena, M. Pazoki, M. Saliba, K. Schenk, M. Gratzel and A. Hagfeldt, *Energy Environ. Sci.*, 2016, **9**, 1706-1724.
94. W. Tress, *Adv. Energy Mater.*, 2017, **7**, 1602358.
95. W. S. Yang, B.-W. Park, E. H. Jung, N. J. Jeon, Y. C. Kim, D. U. Lee, S. S. Shin, J. Seo, E. K. Kim, J. H. Noh and S. I. Seok, *Science*, 2017, **356**, 1376-1379.
96. W. S. Yang, J. H. Noh, N. J. Jeon, Y. C. Kim, S. Ryu, J. Seo and S. I. Seok, *Science*, 2015, **348**, 1234-1237.
97. D. Bi, W. Tress, M. I. Dar, P. Gao, J. Luo, C. Renevier, K. Schenk, A. Abate, F. Giordano, J.-P. Correa Baena, J.-D. Decoppet, S. M. Zakeeruddin, M. K. Nazeeruddin, M. Grätzel and A. Hagfeldt, *Sci. Adv.*, 2016, **2**, e1501170.
98. D.-Y. Son, J.-W. Lee, Y. J. Choi, I.-H. Jang, S. Lee, P. J. Yoo, H. Shin, N. Ahn, M. Choi, D. Kim and N.-G. Park, *Nat. Energy*, 2016, **1**, 16081.
99. E. H. Anaraki, A. Kermanpur, L. Steier, K. Domanski, T. Matsui, W. Tress, M. Saliba, A. Abate, M. Gratzel, A. Hagfeldt and J.-P. Correa-Baena, *Energy Environ. Sci.*, 2016, **9**, 3128-3134.
100. E. T. Hoke, D. J. Slotcavage, E. R. Dohner, A. R. Bowring, H. I. Karunadasa and M. D. McGehee, *Chem. Sci.*, 2015, **6**, 613-617.

Chapter 2. Plasmon-Enhanced Triplet-Triplet Annihilation Using Silver Nanoplates[1]

2.1 Transition Section

This chapter deals with photon upconversion, a very different topic from what is discussed in other chapters; however, ultimately the goal of the photon upconversion process is still to improve solar cell efficiency. This chapter discusses our first approach to improving solar cell technology, and the specific goal of the work is to improve TTA efficiency using plasmonic metal nanoparticles. One aspect of solar cell technology that can be improved is the power conversion efficiency, and one way of improving the efficiency is by increasing the photocurrent. To improve the photocurrent of any type of solar cell, TTA can be used as an upconversion process. However, TTA must occur in the solid state to be compatible with solar cell fabrication and operations. This causes a significant decrease in the efficiency of the TTA itself. Therefore, to help improve the solar technology, as the overall objective of this thesis, metal-enhanced fluorescence is used to increase the intensity of TTA in this chapter. Either in this chapter or in any chapters of 3-5, materials will be briefly discussed in their introduction (sections 2.2, 3.2, 4.2, and 5.2). These

[1] Reprinted with permission from: K. Poorkazem, A. V. Hesketh and T. L. Kelly, *J. Phys. Chem. C*, 2014, **118**, 6398-6404. © 2014 American Chemical Society.
Differences between the published article and the current chapter: adding a transition section, changing the tense of sentences from first-person plural to third-person singular, adding Figure 2.1, embedding supporting information contents in the main text, and other minor corrections based on thesis defense examiners' comments.
Contributions: K.P. carried out the research (except where noted below) and wrote the manuscript. A.V.H. synthesized and phase-transferred the silver nanoplates, captured the TEM image in Figure 2.2b, and measured the particles sizes in Figure 2.2c and the absorption spectrum of silver nanoplates in solution in Figure 2.3a. T.L.K. directed the study, made Figure 2.2a and 2.4, and revised the manuscript.

materials are theories, mechanism, concepts, requirements, and methods, which are already discussed in detail in the introduction chapter of this thesis (sections 1.2-1.6).

2.2 Introduction

The Shockley-Queisser limit places a fundamental limit on the efficiency of single-junction photovoltaic devices.[1] This limit is caused by the inevitable increase in thermalization losses as the bandgap of a semiconductor is lowered, meaning that either transmission or thermalization losses can be minimized, but not both simultaneously. This restricts the power conversion efficiencies of single-junction solar cells to 31%, and devices based on crystalline Si and GaAs have already begun to approach this limit.[2] Recently, photon upconversion has been proposed as a way of circumventing the Shockley-Queisser limit; by converting two photons of low-energy light into a single photon of higher energy, photovoltaic materials with wider bandgaps can be utilized while still harvesting the low energy portion of the solar spectrum.[3] In order to fully realize this approach, the development of highly efficient upconverting systems is required.

Upconversion processes are known to occur for a variety of small molecule dyes,[4, 5] quantum dots,[6] and lanthanide compounds.[7-10] Of these, the lanthanide systems (e.g., $NaYF_4$:Yb,Er) are perhaps the most well known; however, despite undergoing efficient photon upconversion via an energy transfer mechanism, these lanthanide phosphors suffer from narrow absorption bands in the near-infrared region due to the ionic nature of the *f–f* electronic transitions. This makes them highly dependent on sensitization by other chromophores,[10] and limits their utility in harvesting solar radiation. In contrast, small molecule chromophores have inherently broad absorption spectra which can be readily tuned throughout the visible region by tailoring the

molecular structure and through the judicious choice of functional groups. In these systems, TTA is a well-known upconversion mechanism in which two molecules in excited triplet states combine to produce both ground state and higher-lying singlet products.[4, 5] Numerous examples of TTA-based upconversion systems exist in the literature;[11-16] however, of these, the most efficient are those that utilize both a triplet sensitizer and a fluorescent emitter. The triplet sensitizer combines a high extinction coefficient with a large quantum yield for intersystem crossing, thereby producing a high concentration of excited triplet states.[17] Triplet-triplet energy transfer results in the fluorescent emitter being promoted to an excited triplet state, after which two emitter molecules undergo TTA to produce both S_0 and S_n-state ($n \geq 1$) products. Assuming that the emitter has a high fluorescence quantum yield, the net result of this process is the absorption of two low energy photons and the re-emission of one photon of higher energy. While TTA has been previously observed in thin films (as would be required in photovoltaic applications),[18-21] it is inherently a bimolecular process; as such, diffusion limitations mean that its efficiency in condensed media is often quite low.

The localized surface plasmons of noble metal nanoparticles have been shown to effectively improve the efficiency of a variety of optical and optoelectronic phenomena,[22] including Raman scattering,[23] second harmonic generation,[24] and the performance of organic light emitting diodes and photovoltaic devices.[25, 26] One particularly important application of these plasmonic nanomaterials is MEF.[27] This phenomenon manifests as a large increase in emission intensity when there is an overlap between the absorption or emission band of a fluorophore and the LSPR of a metal nanoparticle in close proximity. The origins of the effect are two-fold: (i) the nanoparticle can lead to increased light absorption by the fluorophore due to enhancements of the local electric field; and (ii) coupling of the fluorophore excited state to localized surface plasmons

gives rise to faster emission rates and shorter excited state lifetimes. While MEF has been shown to result in enhanced emission from a wide variety of materials,[28-31] including lanthanide upconversion phosphors,[32] there are very few reports of metal-enhanced triplet-triplet annihilation. Baluschev *et al.* first reported a substantial increase in upconverted emission from a platinum porphyrin / polyfluorene film when it was deposited on top of a thin film of silver;[33] however, this study utilized an optical prism in a Kretschmann-configuration to excite surface plasmon polariton modes in the silver film, and the necessity of the prism makes it very difficult to integrate the resultant film into most devices. Similarly, Uemura *et al.* were able to observe tip-enhanced upconverted emission from copper phthalocyanine films;[34] however, the necessity of the scanning tunneling microscope tip again makes this approach impractical for real-world applications. While recent studies utilizing numerical techniques have suggested that the efficiency of TTA can be dramatically improved using nanoparticle systems (e.g., silver nanocrescents),[35] there is a clear impetus to experimentally demonstrate plasmon-enhanced TTA using a simple, scalable process (e.g., nanoparticle-embedded thin films).

In this study, the plasmonic enhancement of triplet-triplet annihilation are reported by the incorporation of silver nanoplates (AgNPs) into poly(methyl methacrylate) (PMMA) thin films containing PdOEP as a triplet sensitizer and DPA as a fluorescent emitter. This process is both efficient and highly scalable, producing measurable upconversion from films as thin as 40 nm, and resulting in a nearly 10-fold enhancement of the upconverted emission intensity for optimized loadings of the silver nanoplates. The design of more efficient photon upconversion systems is expected to have important implications for the efficiency of a variety of optical and optoelectronic processes, most notably photovoltaic devices.

2.1 Experimental Methods

2.1.1 Materials and Methods.

Silver nitrate, sodium borohydride, L-ascorbic acid, trisodium citrate dihydrate, poly(sodium styrenesulfonate) ($M_w \sim 1000$ kDa), 16-mercaptohexadecanoic acid, *N*-(3-dimethylaminopropyl)-*N*′-ethylcarbodiimide hydrochloride, dicyclohexylamine, poly (methyl methacrylate), palladium(II) octaethylporphyrin, and DPA were purchased from commercial suppliers (Fisher Scientific or Sigma-Aldrich) and used as received.

Transmission electron microscopy was performed on a Philips CM10 microscope operated at 80 kV. Dynamic light scattering measurements were made using a Malvern Zetasizer Nano S. Film thicknesses were measured using a D-120 Stylus Profilometer from KLA Tencor. Steady state absorption spectra were acquired with a Cary 6000i UV-Vis-NIR spectrophotometer. Routine emission spectra were measured using a PTI fluorometer. Photon upconversion measurements were made using a 532 nm cw laser excitation source and a custom-modified SPEX fluorometer. The detector was placed at a 45° angle relative to the excitation source in order to eliminate reflected light, and a 532 nm notch filter was used to further prevent any scattered laser light from reaching the detector. A 10-step calibrated neutral density filter was used to control the excitation power density.

2.1.2 Synthesis of Silver Nanoplates.

The AgNPs were synthesized according to literature procedures.[1] Silver seed particles were prepared by combining aqueous trisodium citrate (5 mL, 2.5 mM), aqueous poly(sodium styrenesulfonate) (0.25 mL, 500 $mg \cdot L^{-1}$), and aqueous sodium borohydride (0.3 mL, 10 mM), followed by the addition of aqueous $AgNO_3$ (5 mL, 0.5 mM) at a rate of 2 $mL \cdot min^{-1}$. The silver

nanoplates were then synthesized by combining 50 mL of deionized water, 750 μL of 10 mM aqueous ascorbic acid, and 9–10 mL of silver seed solution (the exact amount required to produce nanoplates with $\lambda_{LSPR} \sim 560$ nm varied slightly with each preparation), followed by the addition of aqueous $AgNO_3$ (30 mL, 0.5 mM) at a rate of 1 mL·min^{-1}. Additional trisodium citrate solution (5 mL, 25 mM) was then added to further stabilize the AgNPs.

2.1.3 Phase Transfer of Silver Nanoplates.

The AgNPs were functionalized and transferred to chloroform following a literature procedure.[2] A solution of 16-mercaptohexadecanoic acid (1.17 mL, 5 mM in ethanol) was added to 96 mL of the as-prepared silver nanoprism solution and the mixture was stirred for 20 min. The product was centrifuged for 2 h at 13000 rpm. The supernatant was discarded and the thiol-functionalized AgNPs were resuspended in ethanol to a final volume of 4 mL. A portion of the resulting solution (1 mL) was added dropwise to 10 mL of an ethanolic solution composed of 50 mM *N*-(3-dimethylaminopropyl)-*N*′-ethylcarbodiimide hydrochloride and 50 mM dicyclohexylamine. After 15 min the functionalized silver nanoplates precipitated and were isolated by centrifugation at 13000 rpm for 1 h. The supernatant was decanted and the precipitate, once dry, was resuspended in chloroform.

2.1.4 Film Preparation.

Glass slides are pre-cleaned by sonicating sequentially in detergent, distilled water, and ethanol, followed by a UV-ozone treatment (15 min). Chloroform solutions containing PMMA, PdOEP, and DPA at concentrations of 2.1 mg/mL, 0.15 mM, and 5.1 mM, and varying amounts of the AgNP stock solution were prepared. Films were prepared by spin coating at 3000 rpm for 20 s followed by 100 rpm for 5 s. All solutions and samples were kept in the dark when not in use.

2.2 Results and Discussion

2.2.1 Synthesis and Phase Transfer of Silver Nanoplates.

In thin films of even the most highly absorbing materials, a substantial portion of the incident light is lost due to transmission. In order to minimize these losses in the PdOEP/DPA/PMMA system, silver nanoplates were synthesized using a highly tunable process,[36] such that their in-plane dipole LSPR band overlapped strongly with the Q-band of the PdOEP (**Figures 2.1 and 2.2**). In the first step of the nanoplate synthesis, small silver nanoparticles were synthesized as seed particles. The nanoseeds were subsequently grown into plate-like nanoparticles via the addition of $AgNO_3$ in the presence of ascorbic acid.[36] Based on the relative ratio of seed particles to $AgNO_3$, the nanoparticles can be grown into nanoplates with varying aspect ratios; since the aspect ratio of the nanoparticle controls the frequency of its localized surface plasmons, this process enables the synthesis of AgNPs with highly tunable LSPR bands. In order to maximize plasmonic effects throughout the entire thickness of the PMMA film, the approach of directly embedding the AgNPs into the polymer matrix is adopted, rather than confining them to either the substrate/polymer or polymer/air interfaces. This requires that the AgNPs be co-dissolved in a common solvent along with the PdOEP, DPA, and PMMA. This was accomplished by first functionalizing the surface of the AgNPs with 16-mercaptohexadecanoic acid. The terminal carboxylate of the thiol ligand provides a functional group that can be readily modified with hydrophobic head-groups. Following an established phase transfer protocol,[37] the 16-mercaptohexadecanoic acid-derivatized nanoplates were reacted with dicyclohexylamine and a carbodiimide coupling agent to produce a hydrophobic nanoparticle surface. The AgNPs were then isolated by centrifugation and were readily re-dispersed in chloroform.

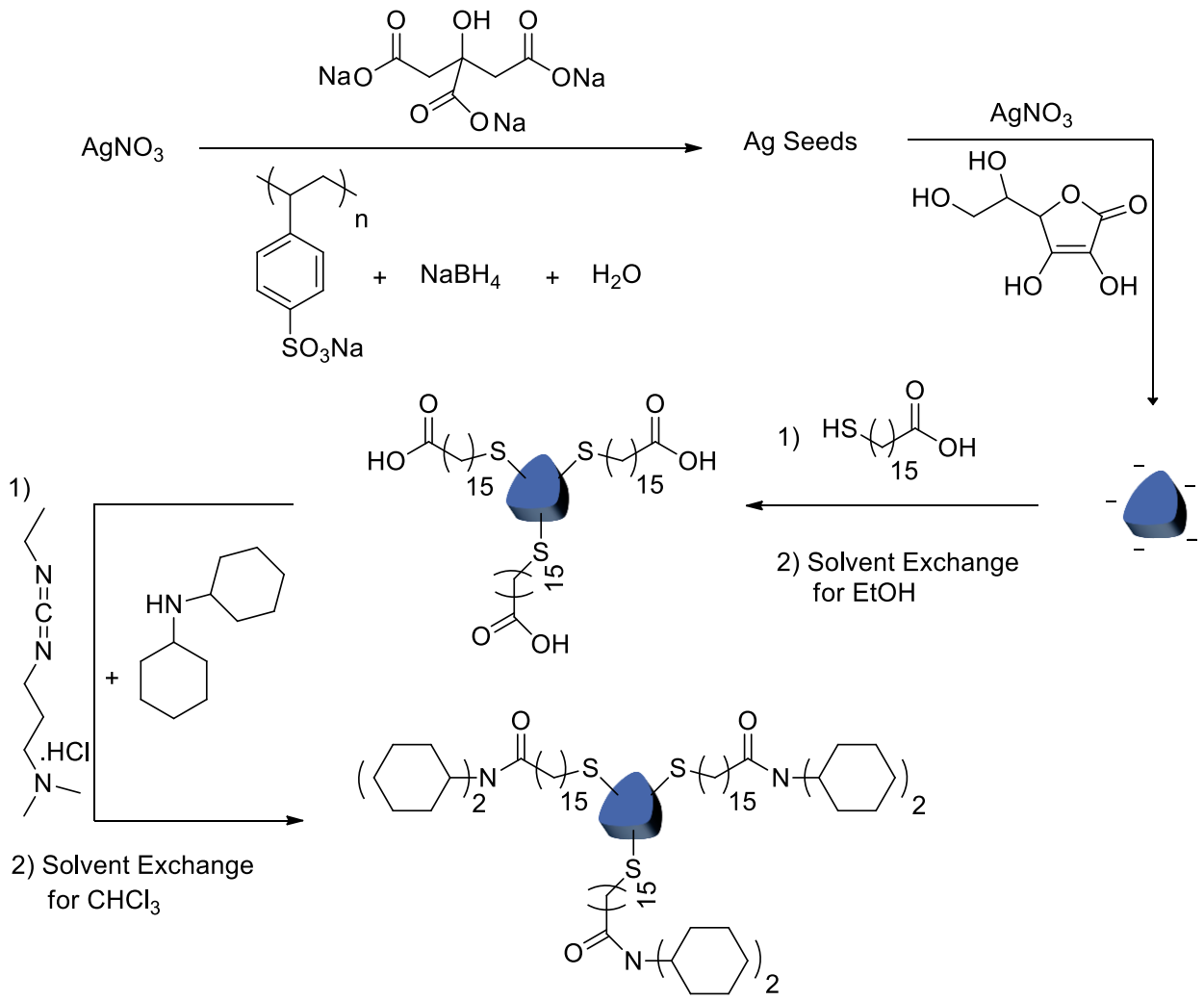

Figure 2.1. The synthesis and aqueous-to-organic phase transfer of Ag nanoplates.

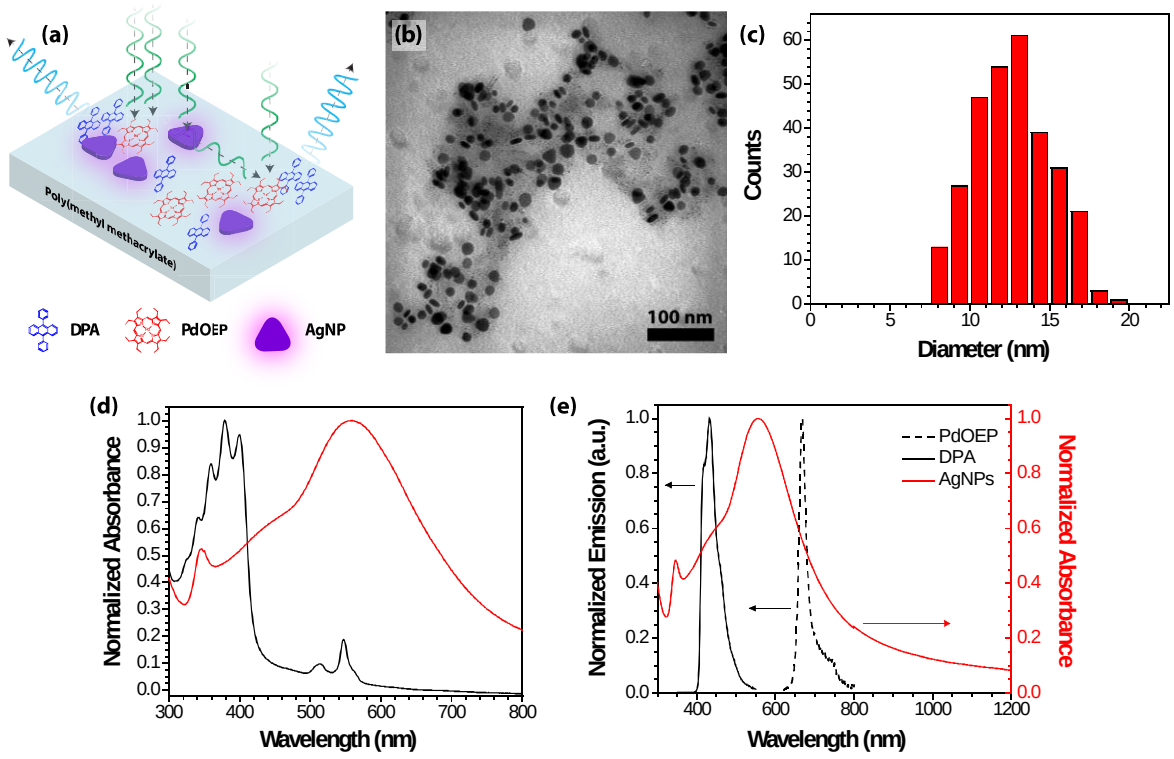

Figure 2.2. (a) Schematic depiction of the metal enhanced triplet-triplet annihilation process in PMMA thin films. (b) TEM image of the AgNPs after functionalization and phase transfer to chloroform. (c) AgNP particle size distribution as-determined by TEM using photoshop. (d) Normalized absorption spectra of both DPA/PdOEP (black line) and the AgNPs (red line) in PMMA films. (e) Emission spectra of DPA (solid black line) and PdOEP (dashed black line) in chloroform solution when directly excited at 288 nm and 550 nm, respectively. The absorption spectrum of the AgNPs in chloroform solution (solid red line) is shown for comparison.

Figure 2.2b shows a TEM image of the silver nanoparticles after undergoing the phase transfer process. As can be seen from the image, the particles are plate-like in structure, and range from round to pseudo-triangular in shape. The anisotropic particle shape plays two important roles in the present study. First, it red-shifts the position of the LSPR band well into the visible region (**Figure 2.3a**), which is not feasible with spherical silver nanoparticles.[38] Second, anisotropic nanoparticles have been shown to produce larger near-field enhancements when compared to their spherical analogues;[22, 38] as such, silver nanoplates and nanoprisms have found extensive use in a

variety of plasmonic applications.[22, 39, 40] The size distribution of the AgNPs is shown in Figure 2.2c. The average diameter of the nanoplates was determined to be 13 ± 2 nm, which is noticeably smaller than the average diameter determined by dynamic light scattering (Figure 2.3b). The dicyclohexylamide-terminated nanoparticles are known to exist as stable aggregates in chloroform solution,[37] and it is these aggregates that are reflected in the light scattering data. This may give rise to several important effects, including the formation of "hot spots" within the polymer film, where multiple nanoparticles in close proximity produce coupled plasmon modes and strongly increased near-field enhancements. Previous work has shown that the aggregation state of the metal nanoparticle can dramatically affect the relative degree of MEF (as compared to fluorescence quenching), with aggregated nanoparticles giving rise to higher emission quantum yields.[41] As such, the morphology of the AgNPs used in the current study suggests that they may be of great utility in MEF applications.

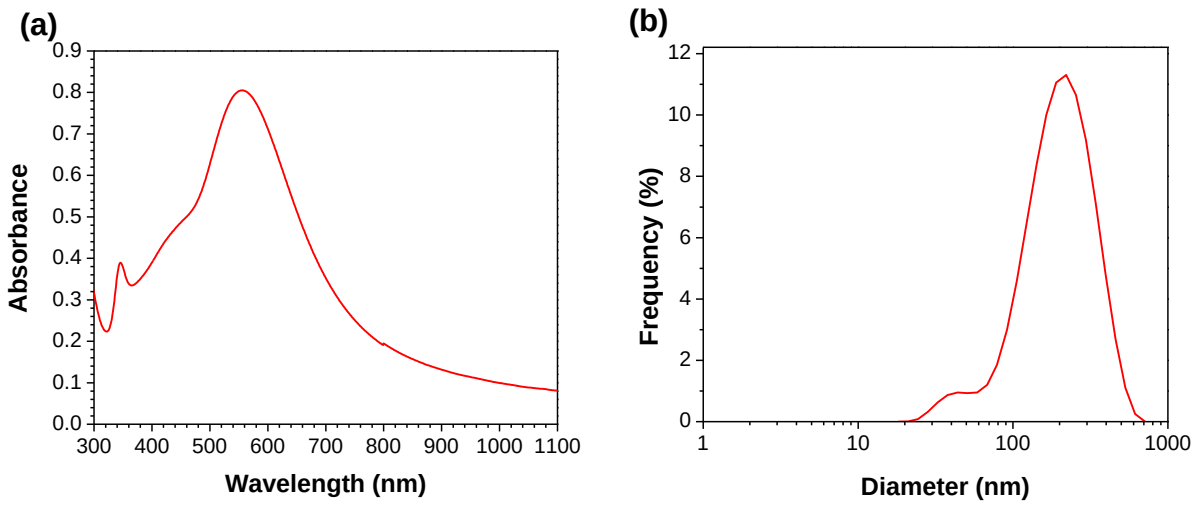

Figure 2.3. (a) Absorption spectrum (acquired using a 1-mm width cuvette) and (b) size distribution (from dynamic light scattering data) of the AgNPs after functionalization and phase transfer to chloroform. The peak and O.D. of the LSPR band in (a) are 556 nm and 0.81, respectively.

Figure 2.2 illustrates the overall strategy used in this work. When excited by light resonant with the LSPR mode, the AgNPs create substantial near-field enhancements within the thin film, leading to increased levels of light absorption by the PdOEP. This should in turn lead to an increased local concentration of excited triplet states (of both sensitizer and emitter) within the film, and a corresponding increase in both phosphorescence and upconverted emission intensities. Alternatively, resonant scattering from the AgNPs could also lead to an increase in light absorption by the sensitizer. Since the oscillating dipole of a localized surface plasmon is an excellent emitter of electromagnetic radiation, larger metal nanoparticles become highly efficient scatterers of light when the frequency is resonant with the LSPR band. As such, by angularly dispersing the incident light, the AgNPs may serve to increase the effective optical path length of the film, thereby leading to increased levels of light absorption and TTA. However, in order for either of these upconversion mechanisms to be active, a primary requirement is that there has to be substantial overlap between

the absorption spectrum of the triplet sensitizer and the LSPR band of the metal nanoparticle. The absorption spectra of both PdOEP/DPA/PMMA and AgNP/PMMA films are shown in Figure 2.2d. When embedded in the PMMA matrix, the AgNPs have a broad in-plane dipole LSPR band[38] centered at 560 nm. Given the breadth of this peak, it overlaps very well with both the Q-bands of the PdOEP (centered at 512 and 546 nm) and the wavelength of the laser excitation source used in this study (532 nm). As such, the AgNPs are expected to give rise to substantial near-field enhancements at the wavelengths relevant to this work. Radiative decay engineering (coupling of the emitter excited state to the LSPR) is also known to give rise to increased luminescence intensities; however, this mechanism requires overlap between the LSPR and the *emission* band of the luminophore. Very poor overlap is observed between the AgNP LSPR band and both the DPA fluorescence and PdOEP phosphorescence bands (Figure 2.2e), and therefore any observed increases in upconverted emission is expected to be due to an increase in light absorption by the PdOEP.

2.2.2 Photon Upconversion Measurements.

In order to study metal enhanced TTA in the solid-state, both PdOEP/DPA/PMMA and PdOEP/DPA/AgNP/PMMA solutions were prepared in chloroform, and thin films of the materials were spin-coated onto pre-cleaned glass slides. Both solutions maintained equal concentrations of the PdOEP, DPA and PMMA, with the only variable being either the presence or absence of the silver nanoplates. Profilometry measurements indicated an average film thickness of 30 ± 20 nm and 40 ± 20 nm for the films with and without AgNPs, respectively. The samples were mounted in a custom-made sample holder such that the PMMA films were held under vacuum during the measurements (**Figure 2.4**). This eliminates the diffusion of oxygen into the films, which would otherwise be expected to efficiently quench the PdOEP T_1 states. **Figure 2.5** shows both the Stokes

and anti-Stokes shifted emission for the thin films when excited with a 532 nm cw laser. In order to ensure the reproducibility of the results, and to eliminate the effects of any variations in film thickness or homogeneity, 6 separate PdOEP/DPA/AgNP/PMMA films and 20 separate PdOEP/DPA/PMMA control samples were measured, and the spectra were averaged. The emission data in the region of 600 – 680 nm (Figure 2.5b), reveals an approximately 3.5-fold increase in the PdOEP phosphorescence intensity upon inclusion of the silver nanoplates into the film. This result is entirely consistent with an increase in the absorption cross-section of the PdOEP chromophore when placed in the AgNP near-field. Based on this increase in the PdOEP triplet concentration, one would further expect that the intensity of upconverted emission would also be enhanced. Figure 2.5a shows the anti-Stokes shifted emission that occurs as a result of the TTA process. Again, a clear increase in emission intensity is observed for the films containing the AgNPs; however, in this case, the difference is much more pronounced, with the upconverted emission intensity from the AgNP-containing films a factor of 6.6 times higher than that of the PdOEP/DPA/PMMA control samples. This yields an approximately 2:1 ratio for the plasmonic enhancement of TTA and phosphorescence. Since TTA is inherently bimolecular in the concentration of PdOEP T_1 states, it is expected to have a non-linear response to the number of absorbed photons,[42] whereas the PdOEP phosphorescence is inherently linear in absorbed photon flux. As such, the upconverted emission intensity is much more sensitive to the absorption cross-section of the triplet sensitizer than the phosphorescence intensity. Therefore, the observed 2:1 ratio of enhancement in TTA / phosphorescence is entirely consistent with an increase in the PdOEP absorption cross-section. However, as discussed previously, one other possibility is that these changes are due to increased emission rates in both the DPA and PdOEP.[27] If this were the case, the shorter PdOEP excited state lifetime would be expected to rapidly deplete the reservoir

of excited triplets, in turn leading to a net reduction in the TTA efficiency. Since this is not observed, and given that neither the DPA nor the PdOEP emission band overlaps significantly with the LSPR of the AgNPs (Figure 2.2e), this is considered unlikely. In order to further prove that an increase in the emission rate is not responsible for the observed increase in emission intensity, both DPA/PMMA and DPA/AgNP/PMMA films were prepared. Addition of the AgNPs results in no measurable increase in fluorescence intensity upon direct excitation of the DPA (λ_{exc} = 350 nm) (**Figure 2.6**), suggesting that the intensity increases observed in Figure 2.5 arise solely from an increase in the PdOEP absorption cross-section.

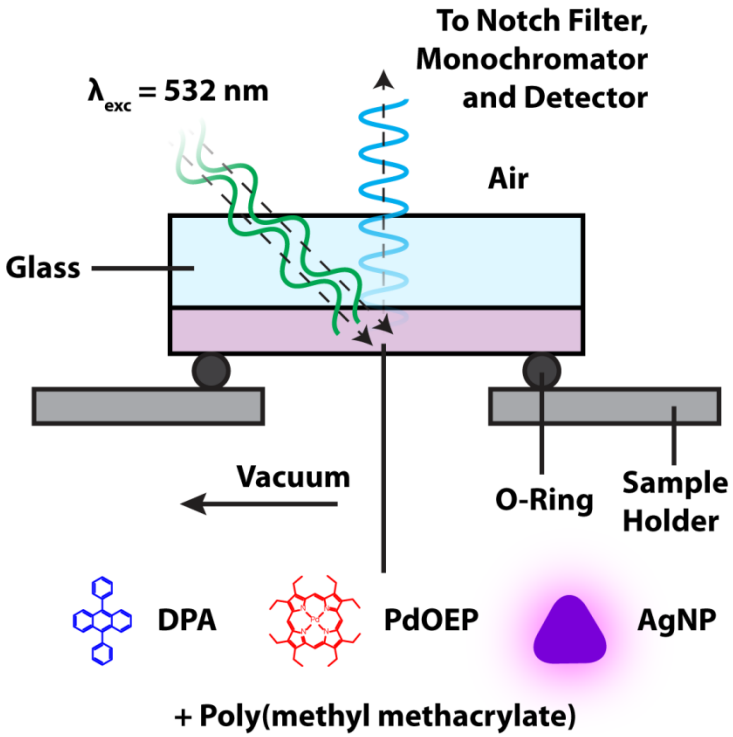

Figure 2.4. Schematic of the sample holder used in the photon upconversion measurements.

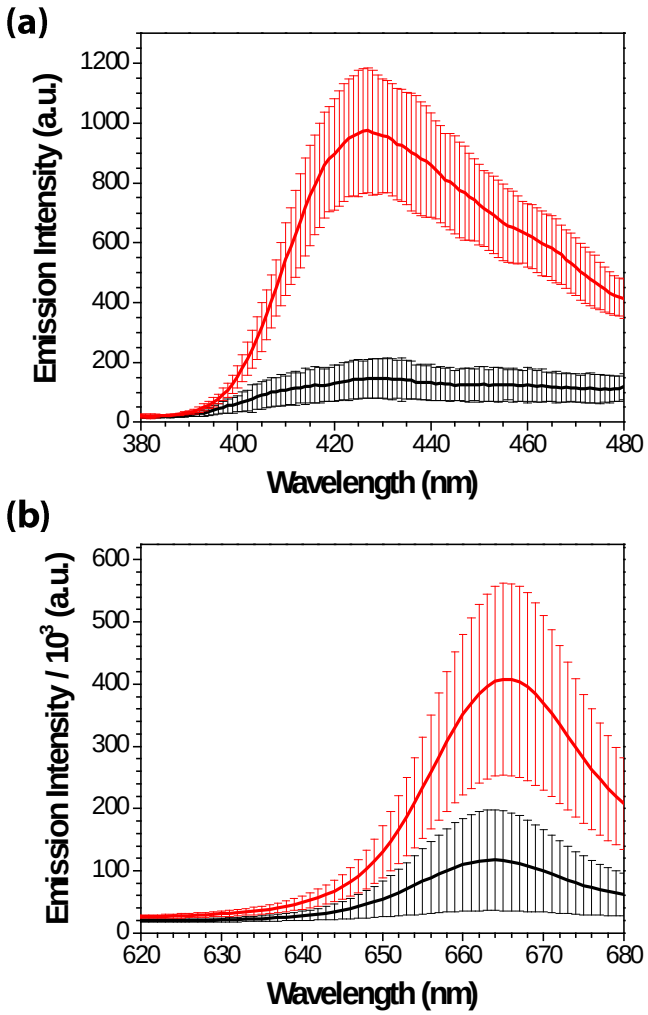

Figure 2.5. Emission spectra of the control (black lines) and AgNP-containing (red lines) DPA/PdOEP/PMMA films showing both (a) DPA fluorescence as a result of TTA, and (b) PdOEP phosphorescence. Spectra are the average of either 20 (for DPA fluorescence of the control samples) or 6 (all other spectra) separate films. The error bars correspond to plus or minus one standard deviation from the mean.

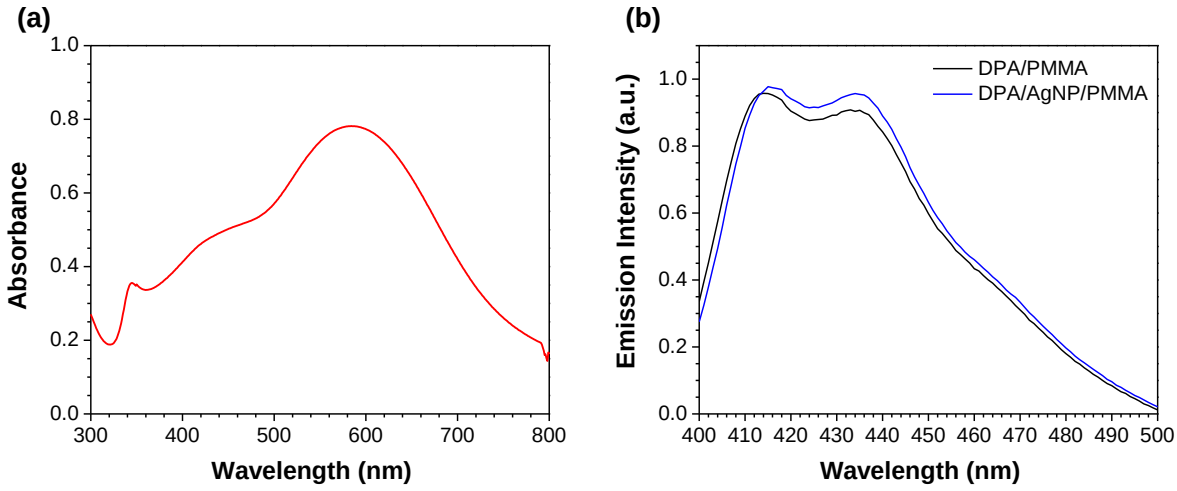

Figure 2.6. (a) UV-vis absorption spectrum of a second batch of silver nanoplates in chloroform solution; (b) emission spectra for both DPA/PMMA and DPA/AgNP/PMMA films (λ_{exc} = 350 nm). The spectra in (b) are average data acquired by measuring four separate films for both the DPA/PMMA and DPA/AgNP/PMMA samples.

2.2.3 Power Dependency Measurements.

The extinction coefficient of the Q-band for most Pd porphyrins is low, and therefore excitation into the Q-band typically results in a low density of triplet states and a low TTA efficiency. As a result, triplet decay is primarily unimolecular in nature, leading to a quadratic dependence of TTA on excitation power (especially at low excitation intensities).[42] If the concentration of excited-state triplets is increased (either by increasing the extinction coefficient at the excitation wavelength or by increasing the excitation power), bimolecular triplet decay (i.e., TTA) becomes favored, leading to a more linear dependence on excitation power. The development of new triplet sensitizers, such as Ir,[43] Pt,[44] and Ru[45] complexes, and organic molecules such as C_{60}[17] and various BODIPY dyes,[46, 47] has been shown to lead to more linear power dependencies in the TTA process. In this work, the plasmon-based increase of the PdOEP absorption cross-section is used in a similar way.

In order to further probe the dependency of the TTA process on the PdOEP triplet concentration, power dependency measurements were carried out on two separate films for both control and AgNP-containing samples. Six separate combinations of neutral density filters were used to attenuate the 532 nm excitation source over a range of power densities. **Figure 2.7** shows the results of these measurements. The intensity of DPA fluorescence is plotted against the intensity of PdOEP phosphorescence in a double logarithmic plot. Since the PdOEP phosphorescence is directly related to the overall yield of T_1 states, the PdOEP phosphorescence intensity is a convenient surrogate for the total number of photons absorbed by the porphyrin. Additionally, by plotting the upconverted emission against the phosphorescence intensity (rather than the incident power density), the data is automatically corrected for any photobleaching or two photon absorption that may occur at the high power densities used.

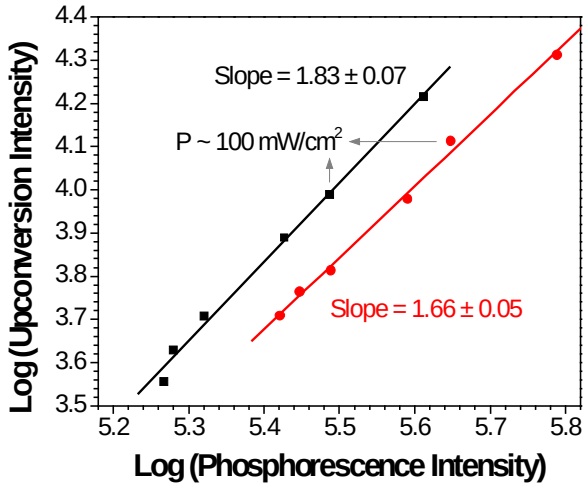

Figure 2.7. Power dependency measurements obtained for both the control (black squares) and AgNP-containing (red circles) films. The data are the average of two separate films. The six data points in each data set correspond to six different power densities, which increase from left to right. The data points corresponding to ~ 1 sun intensity (100 mW/cm^2) are labeled. Upconverted and phosphorescence peak intensities were measured at 430 nm and 662 nm, respectively.

As can be seen in Figure 2.7, the line of best fit for the DPA/PdOEP/PMMA control samples has a slope of 1.83 ± 0.07, indicative of a roughly quadratic dependence of the TTA process on the number of T_1 states. This is consistent with predominantly pseudo-first order decay of the sensitizer/annihilator triplets, typical of low power regimes.[42] In contrast, the line of best fit for the samples containing AgNPs has a slope of 1.66 ± 0.05. This lower slope suggests that a greater proportion of the triplets are decaying *via* bimolecular processes than in the case of the control samples. This implies a higher triplet concentration within the AgNP-containing film (as would typically be observed at higher power densities), and is entirely consistent with plasmonic near-field effects producing an increased level of light absorption within the film (i.e., effectively increasing the local power density). This results in an intermediate power dependency that falls midway between the linear and quadratic regimes.

Importantly, the data also reveal that both the phosphorescence and upconversion emission intensities are higher for the AgNP-containing samples than the controls at a given power density. This is seen as an offset (both horizontal and vertical) between the two power density plots in Figure 2.7, and further reinforces the effectiveness of both the metal enhanced phosphorescence and metal enhanced TTA processes.

2.2.4 Optimization of Silver Nanoplate Loading.

In order to optimize the silver nanoplate loading, the concentration of the silver nanoplates in the DPA/PdOEP/AgNP/PMMA stock solutions was systematically varied. Owing to the difficulties involved in quantifying the AgNP concentration after several synthesis and phase transfer steps, a common AgNP stock solution with an optical density of 0.81 (as measured at the λ_{LSPR} in chloroform solution using a 1 mm path length cuvette) was employed. Varying amounts of this stock solution were blended with aliquots of a common DPA/PdOEP/PMMA stock solution and

diluted with chloroform to the same final volume, producing solutions that were 0% (control samples), 5%, 10%, 20% and 30% AgNP stock solution by volume. Thin films were again prepared by spin coating, and their emissive properties evaluated using a 532 nm cw laser excitation source. **Figure 2.8** and **2.9** show the averaged emission spectra for each set of samples in the DPA fluorescence and PdOEP phosphorescence spectral ranges, respectively. **Figure 2.10** shows the peak intensity (measured at 430 nm for DPA fluorescence and 662 nm for PdOEP phosphorescence) as a function of the silver nanoplate loading. At very low AgNP concentrations (5 – 10%) there is very little change in the emissive properties of the films, but there is a substantial increase in both emission intensities as the AgNP concentration is increased to 20%. After this point, the emission intensities begin to level off, likely because of competitive quenching effects as the concentration of Ag within the film is increased. For the optimized AgNP concentration of 30%, however, it was possible to realize an 8.5-fold increase in the DPA fluorescent emission, indicating that the efficiency of the TTA process increased by nearly an order of magnitude.

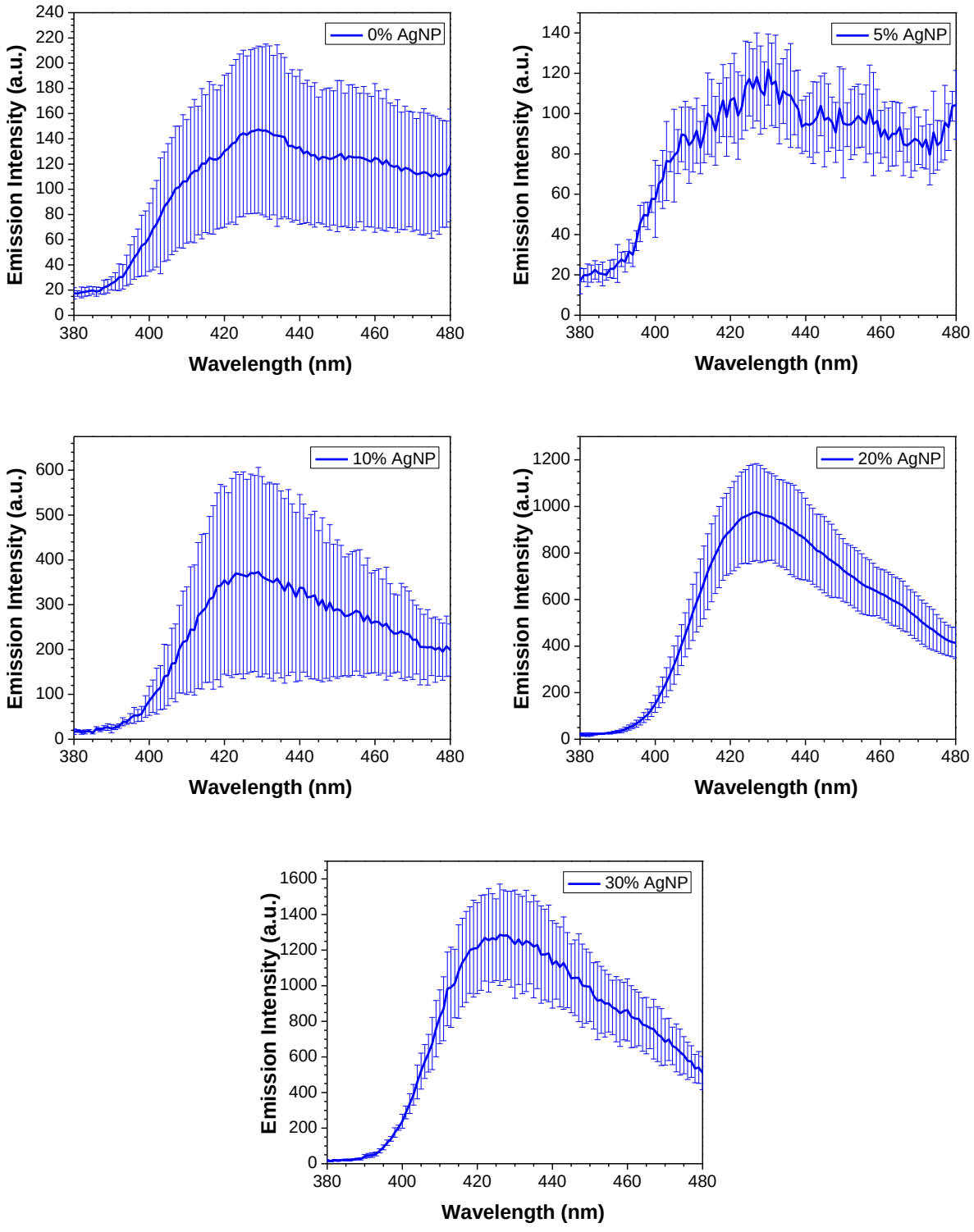

Figure 2.8. Emission spectra (in the DPA fluorescence region) for films prepared with varying AgNP loadings. Spectra are the average of either 20 (0% AgNP), 6 (5 – 20% AgNP) or 5 (30% AgNP) separate films. The error bars represent plus or minus one standard deviation from the mean.

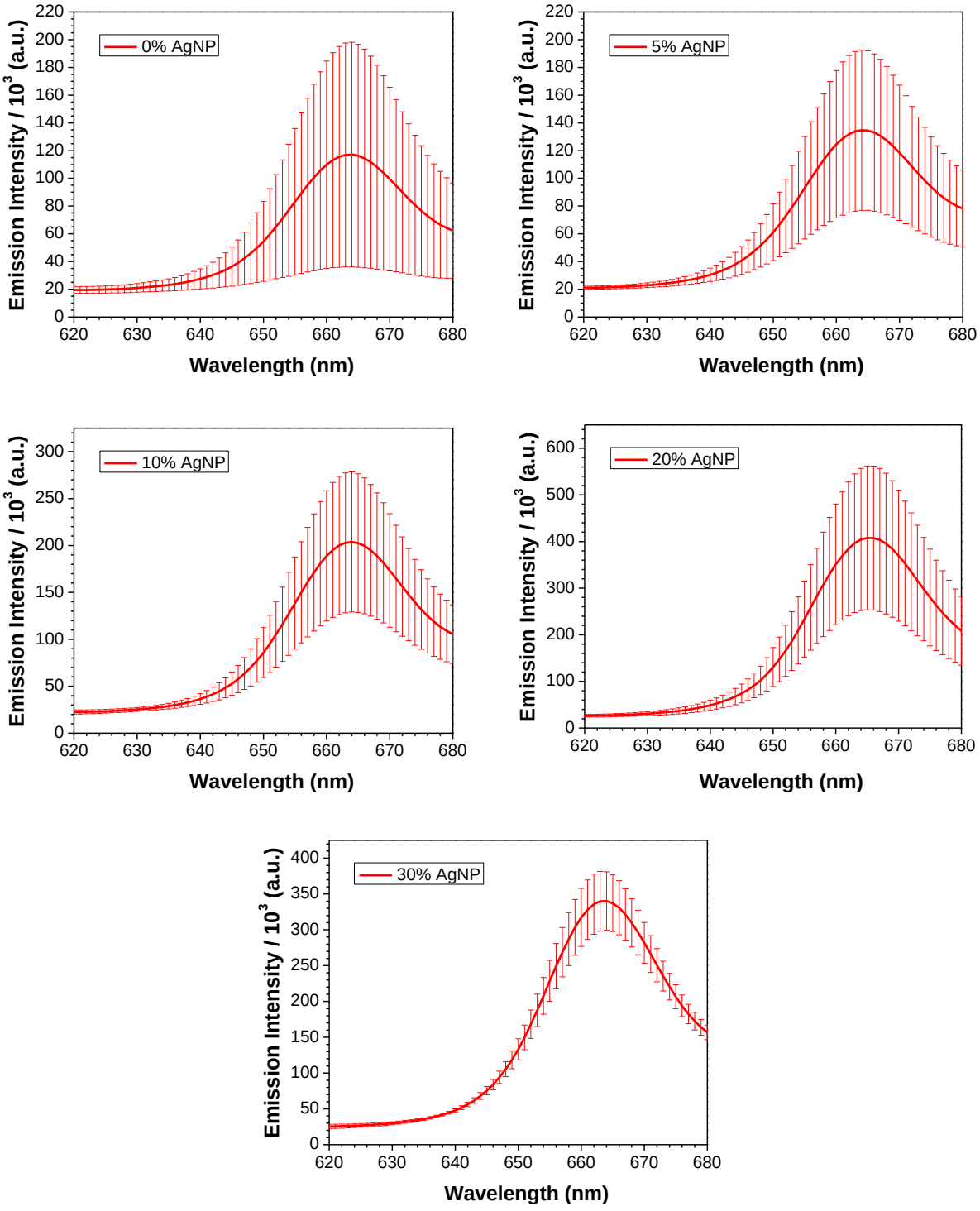

Figure 2.9. Emission spectra (in the PdOEP phosphorescence region) for films prepared with varying AgNP loadings. Spectra are the average of either 20 (0% AgNP), 6 (5 – 20% AgNP) or 5 (30% AgNP) separate films. The error bars represent plus or minus one standard deviation from the mean.

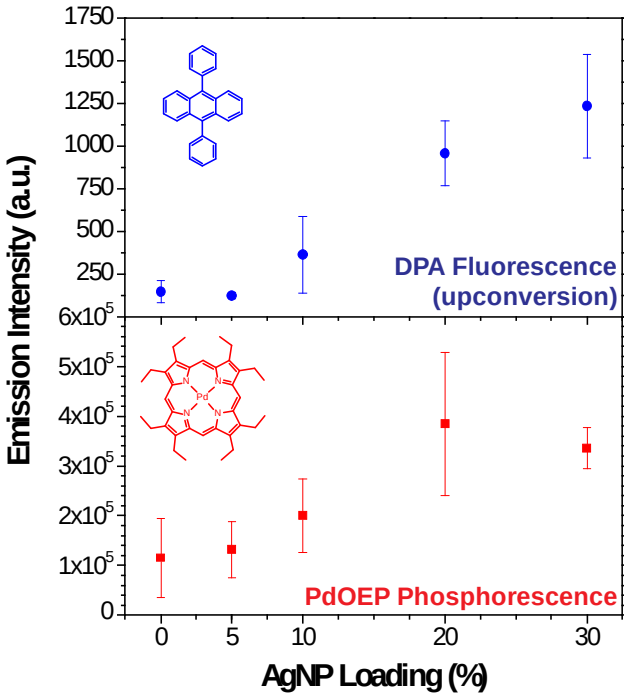

Figure 2.10. Emission intensity of DPA fluorescence resulting from TTA (top, blue circles) and PdOEP phosphorescence (bottom, red squares) as a function of AgNP loading. The error bars represent plus or minus one standard deviation from the mean. Upconverted and phosphorescence peak intensities were measured at 430 nm and 662 nm, respectively.

In order to validate our results, a series of statistical tests are carried out on the data, including both ANOVA and pairwise t-tests at the 95% confidence level. The results of these tests are shown in **Tables 2.1-2.3**. The ANOVA test clearly reveals a dependence of both the phosphorescence emission intensity and upconverted emission intensity on the silver nanoplate loading. The t-tests further reveal that there is no statistically significant change in either DPA fluorescence or PdOEP phosphorescence upon increasing the AgNP concentration to either 5% or 10%; however, upon increasing the concentration to 20%, the change becomes significant for both the upconverted emission and phosphorescence. Profilometry measurements were again carried out on all films to ensure that the observed differences were not due to differences in film thickness

(**Figure 2.11**). Power dependency measurements were also carried out on representative films (**Figure 2.12**), with the slopes of the double logarithmic plots all lying in the range of 1.7 – 2.0, as expected. As observed, the slope was decreased to the lowest value of 1.66 ± 0.05 for the 20% loading of AgNP, and it was increased to 1.99 ± 0.12 when the AgNP loading was further increased to 30%. This was in line with the optimum conditions of 20% AgNP samples, where the maximum possible effects of nanoparticle plasmonics with characteristics specified in this thesis were used to enhance the efficiency of the TTA process.

Table 2.1. Single factor ANOVA test at the 95% confidence level to determine whether the upconversion and phosphorescence emission intensities depend on the AgNP loading. In both cases, $F > F_{critical}$, implying a statistically significant dependence.

	F (Statistic)	**P-value**	**F (Critical)**
Upconversion	76	1.3×10^{-17}	2.6
Phosphorescence	14	6.8×10^{-6}	2.8

Table 2.2. Pairwise student t-tests at the 95% confidence level to determine whether the upconversion emission intensities differ between AgNP loadings. Compared to the controls (0.0% loading), the samples containing 20% and 30% AgNPs show a statistically significant increase in intensity ($t > t_{critical}$).

	t (Statistic) two-tail	**P-value**	**t (Critical) two-tail**
0.0% and 5.0%	1.5	1.5×10^{-1}	2.1
0.0% and 10%	2.3	6.6×10^{-2}	2.6
0.0% and 20%	10	1.5×10^{-4}	2.6
0.0% and 30%	7.9	1.4×10^{-3}	2.8
5.0% and 10%	2.6	4.6×10^{-2}	2.6
10% and 20%	5.0	5.6×10^{-4}	2.2
20% and 30%	1.8	1.3×10^{-1}	2.4

Table 2.3. Pairwise student t-tests at the 95% confidence level to determine whether the phosphorescence emission intensities differ between AgNP loadings. Compared to the controls (0.0% loading), the samples containing 20% and 30% AgNPs show a statistically significant increase in intensity ($t > t_{critical}$).

	t (Statistic) two-tail	**P-value**	**t (Critical) two-tail**
0.0% and 5.0%	0.41	7.0×10^{-1}	2.4
0.0% and 10%	1.8	1.0×10^{-1}	2.3
0.0% and 20%	4.7	1.6×10^{-3}	2.3
0.0% and 30%	5.5	1.5×10^{-3}	2.4
5.0% and 10%	1.8	1.1×10^{-1}	2.3
10% and 20%	3.6	7.4×10^{-3}	2.3
20% and 30%	1.6	1.6×10^{-1}	2.4

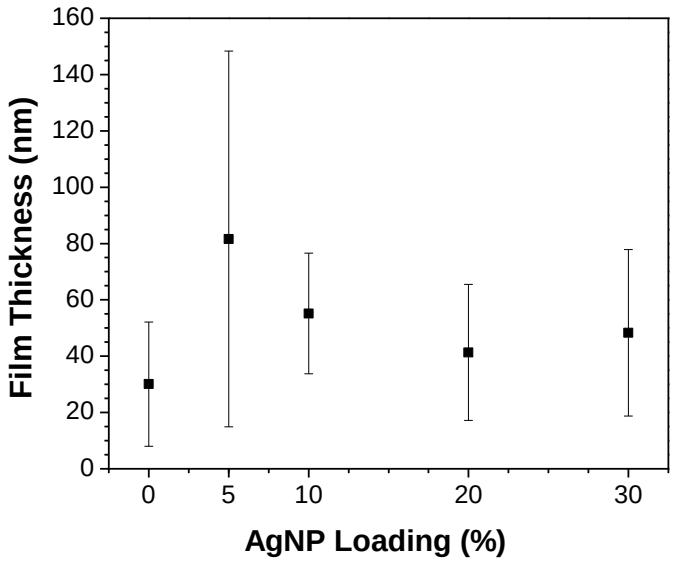

Figure 2.11. Average film thickness (as measured by profilometry) for the films used in this study. Measurements were made on either 3 (0% AgNP) or 2 (5 – 30% AgNP) separate films, and each film was measured multiple times.

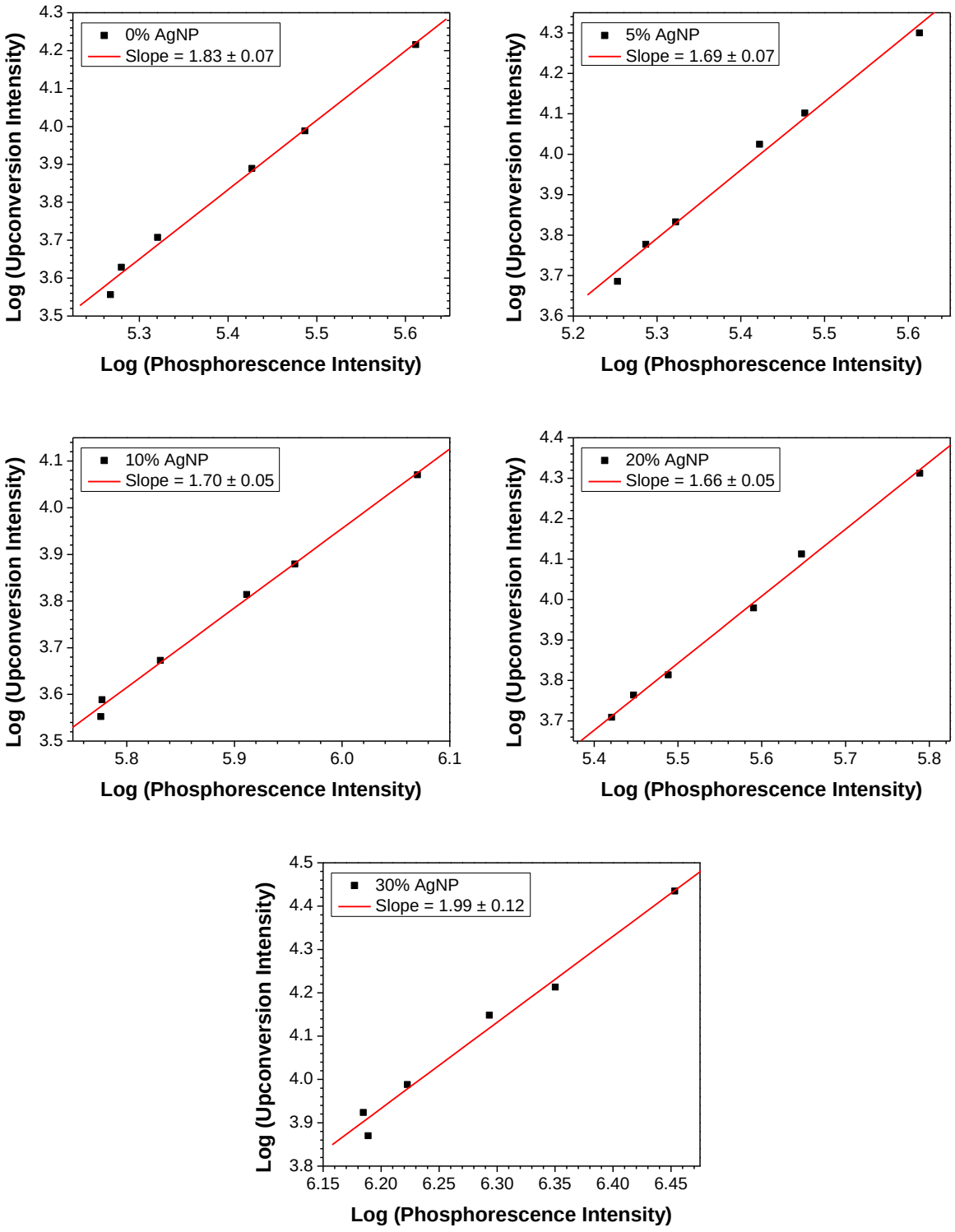

Figure 2.12. Power dependency measurements for films made using different AgNP loadings. Each dataset is the average of measurements on two separate films.

2.3 Conclusions

The plasmonic effects of anisotropic silver nanoplates have been successfully used to realize substantial increases in the efficiency of the triplet-triplet annihilation process. The increase in upconverted emission is attributed to an increase in the local density of excited triplets, owing to an increased absorption cross-section of the PdOEP sensitizer in the presence of the AgNP near-field. The 8.5-fold increase in upconverted emission intensity is extremely promising, and it is expected that with further modifications to the nanoparticle size and shape, as well as the mechanical properties of the polymer,[20] this increase may be further improved. These results suggest that TTA may soon become a viable method of photon upconversion in thin film devices, even at the relatively low power densities typical of unconcentrated solar radiation. This has important implications for the efficiency of photovoltaic devices, in particular for the Shockley-Queisser efficiency limit.

2.4 References

1. W. Shockley and H. J. Queisser, *J. Appl. Phys.*, 1961, **32**, 510-519.
2. M. A. Green, K. Emery, Y. Hishikawa, W. Warta and E. D. Dunlop, *Prog. Photovolt. Res. Appl.*, 2013, **21**, 1-11.
3. X. Huang, S. Han, W. Huang and X. Liu, *Chem. Soc. Rev.*, 2013, **42**, 173-201.
4. J. Zhao, S. Ji and H. Guo, *RSC Advances*, 2011, **1**, 937-950.
5. T. N. Singh-Rachford and F. N. Castellano, *Coord. Chem. Rev.*, 2010, **254**, 2560-2573.
6. Z. Deutsch, L. Neeman and D. Oron, *Nature Nanotech.*, 2013, **8**, 649-653.
7. J.-C. Boyer, L. A. Cuccia and J. A. Capobianco, *Nano Lett.*, 2007, **7**, 847-852.
8. F. Wang, Y. Han, C. S. Lim, Y. Lu, J. Wang, J. Xu, H. Chen, C. Zhang, M. Hong and X. Liu, *Nature*, 2010, **463**, 1061-1065.
9. F. Wang and X. Liu, *Chem. Soc. Rev.*, 2009, **38**, 976-989.
10. W. Zou, C. Visser, J. A. Maduro, M. S. Pshenichnikov and J. C. Hummelen, *Nat. Photonics*, 2012, **6**, 560-564.
11. R. R. Islangulov, D. V. Kozlov and F. N. Castellano, *Chem. Commun.*, 2005, 3776-3778.

12. S. Baluschev, V. Yakutkin, T. Miteva, Y. Avlasevich, S. Chernov, S. Aleshchenkov, G. Nelles, A. Cheprakov, A. Yasuda, K. Müllen and G. Wegner, *Angew. Chem., Int. Ed.*, 2007, **46**, 7693-7696.
13. S. Baluschev, J. Jacob, Y. S. Avlasevich, P. E. Keivanidis, T. Miteva, A. Yasuda, G. Nelles, A. C. Grimsdale, K. Müllen and G. Wegner, *ChemPhysChem*, 2005, **6**, 1250-1253.
14. S. K. Sugunan, C. Greenwald, M. F. Paige and R. P. Steer, *J. Phys. Chem. A*, 2013, **117**, 5419-5427.
15. P. E. Keivanidis, S. Baluschev, T. Miteva, G. Nelles, U. Scherf, A. Yasuda and G. Wegner, *Adv. Mater.*, 2003, **15**, 2095-2098.
16. P. Du and R. Eisenberg, *Chem. Sci.*, 2010, **1**, 502-506.
17. J. Zhao, W. Wu, J. Sun and S. Guo, *Chem. Soc. Rev.*, 2013, **42**, 5323-5351.
18. Y. C. Simon and C. Weder, *J. Mater. Chem.*, 2012, **22**, 20817-20830.
19. R. R. Islangulov, J. Lott, C. Weder and F. N. Castellano, *J. Am. Chem. Soc.*, 2007, **129**, 12652-12653.
20. T. N. Singh-Rachford, J. Lott, C. Weder and F. N. Castellano, *J. Am. Chem. Soc.*, 2009, **131**, 12007-12014.
21. J. A. O'Brien, S. Rallabandi, U. Tripathy, M. F. Paige and R. P. Steer, *Chem. Phys. Lett.*, 2009, **475**, 220-222.
22. J. A. Schuller, E. S. Barnard, W. Cai, Y. C. Jun, J. S. White and M. L. Brongersma, *Nat. Mater.*, 2010, **9**, 193-204.
23. Y. C. Cao, R. Jin and C. A. Mirkin, *Science*, 2002, **297**, 1536-1540.
24. A. Bouhelier, M. Beversluis, A. Hartschuh and L. Novotny, *Phys. Rev. Lett.*, 2003, **90**, 013903.
25. E. Ozbay, *Science*, 2006, **311**, 189-193.
26. H. A. Atwater and A. Polman, *Nat. Mater.*, 2010, **9**, 205-213.
27. C. D. Geddes, *Metal Enhanced Fluorescence*, John Wiley & Sons, Inc., Hoboken, New Jersey, USA, 2010.
28. Y. Zhang, K. Aslan, M. J. R. Previte and C. D. Geddes, *Chem. Phys. Lett.*, 2006, **432**, 528-532.
29. M. J. R. Previte, K. Aslan, Y. Zhang and C. D. Geddes, *J. Phys. Chem. C*, 2007, **111**, 6051-6059.
30. K. Aslan, P. Holley and C. D. Geddes, *J. Mater. Chem.*, 2006, **16**, 2846-2852.
31. K. Aslan, M. Wu, J. R. Lakowicz and C. D. Geddes, *J. Am. Chem. Soc.*, 2007, **129**, 1524-1525.
32. W. Zhang, F. Ding and S. Y. Chou, *Adv. Mater.*, 2012, **24**, OP236-OP241.
33. S. Baluschev, F. Yu, T. Miteva, S. Ahl, A. Yasuda, G. Nelles, W. Knoll and G. Wegner, *Nano Lett.*, 2005, **5**, 2482-2484.
34. T. Uemura, M. Furumoto, T. Nakano, M. Akai-Kasaya, A. Saito, M. Aono and Y. Kuwahara, *Chem. Phys. Lett.*, 2007, **448**, 232-236.
35. C. A. Ashwin, G.-E. Aitzol, A. Hadiseh and A. D. Jennifer, *J. Opt.*, 2012, **14**, 024008.
36. D. Aherne, D. M. Ledwith, M. Gara and J. M. Kelly, *Adv. Funct. Mater.*, 2008, **18**, 2005-2016.
37. L. Liu and T. L. Kelly, *Langmuir*, 2013, **29**, 7052-7060.
38. K. L. Kelly, E. Coronado, L. L. Zhao and G. C. Schatz, *J. Phys. Chem. B*, 2003, **107**, 668-677.
39. Y. Chen, K. Munechika and D. S. Ginger, *Nano Lett.*, 2007, **7**, 690-696.

40. A. P. Kulkarni, K. M. Noone, K. Munechika, S. R. Guyer and D. S. Ginger, *Nano Lett.*, 2010, **10**, 1501-1505.
41. J. C. Ostrowski, A. Mikhailovsky, D. A. Bussian, M. A. Summers, S. K. Buratto and G. C. Bazan, *Adv. Funct. Mater.*, 2006, **16**, 1221-1227.
42. A. Haefele, J. Blumhoff, R. S. Khnayzer and F. N. Castellano, *J. Phys. Chem. Lett.*, 2012, **3**, 299-303.
43. L. Ma, H. Guo, Q. Li, S. Guo and J. Zhao, *Dalton Trans.*, 2012, **41**, 10680-10689.
44. R. C. Kwong, S. Sibley, T. Dubovoy, M. Baldo, S. R. Forrest and M. E. Thompson, *Chem. Mater.*, 1999, **11**, 3709-3713.
45. W. Wu, J. Sun, X. Cui and J. Zhao, *J. Mater. Chem. C*, 2013, **1**, 4577-4589.
46. Y. Chen, J. Zhao, L. Xie, H. Guo and Q. Li, *RSC Advances*, 2012, **2**, 3942-3953.
47. W. H. Wu, H. M. Guo, W. T. Wu, S. M. Ji and J. Z. Zhao, *J. Org. Chem.*, 2011, **76**, 7056-7064.

Chapter 3. Fatigue Resistance of a Flexible, Efficient, and Metal Oxide-Free Perovskite Solar Cell[2]

3.1 Transition Section

The overall goal of this thesis is to improve solar cell technology. As discussed in the previous chapter, one way to achieve this is through the use of photon upconversion, which can improve the device photocurrent and efficiency. This approach can be used to increase the efficiency of any type of solar cell, and therefore is very important for the photovoltaics community. However, although TTA is a flexible upconversion system that can be tailored for use with different types of solar cells, its diffusion-dependent bimolecular nature significantly decreases its efficiency in the solid state. In addition, TTA can only occur when there is no oxygen in the environment; otherwise, the triplet states are quenched. This even further limits the use of TTA, since very effective encapsulation systems are required to prevent the ingress of oxygen molecules. Therefore, in the previous chapter, metal nanoparticles were used to improve the efficiency of TTA, which resulted in an 8.5-fold increase in the intensity of the upconverted light. Although this increase is promising, it is still not enough to significantly increase the photocurrent and efficiency of solar cells. Therefore, other approaches are required to improve solar cell technology in the short term.

[2] Reprinted with permission from: K. Poorkazem, D. Liu, T. L. Kelly, *J. Mater. Chem. A* 2015, **3**, 9241-9248. © The Royal Society of Chemistry 2015.
Differences between the published article and the current chapter: adding a transition section, changing the tense of sentences from first-person plural to third-person singular, embedding supporting information contents in the main text, and other minor corrections based thesis defense examiners' comments.
Contributions: K.P. carried out the research (except where noted below) and wrote the manuscript. D.L. fabricated the M-In_2O_3/ZnO/P3HT:$PC_{61}BM$ and ITO/ZnO/$CH_3NH_3PbI_3$ devices, captured the SEM images in Figure 3.8, 3.9, and 3.13, and measured the *JV* curves and the IPCE spectra in Figures 3.11b and 3.11c. T.L.K. directed the study and revised the manuscript.

Perovskite solar cells have been shown to be a rapidly growing technology. In a short period of time, they have reached comparable efficiencies to those of conventional silicon solar cells, and in contrast to silicon, they can be highly flexible and lightweight. As a result, this chapter deals with finding and removing the key factor limiting the flexibility of perovskite solar cells, and measuring the fatigue resistance of $MAPbI_3$ perovskites.

3.2 Introduction

PSCs have emerged as a potential alternative to silicon solar cells, which are heavy, expensive, and brittle. This brittleness does not allow for the fabrication of silicon-based devices using R2R production. R2R manufacturing is fast and economical, making it ideal for mass-production; however, it only works well for thin-film devices that are light and flexible, and can be processed at low temperatures using solution-based processing techniques. OSCs possess all of these characteristics, and for many years research on flexible photovoltaics has focused on this type of device. Unfortunately, the efficiencies of OSCs are modest, making them less competitive with silicon and CdTe-based devices.[1] In contrast, perovskite solar cells can now be fabricated with excellent power conversion efficiencies,[2-5] and with record-setting efficiencies now exceeding 17%, PSCs are increasingly competitive with silicon and CdTe-based technology.[1, 6] Moreover, the $CH_3NH_3PbI_3$ perovskite is made from inexpensive starting materials, and many researchers have tried to decrease costs even further by using cheaper alternatives for the electron- and hole-transport layers.[7, 8] However, in order to encourage the commercialization of this technology, the toxicity of lead,[9-12] the perovskite's sensitivity to moisture,[3, 10, 11] and the limited flexibility of the device architecture are all issues that must be addressed.[2, 13-15]

The majority of flexible PSCs fabricated to date have been based on ITO transparent conductive electrodes, and are fabricated using solution-based processing[16] and low-temperature methods.[17-19] Early work evaluated the flexibility of the perovskite solar cell by bending the device over cylinders with different radii of curvature.[2] It suggested that the device flexibility was limited by the elastic limit of the ITO/PET substrate and not the perovskite layer; however, no data on the fatigue resistance of the device was reported. Three important studies have been carried out since. In one, the perovskite layer was fabricated on stainless steel fibre/TiO_2 substrates.[20] In another, a layer of Ag was sandwiched between two layers of Al-doped ZnO on a PET substrate, and the whole was used as the transparent conductive electrode in a PSC.[14] In both of these studies, the fatigue resistance of the devices was measured by bending the devices over a cylinder with a fixed radius of curvature for, at most, 50 bending cycles. Given the limited number of cycles, it is not clear if these devices are mechanically robust enough to survive the many cycles of bending necessitated by R2R manufacture, packaging, transportation, installation and use. In recent work, the fatigue resistance of a PSC was studied by bending a device to a 4 mm radius of curvature for 1000 cycles, and the failure in device performance was attributed to crack formation in the ITO layer.[21] In additional work based on density functional theory, the flexibility of $CH_3NH_3BX_3$ perovskites was shown to be dependent on the shear modulus and the strength of the B-X bond, and be independent of organic−inorganic ion interactions.[22] In addition, the Poisson's ratio (τ) of the $CH_3NH_3PbI_3$ perovskite was shown to be larger than 0.30, which places it between that of rigid glass (0.18) and rubber (0.50). These values indicate a more molecular (rather than ionic or ionic-covalent) crystal, and suggest that the perovskite possess a higher level of flexibility than conventional crystalline inorganic semiconductors. However, despite this theoretical prediction,

and the studies on flexible PSCs reported to date, very little is known about the flexibility and mechanical robustness of $CH_3NH_3PbI_3$ films.

The ITO electrodes predominantly used in flexible solar cell technology have a number of disadvantages which limit their utility. The scarcity and expense of indium increases the overall production cost associated with the fabrication process,[23, 24] and the high temperatures required to process indium-free alternatives (such as FTO) make them unsuitable for deposition on plastic substrates. Most importantly for this work, however, is the brittleness of the metal oxide films.[23, 24] Their poor mechanical performance means that they are not ideal electrodes for flexible applications and R2R production. A literature report of an ITO-based transparent thin-film transistor showed that the semiconductor field effect mobility decreased to 85% of its original value after bending the device to a 2 mm radius of curvature just once.[25] In another report, an ITO/PET-containing dye-sensitized solar cell was bent 1000 times around a cylinder of 7 mm radius, and the observed cracks were attributed to the inflexibility of ITO.[26]

Alternative transparent conductive electrodes, in addition to possessing good mechanical flexibility, must also display high transmittance and low sheet resistance.[23, 27, 28] Very few materials possess all three of these characteristics. Metal films typically have low transmittance when they are thick,[27] and low conductivity (as well as a tendency to oxidize) when they are thin.[28] Silver nanowires have both high transmittance and a low sheet resistance; however, nanowire and nanofiber structures often lead to device shorting unless flattened under high pressures.[29] Carbon nanotubes[28] and graphene[28, 30-32] are other materials that have been widely used in optoelectronic devices. However, carbon nanotubes often suffer from poor charge transfer between nanotubes, and need to be fabricated in high densities.[24] In contrast, highly conductive HC-PEDOT electrodes can be prepared with low sheet resistance, high surface coverage, and high transmittance, using

simple fabrication methods. They also have highly favourable mechanical properties, and have already been applied in the fabrication of highly flexible OSCs.[33-38]

In this report, both perovskite and organic solar cells are fabricated on PET substrates. In comparing the fatigue resistance of the PSCs prepared using a metal oxide electrode with those prepared on HC-PEDOT, it is found that cracks in the metal oxide electrode are the primary reason for device failure after repeated bending cycles. The devices prepared using HC-PEDOT are entirely metal oxide free, and display good power conversion efficiencies (up to 7.6%) with very little hysteresis. Our results further show that the perovskite film, while more flexible than the underlying metal oxide electrode, is still more prone to cracking than conventional polymer-based active layers. This has a deleterious effect on device performance, suggesting that for applications demanding high flexibility and many repeated bending cycles (e.g., textile or fabric-integrated photovoltaics), organic semiconductors remain the material of choice.

3.3 Experimental

3.3.1 Materials

0.25 mm thick PET, 0.2 mm thick M-In_2O_3-coated PET ($R_s \leq 10$ Ω/□), and 0.15 mm thick ITO-coated PET ($R_s = 60$ Ω/□) substrates were purchased from McMaster-Carr, Delta Technologies, and Sigma-Aldrich, respectively. HC-PEDOT and SC-PEDOT were purchased from Clevios (PH1000 and P VP AI 4083, respectively). Zonyl F-300 fluorosurfactant (40% solids in H_2O) was purchased from Fluka. ZnO nanoparticle[1] and CH_3NH_3I[2] solutions was synthesized according to literature procedures. Zinc acetate dihydrate, methylamine solution (33% in ethanol), hydriodic acid, lead(II) iodide, 4-*tert*-butylpyridine, and lithium bis(trifluoromethylsulphonyl)imide were

purchased from Sigma-Aldrich, Alfa Aesar or Fisher Scientific. 2,2′,7,7′-tetrakis-(*N*,*N*-di-*p*-methoxyphenylamine)-9,9′-bifluorene (Spiro-OMeTAD) was purchased from Merck KGaA. $PC_{61}BM$ was purchased from Nano-C, and P3HT was purchased from Rieke Metals, Inc. Silver paint was purchased from SPI.

3.3.2 Methods

3.3.2.1 HC-PEDOT/SC-PEDOT/$CH_3NH_3PbI_3$ device fabrication

The HC-PEDOT solution (Clevios PH1000) was mixed with 5% (v/v) dimethyl sulfoxide and 0.5% (v/v) Zonyl F-300 fluorosurfactant. After filtration through a 0.45 μm polyvinylidene difluoride (PVDF) syringe filter, 300 μL of the solution was dispensed onto a 2.54 cm × 2.54 cm pre-cleaned PET substrate. The sample was spin-coated at 1000 rpm for 1 min and 2000 rpm for 1 min. A highly porous chuck was used for all spin-coating steps. The samples were thermally annealed at 120 ºC for 30 min.[35] A thin strip of silver paint was used to deposit a mechanically-robust electrical contact to the HC-PEDOT electrode. A SC-PEDOT solution (Clevios P VP AI 4083) was filtered through a 0.45 μm filter, and 300 μL spin-coated (1200 rpm for 30 s followed by 3000 rpm for 10 s) onto the substrate.[39] The samples were again annealed at 120 °C for 5-10 min, after which they were immediately transferred into a glovebox (< 0.1 ppm O_2 and H_2O). A 460 mg/mL PbI_2 solution was prepared in dry *N*,*N*-dimethylformamide and kept at 100 ºC. Samples were again thermally annealed at 100 °C for 5-10 min, immediately after which the PbI_2 solution (100 μL) was deposited by spin-coating (3000 rpm for 20-25 s, using a dynamic dispensing step). The PbI_2 layer was allowed to dry for 2 h, after which the samples were brought out of the glovebox, immersed in a 10 mg/mL CH_3NH_3I solution in dry isopropanol for 60 s, and then spin-dried at 2000 rpm for 10 s. They were immediately transferred back into the glovebox. $PC_{61}BM$ was deposited by spin-coating (1000 rpm for 45 s, followed by 4000 rpm for 10 s) from

100 μL of a 20 mg/mL $PC_{61}BM$ in chlorobenzene solution, which was pre-stirred for at least 2 h. Al counter-electrodes were deposited by thermal evaporation at a base pressure of 2×10^{-6} mbar at a rate of 1 Å/s for the first ~ 40 nm and at a rate of 3 Å/s for another ~ 145 nm.

3.3.2.2 M-In_2O_3/ZnO/$CH_3NH_3PbI_3$ device fabrication.

This process was adapted from literature procedures.[1] A 3 mg/mL ZnO nanoparticle (~ 5 nm diameter) solution was prepared in butanol containing 6.25% (v/v) methanol and 6.25% (v/v) chloroform. Three layers of ZnO nanoparticles were deposited on the PET/M-In_2O_3 substrate via sequential spin-coating steps (3000 rpm for 30 s). The ZnO layer was allowed to dry for at least 0.5 h. A solution of 460 mg/mL PbI_2 in *N*,*N*-dimethylformamide (DMF) was prepared and heated to 100 ^oC, and used to deposit a PbI_2 thin film by spin coating (3000 rpm for 20-25 s). The PbI_2 layer was allowed to dry for 1 h. Afterward, the samples were immersed in a solution of 10 mg/mL CH_3NH_3I in dry isopropanol for 60 s and then spin-dried immediately at 2000 rpm for 10 s. Spiro-OMeTAD was deposited by spin-coating (4000 rpm for 30 s) from a solution of 80 mg spiro-OMeTAD, 28.5 μL 4-*tert*-butylpyridine and 17.5 μL lithium-bis(trifluoromethanesulfonyl)imide (Li-TFSI) solution (520 mg Li-TFSI in 1 mL acetonitrile) all dissolved in 1 mL chlorobenzene. Ag counter-electrodes (150 nm) were deposited by thermal evaporation at a base pressure of 2×10^{-6} mbar at a rate of 0.1 Å/s for the first 15 nm and at a rate of 0.3 Å/s for another 135 nm.

3.3.2.3 HC-PEDOT/SC-PEDOT/P3HT:$PC_{61}BM$ device fabrication.

The PET/HC-PEDOT/SC-PEDOT layers were fabricated as in section 3.3.2.1 and allowed to cool to room temperature. The P3HT:$PC_{61}BM$ active layer was spin-coated (1000 rpm for 30 s) from a solution of 15 mg/mL P3HT and 12 mg/mL $PC_{61}BM$ in chlorobenzene (the solution was stirred for at least 2 h prior to deposition). The samples were then thermally annealed at 120 ^oC for 20

min. A 6 mg/mL solution of ZnO nanoparticles (in the same solvent mixture as above) was spin-coated onto the active layer (1000 rpm for 30 s, followed by 3000 rpm for 10 s). Evaporation of Al electrodes was carried out as in section 3.3.2.1.

3.3.2.4 M-In_2O_3/ZnO/P3HT:$PC_{61}BM$ device fabrication.

The PET/M-In_2O_3/ZnO layers were prepared as described above. The P3HT:$PC_{61}BM$ active layer was spin-coated (1000 rpm for 30 s) from a solution of 15 mg/mL P3HT and 12 mg/mL $PC_{61}BM$ in chlorobenzene (the solution was stirred for at least 2 h prior to deposition). After annealing at 120˚ C for 15 min, a SC-PEDOT layer was deposited by spin-coating (4000 rpm for 60 s) and then further annealed at 120 ºC for 15 min. For these devices, all spin-coating procedures were performed under ambient conditions, and all annealing steps were done inside the glovebox. Ag counter-electrodes (150 nm) were deposited as above.

3.3.3 Characterization

3.3.3.1 Device characterization

Device illumination was provided by a 450 W Class AAA solar simulator equipped with an AM1.5G filter (Sol3A, Oriel Instruments). The light intensity was set to 100 mA/cm^2 using a standard silicon reference cell (91150V, Oriel Instruments). *J-V* curves were obtained with a Keithley 2400 source-measure unit. The area of the device under illumination was fixed at 0.0708 cm^2 using a non-reflective metal mask. The pre-sweep delay time was 1 s, the dwell time at each voltage step was 30 ms (unless otherwise specified in figure captions), and 85 data points were measured between –0.4 and 2.0 V. All bending tests were done in a glovebox environment (< 0.1 ppm O_2 and H_2O), and care was taken to ensure that the entire device area was uniformly bent

around the cylindrical object. Before remeasuring the *J-V* curves, the devices were bent gently in the converse direction to minimize any curvature caused by bending.

3.3.3.2 Other instruments

Absorption spectra were obtained using a Cary 6000i UV-vis-NIR spectrophotometer. Film thicknesses were measured using a KLA Tencor profilometer. IPCE spectra were acquired using a commercial setup (QE-PV-Si, Oriel Instruments) consisting of a 300 W Xe arc lamp, filter wheel, and monochromator. The incident light was chopped at a frequency of 30 Hz and photocurrents measured using a lock-in amplifier. Scanning electron microscopy (SEM) images were acquired using a JEOL JSM-6010LV microscope at an accelerating voltage of 15 kV and a working distance of 11 mm. Powder X-ray diffraction patterns were obtained with a Bruker D8 Advance Series II diffractometer equipped with a Cu $K_{\alpha 1,2}$ X-ray source. The data were collected with a 0.0469° step size (2θ).

3.4 Results and discussion

3.4.1 Device Characteristics

Figure 3.1 shows the two types of flexible PSC architectures used in the current study. The first design (PET/M-In_2O_3/ZnO/$CH_3NH_3PbI_3$/Spiro-OMeTAD/Ag, hereafter abbreviated as M-In_2O_3/ZnO/$CH_3NH_3PbI_3$) is already established as one that yields high efficiency PSCs;[2] the second architecture (PET/HC-PEDOT/SC-PEDOT/$CH_3NH_3PbI_3$/$PC_{61}BM$/Al, hereafter abbreviated as HC-PEDOT/SC-PEDOT/$CH_3NH_3PbI_3$) is fabricated for the first time here, and introduces a HC-PEDOT layer to replace the metallized indium oxide (M-In_2O_3) electrode. The M-In_2O_3 film is a commercially available Au- and Ag-coated In_2O_3 layer, and has mechanical

properties, transmittance, and sheet resistance qualitatively similar to a typical ITO electrode. The HC-PEDOT is expected to be substantially more flexible than the indium oxide layer, such that the mechanical properties of the perovskite film can be evaluated. It was spin-coated from a solution containing 5% (v/v) dimethyl sulfoxide and 0.5% (v/v) Zonyl F-300 fluorosurfactant,[35] producing a 190 nm thick film measured by a profiler. In both architectures, the perovskite layer is fabricated through a two-step deposition process (spin-coating a layer of PbI_2, followed by immersion in a CH_3NH_3I solution).[2, 40] The absorption spectrum and pXRD pattern of the perovskite layer are shown in **Figure 3.2**. The absorption onset at ~ 780 nm, a high-energy absorption peak at ~ 500 nm, and the perovskite diffraction peaks shown in this figure proves the formation of the perovskite layer. In both cases, the perovskite is placed between electron- and hole-transport layers: either ZnO and Spiro-OMeTAD, or $PC_{61}BM$ and semiconducting poly(3,4-ethylenedioxythiophene):poly(styrene sulfonate) (SC-PEDOT). Importantly, for the device based on the HC-PEDOT electrode, all layers (with the exception of the aluminium counter electrode) are deposited from solution by spin-coating. With a maximum processing temperature of 120 ^oC, these processing steps are highly compatible with R2R manufacturing processes. The thicknesses of the various device layers (as determined by profilometry) are consistent with previous literature reports of high performance devices.[2, 39, 41, 42]

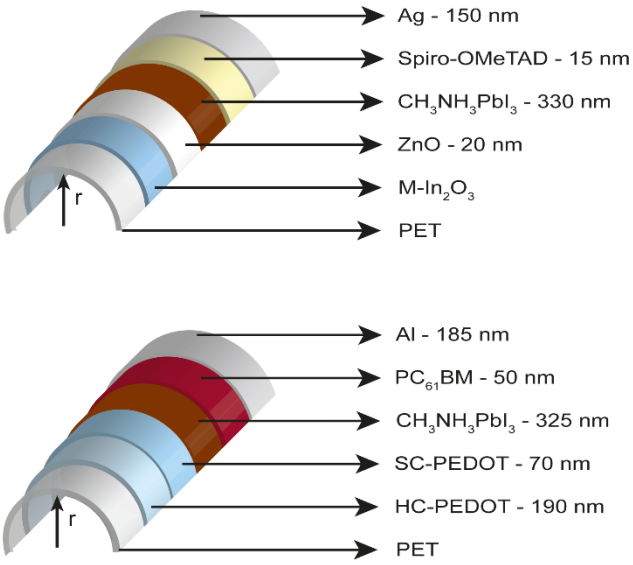

Figure 3.1. Schematic of the device architecture for M-In_2O_3/ZnO/$CH_3NH_3PbI_3$ (top) and HC-PEDOT/SC-PEDOT/$CH_3NH_3PbI_3$ (bottom) cells, bent at a radius of curvature, *r*.

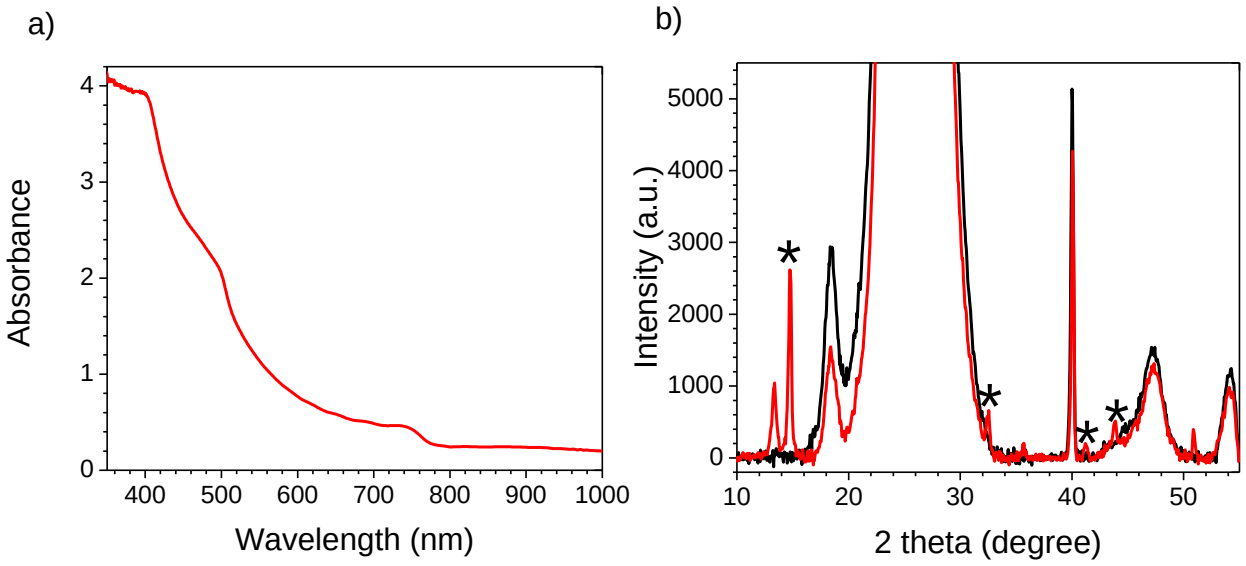

Figure 3.2. (a) Absorption spectrum and (b) pXRD pattern of PET/HC-PEDOT/SC-PEDOT/$CH_3NH_3PbI_3$ films (red lines). The pXRD pattern of the PET/HC-PEDOT/SC-PEDOT substrate (black line) is shown for comparison. Peaks marked with an asterisk (*) are due to the perovskite, the peak at 13.4° is for PbI_2, and large peaks in 16-30° are for PET substrates.

Figure 3.3a shows the transmission spectrum of each transparent conductive thin film electrode. Both electrodes have similar transmittance at wavelengths < 610 nm; however, at longer wavelengths, the HC-PEDOT electrode significantly outperforms the M-In_2O_3 analogue. At 800 nm, at the absorption onset of the perovskite, the transmittances of these electrodes are 85% and 64%, respectively. The higher transmittance for the HC-PEDOT leads to a larger portion of the light reaching the perovskite layer. This is likely to be even more significant for tandem solar cells,[10, 11] where the perovskite is paired with an additional red-to-near infrared absorber.

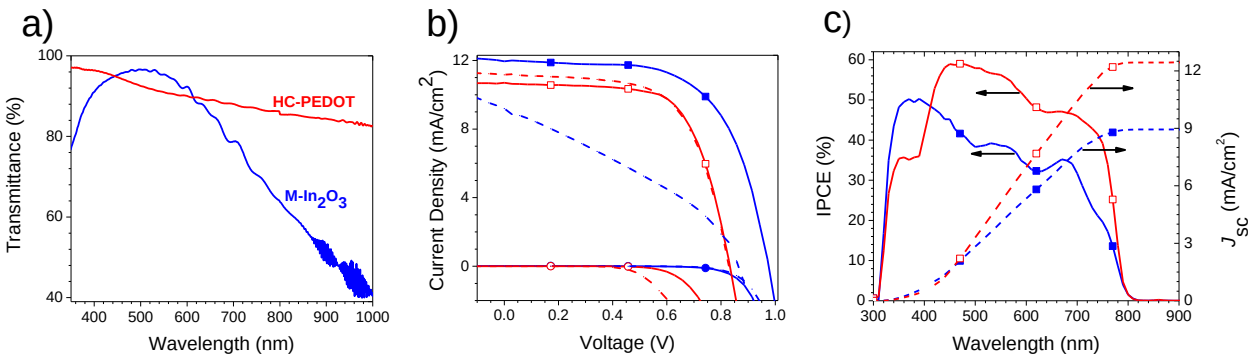

Figure 3.3. (a) Transmission spectra of M-In_2O_3 and HC-PEDOT electrodes, after subtraction of the PET background spectrum. (b) *J-V* curves of representative M-In_2O_3/ZnO/$CH_3NH_3PbI_3$ (blue) and HC-PEDOT/SC-PEDOT/$CH_3NH_3PbI_3$ (red) devices, measured from forward bias to short-circuit (solid lines), and from short-circuit to forward bias (dashed lines), in both the light (squares) and in the dark (circles). (c) IPCE spectra (solid lines) and calculated J_{sc} values (dashed lines) for M-In_2O_3/ZnO/$CH_3NH_3PbI_3$ (solid blue squares) and HC-PEDOT/SC-PEDOT/$CH_3NH_3PbI_3$ (open red squares) devices.

The two different types of PSC were tested under AM1.5G illumination, and **Table 3.1** shows both the average and the best results. By comparing the results of the HC-PEDOT/SC-PEDOT/$CH_3NH_3PbI_3$ cells with those of the M-In_2O_3/ZnO/$CH_3NH_3PbI_3$ analogues, it is found that there is very little difference in either the J_{sc} or the fill factor (FF). Given that the perovskite films were deposited in the same way, and have similar thicknesses, the similarity in performance is

perhaps unsurprising. The main difference in the two devices is the lower V_{oc} of the HC-PEDOT/SC-PEDOT/$CH_3NH_3PbI_3$ device. Pairwise *t*-tests were carried out at the 95% confidence level to statistically validate these comparisons (**Table 3.2**). The efficiency of 7.6% for the HC-PEDOT/SC-PEDOT/$CH_3NH_3PbI_3$ device is highly encouraging, as it is a first step toward combining the high efficiency of the PSCs with the high flexibility of all-organic electron- and hole-transport layers and electrodes.

Table 3.1. Device performance parameters for 67 M-In_2O_3/ZnO/$CH_3NH_3PbI_3$ and 103 HC-PEDOT/SC-PEDOT/$CH_3NH_3PbI_3$ devices.

Electrode	V_{oc} **(V)**	J_{sc} **(mA/cm^2)**	**FF**	**PCE (%)**	R_s **(Ω·cm^2)**	R_{sh} **(Ω·cm^2)**
M-In_2O_3 (Average)	0.90 ± 0.07	11 ± 2	0.51 ± 0.07	5 ± 2	(3 ± 1) × 10	(5 ± 2) × 10^2
M-In_2O_3 (Best)	0.96	12	0.66	7.8	9	5 × 10^2
HC-PEDOT (Average)	0.7 ± 0.2	11 ± 2	0.5 ± 0.1	4 ± 2	17 ± 7	(1 ± 2) × 10^3
HC-PEDOT (Best)	0.8	15	0.6	7.6	12	5 × 10^3

Table 3.2. Results of pairwise *t*-tests comparing the two PSCs at the 95% confidence level. Averages and standard deviations are calculated from 67 and 103 M-In_2O_3/ZnO/$CH_3NH_3PbI_3$ and HC-PEDOT/SC-PEDOT/$CH_3NH_3PbI_3$ devices, respectively. For each set of parameters, the critical *t*-value is 2.0.

Device Performance Parameters	**M-In_2O_3/ ZnO/$CH_3NH_3PbI_3$**	**HC-PEDOT/ SC-PEDOT/$CH_3NH_3PbI_3$**	***t*-statistic**	***p*-value**
V_{oc} (V)	0.90 ± 0.07	0.7 ± 0.2	12	1.2×10^{-24}
J_{sc} (mA/cm^2)	11 ± 2	11 ± 2	0.89	3.8×10^{-1}
FF	0.51 ± 0.07	0.5 ± 0.1	1.0	3.1×10^{-1}
PCE (%)	5 ± 2	4 ± 2	4.1	6.5×10^{-5}
R_s (ohm·cm^2)	(3 ± 1) × 10	17 ± 7	5.1	1.5×10^{-6}
R_{sh} (ohm·cm^2)	(5 ± 2) × 10^2	(1 ± 2) × 10^3	6.0	2.5×10^{-8}

Figures. 3.3b and 3.3c show the *J-V* curves and IPCE spectra for representative devices of both architectures. Hysteresis (a difference in the current response with the bias scanning direction) is a major concern in perovskite solar cells,[43-45] and as such, the hysteretic behaviour of both types of devices have been investigated. As reported in Table 3.1, the PCEs of the best M-In_2O_3/ZnO/$CH_3NH_3PbI_3$ and HC-PEDOT/SC-PEDOT/$CH_3NH_3PbI_3$ cells were 7.8% and 7.6%, respectively. However, Figure 3.3b indicates that the hysteretic effect is much less pronounced for the latter, as the *J-V* curves for reverse and forward directions are quite similar. In **Figure 3.4**, the *J-V* curves of representative devices are shown with various dwell times spent on each voltage step. With increasing dwell times, the reverse- and the forward-direction *J-V* curves become more similar, eventually becoming virtually superimposable under pseudo-steady state conditions. As a

result, for relatively fast measurements, there is a discrepancy in the PCE obtained from the two scans: for the M- In_2O_3/ZnO/$CH_3NH_3PbI_3$ device, the reverse and forward-scans yielded PCEs of 7.8% and 4.2% respectively, while for the HC-PEDOT/SC-PEDOT/$CH_3NH_3PbI_3$ device, both scans produced a PCE of 7.6%.

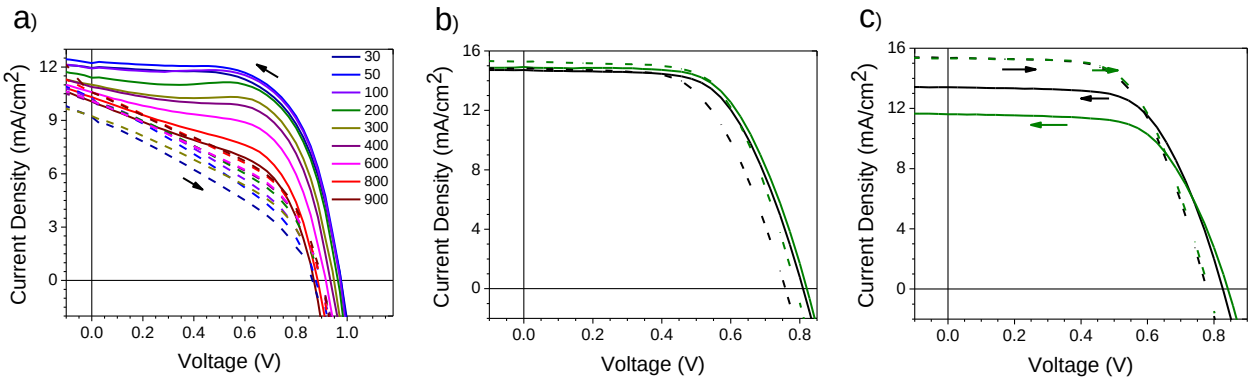

Figure 3.4. *J-V* curves of (a) M-In_2O_3/ZnO/$CH_3NH_3PbI_3$ devices, and HC-PEDOT/SC-PEDOT/$CH_3NH_3PbI_3$ devices at (b) short and (c) long dwell times. Scans from forward bias to short-circuit, and short-circuit to forward bias are shown as solid and dashed lines, respectively. In (a), the dwell time at each voltage step (in ms) is shown. In (b), dwell times were either 30 (black line) or 35 ms (green line). In (c), dwell times were either 100 (black line) or 200 ms (green line).

Further insight into the hysteretic behavior of the devices can be gained from the IPCE spectra. Figure 3.3c shows the IPCE spectra of the M-In_2O_3/ZnO/$CH_3NH_3PbI_3$ and HC-PEDOT/SC-PEDOT/$CH_3NH_3PbI_3$ devices, as well as the J_{sc} calculated by integration of the IPCE spectra with the AM1.5G solar flux. The HC-PEDOT/SC-PEDOT/$CH_3NH_3PbI_3$ device clearly outperforms the M-In_2O_3 counterpart in the red region of the spectrum, reflecting the improved transmission of the HC-PEDOT electrode (Figure 3.3a). Furthermore, since the IPCE spectra are measured under pseudo-steady state conditions, the calculated J_{sc} values should provide a good

representation of the actual solar cell performance.[46] Both IPCE spectra in Figure 3.3c were measured for devices with a J_{sc} of 12 mA/cm^2 (as determined from the reverse scan of the *J-V* curve). The short-circuit current densities calculated from the IPCE spectra were 9 and 12 mA/cm^2 for the M-In_2O_3 and HC-PEDOT/SC-PEDOT/$CH_3NH_3PbI_3$ devices, respectively. The fact that the J_{sc} values for the M-In_2O_3 devices are inconsistent (9 mA/cm^2 from the IPCE spectrum compared to 12 mA/cm^2 from the *J-V* curve) is in keeping with the substantial degree of hysteresis observed in these devices, whereas the excellent agreement observed for the HC-PEDOT-based cells reflects the lack of observed hysteresis. This result is significant in that many reports promote the limited hysteresis of mesoscopic PSCs as a substantial advantage over their planar heterojunction counterparts;[11, 45] however, here it is demonstrated that planar heterojunction devices can also be prepared with very limited hysteresis in the *J-V* curve. These findings are consistent with literature reports on the hysteretic behaviour of inverted architectures.[19, 47-51] Mitigation of hysteresis has been observed when either SC-PEDOT[50] or C_{60}-fullerenes[52] have been used as charge extraction layers. This has been attributed to a low number of interfacial charge traps[47, 51] and (in the case of fullerene-based acceptors) to strong charge carrier extraction.[52] Very recently, spin-coating of $PC_{61}BM$ on top of the perovskite layer was shown to passivate trap states by permeating into nano-pathways between perovskite grain boundaries. This permeation decreases the charge transport barrier and increases the charge extraction efficiency; as a result, it substantially reduces the amount of hysteresis that is observed.[53] Our own observations are consistent with these findings and highlight the importance of interfacial layers on the hysteretic effect.[45, 49] If the HC-PEDOT devices are measured using a long dwell time at each voltage step (Figure 3.4c), the J_{sc} of the reverse direction is found to be slightly lower (and the V_{oc} slightly higher) than that measured in the forward scan.

3.4.2 Fatigue Resistance

One of the most important questions surrounding flexible PSCs is their resistance to mechanical fatigue. In order to better understand the mechanical flexibility and failure mechanisms of these PSCs, they were subjected to a lengthy fatigue test alongside two polymer-based devices with the same transparent conductive electrodes: PET/M-In_2O_3/ZnO/P3HT:$PC_{61}BM$/SC-PEDOT/Ag (hereafter abbreviated as M-In_2O_3/ZnO/P3HT:$PC_{61}BM$), and PET/HC-PEDOT/SC-PEDOT/P3HT:$PC_{61}BM$/ZnO/Al (hereafter abbreviated as HC-PEDOT/SC-PEDOT/P3HT:$PC_{61}BM$). The electrical parameters of these devices are presented in **Table 3.3**.

Table 3.3. Device performance parameters for P3HT:$PC_{61}BM$ solar cells. Averages and standard deviations are calculated from 66 devices of each type.

Electrode	V_{oc} **(V)**	J_{sc} **(mA/cm^2)**	**FF**	**PCE (%)**	R_s **(Ω·cm^2)**	R_{sh} **(Ω·cm^2)**
M-In_2O_3 (Average)	0.52 ± 0.08	6.6 ± 0.7	0.40 ± 0.06	1.4 ± 0.4	26 ± 9	(2.1 ± 0.7) × 10^2
M-In_2O_3 (Best)	0.58	7.3	0.50	2.1	14	3.5 × 10^2
HC-PEDOT (Average)	0.5 ± 0.1	6.4 ± 0.4	0.38 ± 0.06	1.2 ± 0.5	31 ± 7	(2.4 ± 1.3) × 10^2
HC-PEDOT (Best)	0.6	6.8	0.47	1.9	26	4.6 × 10^2

Fatigue tests were carried out on 9 separate cells (3 cells on each of 3 separate substrates) for each of the four types of devices. The cells were bent around a cylindrical object of 4 mm radius until they either shorted or 2000 bending cycles were reached. By carrying out > 1000 bending cycles, a much more realistic measure of the suitability of perovskite devices for flexible photovoltaic applications was provided than any previous work.[2, 14, 20] The effect of repeated bending on device PCE is presented in **Figure 3.5**, and the changes in the other electrical parameters (V_{oc}, J_{sc}, *FF*, R_s and R_{sh}) as a function of the number of bending cycles are reported in

Figure 3.6. As shown in Figure 3.5a, the nine devices with the M- In_2O_3/ZnO/$CH_3NH_3PbI_3$ architecture all short-circuit quite suddenly after 100 to 1100 bending cycles. The changes in the *J-V* curves prior to short-circuit can be seen in Figure 3.5a. Although there is little change in performance for the first 100 cycles, immediately thereafter the V_{oc} and the J_{sc} both decrease sharply. This is likely due to the sudden and concurrent drop in the fill factor; a sharp increase in the series resistance and a decrease in the shunt resistance lead to a roughly 60% loss in *FF*. Immediately thereafter, the device fails by short-circuit. In contrast, the HC-PEDOT/SC-PEDOT/$CH_3NH_3PbI_3$ devices degrade by a very different mechanism (Figure 3.5b). Although the PCE of the HC-PEDOT/SC-PEDOT/$CH_3NH_3PbI_3$ device drops rapidly in the first 300 bending cycles (similar to many of the M-In_2O_3/ZnO/$CH_3NH_3PbI_3$ cells), the device performance then stabilizes, and none of the nine devices shorted, even after 2000 bending cycles. In these devices, there is very little change in the V_{oc}; instead, the J_{sc} gradually decreases, driven primarily by an increase in the R_s. Combined with a decrease in R_{sh}, this leads to a substantial loss in FF after 2000 bending cycles.

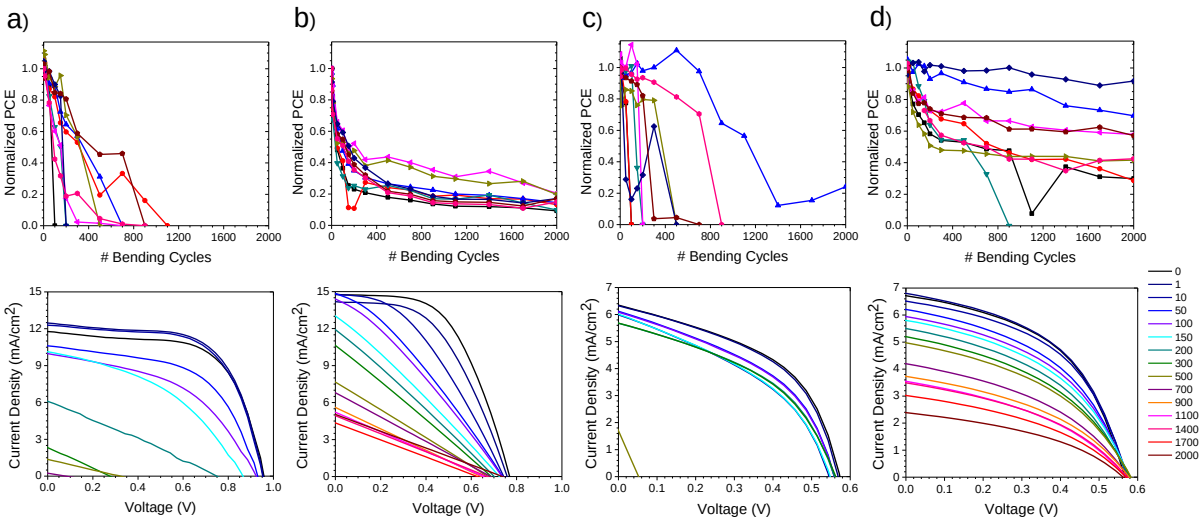

Figure 3.5. Results of the fatigue tests for the (a) M-In_2O_3/ZnO/$CH_3NH_3PbI_3$, (b) HC-PEDOT/SC-PEDOT/$CH_3NH_3PbI_3$, (c) M-In_2O_3/ZnO/P3HT:$PC_{61}BM$, and (d) HC-PEDOT/SC-PEDOT/P3HT:$PC_{61}BM$ devices. The top row shows the normalized PCE for each of 9 separate devices. The bottom row shows the *J*-*V* curves as a function of the number of bending cycles for a typical device.

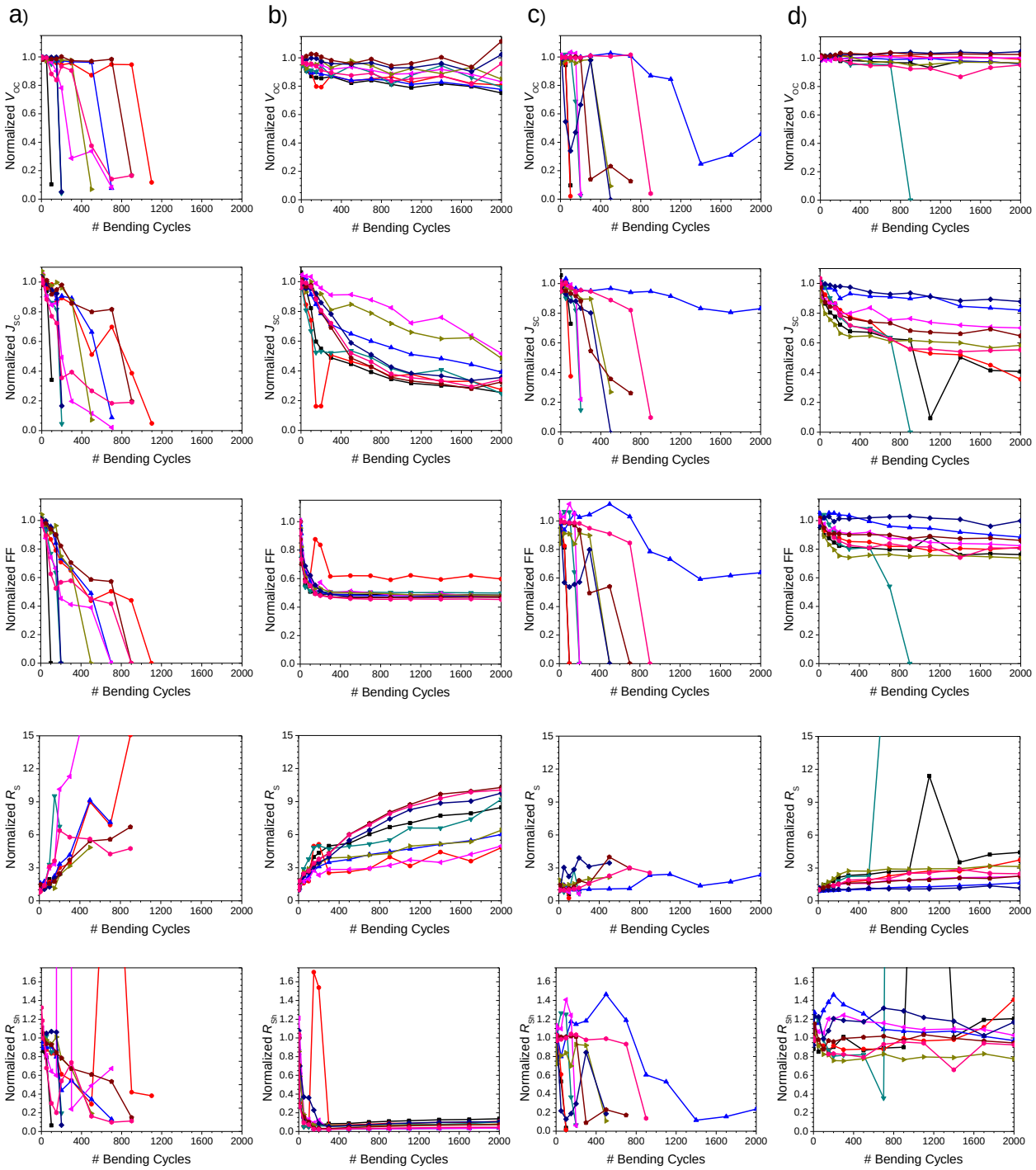

Figure 3.6. Results of the fatigue tests done on 9 separate devices (3 devices on each of 3 different substrates): (a) M-In_2O_3/ZnO/$CH_3NH_3PbI_3$, (b) HC-PEDOT/SC-PEDOT/$CH_3NH_3PbI_3$, (c) M-In_2O_3/ZnO/P3HT:$PC_{61}BM$, and (d) HC-PEDOT/SC-PEDOT/P3HT:$PC_{61}BM$. The rows (from top to bottom) show the normalized V_{oc} J_{sc}, FF, R_s, and R_{sh} values as a function of the number of bending cycles.

Figures. 3.5c and 3.5d show the results of the fatigue test for the OSCs. The majority of the M-In_2O_3/ZnO/P3HT:PC_{61}BM devices fail by short-circuit in the range of 100 to 900 bending cycles, with only one device remaining functional after 2000 cycles. The similarity of these results with those in Figure 3.5a suggests that both M-In_2O_3/ZnO/$CH_3NH_3PbI_3$ and M-In_2O_3/ZnO/P3HT:PC_{61}BM devices fail by a similar degradation mechanism; this implies that changes in the M-In_2O_3 electrode may be the underlying reason for device failure. Despite this broad similarity, there are small differences in the rate of change in PCE. In Figure 3.5a a steady loss in PCE is observed, followed by catastrophic short-circuit, whereas in the P3HT:PC_{61}BM devices (Figure 3.5c), the initial device performance is better retained prior to a sudden device failure. This suggests that the perovskite film may be contributing to the initial drop in efficiency, with breakage of the M-In_2O_3 electrode being responsible for the ultimate short-circuit of the device. This theory is supported by a comparison of the fatigue resistance of the perovskite and polymer solar cells on HC-PEDOT electrodes. From Figure 3.5d, it can be observed that all but one of the HC-PEDOT/SC-PEDOT/P3HT:PC_{61}BM devices still work after 2000 bending cycles. The V_{oc} is almost entirely unchanged throughout the test, and only a modest decrease in the fill factor is observed. The device performance does deteriorate slowly, owing almost entirely to losses in J_{sc}. Given the all-organic nature of this device, this level of fatigue resistance is perhaps unsurprising. The average PCEs of the HC-PEDOT/SC-PEDOT/$CH_3NH_3PbI_3$ and HC-PEDOT/SC-PEDOT/P3HT:PC_{61}BM devices after 2000 bending cycles were 15 ± 4% and 50 ± 30% of their initial values, respectively. Given that the same transparent conductive electrode was used in both cases, this is further evidence that the perovskite layer appears to be less flexible than polymer-based semiconductors.

In order to further probe the limitations on the flexibility of these devices, three devices of each type were subjected to single bending cycles at increasingly sharp radii of curvature (**Figure 3.7**). In a manner analogous to the fatigue tests, the devices with the M-In_2O_3 electrodes fail by short-circuit after being bent to radii of less than 2 mm. In contrast, devices based on the HC-PEDOT electrodes do not fail by short-circuit, and instead display a continual loss of efficiency as the radius of curvature is lowered. Again, the perovskite-based device shows a more rapid decline in efficiency, with a noticeable loss in performance beginning at a 4 mm bend radius. In contrast, the HC-PEDOT/SC-PEDOT/P3HT:$PC_{61}BM$ devices maintain ~ 75% of their initial performance up to a bend radius of 2 mm. Bending the devices to radii of less than 1.2 mm exceeds the elastic limit of the PET substrate, and so more severe radii of curvature were not tested.

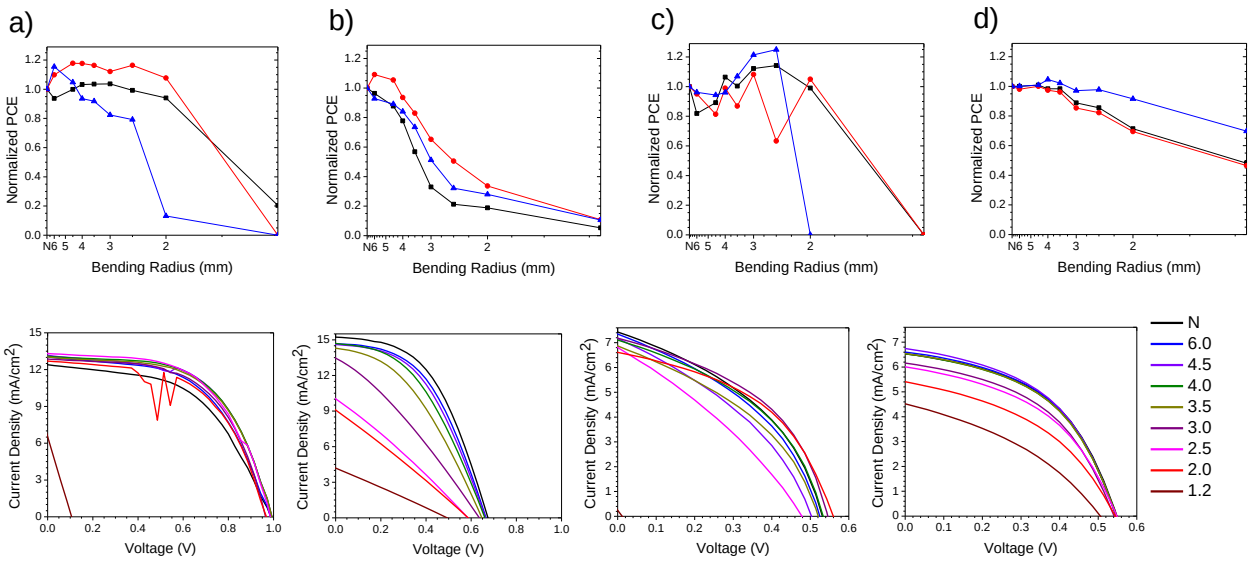

Figure 3.7. Results of the bending radius tests: (a) M-In_2O_3/ZnO/$CH_3NH_3PbI_3$, (b) HC-PEDOT/SC-PEDOT/$CH_3NH_3PbI_3$, (c) M-In_2O_3/ZnO/P3HT:$PC_{61}BM$, and (d) HC-PEDOT/SC-PEDOT/P3HT:$PC_{61}BM$. Devices were bent around cylindrical objects of varying radius, from the largest radius (6 mm) to the smallest (1.2 mm). The initial performance is indicated by *N* (no bending). The top row shows the normalized PCE as a function of bending radius for each of 3 devices on a single substrate. The bottom row shows representative *J-V* curves as a function of the bending radius.

In order to probe the origins of the observed device degradation, sheet resistance measurements were carried out on both the M-In_2O_3 and HC-PEDOT electrodes. Five electrodes of each type were tested with a four-point probe prior to any mechanical deformation. After bending one electrode of each type for 2000 cycles, the sheet resistance was measured again. The sheet resistances of the M-In_2O_3 and the HC-PEDOT electrodes were measured to be 8.1 ± 0.2 Ω/□ and 104 ± 5 Ω/□, respectively. After bending, the sheet resistance of the M-In_2O_3 film was beyond the measurement range of the instrument; however, the resistance of the HC-PEDOT electrode increased only marginally, to 113 Ω/□. This increase in the sheet resistance of the M-In_2O_3 electrode is attributed to the brittleness of the metal oxide matrix, which is clearly not an issue for the HC-PEDOT electrode. **Figure 3.8** shows a scanning electron micrograph of this breakage and the effect that it has on the top perovskite layer. Control images of pristine electrodes (before bending) are shown in **Figure 3.9**. As can be seen in Figure 3.8a, after 2000 bending cycles, a series of large cracks are created on the surface of the M-In_2O_3 electrode, which prevent charge transport and lead to the dramatic increase in sheet resistance described previously. These cracks can then propagate through the perovskite film (Figure 3.8b), and are observed as either horizontal, white-edged lines (where they have broken through to the surface of the perovskite layer), or dark streaks (where the crack is localized below the surface). These breaks lead to short-circuits and, ultimately, device failure. In contrast, Figure 3.8c shows no evidence of crack formation in the HC-PEDOT electrode, which is consistent with the negligible change in the sheet resistance. The surface texture visible in Figure 3.8c is a result of the roughness of the bottom PET layer, and is also visible in the pristine electrode (Figure 3.9c). These results clearly explain the difference in fatigue resistance between the devices prepared on ITO and on HC-PEDOT. Additionally, a careful examination of Figure 3.8d reveals a series of faint horizontal cracks running throughout

the $CH_3NH_3PbI_3$ layer; although not nearly as pronounced as those observed for the M-In_2O_3 electrode, they clearly demonstrate that the perovskite film is not entirely as flexible as first thought. These cracks would greatly impede carrier transport in the direction normal to the propagating crack, leading to the observed increase in R_s and J_{sc}. Additionally, the cracks also likely introduce trap states and recombination pathways, leading to the substantial decrease in R_{sh}. Since there is no observable change in the absorption spectrum of the perovskite film after bending (**Figure 3.10**), it is concluded that the changes in device performance are due to morphological changes in the perovskite film caused by mechanical stress, rather than any chemical degradation of the perovskite layer.

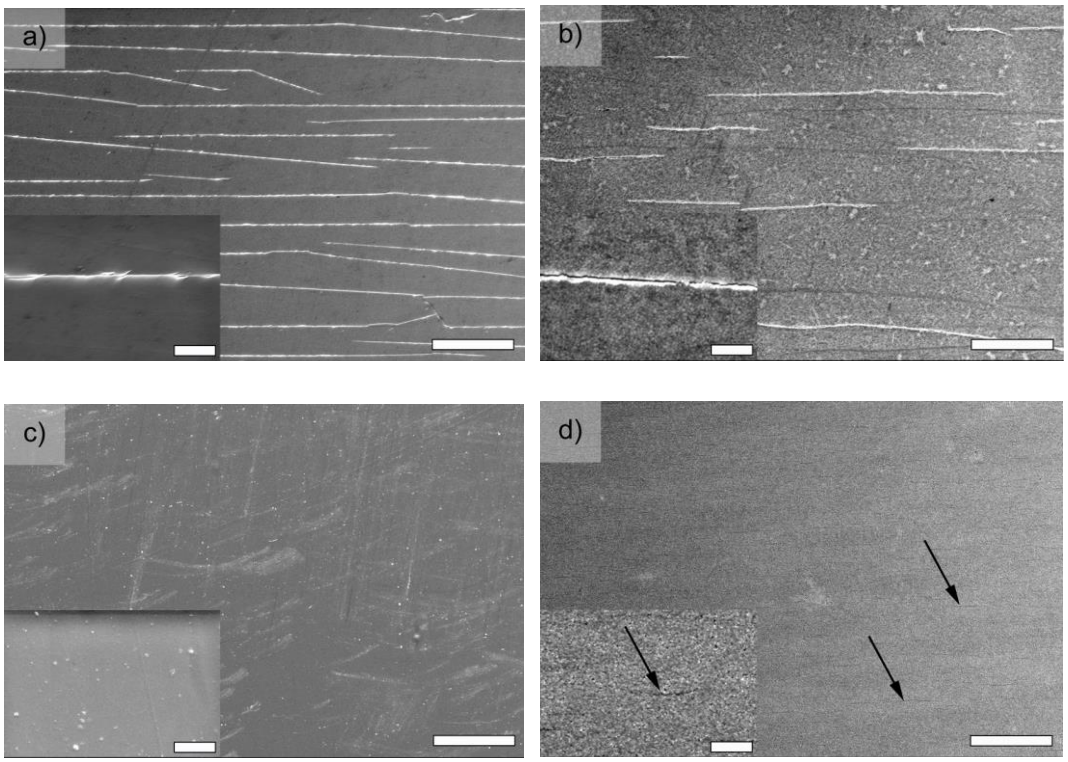

Figure 3.8. Low-magnification (main) and high-magnification (inset) SEM images of: (a) PET/M-In_2O_3, (b) PET/M-In_2O_3/ZnO/$CH_3NH_3PbI_3$, (c) PET/HC-PEDOT, and (d) PET/HC-PEDOT/SC-PEDOT/$CH_3NH_3PbI_3$ films after 2000 bending cycles. The scale bars in the main and inset images are 50 µm and 5 µm, respectively. The arrows in (d) show the location of small cracks in the perovskite layer.

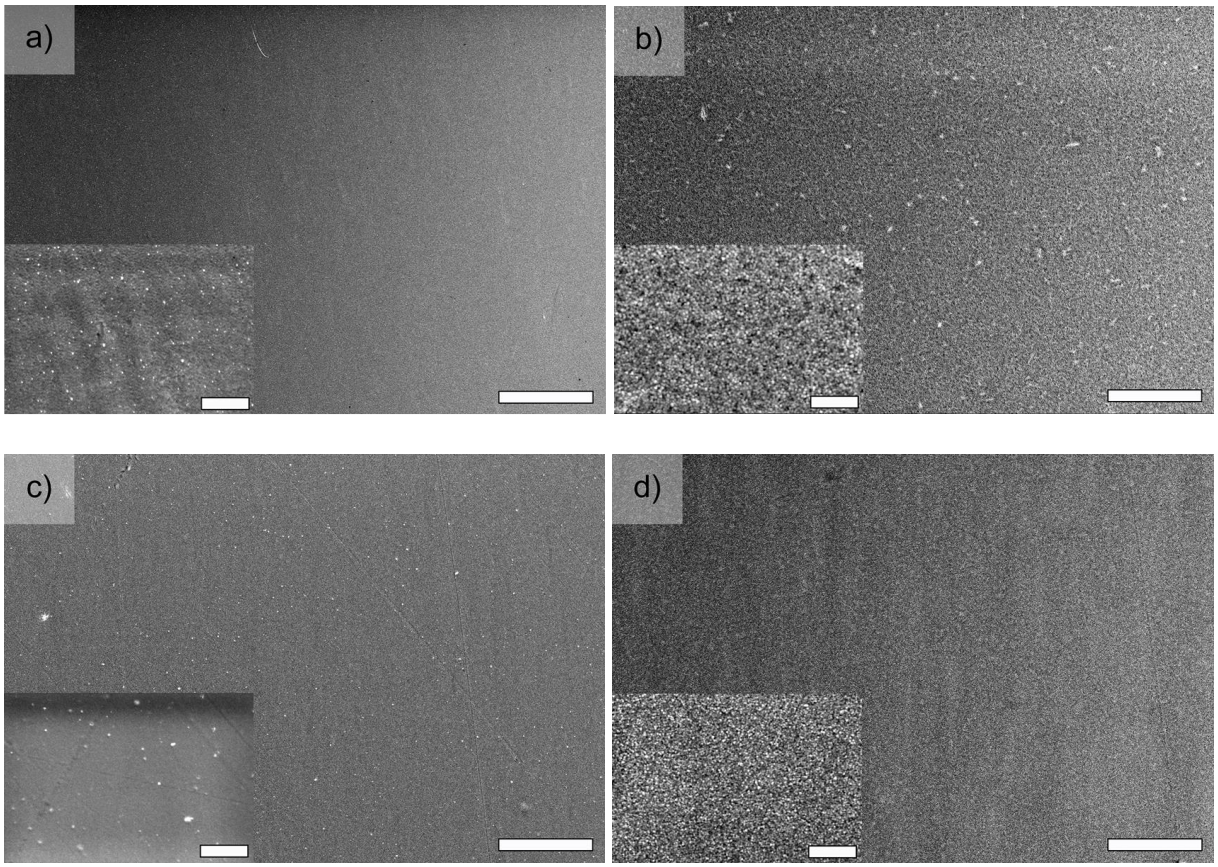

Figure 3.9. Low-magnification (main) and high-magnification (inset) SEM images of (a) PET/M-In_2O_3, (b) PET/M-In_2O_3/ZnO/$CH_3NH_3PbI_3$, (c) PET/HC-PEDOT, and (d) PET/HC-PEDOT/SC-PEDOT/$CH_3NH_3PbI_3$ films before bending. The scale bars in the main and inset images are 50 μm and 5 μm, respectively.

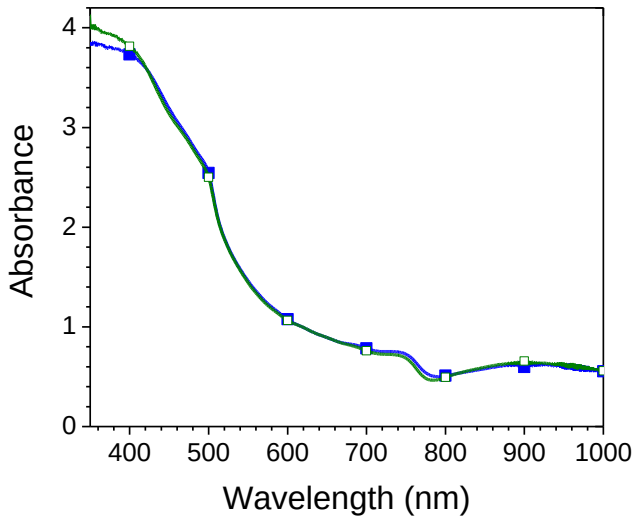

Figure 3.10. Absorption spectra of PET/M-In_2O_3/$CH_3NH_3PbI_3$ films before (solid blue squares) and after (open green squares) bending for 2000 cycles.

Finally, in order to confirm that these results are consistent across both M-In_2O_3 and ITO electrodes, the work was repeated on commercially available ITO/PET substrates. The sheet resistance (ca. 40 Ω/□) was found to be higher than that of the M-In_2O_3 electrodes, with a correspondingly higher optical transmittance (**Figure 3.11**). The device performance (Figure 3.11) was found to be similar to that reported previously,[2] and the fatigue resistance (**Figure 3.12**) was very similar to that of the M-In_2O_3 electrodes (Figure 3.5). Both ITO and M-In_2O_3 devices failed via the same sudden cracking of the transparent conductive oxide (**Figure 3.13**), with the sheet resistance of the ITO electrode increasing to 1.4×10^3 Ω/□ after 2200 bending cycles.

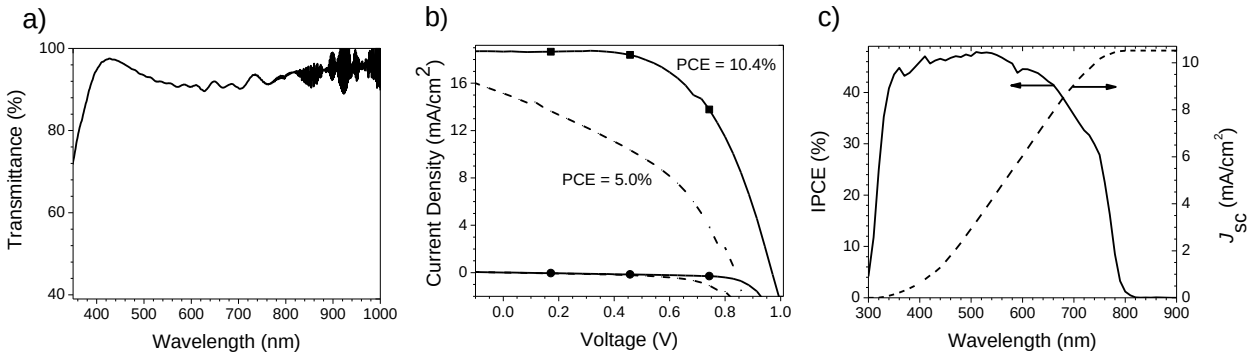

Figure 3.11. (a) Transmission spectrum of the ITO electrode, after subtraction of the PET background spectrum. (b) *J-V* curve of the ITO/ZnO/$CH_3NH_3PbI_3$/spiro-OMeTAD/Ag device, measured from forward bias to short-circuit (solid lines), and from short-circuit to forward bias (dashed lines), in both the light (squares) and in the dark (circles). (c) IPCE spectrum (solid line) and calculated J_{sc} value (dashed line) for a ITO/ZnO/$CH_3NH_3PbI_3$/spiro-OMeTAD/Ag device (the J_{sc} obtained from a reverse-scan *J-V* curve was 12 mA/cm^2).

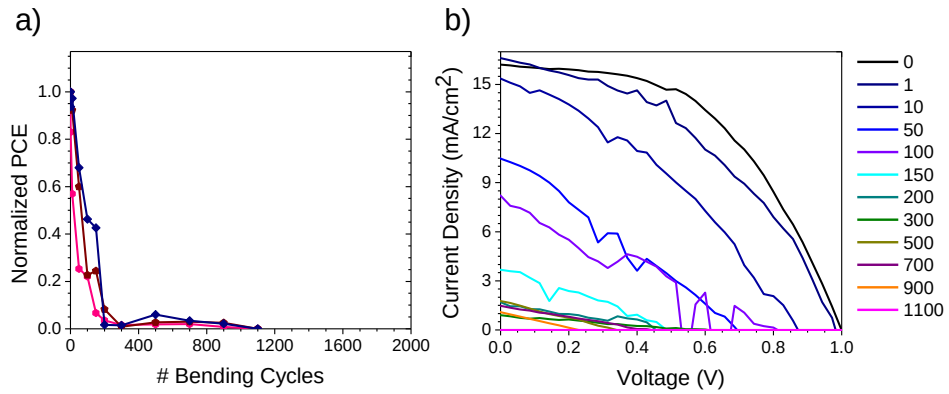

Figure 3.12. Results of the fatigue tests for ITO/ZnO/$CH_3NH_3PbI_3$/spiro-OMeTAD/Ag devices. (a) Normalized PCEs for 3 separate devices. (b) *J-V* curves as a function of the number of bending cycles for a typical device.

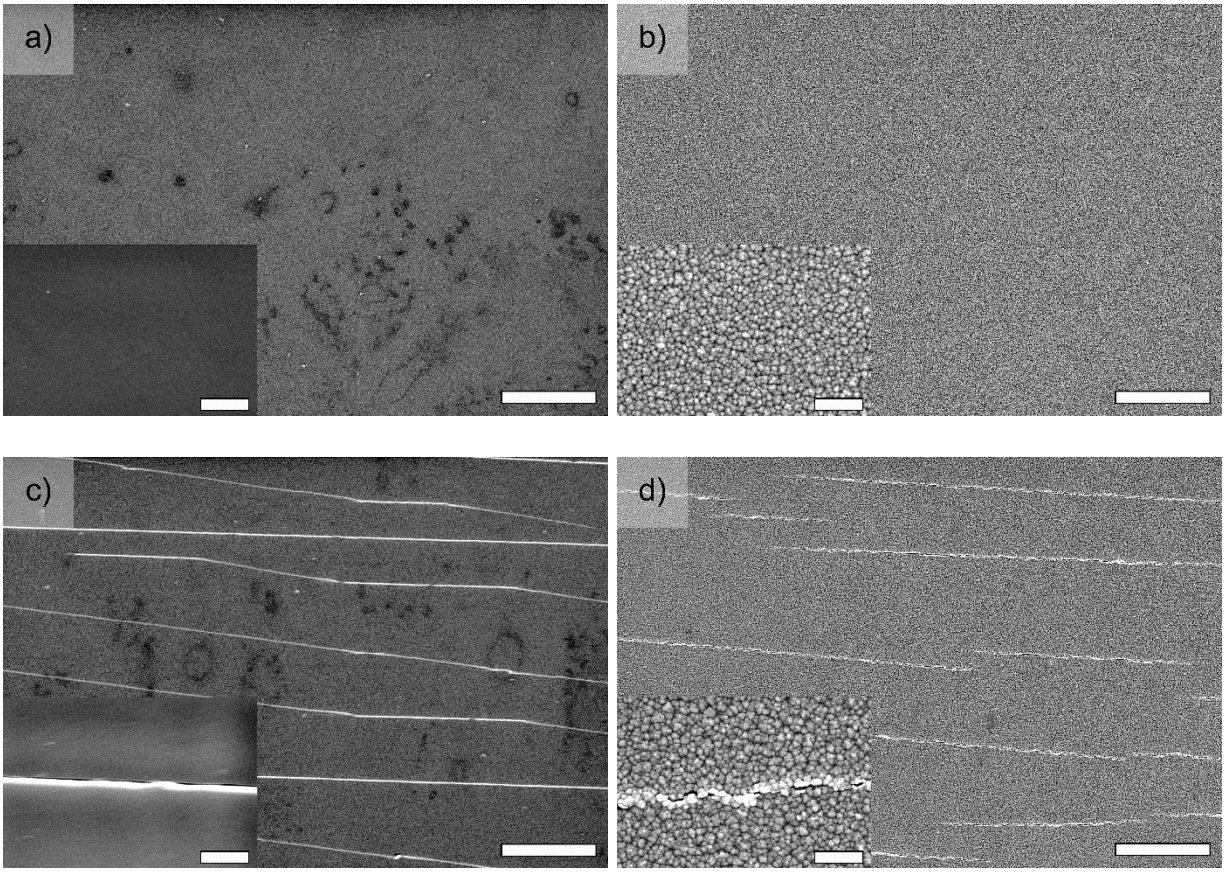

Figure 3.13. Low-magnification (main) and high-magnification (inset) SEM images of PET/ITO (a, c), and PET/ITO/ZnO/$CH_3NH_3PbI_3$ (b, d) films before (a, b) and after (c, d) 2200 bending cycles. The scale bars in the main and inset images are 50 µm and 5 µm, respectively.

3.5 Conclusions

Through the use of a HC-PEDOT transparent electrode, a flexible perovskite solar cell has been successfully fabricated containing no inorganic metal-oxide layers for the first time. The devices show power conversion efficiencies as high as 7.6% and very low hysteresis. The fatigue resistance of these devices, as well as those based on an In_2O_3 transparent electrode, was determined by repeatedly bending them around a cylindrical object of 4 mm radius for 2000 bending cycles. Our observations indicate that it is the metal-oxide transparent electrode that ultimately limits the

mechanical flexibility of these devices, and the use of the HC-PEDOT electrode circumvents this limit. The fatigue resistance of the perovskite solar cells was then compared to that of polymer-based devices, and it was found that the performance of the perovskite devices decreases more rapidly due to the formation of small cracks in the perovskite layer. Our results suggest that although the perovskite layer is incompatible with repeated bending at a low radius of curvature (as might be encountered in textile-integrated photovoltaics), it is more than robust enough for the more moderate conditions typically encountered in R2R manufacturing. This study outlines important limitations on the flexibility of conventional perovskite solar cells, which have important implications for their manufacture and eventual commercial application.

3.6 References

1. M. A. Green, K. Emery, Y. Hishikawa, W. Warta and E. D. Dunlop, *Prog. Photovolt: Res. Appl.*, 2014, **22**, 701-710.
2. D. Liu and T. L. Kelly, *Nat. Photonics*, 2014, **8**, 133-138.
3. H. Zhou, Q. Chen, G. Li, S. Luo, T. B. Song, H. S. Duan, Z. Hong, J. You, Y. Liu and Y. Yang, *Science*, 2014, **345**, 542-546.
4. N. J. Jeon, J. H. Noh, Y. C. Kim, W. S. Yang, S. Ryu and S. I. Seok, *Nat. Mater.*, 2014, **13**, 897-903.
5. J. W. Lee, D. J. Seol, A. N. Cho and N. G. Park, *Adv. Mater.*, 2014, **26**, 4991-4998.
6. R. F. Service, *Science*, 2014, **344**, 458.
7. Z. Wei, K. Yan, H. Chen, Y. Yi, T. Zhang, X. Long, J. Li, L. Zhang, J. Wang and S. Yang, *Energy Environ. Sci.*, 2014, **7**, 3326-3333.
8. J. Liu, Y. Wu, C. Qin, X. Yang, T. Yasuda, A. Islam, K. Zhang, W. Peng, W. Chen and L. Han, *Energy Environ. Sci.*, 2014, **7**, 2963-2967.
9. F. Hao, C. C. Stoumpos, D. H. Cao, R. P. H. Chang and M. G. Kanatzidis, *Nat. Photonics*, 2014, **8**, 489-494.
10. M. D. McGehee, *Nat. Mater.*, 2014, **13**, 845-846.
11. M. Grätzel, *Nat. Mater.*, 2014, **13**, 838-842.
12. F. Zuo, S. T. Williams, P.-W. Liang, C.-C. Chueh, C.-Y. Liao and A. K. Y. Jen, *Adv. Mater.*, 2014, **26**, 6454-6460.
13. P. Docampo, J. M. Ball, M. Darwich, G. E. Eperon and H. J. Snaith, *Nat. Commun.*, 2013, **4**, 2761.

14. C. Roldán-Carmona, O. Malinkiewicz, A. Soriano, G. Mínguez Espallargas, A. Garcia, P. Reinecke, T. Kroyer, M. I. Dar, M. K. Nazeeruddin and H. J. Bolink, *Energy Environ. Sci.*, 2014, **7**, 994-997.
15. Editorial, *Nat. Nanotechnol.*, 2014, **9**, 657.
16. P. Qin, S. Tanaka, S. Ito, N. Tetreault, K. Manabe, H. Nishino, M. K. Nazeeruddin and M. Gratzel, *Nat. Commun.*, 2014, **5**, 3834.
17. K. Wojciechowski, M. Saliba, T. Leijtens, A. Abate and H. J. Snaith, *Energy Environ. Sci.*, 2014, **7**, 1142-1147.
18. S. Kazim, M. K. Nazeeruddin, M. Gratzel and S. Ahmad, *Angew. Chem. Int. Ed.*, 2014, **53**, 2812-2824.
19. Q. Wang, Y. Shao, Q. Dong, Z. Xiao, Y. Yuan and J. Huang, *Energy Environ. Sci.*, 2014, **7**, 2359-2365.
20. L. Qiu, J. Deng, X. Lu, Z. Yang and H. Peng, *Angew. Chem. Int. Ed.*, 2014, **53**, 10425-10428.
21. B. J. Kim, D. H. Kim, Y.-Y. Lee, H.-W. Shin, G. S. Han, J. S. Hong, K. Mahmood, T. K. Ahn, Y.-C. Joo, K. S. Hong, N.-G. Park, S. Lee and H. S. Jung, *Energy Environ. Sci.*, 2015, **8**, 916-921.
22. J. Feng, *APL Materials*, 2014, **2**, 081801.
23. O. Inganas, *Nat. Photonics*, 2011, **5**, 201-202.
24. S. Pang, Y. Hernandez, X. Feng and K. Mullen, *Adv. Mater.*, 2011, **23**, 2779-2795.
25. J. Liu, D. B. Buchholz, R. P. Chang, A. Facchetti and T. J. Marks, *Adv. Mater.*, 2010, **22**, 2333-2337.
26. Y. Li, D.-K. Lee, J. Y. Kim, B. Kim, N.-G. Park, K. Kim, J.-H. Shin, I.-S. Choi and M. J. Ko, *Energy Environ. Sci.*, 2012, **5**, 8950-8957.
27. K. Ellmer, *Nat. Photonics*, 2012, **6**, 809-817.
28. D. S. Hecht, L. Hu and G. Irvin, *Adv. Mater.*, 2011, **23**, 1482-1513.
29. S. Soltanian, R. Rahmanian, B. Gholamkhass, N. M. Kiasari, F. Ko and P. Servati, *Adv. Energy Mater.*, 2013, **3**, 1332-1337.
30. F. Bonaccorso, Z. Sun, T. Hasan and A. C. Ferrari, *Nat. Photonics*, 2010, **4**, 611-622.
31. S. Seo, M. Min, S. M. Lee and H. Lee, *Nat. Commun.*, 2013, **4**, 1920.
32. D. Chen, H. Zhang, Y. Liu and J. Li, *Energy Environ. Sci.*, 2013, **6**, 1362-1387.
33. S.-I. Na, S.-S. Kim, J. Jo and D.-Y. Kim, *Adv. Mater.*, 2008, **20**, 4061-4067.
34. Y. H. Kim, C. Sachse, M. L. Machala, C. May, L. Müller-Meskamp and K. Leo, *Adv. Funct. Mater.*, 2011, **21**, 1076-1081.
35. M. Kaltenbrunner, M. S. White, E. D. Glowacki, T. Sekitani, T. Someya, N. S. Sariciftci and S. Bauer, *Nat. Commun.*, 2012, **3**, 770.
36. D. Alemu, H.-Y. Wei, K.-C. Ho and C.-W. Chu, *Energy Environ. Sci.*, 2012, **5**, 9662-9671.
37. Y. Xia, K. Sun and J. Ouyang, *Adv. Mater.*, 2012, **24**, 2436-2440.
38. C.-Y. Chang, L. Zuo, H.-L. Yip, C.-Z. Li, Y. Li, C.-S. Hsu, Y.-J. Cheng, H. Chen and A. K. Y. Jen, *Adv. Energy Mater.*, 2014, **4**, 1301645.
39. O. Malinkiewicz, A. Yella, Y. H. Lee, G. M. Espallargas, M. Graetzel, M. K. Nazeeruddin and H. J. Bolink, *Nat. Photonics*, 2014, **8**, 128-132.
40. V. W. Bergmann, S. A. L. Weber, F. Javier Ramos, M. K. Nazeeruddin, M. Grätzel, D. Li, A. L. Domanski, I. Lieberwirth, S. Ahmad and R. Berger, *Nat. Commun.*, 2014, **5**, 5001.
41. J. Seo, S. Park, Y. Chan Kim, N. J. Jeon, J. H. Noh, S. C. Yoon and S. I. Seok, *Energy Environ. Sci.*, 2014, **7**, 2642-2646.

42. D. Liu, M. K. Gangishetty and T. L. Kelly, *J. Mater. Chem. A*, 2014, **2**, 19873-19881.
43. H. J. Snaith, A. Abate, J. M. Ball, G. E. Eperon, T. Leijtens, N. K. Noel, S. D. Stranks, J. T.-W. Wang, K. Wojciechowski and W. Zhang, *J. Phys. Chem. Lett.*, 2014, **5**, 1511-1515.
44. R. S. Sanchez, V. Gonzalez-Pedro, J.-W. Lee, N.-G. Park, Y. S. Kang, I. Mora-Sero and J. Bisquert, *J. Phys. Chem. Lett.*, 2014, **5**, 2357-2363.
45. E. L. Unger, E. T. Hoke, C. D. Bailie, W. H. Nguyen, A. R. Bowring, T. Heumuller, M. G. Christoforo and M. D. McGehee, *Energy Environ. Sci.*, 2014, **7**, 3690-3698.
46. E. Zimmermann, P. Ehrenreich, T. Pfadler, J. A. Dorman, J. Weickert and L. Schmidt-Mende, *Nat. Photonics*, 2014, **8**, 669-672.
47. Z. Xiao, C. Bi, Y. Shao, Q. Dong, Q. Wang, Y. Yuan, C. Wang, Y. Gao and J. Huang, *Energy Environ. Sci.*, 2014, **7**, 2619-2623.
48. Z. Xiao, Q. Dong, C. Bi, Y. Shao, Y. Yuan and J. Huang, *Adv. Mater.*, 2014, **26**, 6503-6509.
49. W. Chen, W. Yongzhen, J. Liu, C. Qin, X. Yang, A. Islam, Y.-B. Cheng and L. Han, *Energy Environ. Sci.*, 2014, DOI: 10.1039/c4ee02833c.
50. J. H. Kim, P.-W. Liang, S. T. Williams, N. Cho, C.-C. Chueh, M. S. Glaz, D. S. Ginger and A. K. Y. Jen, *Adv. Mater.*, 2015, **27**, 695-701.
51. P.-W. Liang, C.-C. Chueh, X.-K. Xin, F. Zuo, S. T. Williams, C.-Y. Liao and A. K. Y. Jen, *Adv. Energy Mater.*, 2015, **5**, 1400960.
52. K. Wojciechowski, S. D. Stranks, A. Abate, G. Sadoughi, A. Sadhanala, N. Kopidakis, G. Rumbles, C.-Z. Li, R. H. Friend, A. K. Y. Jen and H. J. Snaith, *ACS Nano*, 2014, **8**, 12701-12709.
53. Y. Shao, Z. Xiao, C. Bi, Y. Yuan and J. Huang, *Nat. Commun.*, 2014, **5**, 5784.

Chapter 4. Compositional Engineering to Improve the Stability of Lead Halide Perovskites: A Comparative Study of Cationic and Anionic Dopants [3]

4.1 Transition Section

In the previous chapter, ways of improving the flexibility and fatigue resistance of perovskite solar cells were proposed and studied. Shortly after this study was completed, other researchers reported that the perovskite layer was very prone to decomposition after exposure to humidity. Later, it was shown that when there are photo- or bias-generated electrons in the perovskite layer, and oxygen is present, the perovskite decomposes and the effect is more serious than the effect of humidity. The consensus of the perovskite photovoltaics community is that perovskite instability is the most crucial issue limiting the commercialization of this promising technology. Afterwards, research by several different groups suggested that a change in the composition of the perovskite layer could have positive effects on the stability of perovskite solar cells. Typical changes included either cationic or anionic ion substitutions. However, it is rare for two papers to test their devices under the same environmental conditions. This made it difficult to compare the effect of changes made by different research groups. Therefore, there was a need to compare the effects of different dopants with each other. In addition, the effect of different environmental factors on perovskites with the same composition is rarely studied. In line with the overall objective of this thesis, the

[3] K. Poorkazem, T. L. Kelly, *In Preparation*.
Contributions: K.P. carried out the research and wrote the manuscript. T.L.K. directed the study and revised the manuscript.

relative stabilities of the conventional $MAPbI_3$ perovskite and four of the most-common cationic or anionic dopants are tested in this chapter. In addition, the relative effect of different environmental factors (humidity, O_2/light, and heat) was studied. As a result, this chapter deals with comparing the effects of different cationic and anionic dopants on the moisture resistance and photochemical stability of perovskite films.

4.2 Introduction

Lead halide perovskites are an exciting class of hybrid organic-inorganic semiconductor, and have found application in a wide variety of optoelectronic devices, such as solar cells,[1] light-emitting diodes,[2] photodetectors,[3] and lasers.[4] In particular, enormous interest has been paid to PSCs, since the perovskites are derived from relatively Earth-abundant materials, and the devices can be manufactured using highly scalable, low-temperature fabrication processes. However, in order to be commercially viable, PSCs need to be robust enough to withstand a wide variety of environmental conditions. Unfortunately, this is not yet the case, and lead halide perovskites have been shown to be unstable under a variety of real-world conditions, such as high temperatures,[5] humidity,[6, 7] and the synergetic effects of oxygen and light.[8] Prolonged exposure to harsh conditions leads to perovskite decomposition, and ultimately, to device failure.

One of the most deleterious environmental stimuli for perovskites is high relative humidity (RH). In high RH environments, the methylammonium lead iodide perovskite absorbs water, which can lead to the reversible formation of a crystalline monohydrate phase.[9] Upon prolonged exposure, further hydration occurs, producing both a dihydrate phase and PbI_2.[6, 7, 9] Ultimately, the hydrate phases have reduced dimensionality (Figure 1.13b), leading to a loss of both light

absorption and carrier transport, rendering them useless in device applications. In addition to water vapor, Bryant *et al.* showed that the synergetic effect of molecular oxygen and light was highly detrimental to $CH_3NH_3PbI_3$ PSCs.[8] The authors demonstrated that the photoexcitation of $CH_3NH_3PbI_3$ in the presence of oxygen led to the formation of superoxide anions via the reduction of oxygen by conduction band electrons. The superoxide then readily deprotonated the methylammonium cation to decompose the perovskite into PbI_2 and CH_3NH_2.[10] As a result of these environmental instabilities, unencapsulated PSCs can fail in a matter of hours or days, depending on the perovskite composition and the device architecture.

Numerous strategies have been proposed to improve the stability of PSCs, including the modification of interfacial layers,[11-16] altering the perovskite deposition method,[17-23] or changing the perovskite composition.[24-33] Although the improvement of interfacial layers and electrodes is obviously extremely important, tuning the perovskite composition itself is a highly attractive strategy, in that a more stable perovskite layer could be used in a variety of different device architectures, and would also be useful in other perovskite-based optoelectronic devices. In an example of this approach, the hydrophobicity of 1,1,1-trifluoroethylammonium iodide was used to impart a higher moisture resistance to $CH_3NH_3PbI_3$-based cells; however, the improvement was limited to a small amount of this additive, since the addition of larger amounts would shift the perovskite structure from 3D to 2D, sacrificing carrier mobility in the process.[33] Therefore, changes to the perovskite composition should ideally be done without reducing the dimensionality.

In general, a lead halide perovskite of the general formula $APbX_3$ is prepared by the reaction of an AX salt with a lead halide (PbX_2), where the A-site cation is of the appropriate size to occupy the void spaces of the PbX_3 framework. Although the $CH_3NH_3PbI_3$ perovskite was the first material used in PSCs, other monovalent cations, such as formamidinium (FA), can be readily

substituted in the A-site.[5, 34] Ethylammonium (EA) has been used in a few studies.[35-37] However, the larger size of EA in pure $EAPbI_3$ causes the formation of layered structures. As for the halides, iodide can be partially replaced by bromide or chloride in order to tune the optoelectronic properties of the resulting material. Although chloride is too small to directly substitute iodide in the $APbX_3$ lattice, its presence in the perovskite precursor solution has been shown to improve the crystallization of the perovskite layer, and affects the photovoltaic performance of fabricated devices.[38, 39] While individual studies have looked at the effect of some of these ion substitutions on perovskite stability, they are often carried out using different testing protocols or environmental conditions, and no single study has directly compared their efficacy.

Here, a comparative study has been carried out on how various ion substitutions affect the stability of lead halide perovskites. Thin films of $MAPbI_3$ and four different mixed-ion perovskites − $MAPbI_{3-x}Br_x$, $MAPbI_3(Cl)$, $(MA)_{1-x}(EA)_xPbI_3$, and $(MA)_{1-x}(FA)_xPbI_3$ − were prepared. Their stability in an 85% RH environment was evaluated, as was their photochemical stability in the presence of molecular oxygen. Overall, the FA-doped samples appeared to have an increased resistance to the effects of moisture, and a lower photochemical reactivity, while the various other ion substitutions had little to no impact on the stability of the films.

4.3 Experimental Section

4.3.1 Materials

HI, CH_3NH_2, HBr, $CH_3CH_2NH_2$, formamidine acetate salt, glass/FTO slides (R_s = 7 Ω/□), PbI_2, Li-TFSI, and 4-*tert*-butylpyridine were purchased from Sigma-Aldrich. Diethyl ether, HCl, 2-propanol, DMF, and chlorobenzene were purchased from Fisher Scientific. Ethanol, glass slides,

Extran 300, and P3HT were purchased from Commercial Alcohols, VWR, EMD, and Rieke Metals, respectively. White light emitting diodes, drivers, and wiring harnesses were purchased from Luxeonstar LEDs, while heat sinks for the LEDs were purchased from Alpha Novatech. MAI,[40] MABr,[41] MACl,[42] EAI,[35] and FAI[41] were synthesized according to literature procedures.

4.3.1.1 MAI synthesis

Hydriodic acid (15 mL, 57% in water) was added dropwise with stirring to a solution of CH_3NH_2 (14.3 mL, 33% in ethanol) in ethanol (100 mL) at 0 °C, and stirred for 2 h. The solution was heated at 50 °C for 1 h to reduce the volume of solvent, and the resulting precipitate was collected by suction filtration and washed with diethyl ether. The product was recrystallized by dissolving in refluxing ethanol and reprecipitated by the addition of diethyl ether. After an additional recrystallization cycle, the product was dried at 80 °C in an oven overnight.

4.3.1.2 MABr synthesis

Hydrobromic acid (44 mL, 48% in water) was added dropwise with stirring to CH_3NH_2 (40 mL, 33% in ethanol) at 0 °C, and stirred for 4 h. The solvent was evaporated at 80 °C and the resulting precipitate was collected by suction filtration and washed with diethyl ether. The product was recrystallized by dissolving in refluxing ethanol and reprecipitated by the addition of diethyl ether. The product was dried *in vacuo* at 60 °C for 24 h.

4.3.1.3 MACl synthesis

Hydrochloric acid (15 mL, 37% in water) was added dropwise with stirring to a solution of

CH_3NH_2 (24 mL, 33% in ethanol) in ethanol (100 mL) at 0 °C, and stirred for 1 h. The solution was heated at 50 °C for 1 h to reduce the solvent volume, and the resulting precipitate was collected by suction filtration and washed with diethyl ether. The product was recrystallized by dissolving

in refluxing ethanol and reprecipitated by the addition of diethyl ether. After an additional recrystallization cycle, the product was dried at 80 °C in an oven overnight.

4.3.1.4 EAI synthesis

Hydriodic acid (10 mL, 57% in water) was added dropwise with stirring to $CH_3CH_2NH_2$ (2.9 mL, 66-72% in H_2O) at 0 °C, and stirred for 2 h. The solvent was evaporated at 80 °C and the resulting precipitate was collected by suction filtration and washed with diethyl ether. The product was recrystallized by dissolving in refluxing ethanol and reprecipitated by the addition of diethyl ether. The product was dried *in vacuo* at 100 °C for 24 h.

4.3.1.5 FAI synthesis

Hydriodic acid (30 mL, 57% in water) was added dropwise with stirring to formamidine acetate (15 g, 0.14 mol) at 0 °C, and stirred for 2 h. The solvent was evaporated at 80 °C and the resulting precipitate was collected by suction filtration and washed with diethyl ether. The product was recrystallized by dissolving in refluxing ethanol and reprecipitated by the addition of diethyl ether. The product was dried *in vacuo* at 60 °C for 24 h.

4.3.1.6 Synthesis of $MAPbI_3$, $MAPbI_{2.8}Br_{0.2}$, $(MA)_{0.8}(EA)_{0.2}PbI_3$, and $(MA)_{0.8}(FA)_{0.2}PbI_3$ powders

To synthesize $MAPbI_3$, 1 mL of a 0.5 M PbI_2 and 0.5 M MAI solution was prepared in DMF. For the other three perovskites, 20 mol% of the MAI was replaced with either MABr, EAI, or FAI. The solutions were stirred at 70 °C for 1 h. The solutions were evaporated to dryness by evaporation under reduced pressure at 60 °C. The resulting powders were brought into the glovebox and ground to a fine powder. They were annealed at either 140 °C ($(MA)_{0.8}(FA)_{0.2}PbI_3$) or 120 °C (all other samples) overnight.

4.3.2 Perovskite Film Fabrication

Glass slides (2.5 cm × 2.5 cm) were cleaned by sequentially sonicating for 20 min in a 2% (v/v) aqueous Extran 300 solution, deionized water, and isopropanol. They were dried for at least 2 h in an oven and UV/ozone treated for 15 min immediately prior to use. A combination of interlayer diffusion[43] and solvent annealing[44] (with minor modifications) was used to prepare the perovskite thin films. In a nitrogen-filled glovebox, a 1.00 M solution of PbI_2 in anhydrous DMF was prepared and pre-heated to 100 °C, as was the glass substrate. A PbI_2 layer was deposited by spin coating at 3000 r.p.m. for 30 s, followed by 3 min of drying at room temperature, and 5 min of annealing at 100 °C. The film was removed from the glovebox, and 700 µL of a 0.050 M solution of MAI (20 mol% of the MAI was replaced by MABr, MACl, EAI or FAI for the mixed-ion perovskites) in anhydrous 2-propanol was dispensed evenly across the film. After 45 s, the substrate was spun at 4000 r.p.m. for 20 s. One of two annealing treatments was then used. In method A, the samples were placed on a hot plate at either 140 °C (for $(MA)_{1-x}(FA)_xPbI_3$) or 100 °C (all other samples) for a period of 5 min. In method B, the same temperatures were used, but the annealing was carried out in the glovebox, in the presence of DMF vapor (as shown in **Figure 4.1**). Method A was used for the samples in Figures 4.2, 4.4-4.6, 4.8, 4.9, 4.12, 4.15, 4.16, while method B was used to prepare samples for all other data sets. For P3HT coated samples, 20 mg P3HT, 3.4 µL 4-*tert*-butylpyridine, and 6.8 µL of a Li-TFSI solution (28 mg/mL acetonitrile) were dissolved in 1 mL of anhydrous chlorobenzene, and a thin film deposited by spin coating at 1000 rpm for 30 s and at 3000 rpm for 10 s.

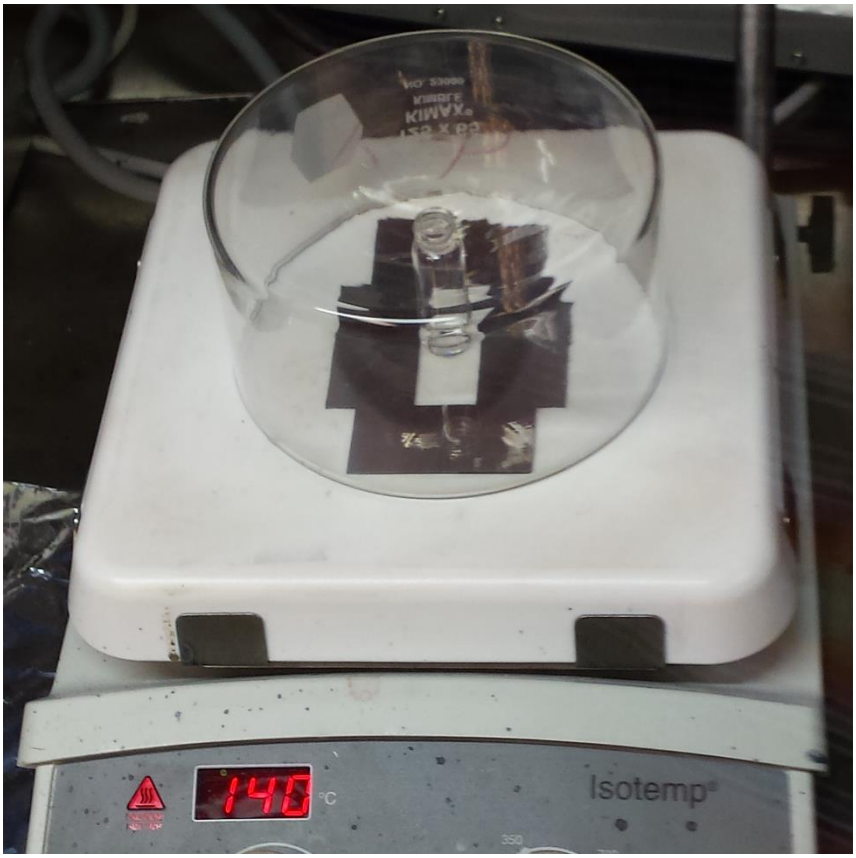

Figure 4.1. Photograph of the experimental setup used to solvent anneal samples. The vial contains 300 µL of anhydrous DMF.

4.3.3 Device Fabrication

FTO-coated glass slides were cleaned as described in the main text. A compact layer of TiO_2, was deposited by spin coating the precursor solution at 2000 rpm for 40 s, as described elsewhere,[45] followed by sintering at 450 °C for 1.5 h. The perovskite and P3HT hole-transport layer were deposited as described in the main text. Finally, a 70 nm Ag or Au electrode was deposited by thermal evaporation at a base pressure of 1×10^{-6} mbar.

4.3.4 Characterization

pXRD patterns were measured by a PANalytical Empyrean diffractometer operating with a Co

source. Absorption spectra were acquired on a Cary 6000i UV-vis-NIR spectrophotometer. SEM images were taken by a Hitachi SU8010 microscope. Fluorescence spectra were acquired on a PTI fluorometer using an excitation wavelength of 460 nm. Atomic force microscopy was carried out using a Dimension Hybrid Nanoscope system (Bruker/Veeco Metrology). Solar cell efficiency measurements were made using a 450 W Class AAA solar simulator, equipped with an AM1.5G filter (Sol3A, Oriel Instruments). The illumination intensity was set to 1 sun using a standard silicon reference cell (91150V, Oriel Instruments). The active area of the cell was defined to be 0.101 cm^2 using a non-reflective metal aperture mask. All measurements were made inside the glovebox using a Keithley 2420 source-measure unit. Density functional theory calculations were carried out using the Spartan software package; optimized equilibrium geometries and electrostatic potential maps were calculated at the M06/6-31+G(d) level of theory.

4.4 Results and discussion

4.4.1 Fabrication and Characterization of Perovskite Thin Films

Perovskite films were first fabricated and characterized based on a two-step spin-coating process (**Figure 4.2a**). In all cases, a thin film of PbI_2 was first deposited by spin-coating from a DMF solution. In the second step, a low concentration (0.050 M) solution of MAI in 2-propanol was spin-coated onto the PbI_2 layer; the solution was left quiescent for 45 s prior to spinning in order to allow time for the MAI to intercalate into the PbI_2 thin film and for conversion to the perovskite to occur.[43] To produce the various mixed-ion perovskites, 20 mol% of the MAI in the second step was replaced by the appropriate halide salt (either MABr, MACl, EAI, or FAI, Figure 4.2a). Importantly, FA-containing perovskites often require a thermal annealing step (with temperatures

as high as 170 ºC) to go from a yellow, hexagonal δ-phase to a black, trigonal α-phase.[46, 47] In this work, it was observed that thermal annealing at 140 °C was sufficient to produce dark films of $(MA)_{1-x}(FA)_xPbI_3$, with no δ-phase observable in the pXRD pattern (Figure 4.2b). The relatively lower temperatures required here are likely due to the substantial mole fraction of MAI used in this case, as opposed to the higher temperatures required to produce pure $FAPbI_3$. All other films were annealed at 100 °C, with details provided in the Experimental Section.

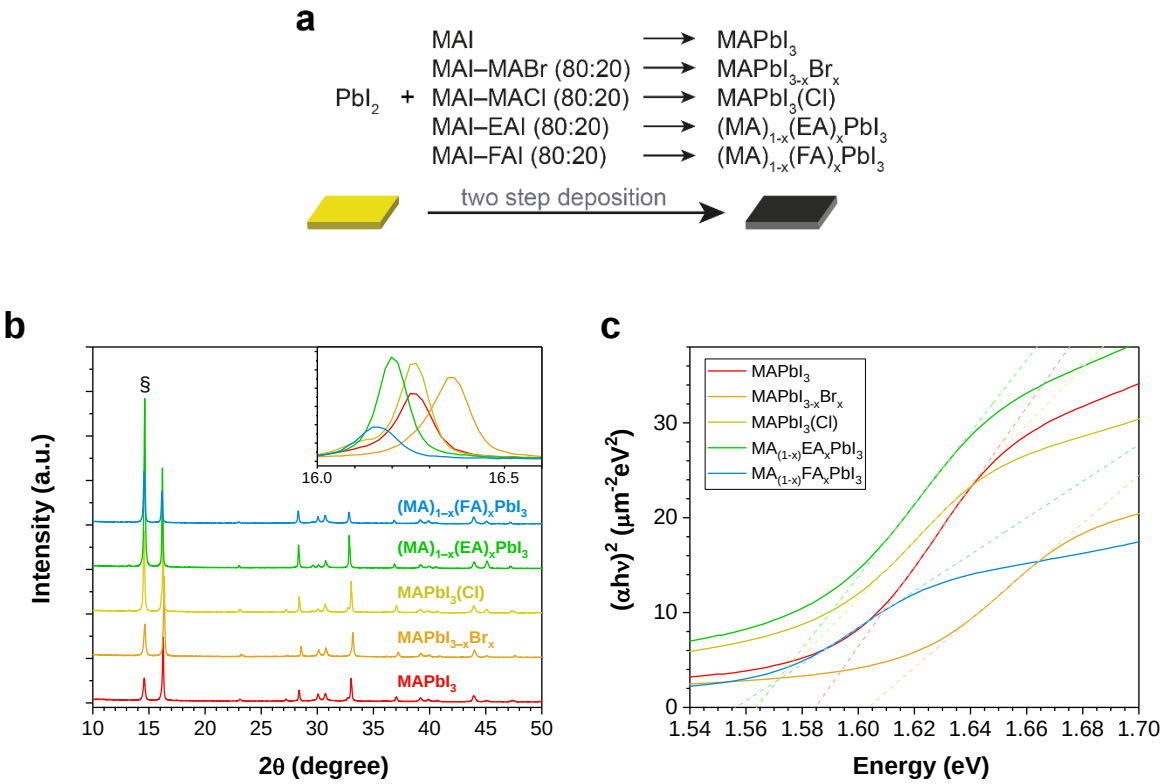

Figure 4.2. (a) Schematic of the two-step spin-coating procedure used for the deposition of mixed-ion perovskites; (b) pXRD patterns and (c) Tauc plots of perovskite thin films. In (b), § indicates the (001) reflection of PbI_2, and the inset shows an expanded view of the perovskite peak at ca. 16°; in (c), experimental data are shown as solid lines, while least squares fits to the linear region are shown as dashed lines.

To assess whether the various dopants were actually incorporated into the perovskite lattice, the pXRD patterns of each film were measured (Figure 4.2b). The most prominent perovskite peak is the (110) reflection, observed at ca. 16° 2θ (Figure 4.2b, inset). With bromide substitution, this peak shifts to higher angle, consistent with a decrease in the lattice parameters, owing to the substitution of the smaller bromide ion. For both the $(MA)_{1-x}(EA)_xPbI_3$ and $(MA)_{1-x}(FA)_xPbI_3$ samples, the peak shifts to smaller diffraction angles, commensurate with the larger size of the EA and FA cations. No shift is observed for the $MAPbI_3(Cl)$ sample; consistent with other literature reports, the chloride ion is too small to effectively replace iodide in the lattice, and so no ion substitution occurs in this sample. Similar shifts (or lack thereof) are observed in the other peaks of the diffraction pattern, and no additional peaks are observed. These shifts were consistent with literature reports of mixed-ion perovskites with these particular dopants;[35, 41, 48] Nonetheless, powdered samples of these same materials were synthesized for comparison, and the same shifts were observed in the pXRD patterns of the powders (**Figure 4.3**).

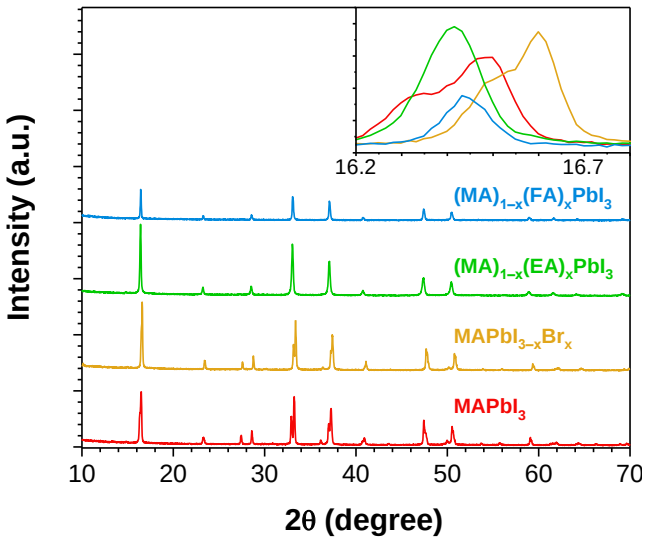

Figure 4.3. pXRD patterns of perovskite powder samples.

The inclusion of the different dopants in the perovskite lattice was further evaluated by absorption spectroscopy (**Figure 4.4**). Tauc plots (Figure 4.2c) were used to estimate the optical bandgap of each sample. In such a plot, α is the absorbance divided by the thickness of the layer, h is Planck constant, ν is the light frequency, and the power of 2 is used for direct-bandgap semiconductors. The data revealed a blue-shift in the bandgap of $MAPbI_{3-x}Br_x$ (1.60 eV) relative to $MAPbI_3$ (1.58 eV), and a red-shift in the bandgap of $(MA)_{1-x}(FA)_xPbI_3$ (1.56 eV); given the bandgaps of pure $MAPbBr_3$ (2.24 eV)[49] and α-$FAPbI_3$ (1.41 eV)[50] single crystals, this is consistent with partial ion substitution in the thin films prepared here. In addition, a small red shift for the $(MA)_{1-x}(EA)_xPbI_3$ and $MAPbI_3$(Cl) samples (both 1.56 eV) was also observed. This may be due to the variations in crystallite size observed (**Figure 4.5**, top row). As shown, the crystallite size of $MAPbI_{3-x}Br_x$ and $(MA)_{1-x}(FA)_xPbI_3$ were very similar to $MAPbI_3$; however, the $MAPbI_3$(Cl) and $(MA)_{1-x}(EA)_xPbI_3$ crystallites were significantly larger. Depth histograms using atomic force microscopy (**Figure 4.6**) further confirmed this size difference. The larger crystallite sizes observed in these two perovskite samples results a higher surface roughness and stronger Mie scattering. This can in turn produce an artificial red-shift in the optical bandgap, as noted by Tian and Scheblykin.[51]

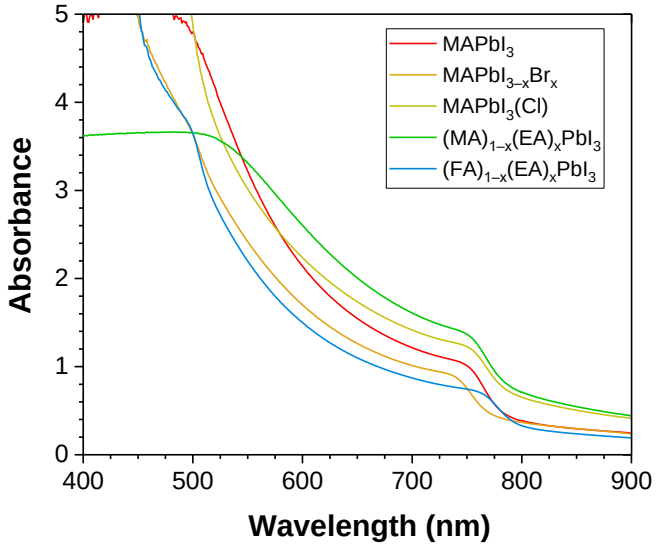

Figure 4.4. UV/vis absorbance spectra of perovskite thin films.

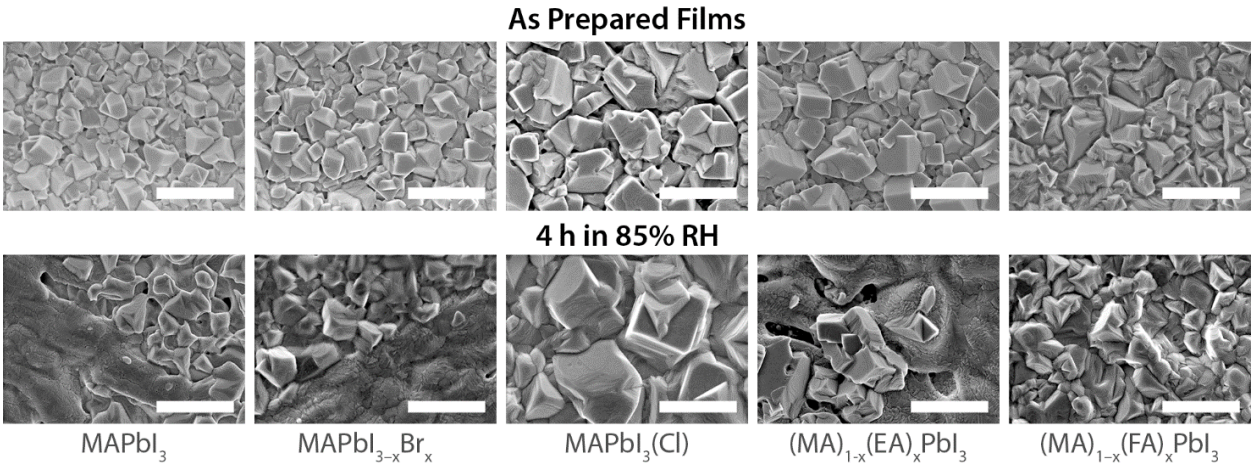

Figure 4.5. SEM images of perovskite thin films before (top row) and after (bottom row) exposure to an 85% RH environment for 4 h. Scale bars are all 1 µm.

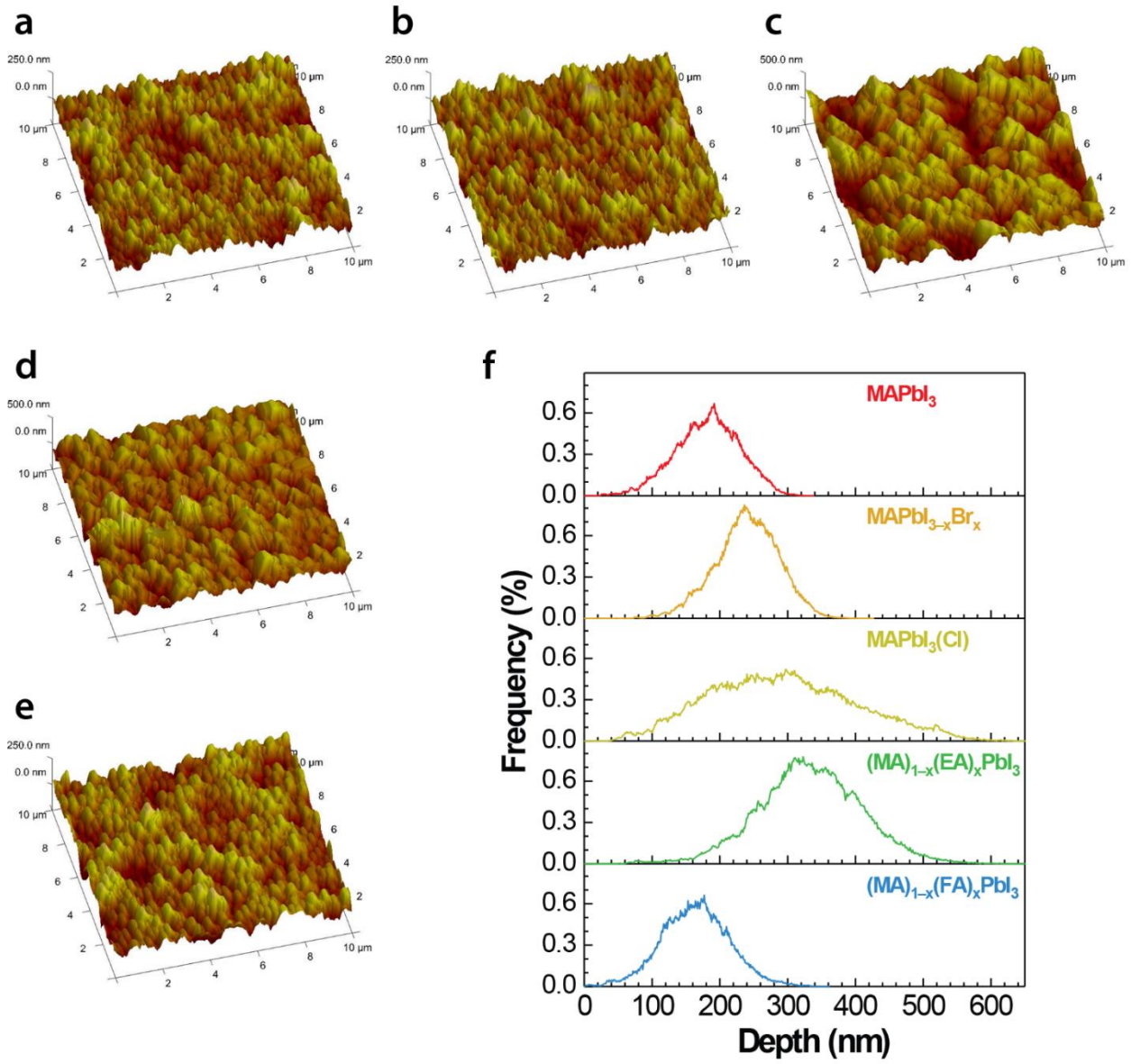

Figure 4.6. AFM images of: (a) $MAPbI_3$, (b) $MAPbI_{3-x}Br_x$, (c) $MAPbI_3(Cl)$, (d) $(MA)_{1-x}(EA)_xPbI_3$, and (e) $(MA)_{1-x}(FA)_xPbI_3$ thin films. (f) Histogram of AFM topography from the films in (a-e).

4.4.2 Moisture Stability

The effect of humidity on the various perovskite thin films was then evaluated. Samples were stored at room temperature in a gas-tight desiccator fitted with inlet and outlet ports (**Figure 4.7**);

a stream of nitrogen gas at 85% RH (prepared using a system of bubblers and flow controllers)[6] was introduced into the chamber, and the humidity was validated downstream of the sample chamber by way of an external sensor. SEM was used to capture the morphological changes occurring in the perovskite films in the early stages of moisture-induced decomposition (Figure 4.5, **Figure 4.8**). In most cases, after 4 h of exposure, two distinct regions could be observed in the SEM images – a bright region where individual perovskite crystallites were still intact, and a darker region with a less well defined, more amorphous appearance. However, even in the brighter, less disturbed regions of the images, there is evidence of rounding at the edges of the crystallites, and adjacent particles have begun to fuse together. This is similar to what Gangishetty *et al.* observed in $MAPbI_3$ films grown in a 40-60% RH environment.[52] It suggests that in the early stages of the hydration process, water is absorbed by the perovskite crystallites; this in turn facilitates ionic diffusion in the solid, disrupting the crystalline perovskite lattice and leading to increased amorphization of the film.

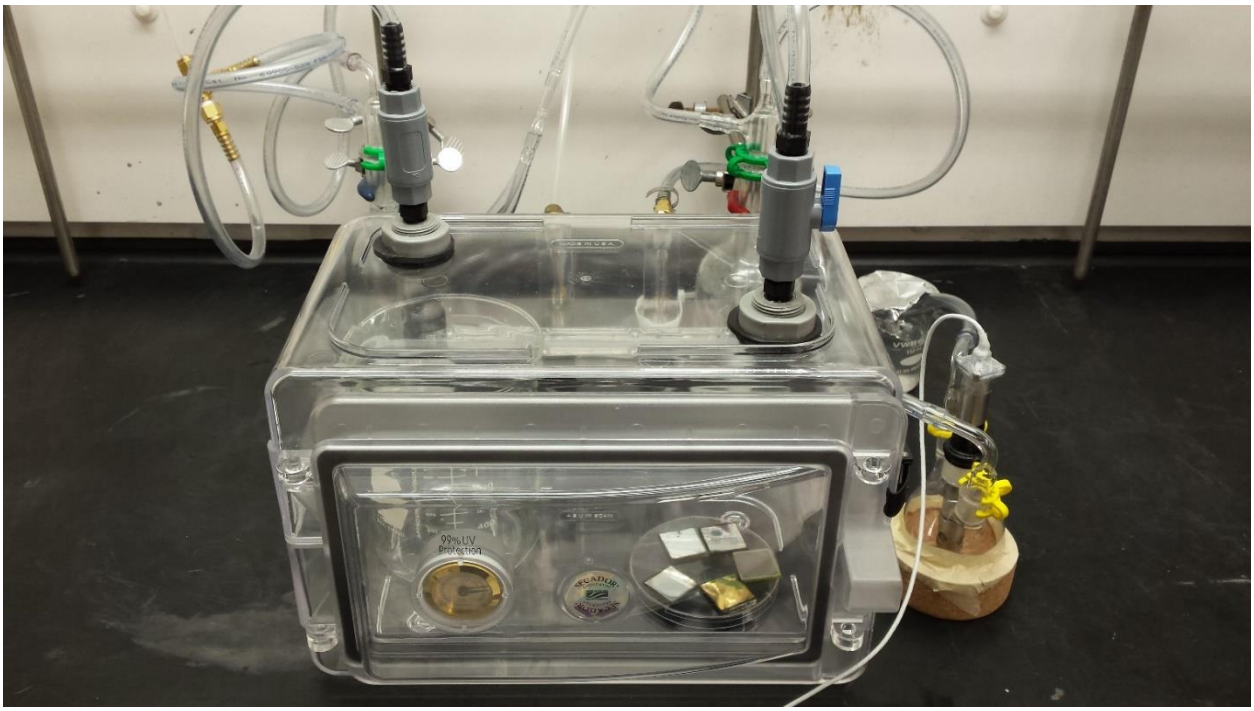

Figure 4.7. Photograph of the sample chamber used to store perovskite thin films in a controlled atmosphere environment.

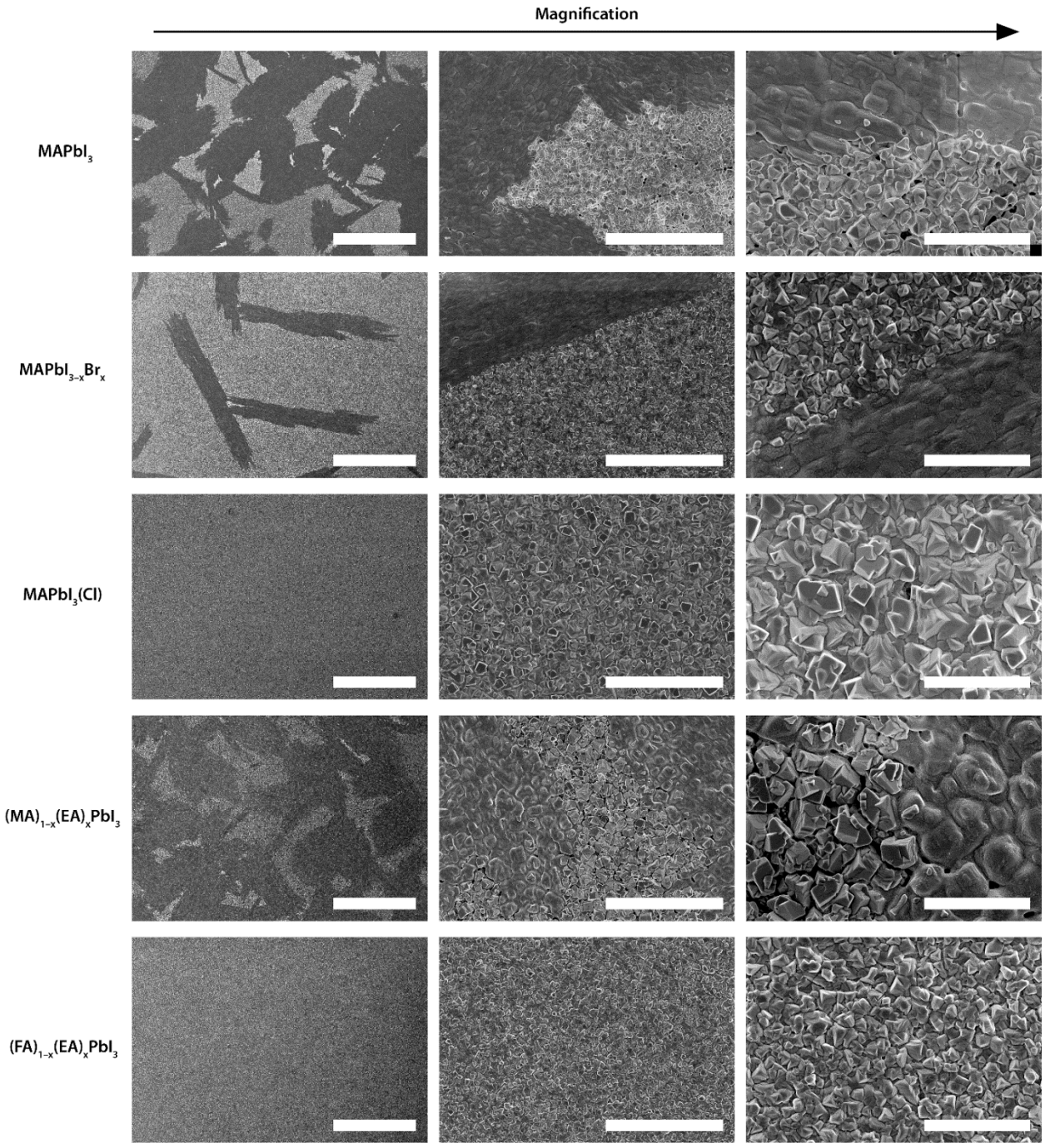

Figure 4.8. SEM images of perovskite films after 4 h of exposure to 85% RH. The scale bars are 50, 10, and 3 μm for the low, medium, and high magnification images, respectively.

In order to evaluate these changes in crystallinity more directly, pXRD was used to monitor the diffraction patterns of the films as a function of exposure time to water vapor (**Figure 4.9**). However, one of the problems with using conventional benchtop diffraction to follow moisture-induced changes in the perovskite structure is that the various hydrate phases are unstable at the low relative humidities typically found in ambient conditions.[7] Therefore, first the perovskite films were coated with a thin layer of the hole-transport material P3HT,[53] which has been shown to decelerate the moisture-induced decomposition of $MAPbI_3$;[6] it therefore also serves to decelerate the reverse dehydration process, enabling us to detect the formation of any intermediate hydrate phases. The pXRD patterns of $MAPbI_3$ follow the general trend expected from previous *in situ* absorbance spectroscopy and *in situ* grazing incidence wide angle X-ray scattering (GIWAXS) experiments; after an initial induction period of 12 – 24 h, in which the water vapor permeates the P3HT capping layer to reach the perovskite below, there is the appearance of a crystalline monohydrate phase (identified by diagnostic diffraction peaks at ca. 9.8 and 12.1°), while the perovskite diffraction peaks decrease substantially in intensity. Upon further exposure to water vapor, the hydrated intermediate also disappears, and is replaced by PbI_2, as indicated by the growth of the (001) PbI_2 reflection at 14.6°. Very similar behavior is observed for the $MAPbI_3$(Cl) and $(MA)_{1-x}(EA)_xPbI_3$ samples, both of which show evidence of intermediate monohydrate phases. However, in contrast, no hydrate phases were observed in the $MAPbI_{3-x}Br_x$ and $(MA)_{1-x}(FA)_xPbI_3$ samples, regardless of exposure time. Additionally, if the normalized intensity of the perovskite reflection at 16° is plotted as a function of time (Figure 4.9b), these two samples display the slowest perovskite decomposition kinetics. The relatively better crystal stability of $MAPbI_{3-x}Br_x$ compared to $MAPbI_3$ is in line with early experiments on bromide-doped PSCs,

although the conditions employed here (85% RH) were substantially harsher than what was studied previously.[54]

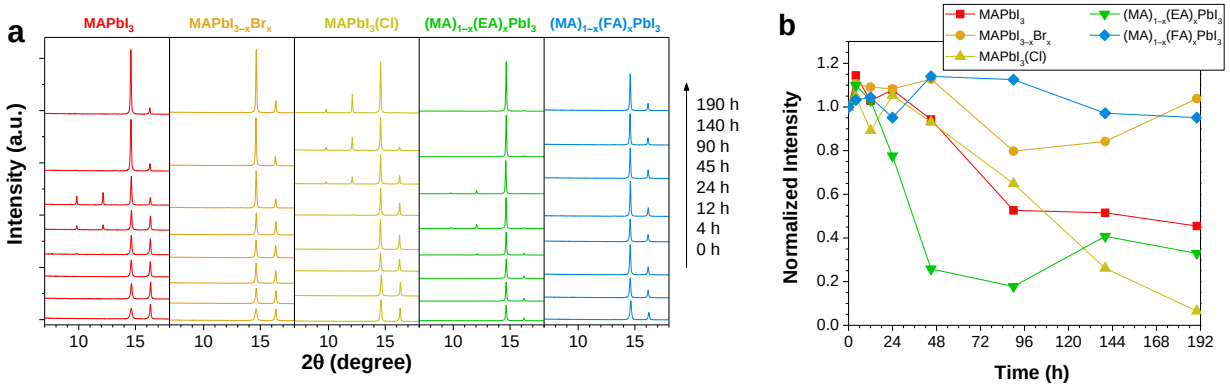

Figure 4.9. (a) pXRD patterns of P3HT-coated perovskite films after exposure to an 85% RH environment for various times; (b) normalized intensity of the perovskite peak at ca. 16° as a function of exposure time. Normalization was done by dividing the maximum intensity at each exposure time by the initial maximum value.

As part of this work, it was also observed that the annealing conditions used to prepare the perovskite films had an effect on their stability. Samples that were annealed for 5 min under ambient laboratory conditions showed slightly less resistance to the effects of moisture than those that were solvent annealed in the presence of DMF vapor (**Figure** 4.1, **4.10**). However, the films otherwise appeared to be quite similar (**Figure 4.11**); with this in mind, solvent-annealing was used to prepare the films for further tests of their humidity and photochemical stability.

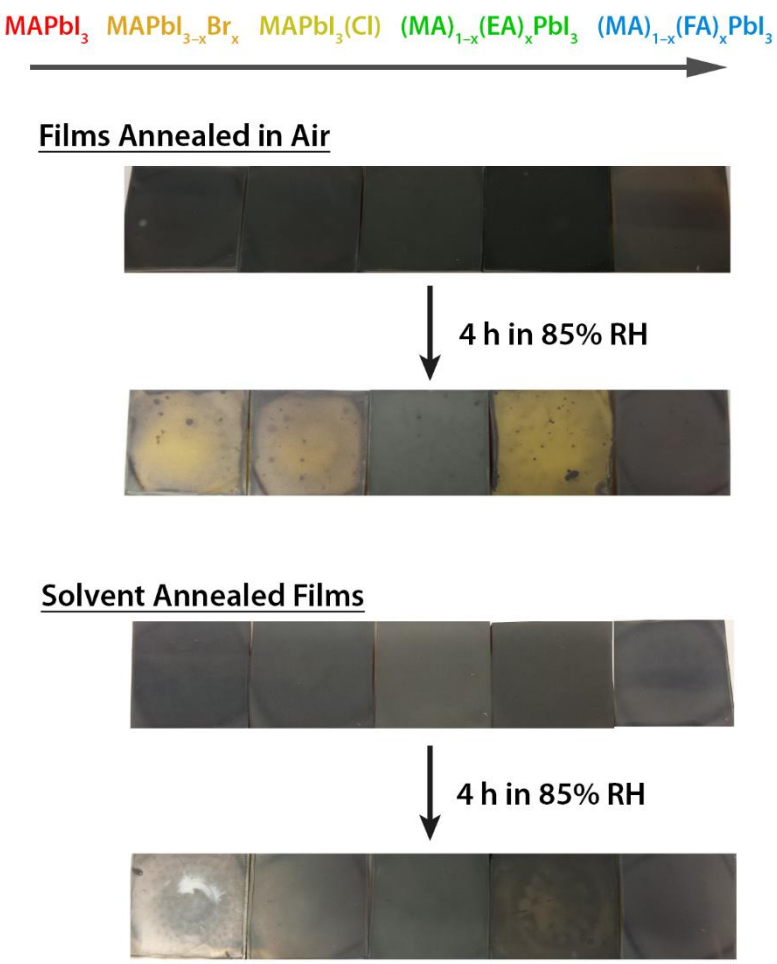

Figure 4.10. Photographs of perovskite thin films before (top row) and after (bottom row) 4 h of exposure to 85% RH, showing the effect of the solvent annealing process on perovskite film stability.

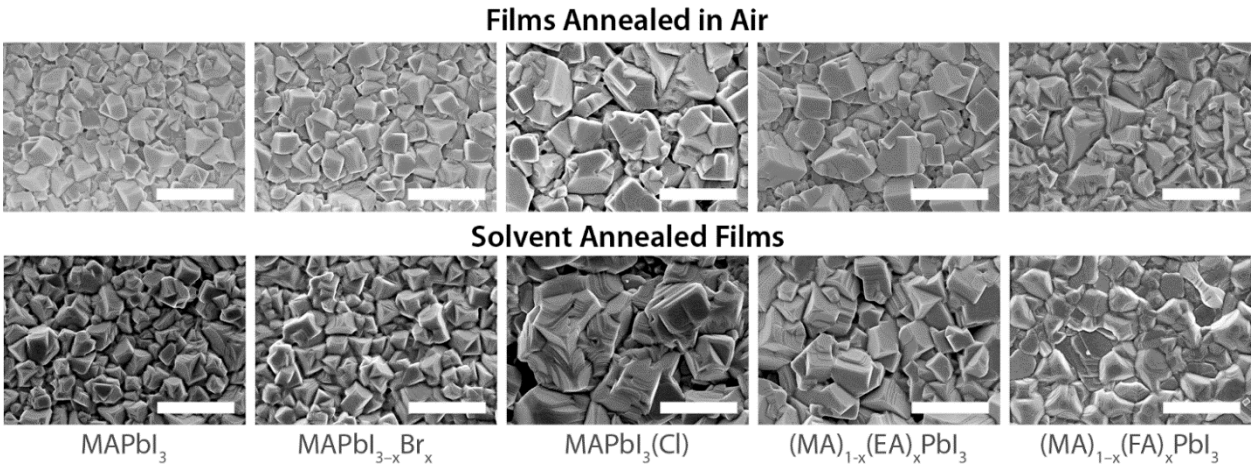

Figure 4.11. SEM of solvent annealed films as compared to films annealed in air. All scale bars are 1 μm.

Since the perovskite undergoes a large decrease in extinction coefficient during decomposition, optical absorption spectroscopy provides a very sensitive means of monitoring the decomposition process (**Figure 4.12**). Even a simple visual inspection of perovskite thin films exposed to 85% RH for a period of 20 h (Figure 4.12a) is revealing; except for $(MA)_{1-x}(FA)_xPbI_3$, all of the other samples showed evidence of almost complete decomposition. On continued exposure, the $(MA)_{1-x}(FA)_xPbI_3$ films only showed signs of significant decomposition after 100 h, again suggesting that the FA was more effective at stabilizing the perovskite structure than other types of ion-substitutions. In order to provide more quantitative information, the optical absorption spectra of P3HT-coated perovskites were monitored (**Figure 4.13**), and the normalized absorbance at 520 nm is shown in Figure 4.12b. Consistent with the more qualitative study, the $(MA)_{1-x}(FA)_xPbI_3$ sample showed the slowest decomposition kinetics, showing less than a 10% loss of absorbance after 100 h; in contrast, the other four samples decomposed 4-6 times faster.

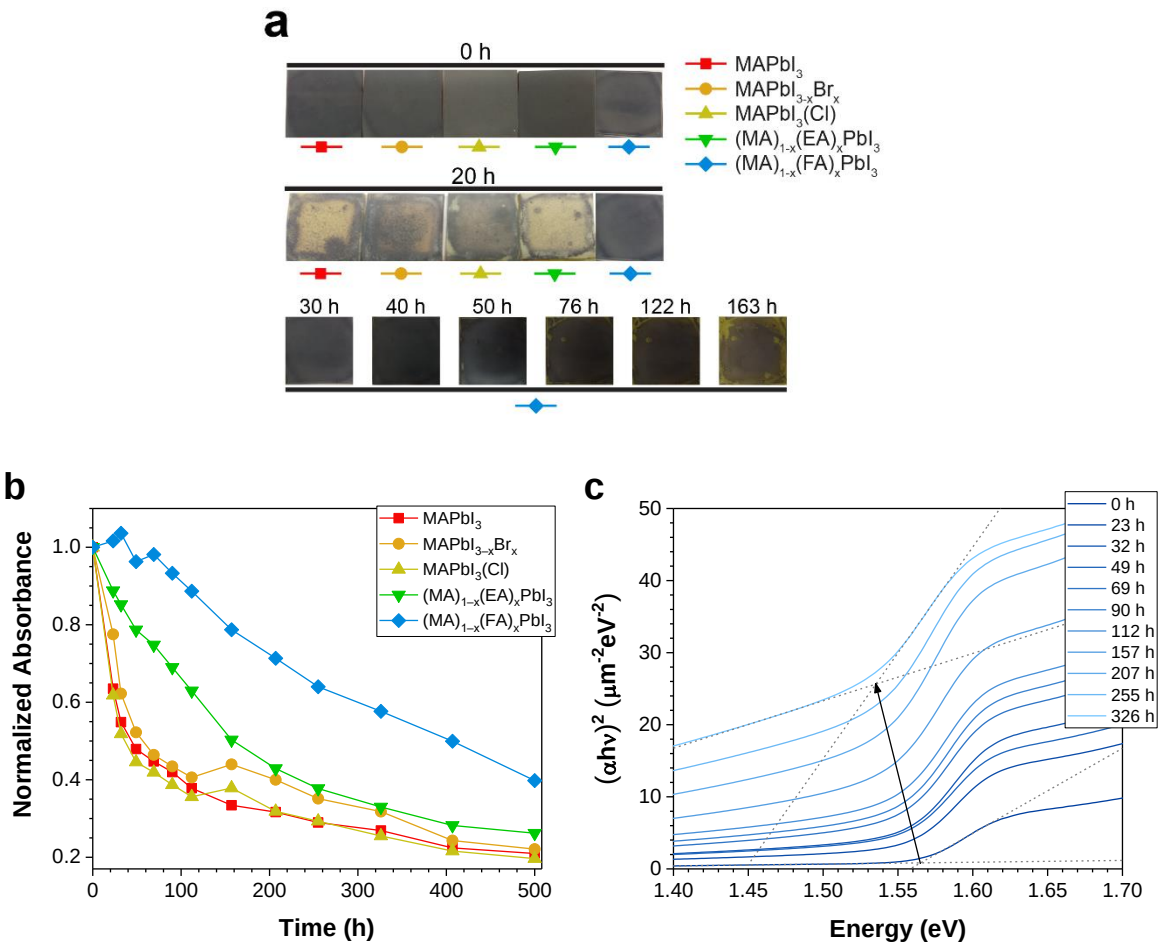

Figure 4.12. (a) Photographs of perovskite thin films, (b) normalized absorbance at 520 nm for P3HT-coated perovskite thin films, and (c) Tauc plot for P3HT-coated $(MA)_{1-x}(FA)_xPbI_3$, as a function of exposure time to an 85% RH environment. The thickness of the perovskite layer was assumed to be constant throughout the damp test.

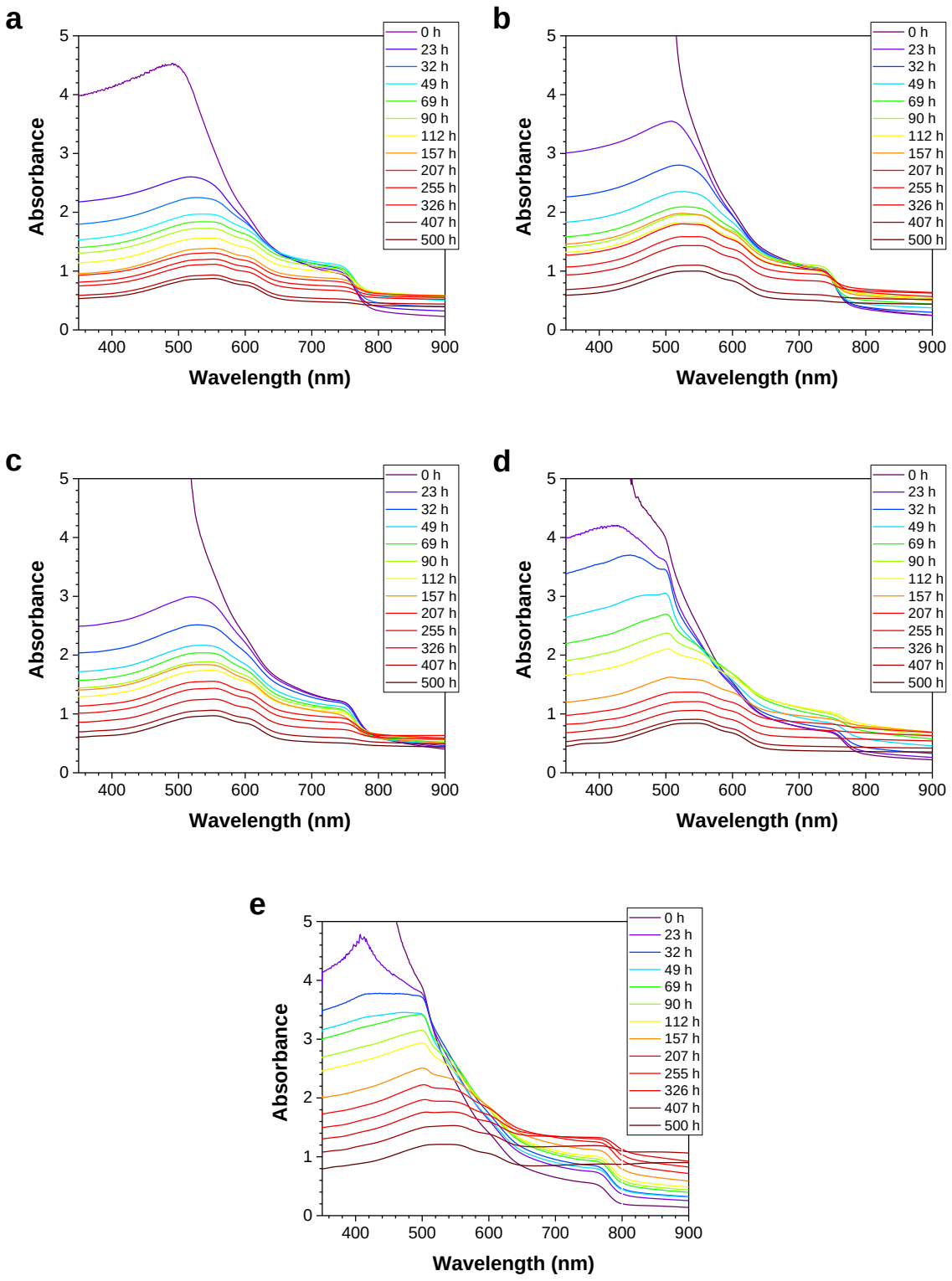

Figure 4.13. UV/vis absorption spectra of perovskite films after various exposure times in an 85% RH environment: (a) $MAPbI_3$, (b) $MAPbI_{3-x}Br_x$, (c) $MAPbI_3(Cl)$, (d) $(MA)_{1-x}(EA)_xPbI_3$, and (e) $(MA)_{1-x}(FA)_xPbI_3$.

The behavior of the $(MA)_{1-x}(FA)_xPbI_3$ perovskite was also different in one other aspect. A Tauc plot (Figure 4.12c) reveals that the bandgap of the perovskite shifts over time, from 1.56 eV originally to 1.45 eV after > 300 h of exposure to the humid environment. This is much closer to the absorption edge of α-phase $FAPbI_3$ (1.41 eV).[50] No such shift was observed in the spectra of the other perovskites. This suggests that the MA cation preferentially interacts with water and is gradually depleted from the perovskite structure, leaving behind a material enriched in the FA component. It underscores the impact that the FA cation can have over the stability of the resultant perovskite.

4.4.3 Thermal Stability and Device Lifetime

The previous studies suggest that out of the various cationic and anionic dopants studied, FA imparts the best protection against the effects of moisture. In order to see whether the same trend would hold true for other environmental stimuli, the various perovskite films were subjected to thermal treatment at 85 °C in the glovebox (0% RH), and measured pXRD patterns and UV/vis spectra as a function of heating time (**Figure 4.14**, **Figure 4.15**). All samples displayed the same trend, which was a slow, monotonic decline in the intensity of both the perovskite diffraction peaks and optical absorption bands over a period of ca. 600 h. Analysis of the films by SEM at the early stages of decomposition showed relatively little change in crystallite morphology, and relatively little difference between the various perovskite compositions (**Figure 4.16**). The data suggests that at least at the doping levels studied here (x = 0.20), none of the ions studied impart any additional thermal stability.

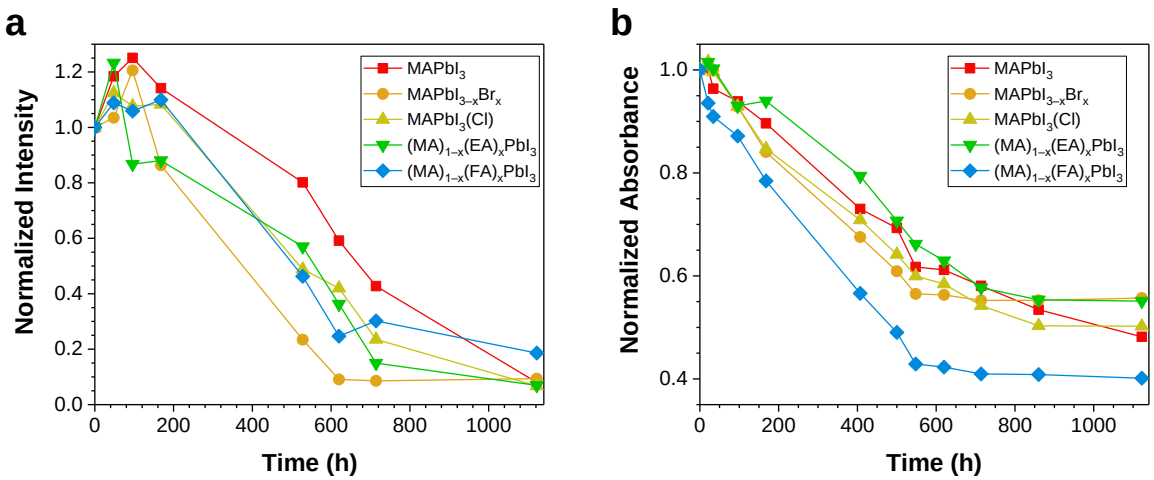

Figure 4.14. (a) Normalized intensity of the perovskite peak at ca. 16°, and (b) normalized absorbance at 520 nm as a function of annealing time at 85 °C. Normalization was done by dividing the maximum intensity at each exposure time by the initial maximum value.

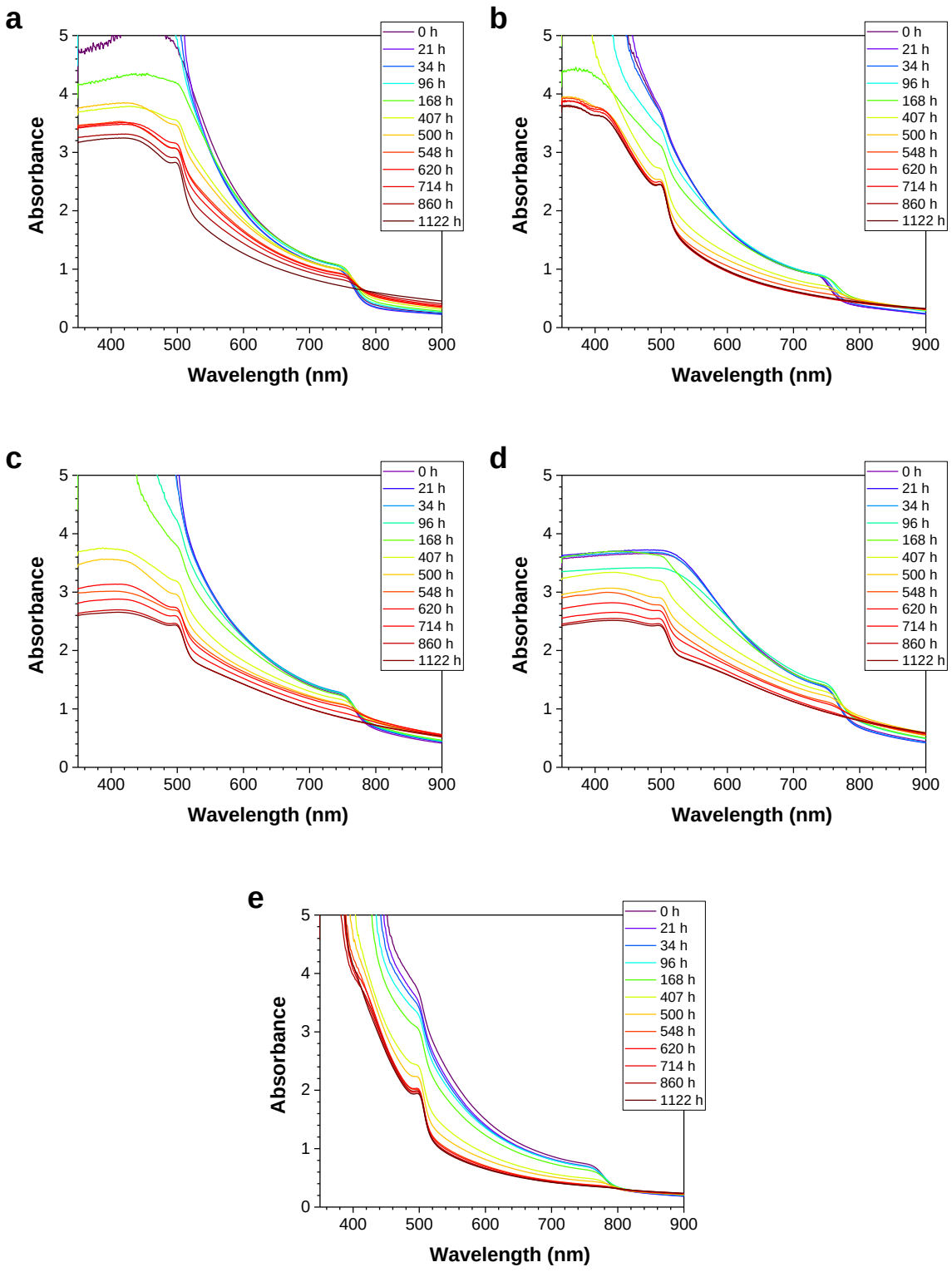

Figure 4.15. UV/vis absorption spectra of perovskite thin films after thermally annealing at 85 ºC for various times: (a) $MAPbI_3$, (b) $MAPbI_{3-x}Br_x$, (c) $MAPbI_3(Cl)$, (d) $(MA)_{1-x}(EA)_xPbI_3$, and (e) $(MA)_{1-x}(FA)_xPbI_3$.

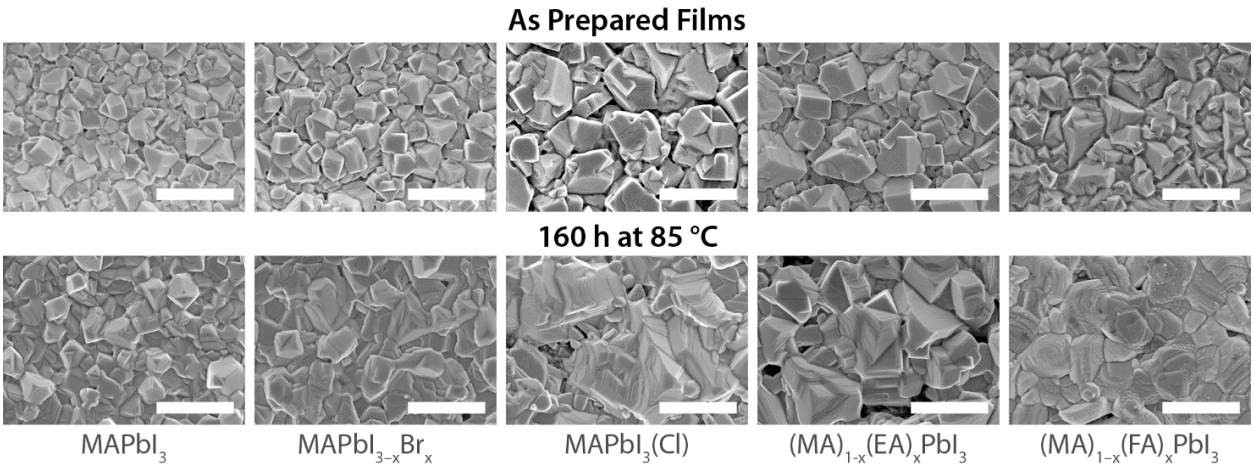

Figure 4.16. SEM images of perovskite samples before (top row) and after (bottom row) heating at 85 °C for 160 h.

In order to elucidate the impact of these two environmental factors – elevated humidity and temperature – on device performance, a series of perovskite solar cells were prepared using either a FTO/TiO_2/perovskite/P3HT/Au or FTO/TiO_2/perovskite/P3HT/Ag device architecture. They were exposed to the same environmental conditions as described previously, and their PCE was measured as a function of time (**Figure 4.17**). The devices stored in a humid environment showed a steady decline in performance over a period of *ca*. one month, while the devices stored at elevated temperature degraded slowly over the first 10 days, followed by rapid cell failure. In both studies, there was little impact of perovskite composition on the device lifetime; however, given the better moisture resistance of the FA-containing perovskites, this suggests that the perovskite itself is not the limiting factor for device lifetime. Instead, the cell degradation observed under humid conditions is ascribed to an increased mobility of iodide ions in the presence of water; this in turns leads to the corrosion of the silver top contact and the formation of AgI, as has been noted elsewhere.[55-58] The data suggest that the stability of electrodes and interfaces may be more significant than the decomposition of the perovskite absorber layer.

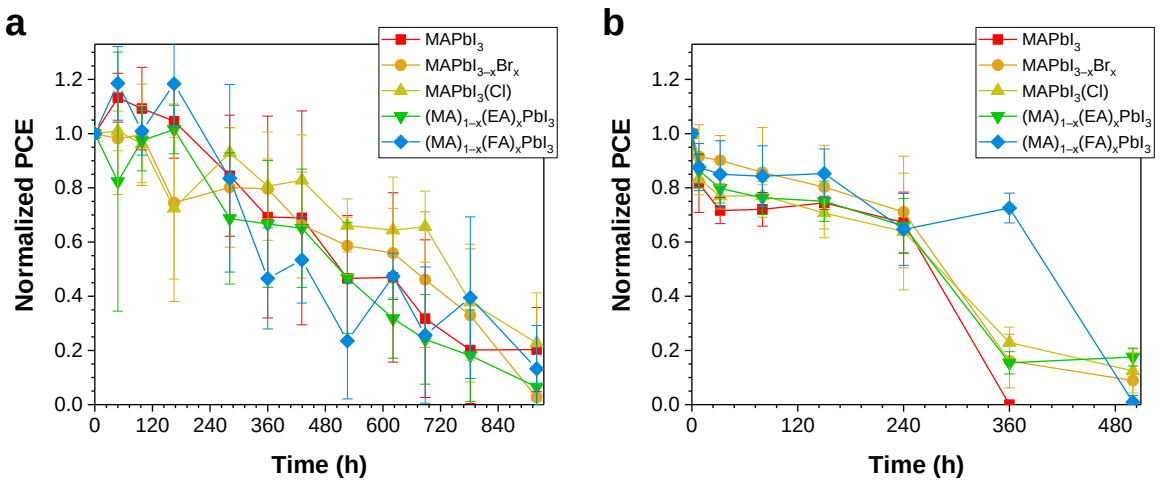

Figure 4.17. Plots of normalized power conversion efficiency for: (a) FTO/TiO_2/perovskite/P3HT/Au solar cells stored in an 85% RH environment, and (b) FTO/TiO_2/perovskite/P3HT/Ag solar cells stored at 85 °C.

4.4.4 Photochemical Stability

Based on the results of the moisture and thermal stability tests, the FA cation were identified as the most promising candidate for producing more stable perovskite layers. Therefore, two additional perovskite films were prepared with higher FA content (x = 0.4 and 0.6), and their photochemical stability (at 1 sun intensity) was evaluated in the presence of molecular oxygen (i.e., in dry air). Again, the effects of perovskite decomposition are apparent from even a qualitative visual inspection (**Figure 4.18**). A color change from brown to yellow began to occur for both the 20% and 40% FA samples after only 16 h of irradiation time, highlighting the deleterious effects of the photochemically-generated superoxide anion.[8] Promisingly, the sample with 60% FA showed a greater resistance to photochemical bleaching, with the appearance of yellow decomposition products only apparent after > 60 h of continuous irradiation.

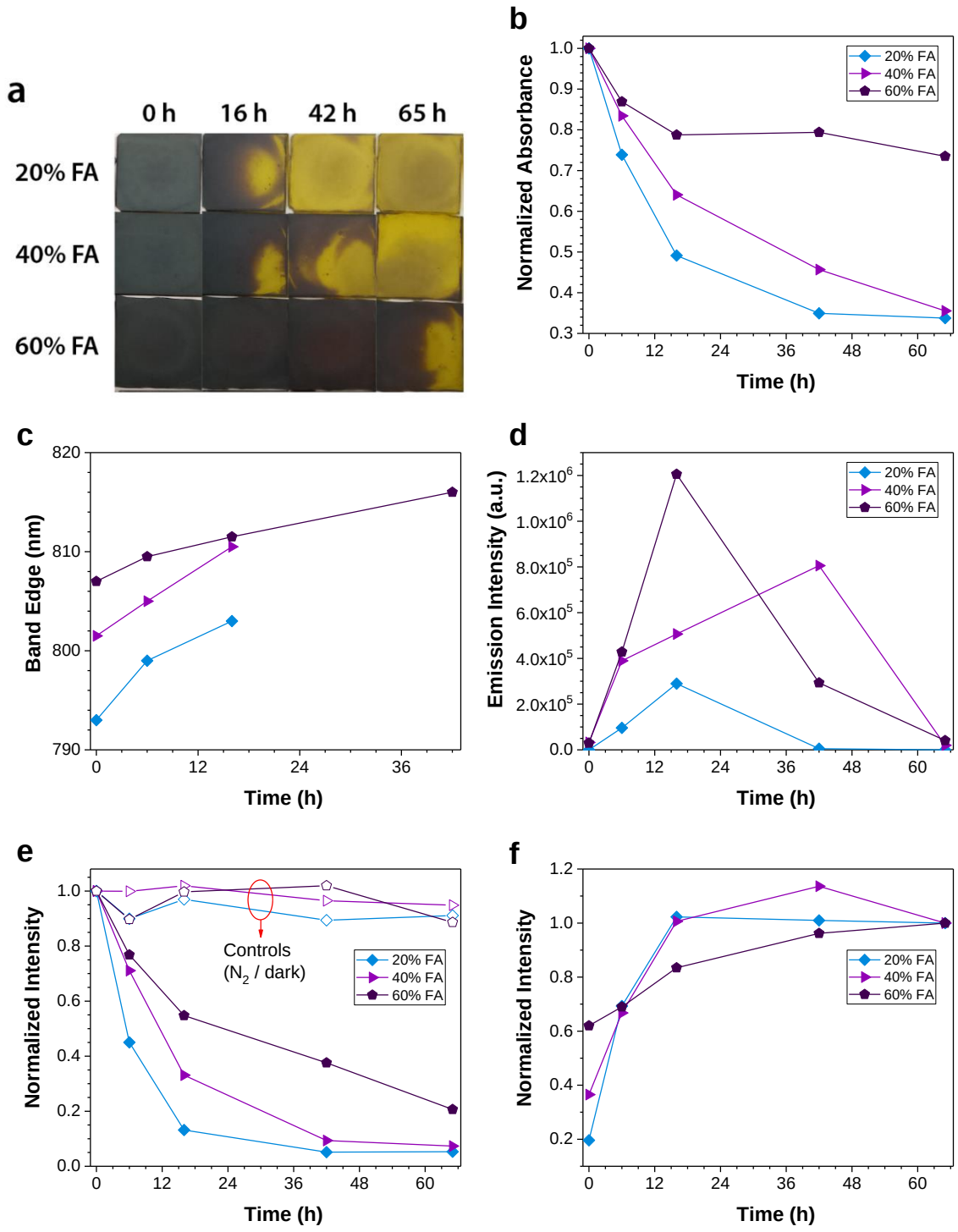

Figure 4.18. (a) Photographs, (b) normalized absorbance at 520 nm, (c) band edge position (as determined from Tauc plots, (d) photoluminescence intensity, (e) normalized intensity of the perovskite diffraction peak at ca. 16°, and (f) normalized intensity of the PbI_2 (001) diffraction peak as a function of irradiation time in air. All data points are the average of two separate measurements. In (e), control sample data are shown by the open symbols of the same shape and color used for the perovskite samples with the same composition.

A more quantitative measure of the photochemical stability of the FA-containing samples can be obtained by monitoring their absorption spectra as a function of irradiation time. There is very little change in the spectra of any of the samples when stored in the dark (**Figure 4.19**), highlighting the photochemical nature of this particular decomposition mechanism. For the samples irradiated in air, the absorbance at 520 nm is normalized and plotted as a function of time (Figure 4.18b), showing that the 60% FA sample decomposes more slowly (and to a lesser overall extent) than the samples with lower FA content. This is accompanied by a shift in the position of the band edge (Figure 4.18c), as determined by Tauc plots of the UV/vis data (**Figure 4.20**). The band edge red-shifts for all three samples, although the red-shift is less pronounced for samples with higher FA content. This is consistent with the superoxide anion preferentially deprotonating the MA cation, leading to an enrichment in FA content over the course of the decomposition process.

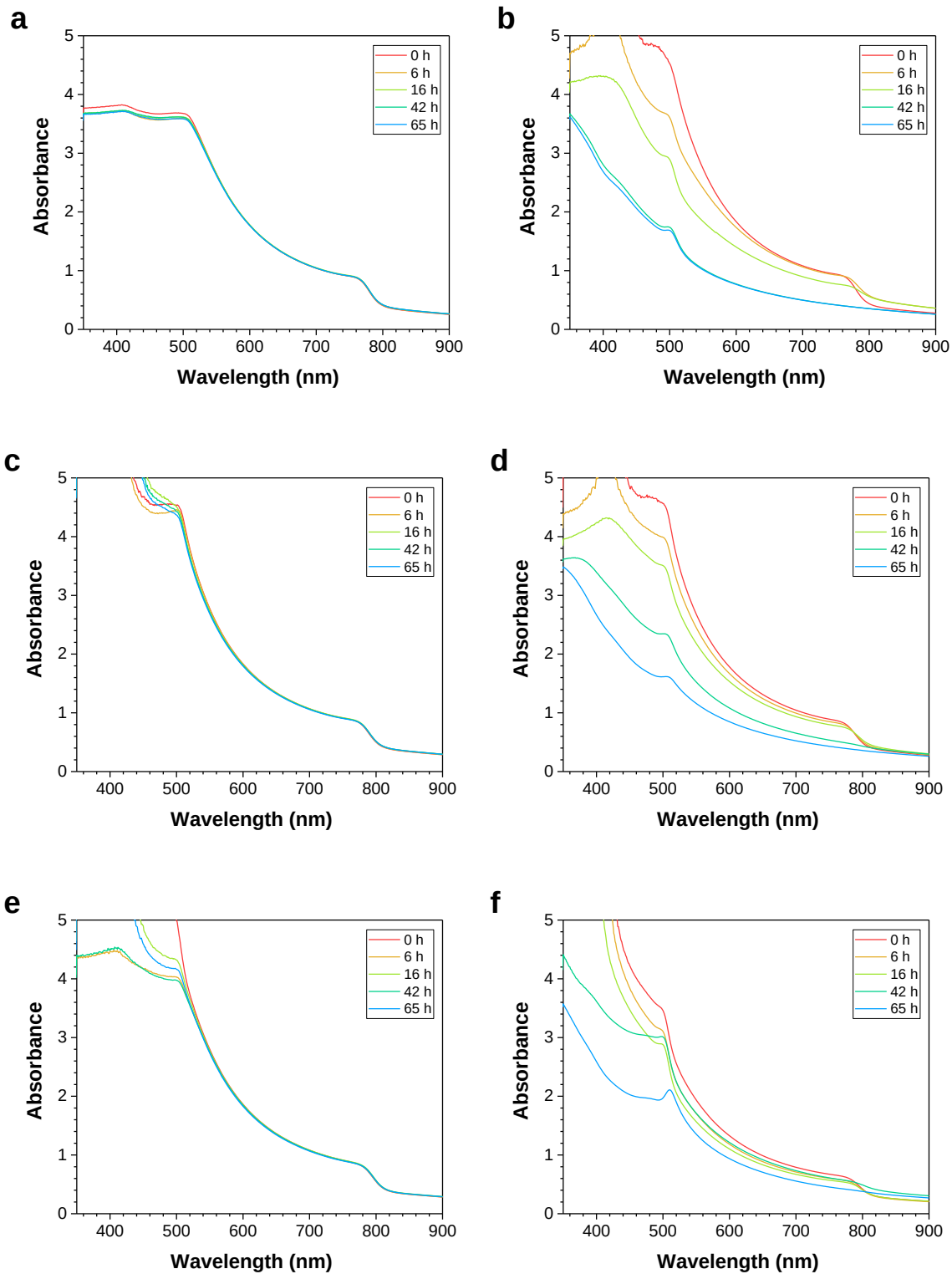

Figure 4.19. UV/vis absorption spectra of $(MA)_{1-x}(FA)_xPbI_3$ perovskite thin films: (a-b) x = 0.2, (c-d) x = 0.4, (e-f) x = 0.6. The samples in (a, c, e) were stored in the dark; the samples in (b, d, f) were irradiated in air.

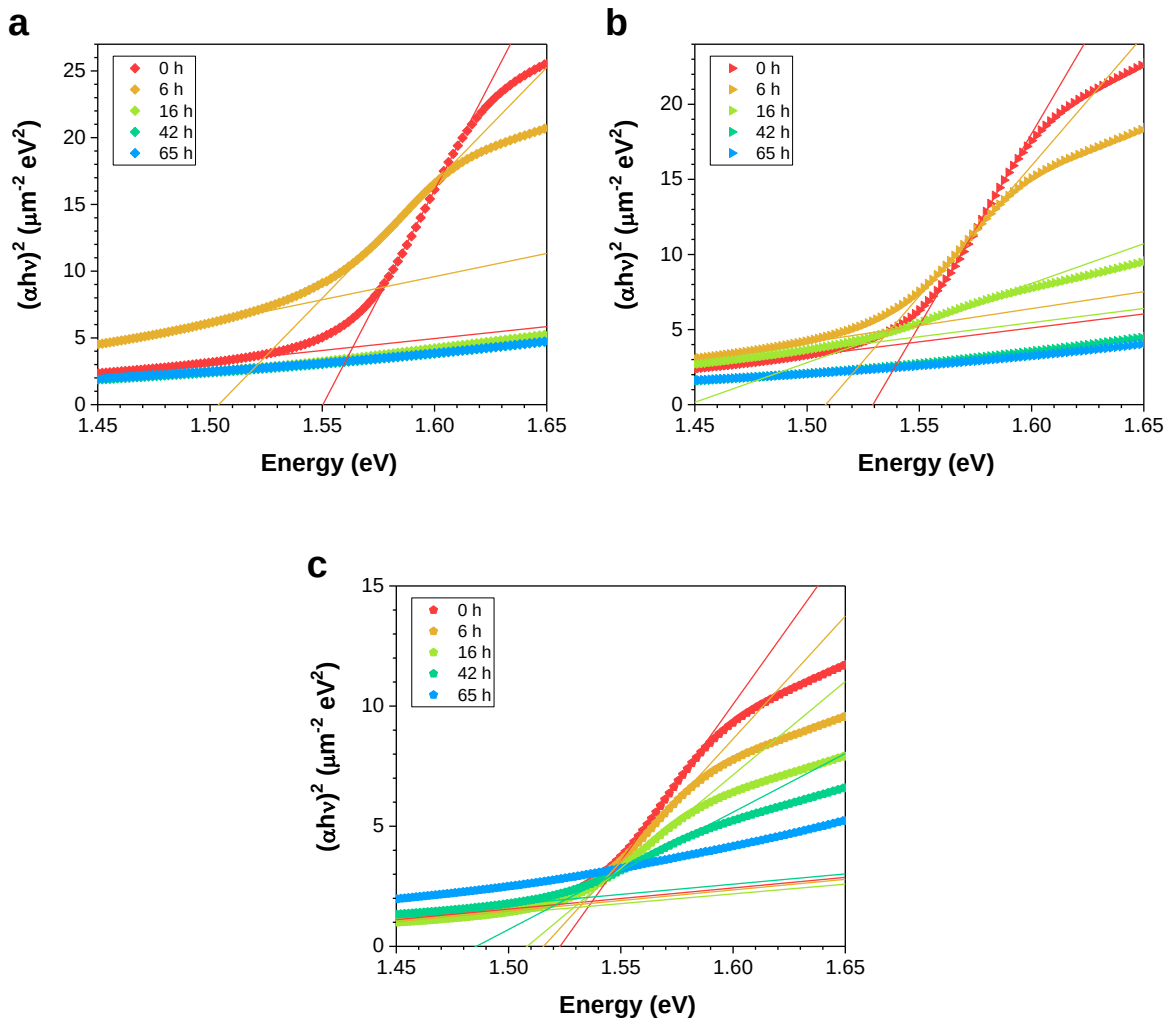

Figure 4.20. Tauc plots of $(MA)_{1-x}(FA)_xPbI_3$ perovskite thin films as a function of irradiation time in air: (a) $x = 0.2$, (b) $x = 0.4$, (c) $x = 0.6$. The thickness of the perovskite layer was assumed to be constant throughout the test.

Changes in the photoluminescence spectra of the films were also observed over the course of the photochemical study (**Figure 4.21**, Figure 4.18d). There is a marked increase in the photoluminescence intensity at early stages of the decomposition process, followed by a pronounced drop at later times. The low emission intensity observed initially may be due to the presence of numerous non-radiative recombination centers and trap states within the perovskite film. As noted by others, the nature of these trap states may be under-coordinated lead ions in the

lead halide framework.[59] These trap states can therefore be passivated by using Lewis bases such as pyridine or thiophene. This is supported by another recent study, which reported an order of magnitude higher photoluminescence when the PbI_2:FAI molar ratio was changed from 1:1 to 0.9:1, producing a slight excess of iodide ions.[60] In the present case, it may be possible that as the photogenerated superoxide deprotonates the methylammonium cation, it leaves behind additional iodide ions that can help passivate trap states; alternatively, the superoxide anion may coordinate to the lead ion itself.[10] However, in either case, as the decomposition process unfolds further, the photoluminescence intensity inevitably drops to zero.

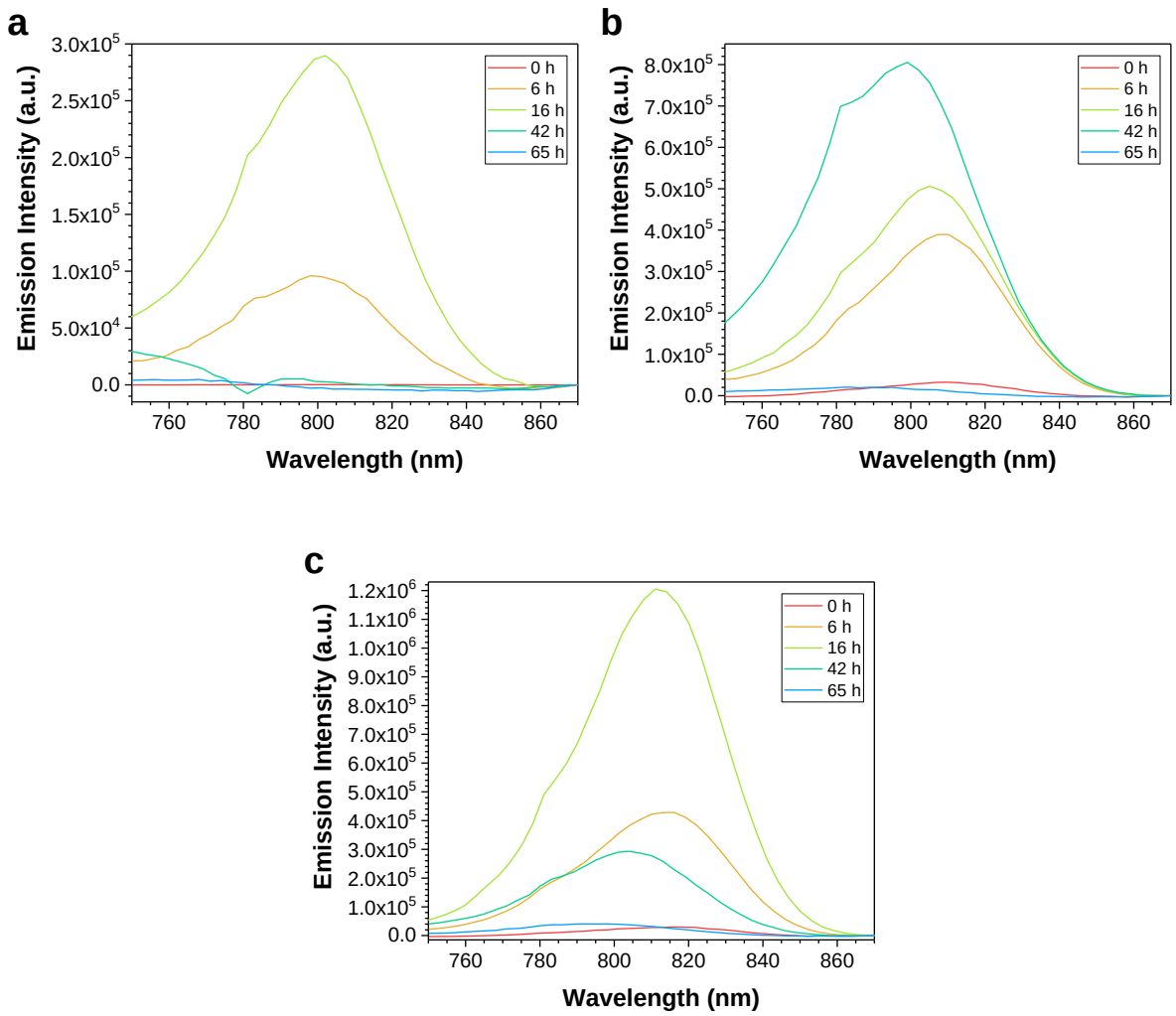

Figure 4.21. Photoluminescence spectra of $(MA)_{1-x}(FA)_xPbI_3$ perovskite thin films as a function of irradiation time in air: (a) $x = 0.2$, (b) $x = 0.4$, (c) $x = 0.6$.

The photochemical decomposition process was also followed by pXRD (**Figure 4.22**, Figure 4.18e,f). The intensity of the perovskite peak at ca. 16° 2θ is plotted in Figure 4.18e, while the intensity of the PbI_2 (001) reflection is plotted in Figure 4.18f. Again, control samples that were stored under nitrogen in the dark showed no evidence of decomposition. When irradiated in air, the intensities of the perovskite reflections drop rapidly, with the rate decreasing as the amount of FA is increased; this is accompanied by a rapid increase in the amount of PbI_2 present. Notably,

in all three samples a small amount of δ-phase $FAPbI_3$ ($2\theta = 13.6°$) was observed at intermediate times (16 h), that quickly disappeared as the decomposition progressed. This may be a result of the preferential decomposition of the MA cation, which leaves behind FA-rich domains that crystallize into the δ-phase. At later times, even the FA-rich perovskite domains decompose, leaving behind PbI_2 as the only crystalline byproduct. All of these results are consistent with previous reports suggesting that $FAPbI_3$[61] and $MA_{0.5}FA_{0.5}PbI_3$[62] have better photochemical stability than $MAPbI_3$; however, the results here more clearly separate out photochemical and moisture-induced effects, both of which have been shown to have an impact on the stability of perovskite thin films.

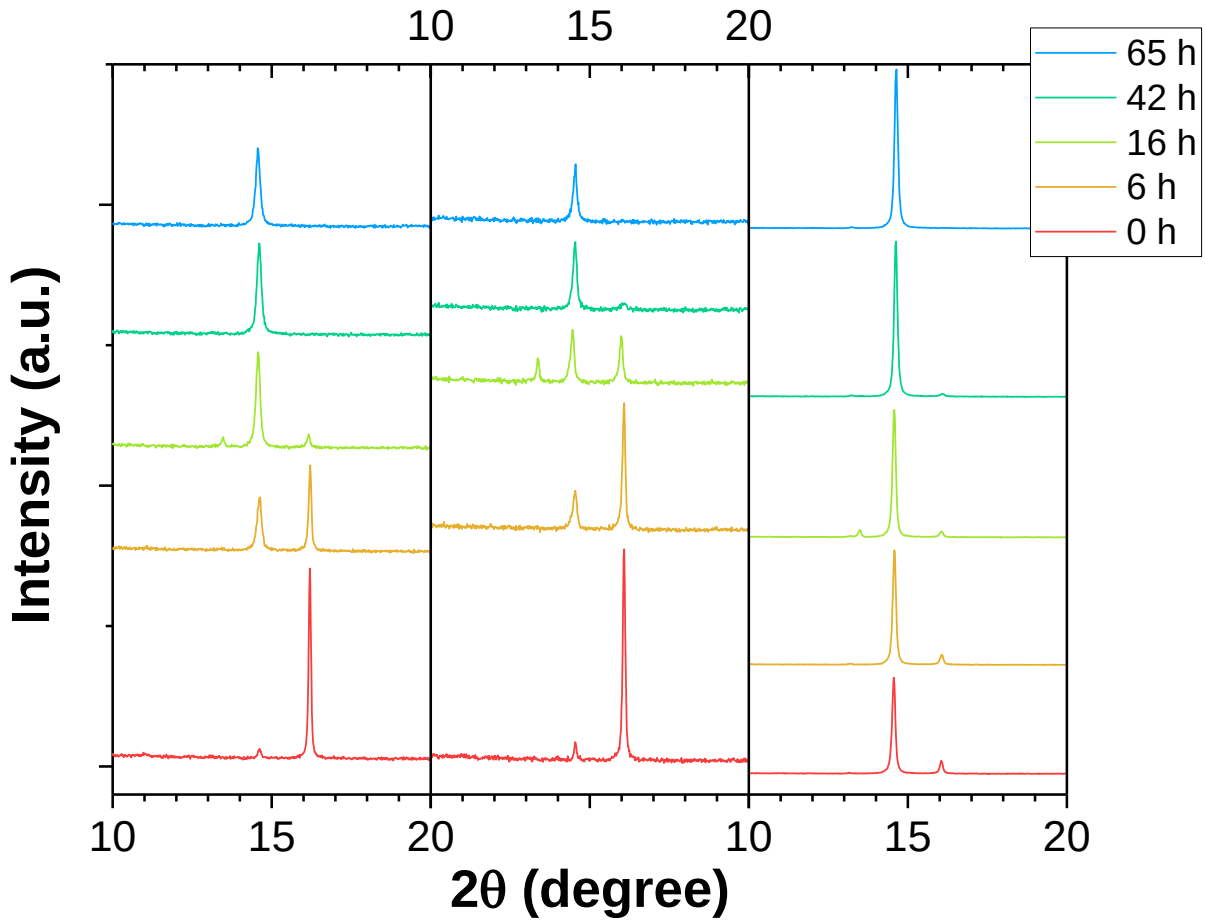

Figure 4.22. pXRD patterns of $(MA)_{1-x}(FA)_xPbI_3$ perovskite thin films as a function of irradiation time in air: (a) $x = 0.2$, (b) $x = 0.4$, (c) $x = 0.6$.

The moisture-induced and photochemical decomposition processes are strongly influenced by the ammonium group of the MA cation: hydrogen bonding between the oxygen of a water molecule the hydrogen of the MA cation drives the formation of crystalline hydrate phases,[6, 63] while the relative acidity of the MA cation leaves it vulnerable to photogenerated superoxide.[8, 10, 64] In contrast, the positive charge on FA is more declocalized, which can be easily visualized in an electrostatic potential map (**Figure 4.23**). This leads to a weaker interaction and a longer hydrogen bond between the FA cation and water, and is likely responsible for the improved moisture resistance of the FA-containing perovskites. Photochemically, the reduced acidity of the FA cation

makes it less vulnerable to deprotonation by photogenerated superoxide. Other studies have also shown that the MA cation is vulnerable to deprotonation by basic surface groups,[65] while the same reaction does not occur with $FAPbI_3$.[66]

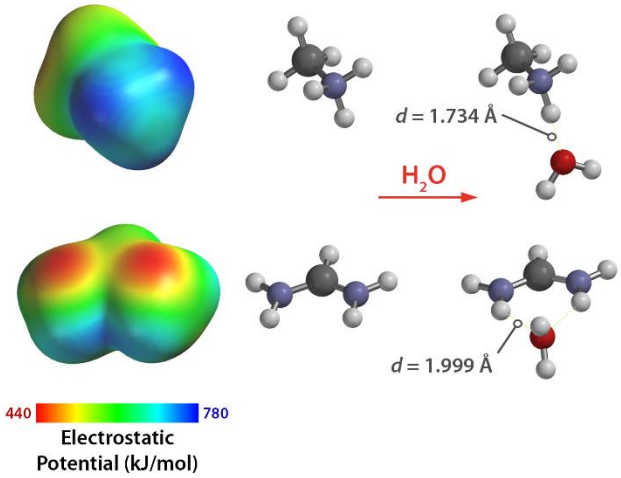

Figure 4.23. Electrostatic potential maps of the MA and FA cations, and the optimized geometry of a 1:1 complex with water. All calculations were carried out at the M06/6-31+G(d) level of theory.

4.5 Conclusion

By fabricating a series of perovskite samples with various ion substitutions, the effects of dopants on the stability of lead halide perovskites have been systematically evaluated. The FA cation was the most effective at stabilizing perovskite films, and provided increased moisture resistance and photochemical stability. This is attributed to the more delocalized positive charge on the FA cation, which reduces its ability to hydrogen bond with water and lowers its acidity. In addition, by carefully controlling the relevant environmental variables (humidity, temperature, light, and atmosphere), it was possible to separate out their individual contributions to the overall

decomposition of lead halide perovskites. These results suggest that FA-based perovskites are among the most promising candidates for efficient perovskite solar cells with long-term stability.

4.6 References

1. M. Ye, X. Hong, F. Zhang and X. Liu, *J. Mater. Chem. A*, 2016, **4**, 6755-6771.
2. S. D. Stranks and H. J. Snaith, *Nat. Nanotechnol.*, 2015, **10**, 391-402.
3. J. Chen, S. Zhou, S. Jin, H. Li and T. Zhai, *J. Mater. Chem. C*, 2016, **4**, 11-27.
4. H. Wei, Y. Fang, P. Mulligan, W. Chuirazzi, H.-H. Fang, C. Wang, B. R. Ecker, Y. Gao, M. A. Loi, L. Cao and J. Huang, *Nat. Photonics*, 2016, **10**, 333-339.
5. G. E. Eperon, S. D. Stranks, C. Menelaou, M. B. Johnston, L. M. Herz and H. J. Snaith, *Energy Environ. Sci.*, 2014, **7**, 982-988.
6. J. Yang, B. D. Siempelkamp, D. Liu and T. L. Kelly, *ACS Nano*, 2015, **9**, 1955-1963.
7. A. M. A. Leguy, Y. Hu, M. Campoy-Quiles, M. I. Alonso, O. J. Weber, P. Azarhoosh, M. van Schilfgaarde, M. T. Weller, T. Bein, J. Nelson, P. Docampo and P. R. F. Barnes, *Chem. Mater.*, 2015, **27**, 3397-3407.
8. D. Bryant, N. Aristidou, S. Pont, I. Sanchez-Molina, T. Chotchunangatchaval, S. Wheeler, J. R. Durrant and S. A. Haque, *Energy Environ. Sci.*, 2016, **9**, 1655-1660.
9. Z. Song, A. Abate, S. C. Watthage, G. K. Liyanage, A. B. Phillips, U. Steiner, M. Graetzel and M. J. Heben, *Adv. Energy Mater.*, 2016, **6**, 1600846.
10. N. Aristidou, C. Eames, I. Sanchez-Molina, X. Bu, J. Kosco, M. S. Islam and S. A. Haque, *Nat. Commun.*, 2017, **8**, 15218.
11. J. Yin, J. Cao, X. He, S. Yuan, S. Sun, J. Li, N. Zheng and L. Lin, *J. Mater. Chem. A*, 2015, **3**, 16860-16866.
12. A. Fakharuddin, F. Di Giacomo, A. L. Palma, F. Matteocci, I. Ahmed, S. Razza, A. D'Epifanio, S. Licoccia, J. Ismail, A. Di Carlo, T. M. Brown and R. Jose, *ACS Nano*, 2015, **9**, 8420-8429.
13. J. Yang, K. M. Fransishyn and T. L. Kelly, *Chem. Mater.*, 2016, **28**, 7344-7352.
14. H. Chen, Y. Hou, C. E. Halbig, S. Chen, H. Zhang, N. Li, F. Guo, X. Tang, N. Gasparini, I. Levchuk, S. Kahmann, C. O. Ramirez Quiroz, A. Osvet, S. Eigler and C. J. Brabec, *J. Mater. Chem. A*, 2016, **4**, 11604-11610.
15. H. Tan, A. Jain, O. Voznyy, X. Lan, F. P. García de Arquer, J. Z. Fan, R. Quintero-Bermudez, M. Yuan, B. Zhang, Y. Zhao, F. Fan, P. Li, L. N. Quan, Y. Zhao, Z.-H. Lu, Z. Yang, S. Hoogland and E. H. Sargent, *Science*, 2017, **355**, 722-726.
16. J. Lee, J. Kim, C.-L. Lee, G. Kim, T. K. Kim, H. Back, S. Jung, K. Yu, S. Hong, S. Lee, S. Kim, S. Jeong, H. Kang and K. Lee, *Adv. Energy Mater.*, 2017, 1700226.
17. Y. Zhao, J. Wei, H. Li, Y. Yan, W. Zhou, D. Yu and Q. Zhao, *Nat. Commun.*, 2016, **7**, 10228.
18. S. Masi, A. Rizzo, R. Munir, A. Listorti, A. Giuri, C. Esposito Corcione, N. D. Treat, G. Gigli, A. Amassian, N. Stingelin and S. Colella, *Adv. Energy Mater.*, 2017, 1602600.

19. J. Lu, L. Jiang, W. Li, F. Li, N. K. Pai, A. D. Scully, C.-M. Tsai, U. Bach, A. N. Simonov, Y.-B. Cheng and L. Spiccia, *Adv. Energy Mater.*, 2017, 1700444.
20. M. Long, T. Zhang, Y. Chai, C.-F. Ng, T. C. W. Mak, J. Xu and K. Yan, *Nat. Commun.*, 2016, **7**, 13503.
21. D. Bi, C. Yi, J. Luo, J.-D. Décoppet, F. Zhang, Shaik M. Zakeeruddin, X. Li, A. Hagfeldt and M. Grätzel, *Nat. Energy*, 2016, **1**, 16142.
22. C. Qin, T. Matsushima, T. Fujihara and C. Adachi, *Adv. Mater.*, 2017, **29**, 1083808.
23. Y. Sun, Y. Wu, X. Fang, L. Xu, Z. Ma, Y. Lu, W.-H. Zhang, Q. Yu, N. Yuan and J. Ding, *J. Mater. Chem. A*, 2017, **5**, 1374-1379.
24. H. Tsai, W. Nie, J.-C. Blancon, C. C. Stoumpos, R. Asadpour, B. Harutyunyan, A. J. Neukirch, R. Verduzco, J. J. Crochet, S. Tretiak, L. Pedesseau, J. Even, M. A. Alam, G. Gupta, J. Lou, P. M. Ajayan, M. J. Bedzyk, M. G. Kanatzidis and A. D. Mohite, *Nature*, 2016, **536**, 312-316.
25. M. Yang, T. Zhang, P. Schulz, Z. Li, G. Li, D. H. Kim, N. Guo, J. J. Berry, K. Zhu and Y. Zhao, *Nat. Commun.*, 2016, **7**, 12305.
26. M. Saliba, T. Matsui, K. Domanski, J.-Y. Seo, A. Ummadisingu, S. M. Zakeeruddin, J.-P. Correa-Baena, W. R. Tress, A. Abate, A. Hagfeldt and M. Grätzel, *Science*, 2016, **354**, 206-209.
27. G. E. Eperon, T. Leijtens, K. A. Bush, R. Prasanna, T. Green, J. T.-W. Wang, D. P. McMeekin, G. Volonakis, R. L. Milot, R. May, A. Palmstrom, D. J. Slotcavage, R. A. Belisle, J. B. Patel, E. S. Parrott, R. J. Sutton, W. Ma, F. Moghadam, B. Conings, A. Babayigit, H.-G. Boyen, S. Bent, F. Giustino, L. M. Herz, M. B. Johnston, M. D. McGehee and H. J. Snaith, *Science*, 2016, **354**, 861-865.
28. Z. Yang, A. Rajagopal, C.-C. Chueh, S. B. Jo, B. Liu, T. Zhao and A. K. Y. Jen, *Adv. Mater.*, 2016, **28**, 8990-8997.
29. F. Wang, W. Geng, Y. Zhou, H.-H. Fang, C.-J. Tong, M. A. Loi, L.-M. Liu and N. Zhao, *Adv. Mater.*, 2016, **28**, 9986-9992.
30. N. Li, Z. Zhu, C.-C. Chueh, H. Liu, B. Peng, A. Petrone, X. Li, L. Wang and A. K. Y. Jen, *Adv. Energy Mater.*, 2017, **7**, 1601307.
31. J. Liang, C. Wang, Y. Wang, Z. Xu, Z. Lu, Y. Ma, H. Zhu, Y. Hu, C. Xiao, X. Yi, G. Zhu, H. Lv, L. Ma, T. Chen, Z. Tie, Z. Jin and J. Liu, *J. Am. Chem. Soc.*, 2016, **138**, 15829-15832.
32. M. Saliba, T. Matsui, J.-Y. Seo, K. Domanski, J.-P. Correa-Baena, M. K. Nazeeruddin, S. M. Zakeeruddin, W. Tress, A. Abate, A. Hagfeldt and M. Gratzel, *Energy Environ. Sci.*, 2016, **9**, 1989-1997.
33. D. Bi, P. Gao, R. Scopelliti, E. Oveisi, J. Luo, M. Grätzel, A. Hagfeldt and M. K. Nazeeruddin, *Adv. Mater.*, 2016, **28**, 2910-2915.
34. C. C. Stoumpos, C. D. Malliakas and M. G. Kanatzidis, *Inorg. Chem.*, 2013, **52**, 9019-9038.
35. J.-H. Im, J. Chung, S.-J. Kim and N.-G. Park, *Nanoscale Res. Lett.*, 2012, **7**, 1-7.
36. S. Gholipour, A. M. Ali, J.-P. Correa-Baena, S.-H. Turren-Cruz, F. Tajabadi, W. Tress, N. Taghavinia, M. Grätzel, A. Abate, F. De Angelis, C. A. Gaggioli, E. Mosconi, A. Hagfeldt and M. Saliba, *Adv. Mater.*, 2017, **29**, 1702005.
37. H.-L. Hsu, C.-C. Chang, C.-P. Chen, B.-H. Jiang, R.-J. Jeng and C.-H. Cheng, *J. Mater. Chem. A*, 2015, **3**, 9271-9277.

38. D. W. de Quilettes, S. M. Vorpahl, S. D. Stranks, H. Nagaoka, G. E. Eperon, M. E. Ziffer, H. J. Snaith and D. S. Ginger, *Science*, 2015, **348**, 683-686.
39. Q. Chen, H. Zhou, Y. Fang, A. Z. Stieg, T.-B. Song, H.-H. Wang, X. Xu, Y. Liu, S. Lu, J. You, P. Sun, J. McKay, M. S. Goorsky and Y. Yang, *Nat. Commun.*, 2015, **6**, 7269.
40. J. H. Im, C. R. Lee, J. W. Lee, S. W. Park and N. G. Park, *Nanoscale*, 2011, **3**, 4088-4093.
41. W. S. Yang, J. H. Noh, N. J. Jeon, Y. C. Kim, S. Ryu, J. Seo and S. I. Seok, *Science*, 2015, **348**, 1234-1237.
42. P. Docampo, F. C. Hanusch, S. D. Stranks, M. Döblinger, J. M. Feckl, M. Ehrensperger, N. K. Minar, M. B. Johnston, H. J. Snaith and T. Bein, *Adv. Energy Mater.*, 2014, **4**, 1400355.
43. J.-H. Im, I.-H. Jang, N. Pellet, M. Grätzel and N.-G. Park, *Nat. Nanotechnol.*, 2014, **9**, 927-932.
44. Z. Xiao, Q. Dong, C. Bi, Y. Shao, Y. Yuan and J. Huang, *Adv. Mater.*, 2014, **26**, 6503-6509.
45. C. Tao, S. Neutzner, L. Colella, S. Marras, A. R. Srimath Kandada, M. Gandini, M. D. Bastiani, G. Pace, L. Manna, M. Caironi, C. Bertarelli and A. Petrozza, *Energy Environ. Sci.*, 2015, **8**, 2365-2370.
46. N. J. Jeon, J. H. Noh, W. S. Yang, Y. C. Kim, S. Ryu, J. Seo and S. I. Seok, *Nature*, 2015, **517**, 476-480.
47. A. Binek, F. C. Hanusch, P. Docampo and T. Bein, *J. Phys. Chem. Lett.*, 2015, **6**, 1249-1253.
48. T. Jesper Jacobsson, J.-P. Correa-Baena, M. Pazoki, M. Saliba, K. Schenk, M. Gratzel and A. Hagfeldt, *Energy Environ. Sci.*, 2016, 10.1039/c6ee00030d.
49. Y. Liu, Z. Yang, D. Cui, X. Ren, J. Sun, X. Liu, J. Zhang, Q. Wei, H. Fan, F. Yu, X. Zhang, C. Zhao and S. Liu, *Adv. Mater.*, 2015, **27**, 5176-5183.
50. A. A. Zhumekenov, M. I. Saidaminov, M. A. Haque, E. Alarousu, S. P. Sarmah, B. Murali, I. Dursun, X.-H. Miao, A. L. Abdelhady, T. Wu, O. F. Mohammed and O. M. Bakr, *ACS Energy Lett.*, 2016, **1**, 32-37.
51. Y. Tian and I. G. Scheblykin, *J. Phys. Chem. Lett.*, 2015, **6**, 3466-3470.
52. M. K. Gangishetty, R. W. J. Scott and T. L. Kelly, *Nanoscale*, 2016, **8**, 6300-6307.
53. D. Liu, J. Yang and T. L. Kelly, *J. Am. Chem. Soc.*, 2014, **136**, 17116-17122.
54. J. H. Noh, S. H. Im, J. H. Heo, T. N. Mandal and S. I. Seok, *Nano Lett.*, 2013, **13**, 1764-1769.
55. J. Li, Q. Dong, N. Li and L. Wang, *Adv. Energy Mater.*, 2017, **7**, 1602922.
56. H. Back, G. Kim, J. Kim, J. Kong, T. K. Kim, H. Kang, H. Kim, J. Lee, S. Lee and K. Lee, *Energy Environ. Sci.*, 2016, **9**, 1258-1263.
57. Y. Han, S. Meyer, Y. Dkhissi, K. Weber, J. M. Pringle, U. Bach, L. Spiccia and Y.-B. Cheng, *J. Mater. Chem. A*, 2015, **3**, 8139-8147.
58. Y. Deng, Q. Dong, C. Bi, Y. Yuan and J. Huang, *Adv. Energy Mater.*, 2016, **6**, 1600372.
59. N. K. Noel, A. Abate, S. D. Stranks, E. S. Parrott, V. M. Burlakov, A. Goriely and H. J. Snaith, *ACS Nano*, 2014, **8**, 9815-9821.
60. T. J. Jacobsson, J.-P. Correa-Baena, E. Halvani Anaraki, B. Philippe, S. D. Stranks, M. E. F. Bouduban, W. Tress, K. Schenk, J. Teuscher, J.-E. Moser, H. Rensmo and A. Hagfeldt, *J. Am. Chem. Soc.*, 2016, **138**, 10331-10343.
61. M. Govindhasamy, T. Soichiro, M. Gai, K. Shusaku, N. Hitoshi, U. Tomokazu, I. Hiroshi and I. Seigo, *Jpn. J. Appl. Phys.*, 2015, **54**, 08KF08.

62. J.-W. Lee, D.-H. Kim, H.-S. Kim, S.-W. Seo, S. M. Cho and N.-G. Park, *Adv. Energy Mater.*, 2015, **5**, 1501310.
63. B. R. Vincent, K. N. Robertson, T. S. Cameron and O. Knop, *Can. J. Chem.*, 1987, **65**, 1042-1046.
64. N. Aristidou, I. Sanchez-Molina, T. Chotchuangchutchaval, M. Brown, L. Martinez, T. Rath and S. A. Haque, *Angew. Chem. Int. Ed.*, 2015, **54**, 8208-8212.
65. J. Yang, B. D. Siempelkamp, E. Mosconi, F. De Angelis and T. L. Kelly, *Chem. Mater.*, 2015, **27**, 4229-4236.
66. J. Song, W. Hu, X.-F. Wang, G. Chen, W. Tian and T. Miyasaka, *J. Mater. Chem. A*, 2016, **4**, 8435-8443.

Chapter 5. Improving the Stability and Decreasing the Trap State Density of Mixed-Cation Perovskite Solar Cells through Compositional Engineering[4]

5.1 Transition Section

As highlighted in the previous chapter, improving perovskite stability is the most important factor in commercializing perovskite solar cell technology. Although there are many examples in the literature that have improved perovskite stability, these improvements often come at the expense of device efficiency. Therefore, to follow-up on the results of the previous chapter, where the stability of perovskite films was systematically evaluated and improved, in this chapter a device that is both efficient and stable is designed. To do this, perovskite compositions that routinely yield devices with >20% efficiency were used as the starting point. Most of these highly efficient devices use the same composition, a combination of $PbBr_2$, MABr, PbI_2 and FAI. As reported in the previous chapter, MA-rich perovskite domains suffer from a low moisture resistance and poor photochemical stability. In addition, mixed I/Br perovskites suffer from a phenomenon known as halide segregation. Therefore, in order to improve perovskite solar cell technology, this chapter reports a method of eliminating both the MA and bromide components from perovskite solar cells, without sacrificing the efficiency. Since this results in a decrease in V_{oc}, it is also shown that the

[4] K. Poorkazem, K. M. Fransishyn, T. L. Kelly, *In Preparation*.
Contributions: K.P. carried out the research and wrote the manuscript. K.M.F helped acquire preliminary film and device stability data, IR spectra, and NMR spectra, which are not included in this thesis. T.L.K. directed the study and revised the manuscript.

addition of PbI_2 and guanidinium iodide can mitigate this voltage loss by decreasing the density of trap states.

5.2 Introduction

Perovskite solar cells have emerged as one of the most promising new solar technologies in decades. These devices are made from low-cost materials, and their low temperature fabrication processes allow them to be used in flexible[1-3] and lightweight[4] applications. Additionally, the PCE of these devices is on-par with market-leading multi-crystalline silicon technology. The high efficiency of these devices is driven by the relatively low bandgap of methylammonium lead iodide (1.53 eV) and a low loss-in potential (the difference between the bandgap energy and the device open-circuit voltage).[5, 6] With single-junction perovskite solar cells now exceeding 20% PCE, further efficiency increases are expected to come from further reductions in the loss-in potential,[7-9] which can be done by decreasing the density of trap states that act as charge recombination centers in a device.[10-13]

Compositional engineering of the perovskite is another strategy to improve device efficiency. Although $MAPbI_3$ was the first compound to be used in a perovskite solar cell, in an ABX_3 perovskite structure, either the A-, B, or X-site ions can be replaced by suitable alternatives. Since the bandgap of the perovskite-structured formamidinium (FA) lead iodide (α-$FAPbI_3$ - 1.48 eV)[14] is narrower than the $MAPbI_3$ bandgap of 1.53 eV,[15] it is possible to entirely replace MA with FA to achieve higher photocurrents. However, at room temperature, pure $FAPbI_3$ is easily converted from the α to a δ phase, which has a wider bandgap and a one-dimensional, non-perovskite structure.[16, 17] Therefore, one of the important goals of compositional engineering is the

stabilization of the α-$FAPbI_3$ phase. Initially, $FAPbI_3$ was mixed with 15 mol% of either $MAPbI_3$[18], $MAPbBr_3$,[14] or $CsPbI_3$.[19] Later, Jacobsson *et al.* comprehensively studied the effect of $FA_{(1-x)}MA_xPbI_{(3-y)}Br_y$ perovskite composition on device efficiency, and reported that the highest efficiency could be achieved when the FA:MA and I:Br ratios were 2:1 and 5:1, respectively.[20] To date, the majority of devices with >20% PCE have used this perovskite composition (or slight modifications thereof).[8, 20-28]

Other examples of compositional engineering have looked at the use of different A-site cations entirely. A few reports have examined the use of guanidinium (GA) cations, owing to their similarities in structure to FA. A computational study calculated a low formation energy for the replacement of FA with GA in $FAPbI_3$,[29] and an experimental study demonstrated a decrease in the number of recombination centers when a small amount of MA was replaced with GA in $MAPbI_3$.[30] However, the compatibility of GA with various state-of-the-art perovskite compositions, and its effect on device efficiency and lifetime remains unknown.

Although improving device efficiency is important, the instability of perovskite devices is the most crucial issue to be addressed. Stability improvements have been made by modifying interfacial layers,[8, 31-36] changing the perovskite deposition method,[23, 37-39] or by altering the perovskite composition.[7, 25, 40-43] Among these, perovskite compositional engineering is the most general strategy, since it can be applied to a wide variety of different device configurations.

In one notable example of compositional engineering, Saliba *et al.* showed that adding CsI to the $FA_{(1-x)}MA_xPbI_{(3-y)}Br_y$ perovskite improved device efficiency, stability, and reproducibility.[22] One reason for this is the small size of Cs^+, which decreases the large Goldschmidt tolerance factor[44] of $FAPbI_3$, making the cubic structure more favorable.[19] Additionally, the α phases of $FAPbI_3$ and $CsPbI_3$ have more similarities in terms of their atomistic structure and unit cell volume,

which is not the case for δ phases. This makes the mixing of the α phases (and not the δ phases) energetically favorable,[45] and helps remove δ-phase impurities from the perovskite film. Later, a third reason was shown to be a more compact perovskite layer, resulting from the stronger interactions of (Cs^+-including) A-site cations with the PbI_3^- framework.[46] A device that used only PbI_2, FAI, and CsI precursors was shown to be both efficient and relatively stable.[47] This calls into question the necessity of including $PbBr_2$ and MABr in the perovskite precursor solution.

Such a complex perovskite formulation (which includes three different A-site cations and two different halide anions) is not necessarily ideal; however, it is still uncertain whether the $PbBr_2$ and MABr precursors are necessary. This is important for two reasons. One is the halide segregation phenomenon observed in mixed I/Br perovskites, where distinct I-rich and Br-rich phases are formed under illumination.[48, 49] This affects the long-term stability of even encapsulated solar cells. Although this segregation is shown to be suppressed in $FA_{1-x}Cs_xPbI_{3-y}Br_y$ perovskites when x = 0.1-0.3, the results were dependent on the perovskite fabrication methods, and on the homogeneity of the Cs distribution.[50] Eliminating the possibility of halide segregation, while retaining excellent device efficiency, would be highly desirable. The other problem with these precursors is the instability of MA-containing perovskites.[51] In a humid environment, $MAPbI_3$ absorbs water, crystallizes into distinct hydrate phases, and eventually decomposes irreversibly.[52-54] The MA-containing perovskites are also prone to oxidative photobleaching. Photoexcitation of the perovskite produces conduction band electrons, which can reduce O_2 to superoxide anions, which in turn deprotonates the MA cation.[55] In our previous work, improved moisture resistance and photostability for $FA_{(1-x)}MA_xPbI_3$ perovskites with higher percentages of FA were observed.[51] The results suggest that the elimination of MA may substantially improve perovskite stability.

Here, a novel mixed-cation perovskite is reported that improves perovskite stability, but at the same time does not reduce PCE. It is shown that the $PbBr_2$ and MABr components of a Cs-containing perovskite are unnecessary; although the elimination of bromide reduces the bandgap (decreasing V_{oc}) This was compensated for by an increase in J_{sc}, and thus no overall change was observed in the PCE. Furthermore, by adding PbI_2 and GAI to the perovskite precursor solution, the density of the trap states is decreased in the perovskite layer and the device loss-in potential is decreased. Ultimately, the elimination of unstable perovskite components leads to an improvement in the moisture resistance and photostability of these perovskite devices.

5.3 Experimental

5.3.1 Materials

HI, HBr, CH_3NH_2, formamidine acetate, glass/FTO slides, PbI_2, CsI, Li-TFSI, 4-tert-butylpyridine and titanium diisopropoxide bis(acetylacetonate) were purchased from Sigma-Aldrich. Diethyl ether, 2-propanol, DMF, dimethylsulfoxide (DMSO), chlorobenzene, butanol, acetonitrile, chloroform, and the mini-cabinet desiccator were purchased from Fisher Scientific. GAI, WO_3 pellets, $PbBr_2$, Au shots, Ag shots, $PC_{61}BM$, PEDOT:PSS, polytetrafluoroethylene syringe filters with the membrane pore size of 0.45 μm, and Extran 300 were purchased from Dyesol, Kurt J. Lesker, Alpha Aesar, AJA International, Strem Chemicals Inc., Nano-C, Heraeus, VWR, and EMD, respectively. Spiro-OMeTAD was purchased from either EMD or Feiming Chemical Ltd.

White light emitting diodes, drivers, and wiring harnesses were purchased from Luxeonstar LEDs. Heat sinks were purchased from Alpha Novatech to cool down the diodes.

5.3.1.1 FAI Synthesis[21]

In a 250-mL round-bottom flask at 0 °C, 15 g formamidine acetate was mixed with 30 mL HI (57% in water) added dropwise using a syringe pump. After stirring for 2 h, the solvent was evaporated at 80 °C for 2 h. After cooling down to room temperature, the precipitate was collected, partially dissolved with a small volume of ethanol, and slowly recrystallized by adding diethyl ether. Finally, it was dried at 60 °C under vacuum for 24 h. The synthesized powder was stored in a dry place.

5.3.1.2 MABr Synthesis[21]

In a 250-mL round-bottom flask at 0 °C, 40 mL CH_3NH_2 (33% in ethanol) was mixed with 44 mL HBr (48% in water) added dropwise using a syringe pump. After stirring for 4 h, the evaporation, recrystallization, and storage were done as for FAI.

5.3.2 Device Fabrication

FTO-coated (2.5 cm × 2.5 cm) glass slides were cleaned by subsequent sonication in a 2% aqueous extran 300 detergent, deionized water, and 2-propanol (20 min each), and drying in an oven at 120 °C for at least 2 h. Then, a 0.1 M solution of titanium diisopropoxide bis(acetylacetonate) in 1-butanol was spin-coated three times at 4000 rpm for 10 s. In between each spin-coating, the slides were annealed at 125 °C for 5-10 min and cooled down for 1 min.[47] After sintering at 450 °C for 0.5 h and cooling down, a 0.1 M solution of Li-TFSI in acetonitrile was spin-coated at 3000 rpm for 10 s, followed by annealing at 450 °C for 0.5 h.[22, 56] Then, hot slides (>150 °C) were transferred to a nitrogen atmosphere glovebox (H_2O and O_2 level ~1ppm). For the perovskite layer, an anhydrous DMF solution of 1.375 M PbI_2, 1.250 M FAI, and 0.0987 M CsI was mixed with an

anhydrous DMSO solution in a 76:24 ratio (v/v) and filtered through a 0.45 μm polytetrafluoroethylene syringe filter. DMSO solutions contained either 0.792 M $PbBr_2$ and 0.792 M MABr (FCM-IB), nothing (FC-I), or 0.0833 M PbI_2 and 0.0833 M GAI (FCG-I). The resulting solution was dispensed on the substrates and spin-coated at 1000 rpm for 10 s followed by 6000 rpm for 20 s. In the last 5 s of spin-coating, 500 μL of a 50/50 (v/v) solution of chlorobenzene and chloroform was dispensed as an antisolvent. Immediately after spinning, the slides were annealed at 140 °C for about 0.5 h, and allowed to slowly cool down to room temperature. A solution of the first hole transport layer was prepared by adding 18 μL of 4-tert-butyl pyridine and 18 μL of a 2.0 M Li-TFSI solution in acetonitrile to 1000 μL of a 70.0 mM Spiro-OMeTAD solution in chlorobenzene. After filtering through a 0.45 um polytetrafluoroethylene syringe filter, this solution was spin-coated at 500 rpm for 3 s, followed by at 4000 rpm for 20 s, in a laminar flow hood. The substrates were left in an open petri dish in the glovebox to dry overnight. The second hole transport layer was deposited by the evaporation of WO_3 pellets in a ~1×10^{-6} mbar pressure and with a rate of ~0.7 Å/s to obtain a ~45 nm layer. Finally, opaque Au or Ag top electrodes were deposited by evaporation.

5.3.3 Characterization

pXRD patterns were measured by a PANalytical Empyrean diffractometer with a Co source. Absorption and fluorescence spectra were acquired by a Cary 6000i UV-vis-NIR spectrophotometer and a PTI fluorometer (excitation at 460 nm), respectively. *J-V* curves were obtained in the glovebox using a 450 W Class AAA solar simulator with a AM1.5G filter (Sol3A, Oriel Instruments), a standard silicon reference cell (91150V, Oriel Instruments) to set the light intensity at 1 Sun, a Keithley 2400 source-measure unit, and with the use of a non-reflective aperture mask with an open area of 0.101 cm^2. IPCE spectra were acquired in air with the setup

QE-PV-Si, Oriel Instruments. A chopper with a frequency of 30 Hz was used for the incident light, and outgoing photocurrents were measured by a lock-in amplifier. SEM images were taken by a Hitachi SU8010 microscope, using the accelerating voltage of 4-5 kV and a working distance of 3-7 mm.

5.4 Results and Discussions

5.4.1 Perovskite Film Deposition and Characterization

In order to fabricate perovskites with different composition, films were spin-coated using three different precursor solutions (**Figure 5.1**). The first perovskite had a mixed, triple A-site cation (MA, FA, Cs) and mixed-anion (I, Br) composition, used previously to produce some of the highest-efficiency devices to date.[22] The precursor solution was made by mixing a DMF solution of PbI_2, FAI, and CsI with a DMSO solution of $PbBr_2$ and MABr (refer to the experimental section for details). The perovskites fabricated from this solution are denoted FCM-IB, based on the first letters of the constituent A-site and X-site ions. In order to determine whether $PbBr_2$ and MABr are needed to produce high-efficiency devices, the second set of samples eliminated these components from the precursor solution. In this case, pure DMSO was added to the same stock DMF solution as before. The resulting $FA_{(1-x)}Cs_xPbI_3$ samples are denoted FC-I. Finally, to explore the effect of ions of similar structure to FA, the stock DMF solution was mixed with a DMSO solution of PbI_2 and GAI. The perovskites produced from this solution are denoted as FCG-I. Both the MA and bromide ions were eliminated from the FC-I and FCG-I samples.

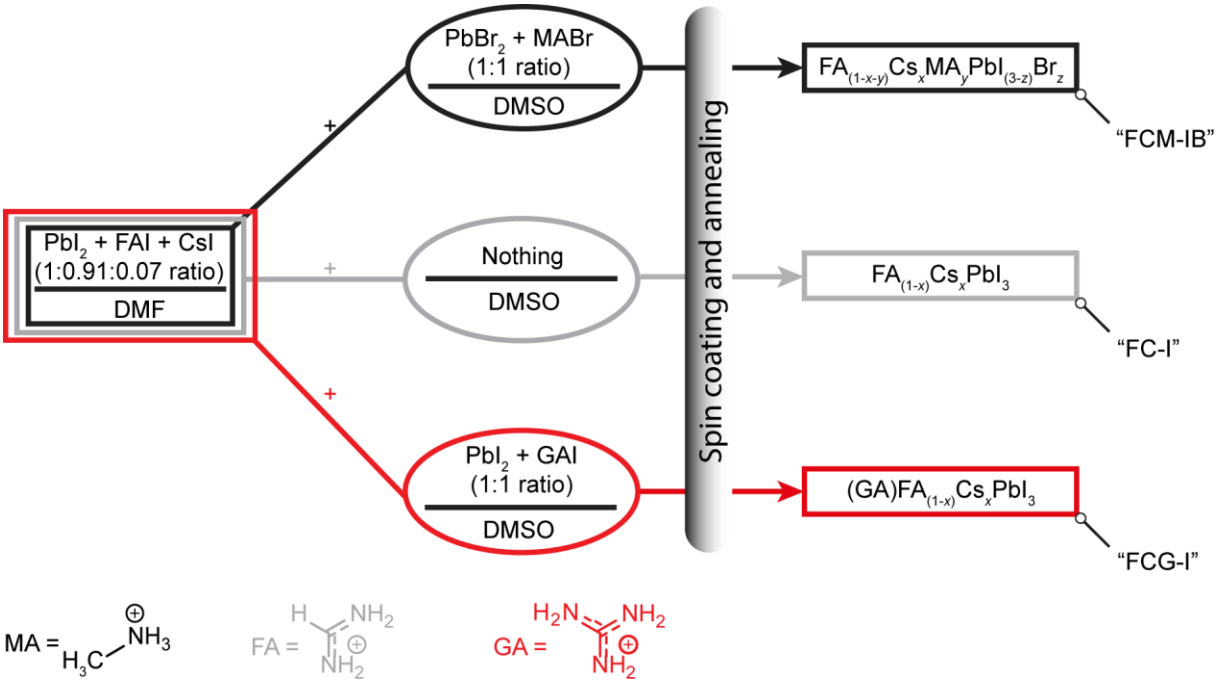

Figure 5.1 Schematics of fabricating perovskites with different composition.

After spin-coating and annealing, the perovskite films were analyzed by pXRD. The pXRD patterns revealed no crystalline PbI_2 phase (at 14.5°) for FC-I and FCG-I (**Figure 5.2a**), highlighting the better phase purity achieved when $PbBr_2$ and MABr are eliminated from the precursor solution. The absorption and emission spectra also clearly show the effect of this elimination (Figure 5.2b). Since pure $MAPbBr_3$ has a higher bandgap (2.24 eV)[15] than pure $FAPbI_3$ (1.48 eV),[14] eliminating MA and bromide from the film led to a red-shift in both the absorption and the emission spectra. The diffraction peaks for FCG-I are also more intense than those of FC-I, suggesting improved crystallinity of the perovskite phase; however, the FCG-I peaks did not shift in position relative to FC-I, and no new peaks were observed in the pXRD pattern. If GA was successfully incorporated into a perovskite lattice, either smaller-angle peaks should appear in the pXRD pattern (for the appearance of a new phase),[30] or the peaks should shift to smaller angles

(resulting from an enlargement of the existing perovskite unit cell). Since neither of these were observed, it is concluded that GA does not incorporate into the perovskite structure. Absorption and emission spectra support this conclusion. Both FCG-I and FC-I were determined to have the same optical bandgap (1.53 eV, **Figure 5.3**); however, pure $GAPbI_3$ has a larger bandgap (1.55 eV)[30] than α-$FAPbI_3$, and inclusion of GA would be expected to blue-shift the bandgap.

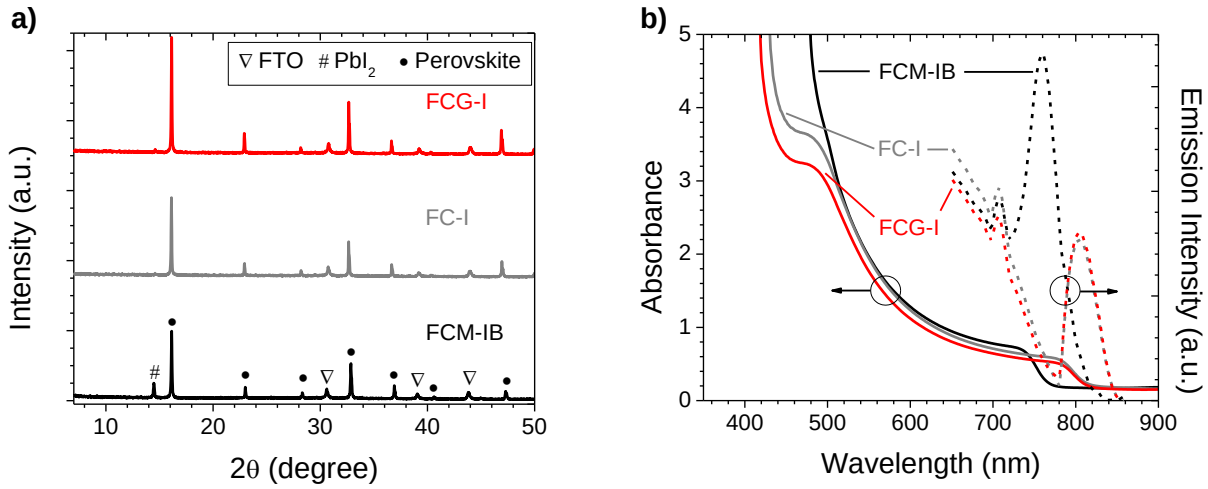

Figure 5.2 (a) X-ray diffraction patterns and (b) absorption and fluorescence spectra, of the perovskite films fabricated on glass/FTO/compact-TiO_2 substrates.

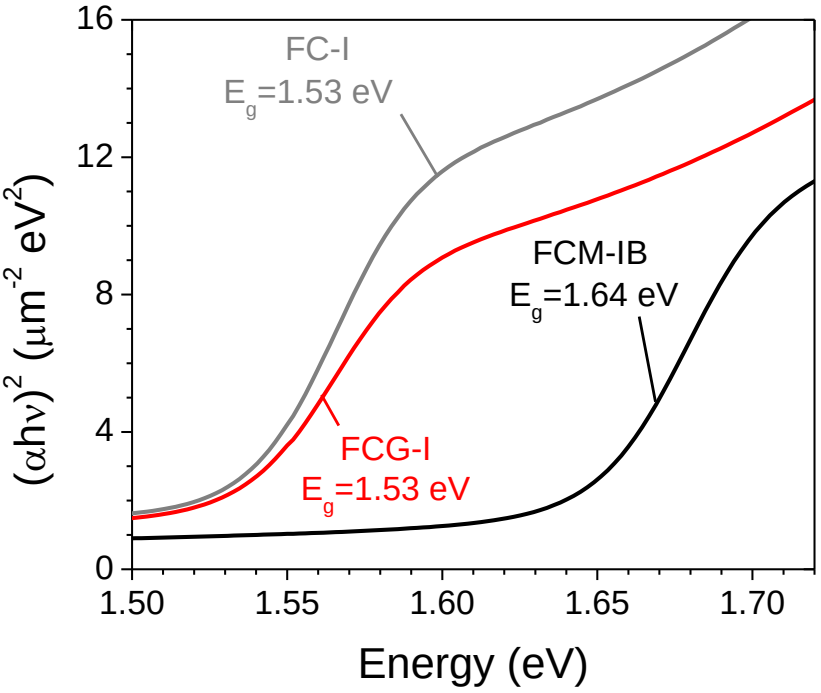

Figure 5.3. Representative Tauc plots to measure bandgaps (by assuming a direct bandgap for the perovskites). Bandgap values were calculated by linear fit, and are the result of averaging the values for 6-11 different measurements.

5.4.2 Device Fabrication and Characterization

After having characterized the perovskite films, they were used in solar cells. Initially, a planar-heterojunction device architecture was used: SiO_2/FTO/c-TiO_2/perovskite/Spiro-OMeTAD/Ag. Because of the low intrinsic hole mobility of Spiro-OMeTAD,[57-61] first, it was attempted to optimize the Li-TFSI doping level (**Table 5.1** and **Figure 5.4**). This resulted in efficient devices, but during the subsequent optimization of the GAI concentration in FCG-I cells (**Table 5.2** and **Figure 5.5**), it was observed that excess Li-TFSI led to more rapid perovskite decomposition (**Figure 5.6**). Instead, a double-layer hole-transport layer was used, consisting of a thin layer of WO_3 deposited on top of a more lightly-doped Spiro-OMeTAD layer.[62-64] This produced devices

with performances similar to those that employed much higher Li-TFSI doping levels (**Table 5.3**, **Figure 5.7**).

Table 5.1. Electrical parameters of 4-10 devices with (FCG-I) perovskite (equimolar with GAI final concentration of 0.050 M) and Spiro-OMeTAD (in 1000 µL chlorobenzene - refer to experimental) mixed with different amount of Li-TFSI solution (volume (µL) : molarity (M)) - No WO_3 top layer.

Li-TFSI solution volume: initial concentration (M)		V_{oc} (V)	J_{sc} (mA/cm2)	FF	PCE (%)
18:2.0	Average	0.87 ± 0.02	22.2 ± 0.1	0.48 ± 0.04	9.3 ± 0.9
	Best	0.886	22.1	0.52	10.1
36:2.0	Average	0.94 ±0.02	22.0 ± 0.3	0.65 ± 0.04	14 ± 1
	Best	0.958	21.6	0.70	14.5
18:4.0	Average	0.96 ± 0.04	22.0 ± 0.4	0.67 ± 0.03	14.1 ± 0.9
	Best	0.977	22.0	0.70	15.1

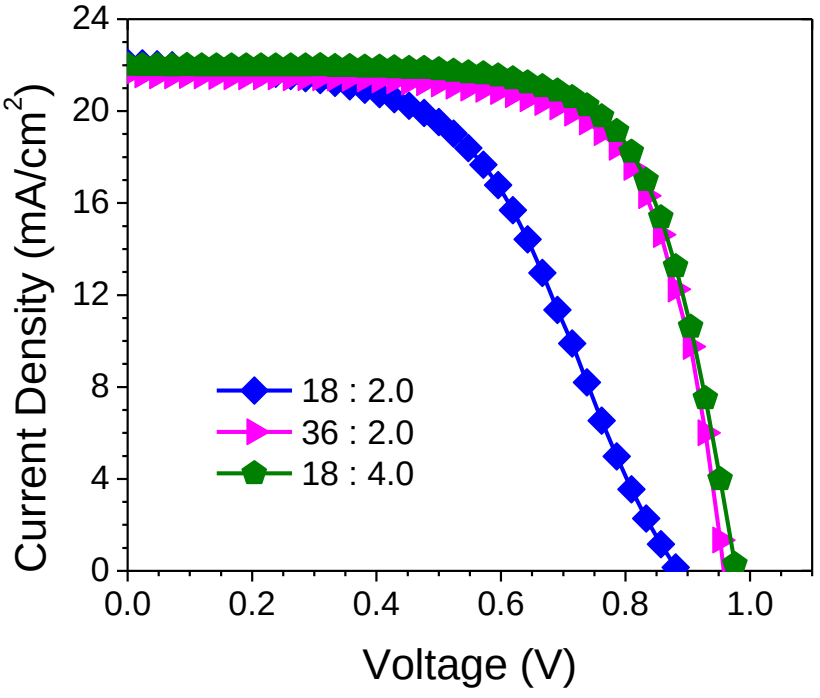

Figure 5.4. *J-V* curves of best devices with (FCG-I) perovskite (equimolar with GAI final concentration of 0.050 M) and Spiro-OMeTAD (in 1000 µL chlorobenzene) mixed with different amount of Li-TFSI solution (volume (µL) : molarity (M)) - No WO_3 top layer.

Table 5.2. Electrical parameters of 7-25 devices with (FCG-I) perovskite (equimolar with different GAI final concentration) and Spiro-OMeTAD (in 1000 µL chlorobenzene) mixed with 18 µL of 4.0 M Li-TFSI solution - No WO_3 top layer.

GAI final Concentration (M)		V_{oc} (V)	J_{sc} (mA/cm2)	FF	PCE (%)
0	Average	0.94 ± 0.02	21.1 ± 0.5	0.71 ± 0.02	14.1 ± 0.6
	Best	0.966	22.3	0.73	15.8
0.010	Average	0.985 ± 0.009	21.0 ± 0.5	0.70 ± 0.03	14.4 ± 0.8
	Best	0.996	21.8	0.74	16.1
0.020	Average	0.99 ± 0.01	22.9 ± 0.6	0.72 ± 0.02	16.3 ± 0.6
	Best	1.009	23.8	0.73	17.5
0.030	Average	0.988 ± 0.004	20.7 ± 0.7	0.69 ± 0.02	14.0 ± 0.5
	Best	0.992	21.3	0.70	14.7

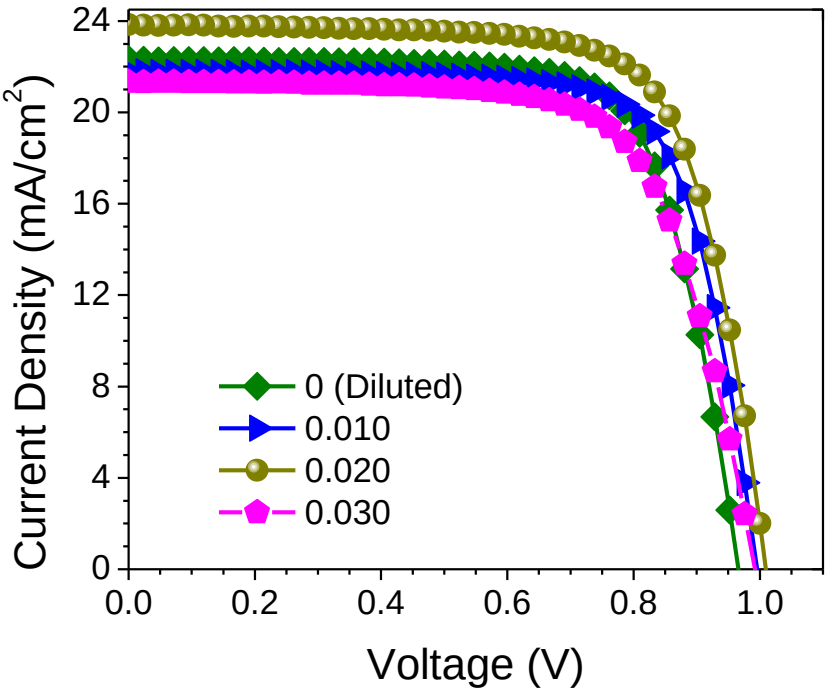

Figure 5.5. *J-V* curves of best devices with (FCG-I) perovskite (equimolar with different GAI final concentration) and Spiro-OMeTAD (in 1000 µL chlorobenzene) mixed with 18 µL of 4.0 M Li-TFSI solution- No WO_3 top layer.

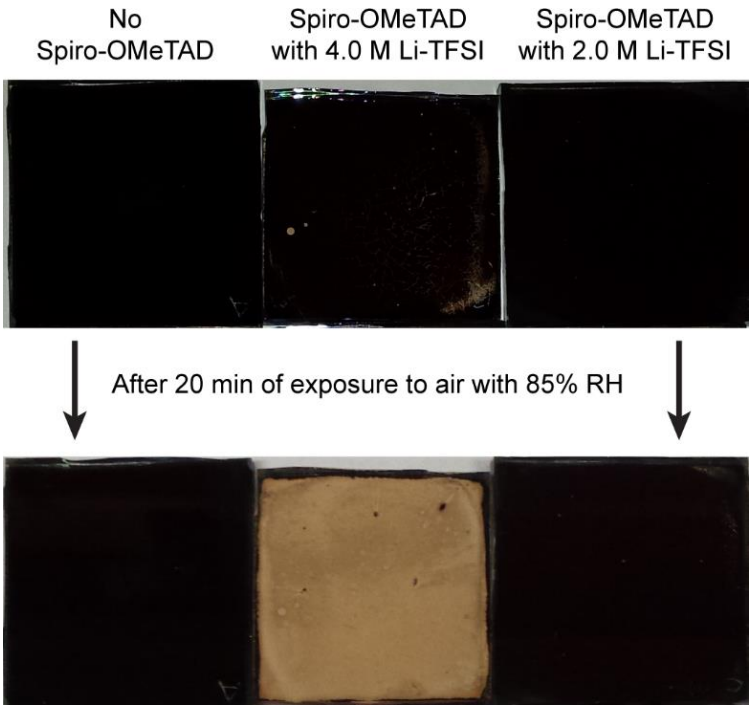

Figure 5.6. Instability of the perovskite layer when Spiro-OMeTAD is doped with a high concentration of Li-TFSI.

Table 5.3. Electrical parameters of 4-11 devices without and with WO_3 top layer. (FCG-I) perovskite (equimolar with GAI final concentration of 0.020 M) and Spiro-OMeTAD (in 1000 μL chlorobenzene) mixed with 18 μL of 2.0 M Li-TFSI solution.

Conditions		**V_{oc} (V)**	**J_{sc} (mA/cm^2)**	**FF**	**PCE (%)**
Without WO_3	Average	0.938 ± 0.08	22.7 ± 0.3	0.60 ± 0.03	12.8 ± 0.7
	Best	0.943	22.8	0.64	13.7
With WO_3	Average	1.015 ± 0.002	21.9 ± 0.7	0.74 ± 0.01	16.4 ± 0.4
	Best	1.013	22.7	0.74	17.1

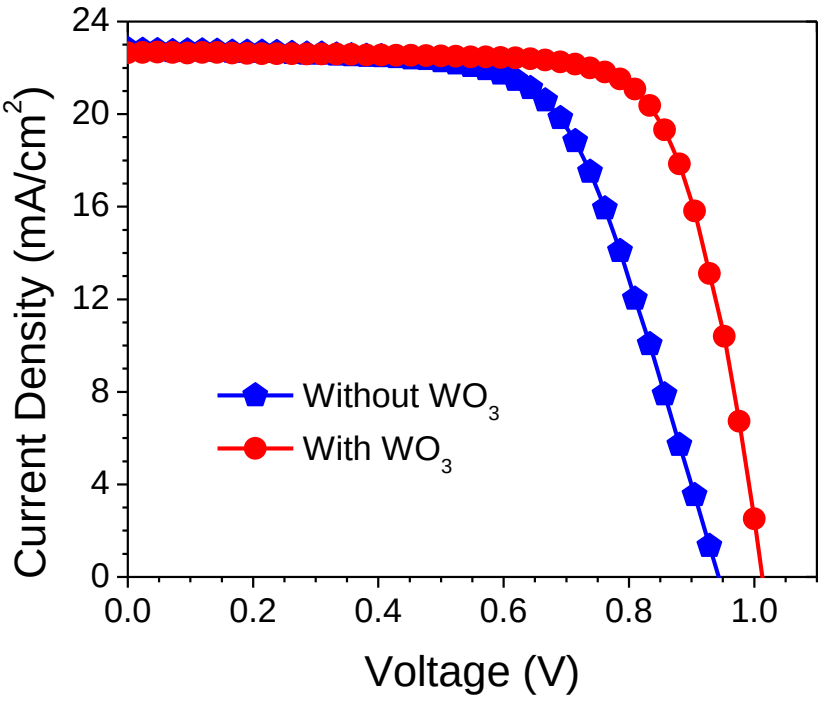

Figure 5.7. *J-V* curves of best devices without and with WO_3 top layer. (FCG-I) perovskite (equimolar with GAI final concentration of 0.020 M) and Spiro-OMeTAD (in 1000 µL chlorobenzene) mixed with 18 µL of 2.0 M Li-TFSI solution.

After settling on the use of a double-layer Spiro-OMeTAD/WO_3 hole-transport layer, perovskite solar cells with each of the three perovskite films were fabricated and tested. The electrical parameters of the devices are tabulated in **Table 5.4**, and the *J-V* curves, IPCE spectra, and loss-in potentials are shown in **Figure 5.8**. Comparing the data for the FCM-IB and FC-I devices, the elimination of bromide results in a lower average V_{oc}, but a higher average J_{sc} and FF. The changes in V_{oc}, and J_{sc} are consistent with the Shockley-Queisser calculations,[65] where a narrower bandgap semiconductor (i.e., FC-I) absorbs more light and produces a higher current density, but at the expense of voltage. This resulted in a net-zero change in performance, and the PCE of both sets of devices was almost identical. In the case of the GA-doped sample (FCG-I), the addition of GAI and PbI_2 to the precursor solution appears to have an overall positive effect on

device performance. The current-density and fill factor do not materially change; however, the open-circuit voltage increases by ca. 23 mV. As a result, the champion device in this study was prepared using FCG- I, and had a PCE of 17.7%.

Table 5.4. Electrical parameters of 20-28 devices of each perovskite.

Perovskite		**V_{oc} (V)**	**J_{sc} (mA/cm^2)**	**FF**	**PCE (%)**
FCM-IB	Average	1.08 ± 0.01	20.6 ± 0.5	0.71 ± 0.01	15.7 ± 0.5
	Best	1.091	21.7	0.70	16.7
FC-I	Average	0.990 ± 0.007	21.6 ± 0.7	0.74 ± 0.01	15.8 ± 0.5
	Best	1.001	22.0	0.76	16.7
FCG-I	Average	1.013 ± 0.006	21.7 ± 0.7	0.74 ± 0.02	16.3 ± 0.5
	Best	1.025	23.4	0.74	17.7

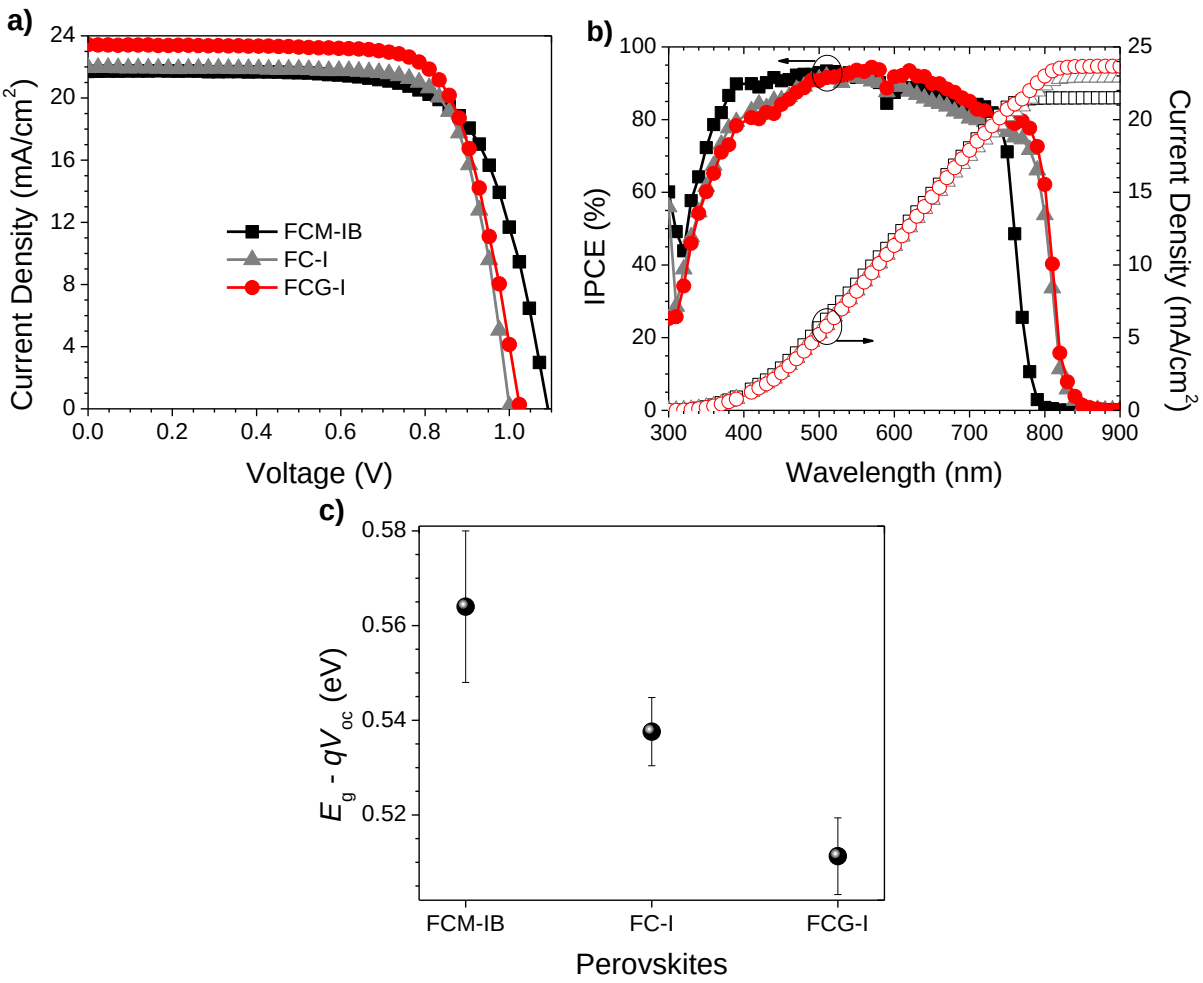

Figure 5.8 (a) *J-V* curves and (b) IPCE spectra (solid symbols) and integrated current density (open symbols with the same color), of the best devices. (c) Voltage loss (and error bars) based on E_g and average V_{oc} (and the propagation of their standard deviation) values.

IPCE spectra were measured to study the photocurrent response in various regions of the solar spectrum (Figure 5.8b). Consistent with the optical absorption spectra (Figure 5.2b), eliminating MA and bromide from the composition produced a red-shift in the IPCE spectra, and the effect on the calculated J_{sc} values is immediately apparent. All of the J_{sc} values calculated from the IPCE spectra (measured under the pseudo-steady-state conditions of the IPCE experiment) agreed to within 5% of the J_{sc} values obtained from the *J-V* curves.

To better understand the reason for the higher performance of the FCG-I devices, the average loss-in potential for each device set was calculated (Figure 5.8c). The loss-in potential was calculated as the difference between the optical bandgap (Figure 5.3) and the open-circuit voltage (qV_{oc}). Although the FCM-IB devices had the highest V_{oc}, they also had the highest loss-in potential. The loss-in potential was slightly lower for FC-I devices, and lower again for FCG-I. This suggests that the elimination of MA and bromide may result in a reduction in the number of trap states, and that the addition of GAI may help further passivate traps.

To evaluate the trap state density in our devices, electron-only and hole-only devices were fabricated by sandwiching each of the three perovskites between two sets of electron transport layers or two sets of hole transport layers, respectively.[11, 66] This produces the conditions for space-charge limited conduction (SCLC).[67]

For SCLC measurements, an *IV* curve is acquired in the dark and plotted in a double logarithmic graph.[67] Such a curve is consisted of four regions, defined with *n*, the slope of the best-fit line in each region. The four regions for ideal SCLC conditions are ohmic ($n = 1$), trap-limited SCLC ($n = 2$), trap-filled limit ($n = \infty$), and trap-free SCLC ($n = 2$). The '$n = \infty$' for the trap-filled limit region occurs when the energy levels of the trap states are ideally identical. However, a distribution of the energy levels in real cases causes a gradual increase of the current with the increase of the voltage. Therefore, any slope higher than 2 can be representative of this region. The end of the trap-limited SCLC region is when all the traps are filled with the charges. The voltage at this point, known as trap-filled limit voltage (V_{TFL}), is used for the calculation of the density of the trap states based on the following equation:

$$V_{\mathrm{TFL}} = \frac{e n_{\mathrm{t}} L^2}{2\varepsilon\varepsilon_0} \qquad \textbf{(Equation 5.1)}$$

where: n_t is the density of the trap states, L is the thickness of materials in between two contacts, ε_0 is the dielectric constant vacuum, and ε is the dielectric constant of materials.

The trap-filled limit voltage (V_{TFL}) of each carrier-specific device was determined from the dark *J-V* curves (**Figure 5.9**); this, in turn, was used to calculate the density of trap states for that carrier (Figure 5.9c), based on Equation 5.1. The dielectric constant of each perovskite sample was assumed to be invariant, and a value of 46.9 was used in all calculations.[68, 69] Given the relatively low levels of ion substitution used here, the value of 46.9 for α-$FAPbI_3$ is likely a good estimate for each of the perovskite samples.[30] The results show that the density of trap states for electrons is similar across all three systems (ca. 3×10^{16} cm^{-3}), but that the hole trap state density drops from ca. 1×10^{17} cm^{-3} for FCM-IB, to 4×10^{16} cm^{-3} for FC-I and 3×10^{16} cm^{-3} for FCG-I. This trend is consistent with the lower loss-in potentials of the FC-I and FCG-I devices (Figure 5.8c). The effect of GAI on the density of trap states is consistent with a previous study on $MAPbI_3$ devices,[30] where it was attributed to two underlying phenomena. One was the passivation of undercoordinated iodide ions at grain boundaries by the Lewis acidic GA ion; the other was the suppression of deep iodide vacancies within the perovskite structure. The latter is consistent with the increase in film crystallinity observed for the FCG-I films, as compared to the FC-I controls.

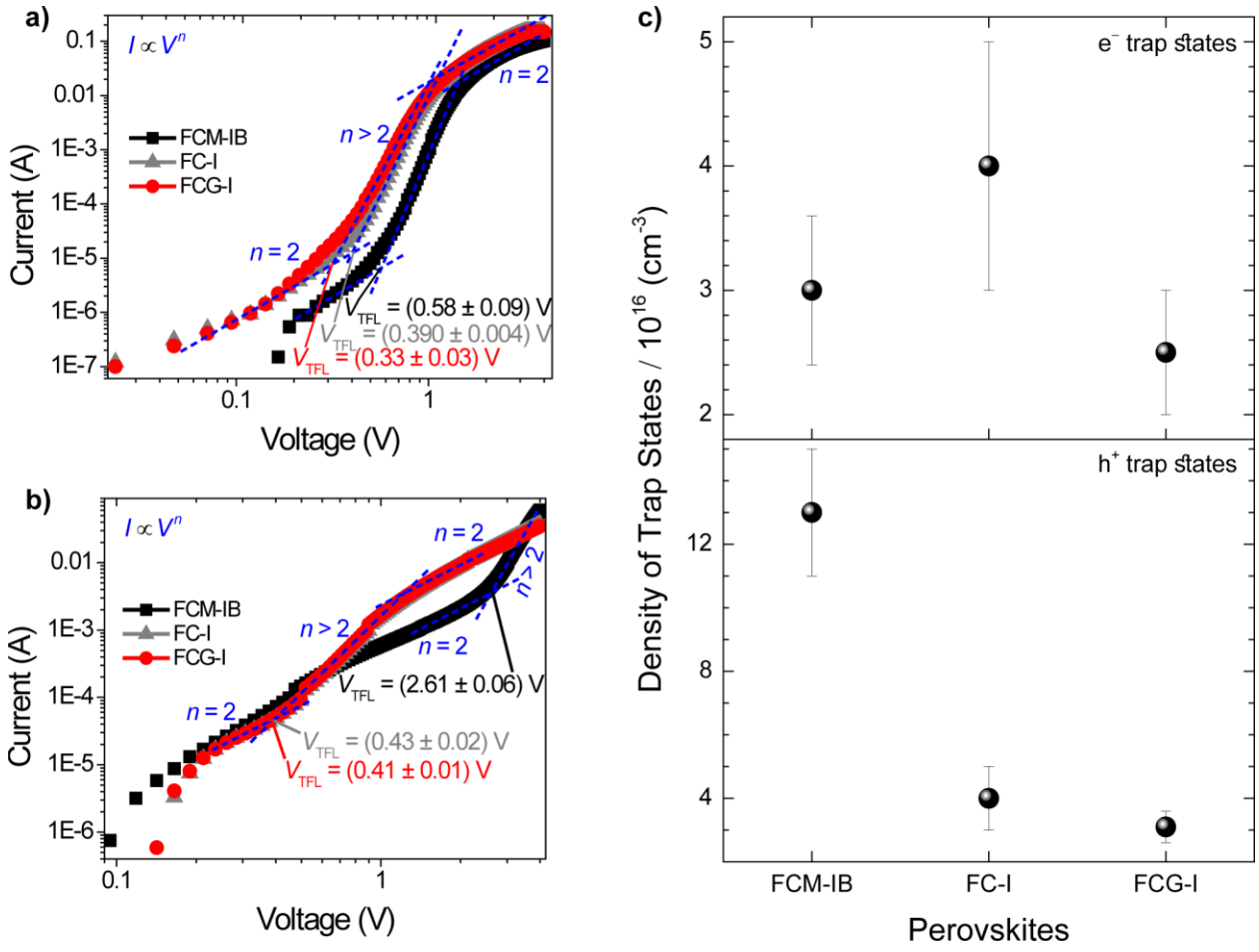

Figure 5.9 Dark current measurements to measure V_{TFL}, showing a representative curve for (a) e^--only (FTO/TiO_2/perovskite/$PC_{61}BM$/Au) and (b) h^+-only (FTO/PEDOT:PSS/perovskite/Spiro-OMeTAD/WO_3/Au) devices. Errors are the standard deviation of the measurements on 5-11 devices of each architecture. (c) The density of trap states of electrons and holes in different perovskite layers. Errors are propagated values based on the standard deviation of thickness and V_{oc} values.

5.4.3 Perovskite Film Stability

In order to determine the relative stability of the various perovskite compositions, the pXRD patterns of the perovskite films were monitored while the films were irradiated at 1 sun intensity in the presence of air at 85% relative humidity (RH, **Figure 5.10**). A flow of saturated water vapor in air was diluted to 85% RH with dry air, and directed into a transparent sample chamber; samples

were irradiated from below using a white LED array.[51] Our stability studies were focused on a high-performing literature composition (FCM-IB) and our highest-performing perovskite composition (FCG-I). For FCM-IB, the intensity of the perovskite diffraction peaks decreased rapidly; after 25 h of exposure, the most intense peak at ~ 16º had almost disappeared (Figure 5.10). Based on previous reports,[51] $MAPbI_3$ decomposes into crystalline PbI_2. In contrast, the amount of crystalline PbI_2 in FCM-IB decreased during exposure, as evidenced by a reduced intensity of the diffraction peak at ~14.5°. Similarly, FCG-I, which initially showed no crystalline PbI_2 in the pXRD pattern (Figure 5.2a), did not produce any crystalline PbI_2 after 30 h of exposure. The lack of PbI_2 was also evidenced by the lack of its distinct yellow color during the decomposition process. Other non-perovskite crystalline phases were also missing from the pXRD pattern (e.g., δ-$FAPbI_3$ at ~13.6°[14, 51] or δ-$CsPbI_3$ at ~13.1°.[50] These results might imply a gradual amorphization of the layers, or an entirely different decomposition mechanism for the $FAPbI_3$-based perovskites (as compared to $MAPbI_3$). Comparing the overall rate of decomposition, the FCG-I samples decomposed more slowly than FCM-IB; the intensity of the perovskite diffraction peaks in the FCG-I sample dropped to approximately half of their initial intensity after 30 h of exposure, whereas the FCM-IB samples had completely decomposed. Similar results were obtained in a duplicate experiment (**Figure 5.11a** and 5.11b). Control samples kept in the dark in a glovebox (~ 1 ppm O_2 and H_2O) showed virtually no decomposition over the same time period, highlighting the moisture and photochemically-driven nature of the decomposition process (**Figure 5.12a** and 5.12b). Full width at half maximum (FWHM) measurements confirmed the results for the loss of crystallinity of two studied perovskite films (**Figure 5.13**). Initially FWHM of the ~16º pXRD peak of FCG-I was smaller than that of FCM-IB, which confirmed the better crystallinity of the former. In addition, the slope of increasing the FWHM for FCG-I throughout

the test was more moderate than that of FCM-IB, which was in line with the minor loss of crystallinity when FCG-I was exposed to 85% RH and O_2/light.

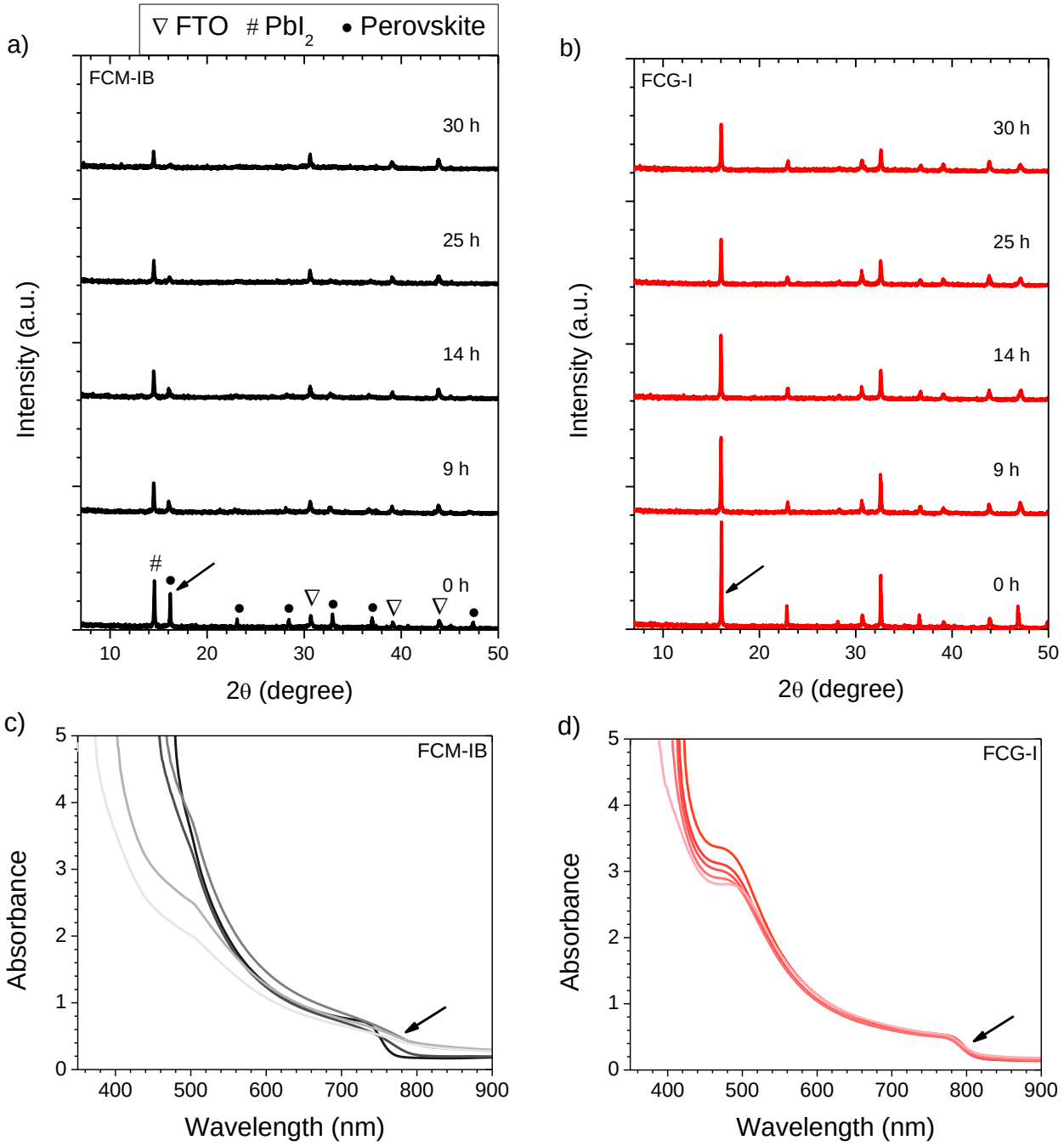

Figure 5.10 (a, b) XRD patterns and (c, d) absorbance spectra of the perovskite films throughout 30 h exposure (from dark to bright colors in (b)) to 85% RH and O_2/light. Arrows show (a) the most intense peak of the perovskite and (b) the change of the band edge regions.

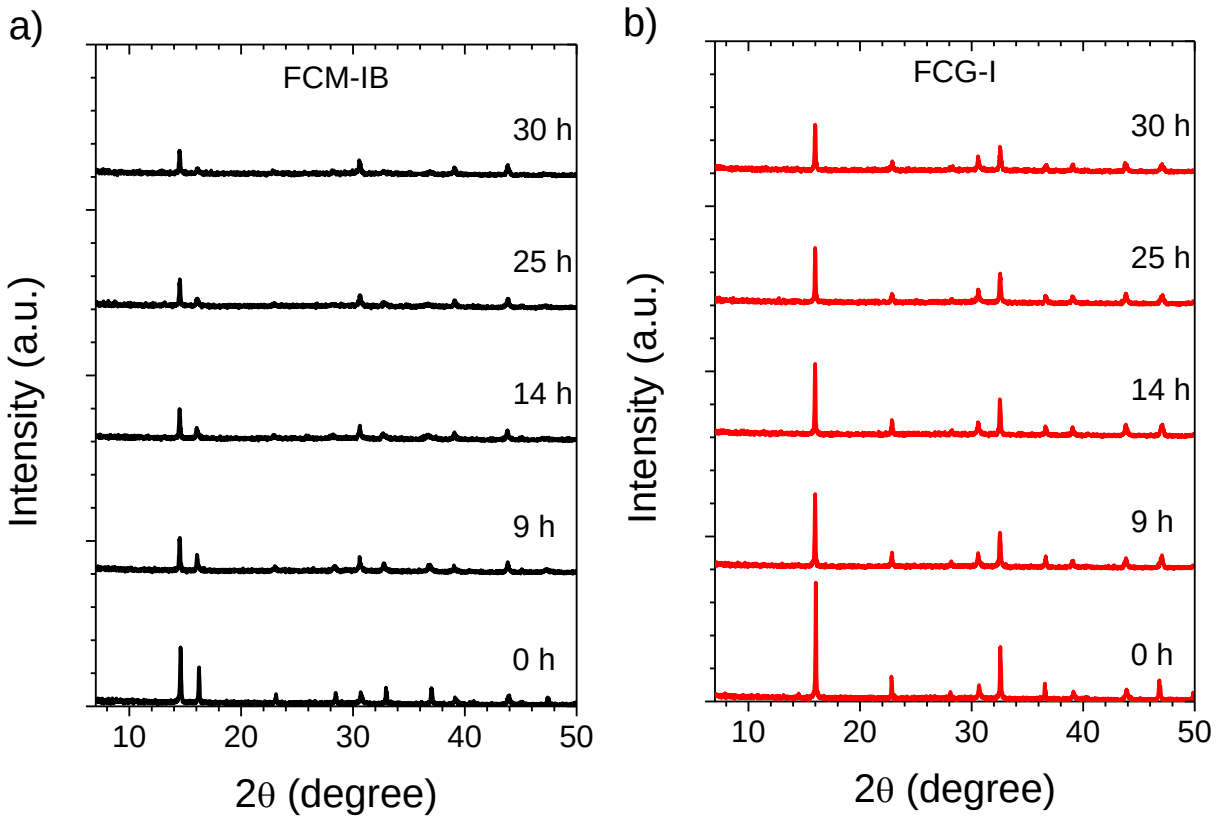

Figure 5.11. XRD patterns of the perovskite film duplicates throughout the exposure to 85% RH and O_2/light.

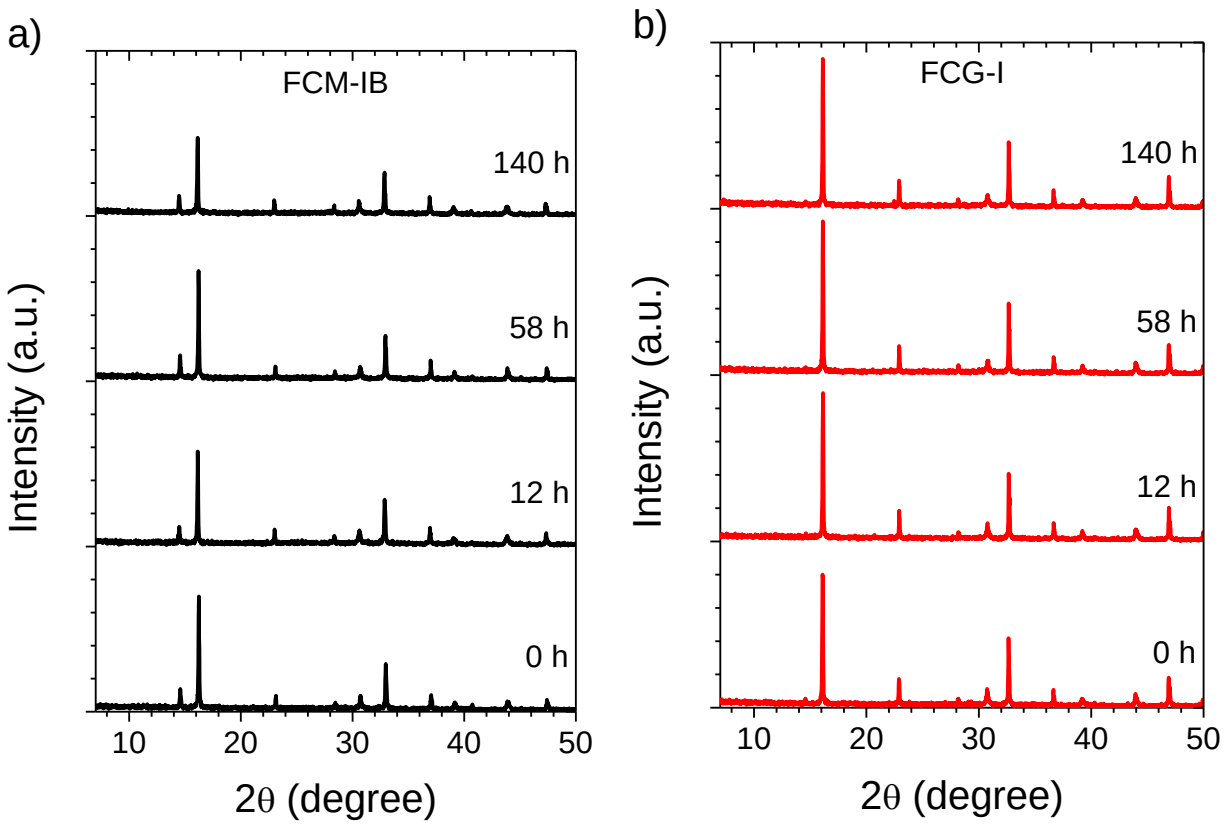

Figure 5.12. XRD patterns of the perovskite films when kept in the dark in a glovebox (~ 1 ppm H_2O and O_2).

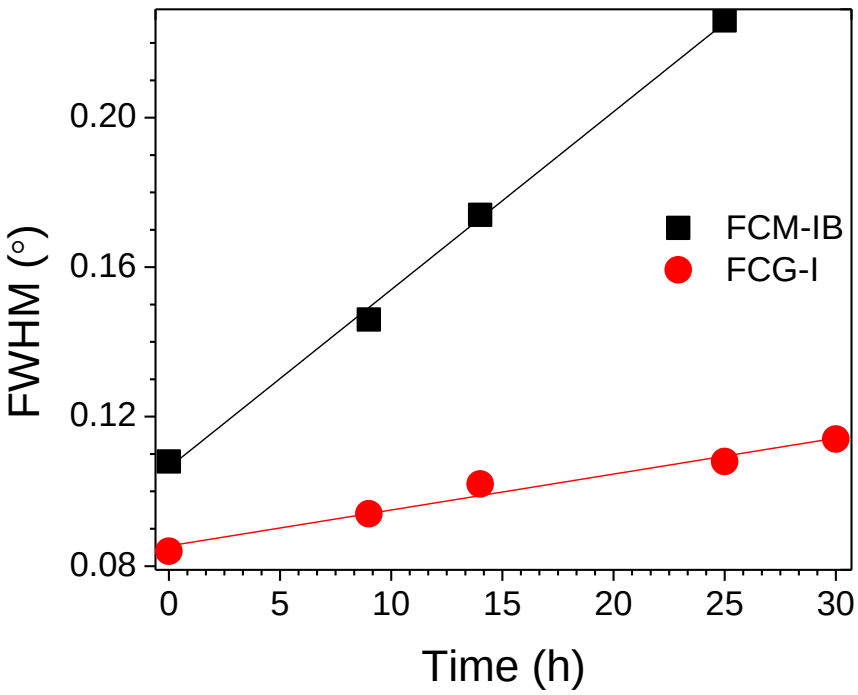

Figure 5.13. FWHM of the perovskite peaks at ~16º throughout the exposure to 85% RH and O_2/light. All data points are the average of two measurements on different films.

Absorption spectroscopy and SEM were used to evaluate the optical and morphological changes that occurred during our stability study. In the UV/vis spectrum, the band-edge features in FCM-IB started to flatten after only the first few hours of exposure (Figure 5.10c); this was accompanied by a pronounced loss of absorbance in the blue region of the spectrum (400 – 500 nm). One key observation is that the band edge of this sample red-shifts after exposure to our environmental chamber. This is consistent with our previous work on $(MA)_{1-x}(FA)_xPbI_3$ perovskites, where selective decomposition of MA-rich domains led to a red-shift in the apparent bandgap.[51] In contrast, the absorption spectra of FCG-I showed smaller changes in the blue region and almost no changes near the band edge over the course of the study (Figure 5.10d). Again, a duplicate experiment (**Figure 5.14a** and 5.14b) showed very similar results, and control samples stored in the dark in the glovebox showed negligible decomposition (**Figure 5.15a** and 5.15b). To

see the effect of these conditions on the film morphology, top-view SEM images were captured before and after 29 h of exposure (**Figure 5.16**). Consistent with the pXRD and UV/vis results, the FCM-IB film had noticeably decomposed, taking on a more porous, sponge-like appearance. In contrast, the FCG-I film retained more of its original structure, with only the appearance of tiny pinholes at the grain boundaries.

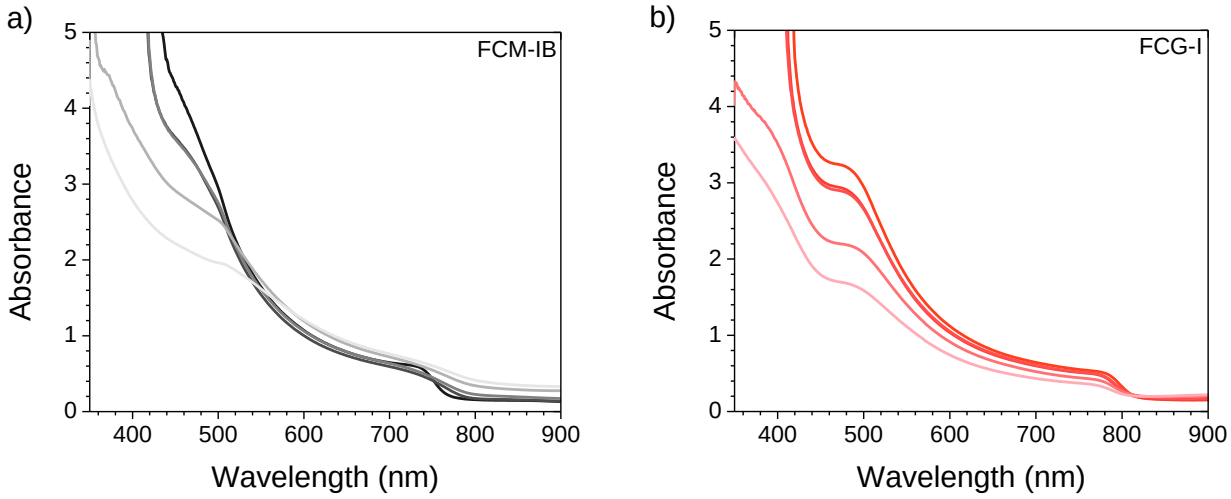

Figure 5.14. Absorption spectra of the perovskite film duplicates throughout a 30 h exposure to 85% RH and O_2/light (from dark to bright colors).

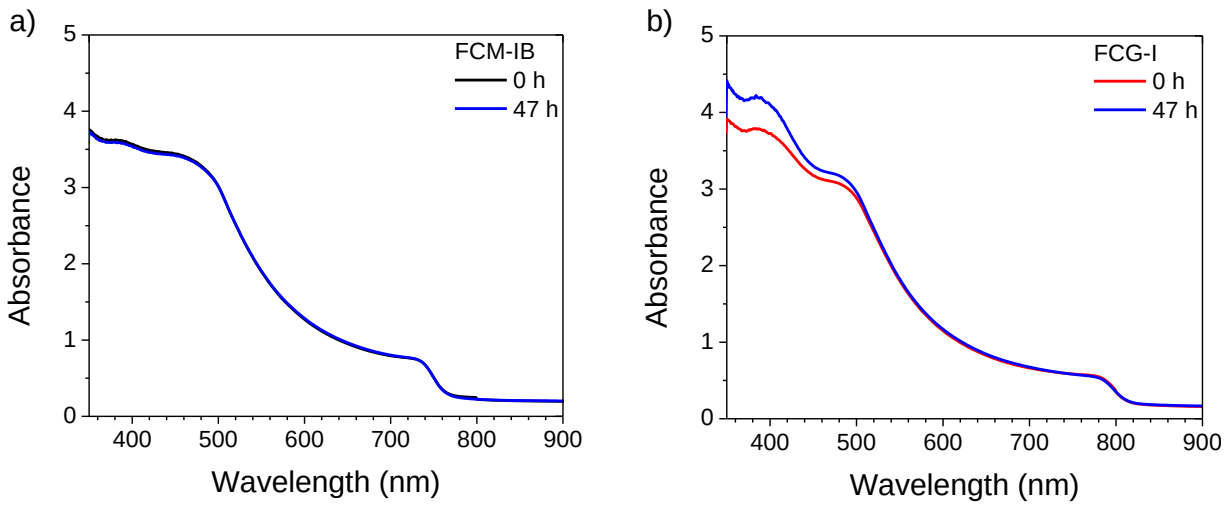

Figure 5.15. Absorption spectra of the perovskite films (a. b) when kept in the dark and in a glovebox (~ 1 ppm H_2O and O_2).

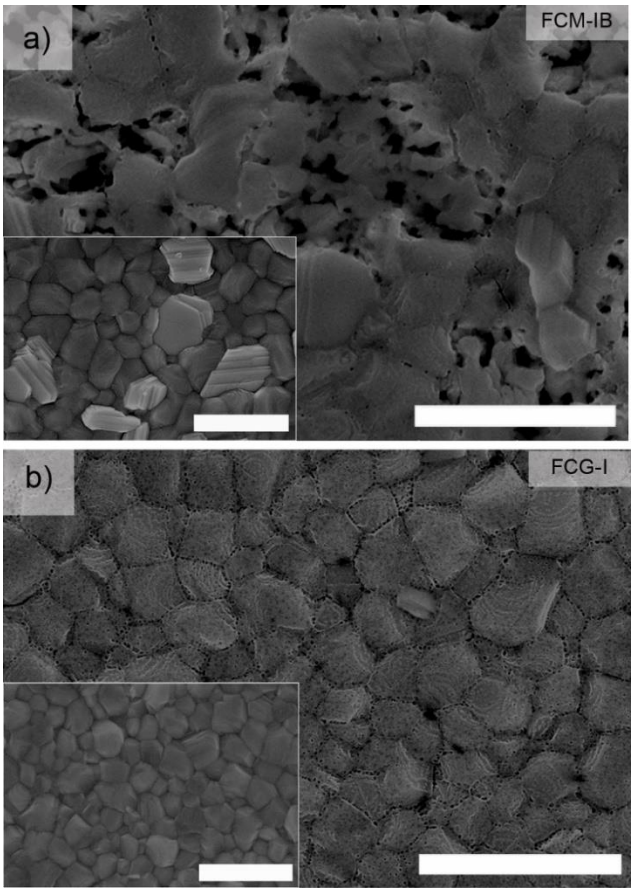

Figure 5.16 SEM images of (a) FCM-IB and (b) FCG-I, after 29 h exposure to 85% RH and O_2/light. Inset images are for fresh films. Size bars are all 1.00 μm.

5.4.4 Device Stability

Finally, the stability of complete devices were evaluated under the same set of environmental conditions (85% RH, 1 sun illumination in air). Gold electrodes were used instead of silver, since silver electrodes have already been demonstrated to accelerate the device degradation process.[51, 70] After 40 min of exposure to the relatively harsh conditions used for our stability test, none of the devices was able to tolerate the applied bias needed to acquire a *J-V* curve. This may be due to more rapid ion migration within the perovskite layer after it has absorbed moisture, and will be the subject of further study. Nonetheless, the IPCE of the devices could still be measured, since it is measured under short-circuit conditions. The IPCE spectrum of 4-5 devices was measured for each

type of perovskite and the spectra were averaged, a process repeated for each exposure time (**Figure 5.17**). In both the FCM-IB and FCG-I devices, the IPCE spectra decreased evenly across the spectrum as a function of aging time, and there was also relatively little change at the red-edge of the spectra. In contrast, however, the FCM-IB devices displayed a more rapid loss in IPCE than the FCG-I cells. After 180 min of exposure, the highest points in their IPCE spectra were ~40% and ~60%, respectively. The J_{sc} values associated with each of the IPCE spectra were then calculated and plotted against exposure time (Figure 5.17). At early exposure times, the FCG-I devices retained almost all of their initial photocurrent, whereas there was a significant loss of performance in the FCM-IB cells. After 40 min of aging, however, the rate of decomposition was similar for both sets of cells.

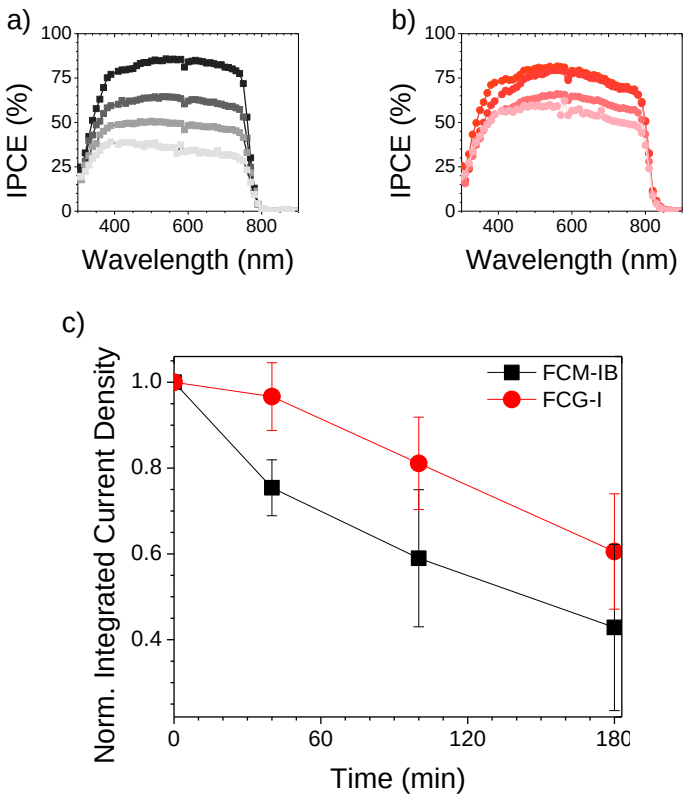

Figure 5.17 Average IPCE spectra of (left) FCM-IB, (middle) FCG-I devices, and (right) integrated current density of devices, throughout 180 min exposure to 85% RH and O2/light (from dark to bright colors). Error bars are standard deviations for 4-5 deviations for 4-5 devices.

To see how the device stack was affected by the test, cross-sectional SEM images were captured after 6 h of exposure (**Figure 5.18**). The SEM images of the fresh devices were quite similar to each other; however, the perovskite/Spiro-OMeTAD interface in the FCM-IB device was completely destroyed after exposure. There was also a marked increase in the total thickness of the perovskite layer, which may be due to swelling of the film after it absorbs moisture during the test. This process appears to have just started in the FCG-I sample; there is a roughening of the perovskite/Spiro-OMeTAD interface, but the effect is much less pronounced than in the FCM-IB device. Overall, these results are consistent with our analysis of the perovskite thin films, which showed improved stability of the FCG-I layer.

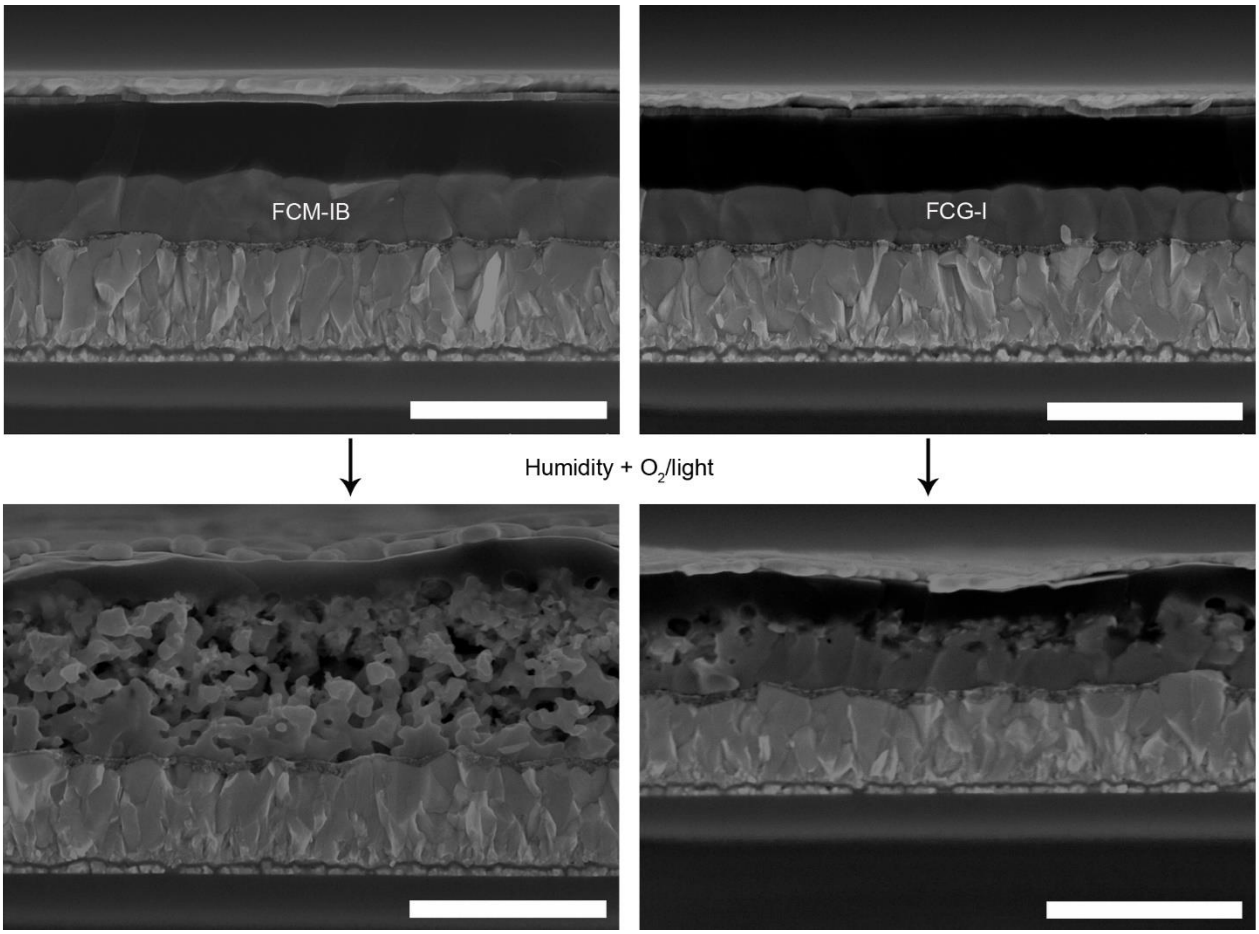

Figure 5.18. Cross-sectional SEM images of glass/FTO/compact-TiO_2/perovskite/Spiro-OMeTAD/WO_3/Au devices before and after 6h of the exposure to 85% RH and O_2/light. Size bars are 1.00 μm.

5.5 Conclusions

In this work, it has been demonstrated that the MA and bromide ions are not essential components in high-performing perovskite solar cells. Devices made using FC-I had performances equal to those of their FCM-IB counterparts. It has been additionally shown that GA ions can be used to passivate trap states in these formamidinium/caesium mixed-cation perovskites, resulting in a decrease in the loss-in potential and an improvement in PCE. Furthermore, these perovskite compositions appear to be more stable than the FCM-IB systems widely used in the literature, and

completely eliminate the possibility of halide segregation. Ultimately, this is a step toward a perovskite solar cell that is both highly efficient and more stable.

5.6 References

1. K. Poorkazem, D. Liu and T. L. Kelly, *J. Mater. Chem. A*, 2015, **3**, 9241-9248.
2. D. Liu and T. L. Kelly, *Nat. Photonics*, 2014, **8**, 133-138.
3. M. Ye, X. Hong, F. Zhang and X. Liu, *J. Mater. Chem. A*, 2016, **4**, 6755-6771.
4. M. Kaltenbrunner, G. Adam, E. D. Glowacki, M. Drack, R. Schwodiauer, L. Leonat, D. H. Apaydin, H. Groiss, M. C. Scharber, M. S. White, N. S. Sariciftci and S. Bauer, *Nat. Mater.*, 2015, **14**, 1032-1039.
5. P. K. Nayak and D. Cahen, *Adv. Mater.*, 2014, **26**, 1622-1628.
6. T. Leijtens, G. E. Eperon, A. J. Barker, G. Grancini, W. Zhang, J. M. Ball, A. R. S. Kandada, H. J. Snaith and A. Petrozza, *Energy Environ. Sci.*, 2016, **9**, 3472-3481.
7. G. E. Eperon, T. Leijtens, K. A. Bush, R. Prasanna, T. Green, J. T.-W. Wang, D. P. McMeekin, G. Volonakis, R. L. Milot, R. May, A. Palmstrom, D. J. Slotcavage, R. A. Belisle, J. B. Patel, E. S. Parrott, R. J. Sutton, W. Ma, F. Moghadam, B. Conings, A. Babayigit, H.-G. Boyen, S. Bent, F. Giustino, L. M. Herz, M. B. Johnston, M. D. McGehee and H. J. Snaith, *Science*, 2016, **354**, 861-865.
8. E. H. Anaraki, A. Kermanpur, L. Steier, K. Domanski, T. Matsui, W. Tress, M. Saliba, A. Abate, M. Gratzel, A. Hagfeldt and J.-P. Correa-Baena, *Energy Environ. Sci.*, 2016, **9**, 3128-3134.
9. M. T. Klug, A. Osherov, A. A. Haghighirad, S. D. Stranks, P. R. Brown, S. Bai, J. T. W. Wang, X. Dang, V. Bulovic, H. J. Snaith and A. M. Belcher, *Energy Environ. Sci.*, 2017, **10**, 236-246.
10. M. Hadadian, J.-P. Correa-Baena, E. K. Goharshadi, A. Ummadisingu, J.-Y. Seo, J. Luo, S. Gholipour, S. M. Zakeeruddin, M. Saliba, A. Abate, M. Grätzel and A. Hagfeldt, *Adv. Mater.*, 2016, **28**, 8681-8686.
11. D. Yang, X. Zhou, R. Yang, Z. Yang, W. Yu, X. Wang, C. Li, S. Liu and R. P. H. Chang, *Energy Environ. Sci.*, 2016, **9**, 3071-3078.
12. S. M. Jain, Z. Qiu, L. Haggman, M. Mirmohades, M. B. Johansson, T. Edvinsson and G. Boschloo, *Energy Environ. Sci.*, 2016, **9**, 3770-3782.
13. J. T.-W. Wang, Z. Wang, S. Pathak, W. Zhang, D. W. deQuilettes, F. Wisnivesky-Rocca-Rivarola, J. Huang, P. K. Nayak, J. B. Patel, H. A. Mohd Yusof, Y. Vaynzof, R. Zhu, I. Ramirez, J. Zhang, C. Ducati, C. Grovenor, M. B. Johnston, D. S. Ginger, R. J. Nicholas and H. J. Snaith, *Energy Environ. Sci.*, 2016, **9**, 2892-2901.
14. N. J. Jeon, J. H. Noh, W. S. Yang, Y. C. Kim, S. Ryu, J. Seo and S. I. Seok, *Nature*, 2015, **517**, 476-480.
15. Y. Liu, Z. Yang, D. Cui, X. Ren, J. Sun, X. Liu, J. Zhang, Q. Wei, H. Fan, F. Yu, X. Zhang, C. Zhao and S. Liu, *Adv. Mater.*, 2015, **27**, 5176-5183.

16. C. C. Stoumpos, C. D. Malliakas and M. G. Kanatzidis, *Inorg. Chem.*, 2013, **52**, 9019-9038.
17. N. Pellet, P. Gao, G. Gregori, T.-Y. Yang, M. K. Nazeeruddin, J. Maier and M. Grätzel, *Angew. Chem. Int. Ed.*, 2014, **53**, 3151-3157.
18. A. Binek, F. C. Hanusch, P. Docampo and T. Bein, *J. Phys. Chem. Lett.*, 2015, **6**, 1249-1253.
19. Z. Li, M. Yang, J.-S. Park, S.-H. Wei, J. J. Berry and K. Zhu, *Chem. Mater.*, 2016, **28**, 284-292.
20. T. Jesper Jacobsson, J.-P. Correa-Baena, M. Pazoki, M. Saliba, K. Schenk, M. Gratzel and A. Hagfeldt, *Energy Environ. Sci.*, 2016, **9**, 1706-1724.
21. W. S. Yang, J. H. Noh, N. J. Jeon, Y. C. Kim, S. Ryu, J. Seo and S. I. Seok, *Science*, 2015, **348**, 1234-1237.
22. M. Saliba, T. Matsui, J.-Y. Seo, K. Domanski, J.-P. Correa-Baena, M. K. Nazeeruddin, S. M. Zakeeruddin, W. Tress, A. Abate, A. Hagfeldt and M. Gratzel, *Energy Environ. Sci.*, 2016, **9**, 1989-1997.
23. D. Bi, C. Yi, J. Luo, J.-D. Décoppet, F. Zhang, Shaik M. Zakeeruddin, X. Li, A. Hagfeldt and M. Grätzel, *Nat. Energy*, 2016, **1**, 16142.
24. X. Li, D. Bi, C. Yi, J.-D. Décoppet, J. Luo, S. M. Zakeeruddin, A. Hagfeldt and M. Grätzel, *Science*, 2016, **353**, 58-62.
25. M. Saliba, T. Matsui, K. Domanski, J.-Y. Seo, A. Ummadisingu, S. M. Zakeeruddin, J.-P. Correa-Baena, W. R. Tress, A. Abate, A. Hagfeldt and M. Grätzel, *Science*, 2016, **354**, 206-209.
26. M. Saliba, S. Orlandi, T. Matsui, S. Aghazada, M. Cavazzini, J.-P. Correa-Baena, P. Gao, R. Scopelliti, E. Mosconi, K.-H. Dahmen, F. De Angelis, A. Abate, A. Hagfeldt, G. Pozzi, M. Graetzel and M. K. Nazeeruddin, *Nat. Energy*, 2016, **1**, 15017.
27. D. Bi, W. Tress, M. I. Dar, P. Gao, J. Luo, C. Renevier, K. Schenk, A. Abate, F. Giordano, J.-P. Correa Baena, J.-D. Decoppet, S. M. Zakeeruddin, M. K. Nazeeruddin, M. Grätzel and A. Hagfeldt, *Sci. Adv.*, 2016, **2**, e1501170.
28. J.-P. Correa-Baena, M. Anaya, G. Lozano, W. Tress, K. Domanski, M. Saliba, T. Matsui, T. J. Jacobsson, M. E. Calvo, A. Abate, M. Grätzel, H. Míguez and A. Hagfeldt, *Adv. Mater.*, 2016, **28**, 5031-5037.
29. G. Giorgi, J.-I. Fujisawa, H. Segawa and K. Yamashita, *J. Phys. Chem. C*, 2015, **119**, 4694-4701.
30. N. D. Marco, H. Zhou, Q. Chen, P. Sun, Z. Liu, L. Meng, E.-P. Yao, Y. Liu, A. Schiffer and Y. Yang, *Nano Lett.*, 2016, **16**, 1009-1016.
31. J. Yang, K. M. Fransishyn and T. L. Kelly, *Chem. Mater.*, 2016, **28**, 7344-7352.
32. F. Bella, G. Griffini, J.-P. Correa-Baena, G. Saracco, M. Grätzel, A. Hagfeldt, S. Turri and C. Gerbaldi, *Science*, 2016, **354**, 203-206.
33. Y. Yue, N. Salim, Y. Wu, X. Yang, A. Islam, W. Chen, J. Liu, E. Bi, F. Xie, M. Cai and L. Han, *Adv. Mater.*, 2016, **28**, 10738-10743.
34. S. Gholipour, J.-P. Correa-Baena, K. Domanski, T. Matsui, L. Steier, F. Giordano, F. Tajabadi, W. Tress, M. Saliba, A. Abate, A. Morteza Ali, N. Taghavinia, M. Grätzel and A. Hagfeldt, *Adv. Energy Mater.*, 2016, **6**, 1601116.
35. H.-C. Kwon, A. Kim, H. Lee, D. Lee, S. Jeong and J. Moon, *Adv. Energy Mater.*, 2016, **6**, 1601055.

36. D. Koushik, W. J. H. Verhees, Y. Kuang, S. Veenstra, D. Zhang, M. A. Verheijen, M. Creatore and R. E. I. Schropp, *Energy Environ. Sci.*, 2017, **10**, 91-100.
37. M. Long, T. Zhang, Y. Chai, C.-F. Ng, T. C. W. Mak, J. Xu and K. Yan, *Nat. Commun.*, 2016, **7**, 13503.
38. C. Qin, T. Matsushima, T. Fujihara and C. Adachi, *Adv. Mater.*, 2017, **29**, 1083808.
39. Y. Sun, Y. Wu, X. Fang, L. Xu, Z. Ma, Y. Lu, W.-H. Zhang, Q. Yu, N. Yuan and J. Ding, *J. Mater. Chem. A*, 2017, **5**, 1374-1379.
40. H. Tsai, W. Nie, J.-C. Blancon, C. C. Stoumpos, R. Asadpour, B. Harutyunyan, A. J. Neukirch, R. Verduzco, J. J. Crochet, S. Tretiak, L. Pedesseau, J. Even, M. A. Alam, G. Gupta, J. Lou, P. M. Ajayan, M. J. Bedzyk, M. G. Kanatzidis and A. D. Mohite, *Nature*, 2016, **536**, 312-316.
41. Z. Yang, A. Rajagopal, C.-C. Chueh, S. B. Jo, B. Liu, T. Zhao and A. K. Y. Jen, *Adv. Mater.*, 2016, **28**, 8990-8997.
42. F. Wang, W. Geng, Y. Zhou, H.-H. Fang, C.-J. Tong, M. A. Loi, L.-M. Liu and N. Zhao, *Adv. Mater.*, 2016, **28**, 9986-9992.
43. J. Liang, C. Wang, Y. Wang, Z. Xu, Z. Lu, Y. Ma, H. Zhu, Y. Hu, C. Xiao, X. Yi, G. Zhu, H. Lv, L. Ma, T. Chen, Z. Tie, Z. Jin and J. Liu, *J. Am. Chem. Soc.*, 2016, **138**, 15829-15832.
44. V. M. Goldschmidt, *Naturwissenschaften*, 1926, **14**, 477-485.
45. C. Yi, J. Luo, S. Meloni, A. Boziki, N. Ashari-Astani, C. Gratzel, S. M. Zakeeruddin, U. Rothlisberger and M. Gratzel, *Energy Environ. Sci.*, 2016, **9**, 656-662.
46. T. Matsui, J.-Y. Seo, M. Saliba, S. M. Zakeeruddin and M. Grätzel, *Adv. Mater.*, 2017, **29**, 1606258.
47. J.-W. Lee, D.-H. Kim, H.-S. Kim, S.-W. Seo, S. M. Cho and N.-G. Park, *Adv. Energy Mater.*, 2015, **5**, 1501310.
48. E. T. Hoke, D. J. Slotcavage, E. R. Dohner, A. R. Bowring, H. I. Karunadasa and M. D. McGehee, *Chem. Sci.*, 2015, **6**, 613-617.
49. D. J. Slotcavage, H. I. Karunadasa and M. D. McGehee, *ACS Energy Lett.*, 2016, **1**, 1199-1205.
50. W. Rehman, D. McMeekin, J. Patel, R. Milot, M. B. Johnston, H. Snaith and L. M. Herz, *Energy Environ. Sci.*, 2017, **10**, 361-369.
51. K. Poorkazem and T. L. Kelly, *In Preparation*.
52. J. Yang, B. D. Siempelkamp, D. Liu and T. L. Kelly, *ACS Nano*, 2015, **9**, 1955-1963.
53. A. M. A. Leguy, Y. Hu, M. Campoy-Quiles, M. I. Alonso, O. J. Weber, P. Azarhoosh, M. van Schilfgaarde, M. T. Weller, T. Bein, J. Nelson, P. Docampo and P. R. F. Barnes, *Chem. Mater.*, 2015, **27**, 3397-3407.
54. Z. Song, A. Abate, S. C. Watthage, G. K. Liyanage, A. B. Phillips, U. Steiner, M. Graetzel and M. J. Heben, *Adv. Energy Mater.*, 2016, **6**, 1600846.
55. D. Bryant, N. Aristidou, S. Pont, I. Sanchez-Molina, T. Chotchunangatchaval, S. Wheeler, J. R. Durrant and S. A. Haque, *Energy Environ. Sci.*, 2016, **9**, 1655-1660.
56. F. Giordano, A. Abate, J. P. Correa Baena, M. Saliba, T. Matsui, S. H. Im, S. M. Zakeeruddin, M. K. Nazeeruddin, A. Hagfeldt and M. Graetzel, *Nat. Commun.*, 2016, **7**, 10379.
57. D. Shi, X. Qin, Y. Li, Y. He, C. Zhong, J. Pan, H. Dong, W. Xu, T. Li, W. Hu, J.-L. Brédas and O. M. Bakr, *Sci. Adv.*, 2016, **2**, e1501491.

58. V. W. Bergmann, S. A. L. Weber, F. Javier Ramos, M. K. Nazeeruddin, M. Grätzel, D. Li, A. L. Domanski, I. Lieberwirth, S. Ahmad and R. Berger, *Nat. Commun.*, 2014, **5**, 5001.
59. Z. Li, J. Tinkham, P. Schulz, M. Yang, D. H. Kim, J. Berry, A. Sellinger and K. Zhu, *Adv. Energy Mater.*, 2017, **7**, 1601451.
60. P. Wang, J. Zhang, Z. Zeng, R. Chen, X. Huang, L. Wang, J. Xu, Z. Hu and Y. Zhu, *J. Mater. Chem. C*, 2016, **4**, 9003-9008.
61. T. Miletić, E. Pavoni, V. Trifiletti, A. Rizzo, A. Listorti, S. Colella, N. Armaroli and D. Bonifazi, *ACS Appl. Mater. Int.*, 2016, **8**, 27966-27973.
62. R. Hock, T. Mayer and W. Jaegermann, *J. Phys. Chem. C*, 2012, **116**, 18146-18154.
63. Y. Liu, Q. Chen, H.-S. Duan, H. Zhou, Y. Yang, H. Chen, S. Luo, T.-B. Song, L. Dou and Z. Hong, *J. Mater. Chem. A*, 2015, **3**, 11940-11947.
64. E. Della Gaspera, Y. Peng, Q. Hou, L. Spiccia, U. Bach, J. J. Jasieniak and Y.-B. Cheng, *Nano Energy*, 2015, **13**, 249-257.
65. W. Shockley and H. J. Queisser, *J. Appl. Phys.*, 1961, **32**, 510-519.
66. V. Adinolfi, M. Yuan, R. Comin, E. S. Thibau, D. Shi, M. I. Saidaminov, P. Kanjanaboos, D. Kopilovic, S. Hoogland, Z.-H. Lu, O. M. Bakr and E. H. Sargent, *Adv. Mater.*, 2016, **28**, 3406-3410.
67. G. Mazzanti and M. Marzinotto, *Extruded Cables for High-Voltage Direct-Current Transmission: Advances in Research and Development*, JohnWiley & Sons, Inc., The Institute of Electrical and Electronics Engineers, Inc., 2013.
68. Q. Han, S.-H. Bae, P. Sun, Y.-T. Hsieh, Y. Yang, Y. S. Rim, H. Zhao, Q. Chen, W. Shi and G. Li, *Adv. Mater.*, 2016, **28**, 2253-2258.
69. Y. Huang, L. Li, Z. Liu, H. Jiao, Y. He, X. Wang, R. Zhu, D. Wang, J. Sun, Q. Chen and H. Zhou, *J. Mater. Chem. A*, 2017, **5**, 8537-8544.
70. Y. Kato, L. K. Ono, M. V. Lee, S. Wang, S. R. Raga and Y. Qi, *Adv. Mater. Interfaces*, 2015, **2**, 1500195.

Chapter 6. CONCLUSIONS

6.1 Summary and Discussion

In order to compete with fossil fuels, the fabrication, installation, operation and maintenance costs of solar technology need to be reduced, and options need to be provided that are not possible for conventional silicon solar cells. To do so, one strategy is to use the upconversion process as a way to improve the efficiency of any type of solar cell. The second strategy is providing the option of device flexibility, useful for either the fabrication or installation of devices. The third strategy is improving the stability of materials used in a device. And the last strategy is to simultaneously improve device efficiency and stability. These various approaches have been the base of the research in this thesis. This discussion section links the four different approaches used in the thesis (**Figure 6.1**), and demonstrates how the objectives listed in the introduction chapter are addressed. It compares the results obtained in this thesis with other literature examples, and shows how the findings of this thesis contribute to the overall goal of improving the solar cell technology. Finally, it discusses follow-up studies to the research reported in this thesis.

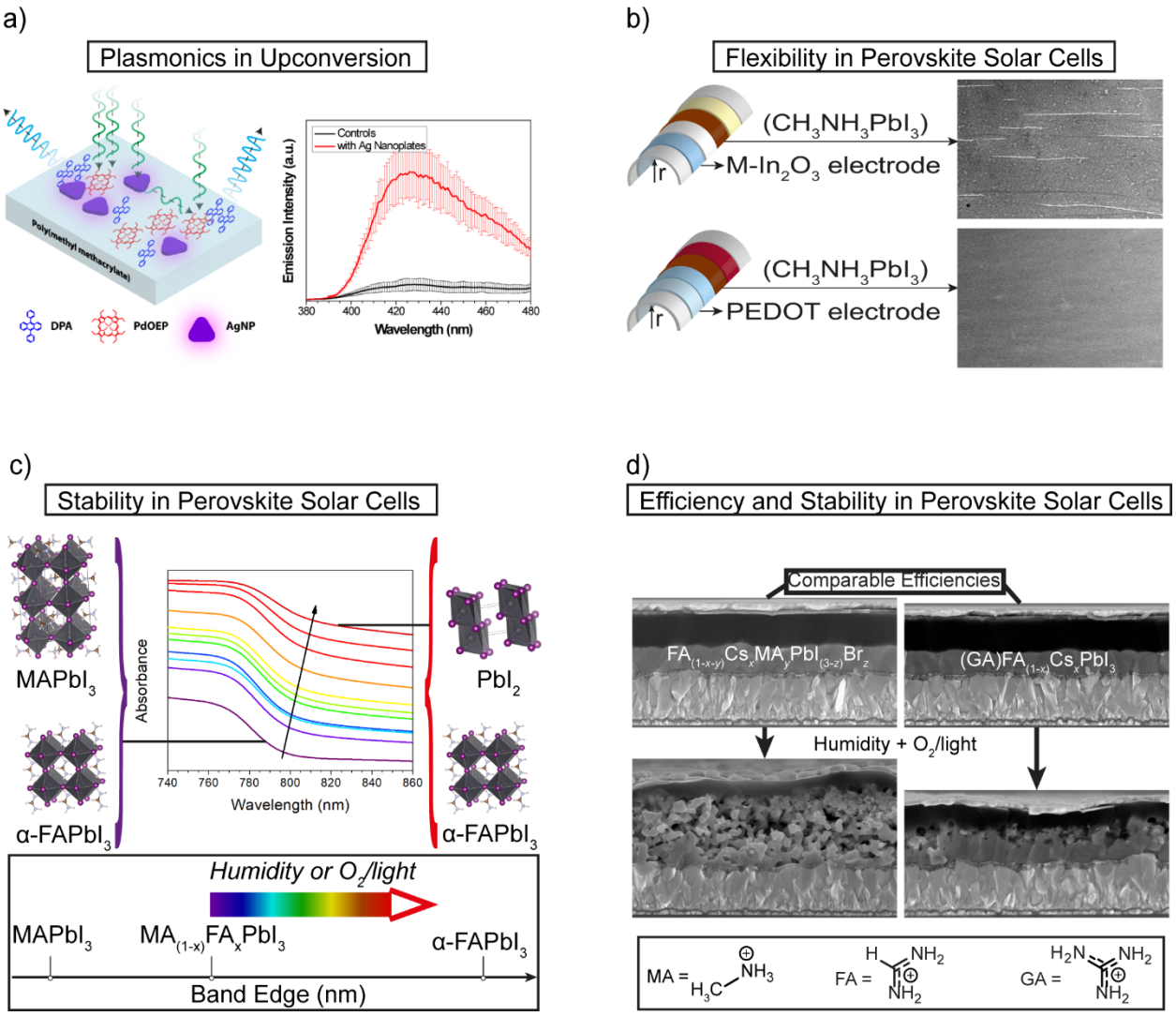

Figure 6.1. Outline of four approaches in this thesis to improving solar cell technology. (a) Using the scattering and near-field effects of Ag nanoplates to enhance the efficiency of TTA. (b) Replacing the inflexible metal oxide electrode with HC-PEDOT to improve the flexibility of PSCs. (c) Doping $MAPbI_3$ with the FA cations to improve the stability of perovskite films when exposed to either humidity or superoxide. (d) Eliminating MABr and $PbBr_2$ from the perovskite solution, and adding GAI and PbI_2, to improve the stability of the efficient state-of-the-art PSCs.

In the first approach, the need to improve the quantum efficiency of TTA (section 1.2.2.2) was addressed using plasmonics. To do this, Ag nanoprisms were first synthesized in an aqueous solution, and then transferred to an organic solvent. As a result, a homogeneous solution of the

TTA materials, the nanoparticles, and the polymer matrix could be made. To reach the objective of plasmon-enhanced TTA (section 1.2.4) in the solid state, the localized surface-plasmon resonance of these anisotropic nanoparticles was tuned to match the Q band of PdOEP. The scattering and near-field effects of the nanoplates helped increase the absorbance of PdOEP, and led to an 8.5-fold increase in the emission intensity of the upconverted light. Prior to this work, a study showed that the surface-plasmon polaritons (SPPs) created in a 50 nm-thick Ag layer could increase TTA efficiency.[1] However, at the same frequency, incident photons have less momentum than polaritons, and therefore may not excite them. In order to excite the SPP modes (and produce plasmon-enhanced TTA), a Kretschmann configuration was required. In addition, the flat layer of Ag could not provide the same scattering and near-field effects of nanoparticle plasmonics. Therefore, the primary achievement in chapter two of this thesis is the first experimental study coupling nanoparticle plasmonics with TTA.

The results of chapter 2 have since been used by other researchers to further enhance the efficiency of TTA, with the overall objective of improving solar cell efficiency. A follow-up study of the work in this thesis used the effects of both the LSPR of Ag nanoprism arrays (AgNA) and the SPPs of SiO_2/Ag layers (**Figure 6.2a**-6.2d).[2] Platinum(II) octaethylporphyrin (PtOEP) and DPA were used as the TTA materials. The intensity of the upconverted light was higher when both effects existed, compared to the SPPs alone. This was further confirmed by power-dependency measurements. There was a pseudo-quadratic dependency when the TTA materials were coated on quartz substrates. However, by adding the SPP and then the LSPR effects, the dependency became more linear. Another follow-up study used Au nanoprisms (AuNP) mixed with Rose Bengal (RB) and 1,3-diphenylisobenzofuran (DPBF) in solution as the upconversion materials (Figure 6.2e, 6.2f).[3] Similar to the results of chapter 3 of this thesis, the intensity of the upconverted

light increased. Although photon upconversion,[4, 5] particularly plasmon-enhanced systems,[6] is promising for the future of solar cell technology, the TTA quantum yield is still too low and requires further research to be practical in photovoltaic cells.

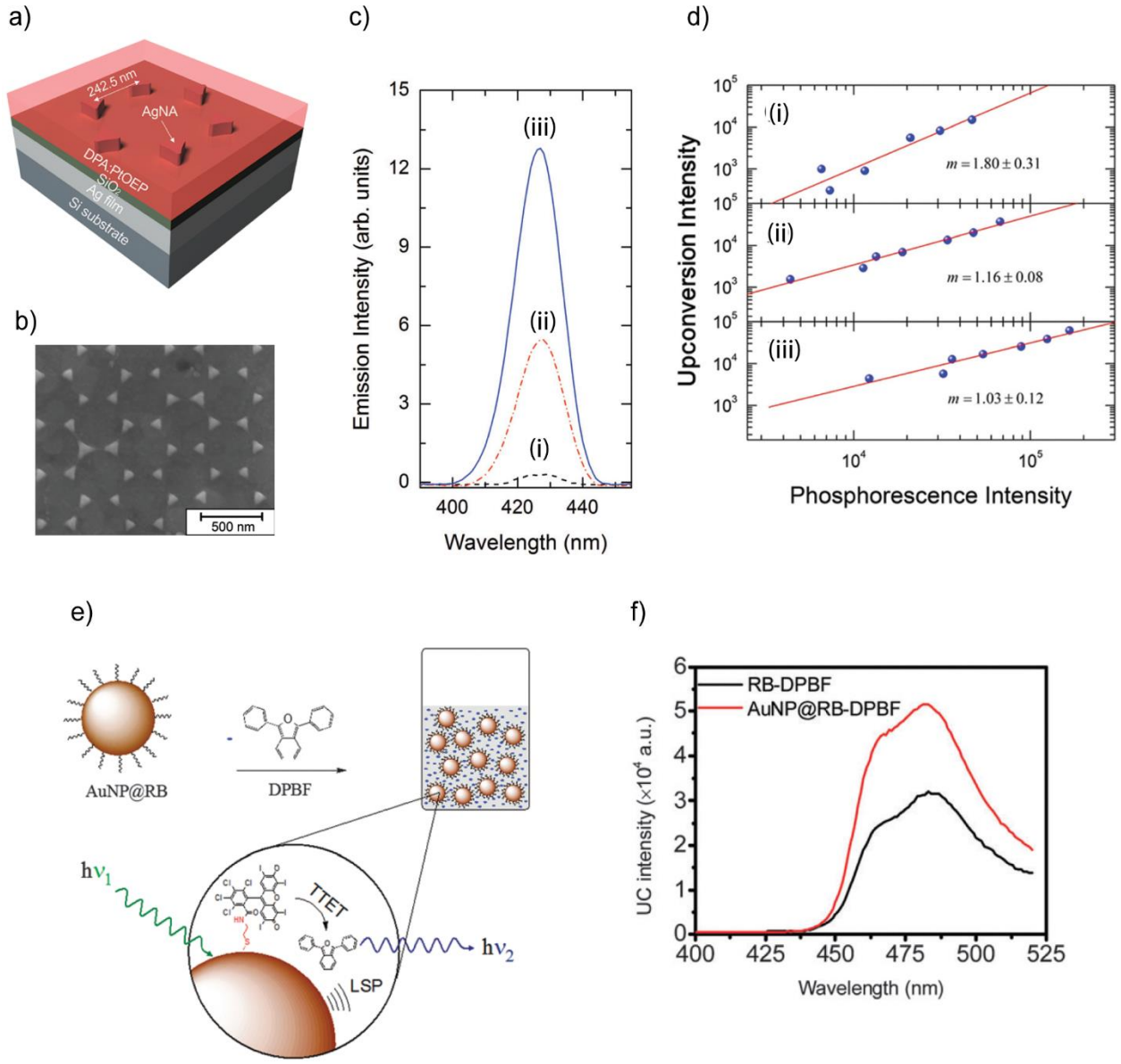

Figure 6.2. Literature examples after the publication of the plasmon-enhanced TTA work (chapter 2 of this thesis). (a) Schematics of using both the SPPs of the SiO_2/Ag layers and the LSPR of AgNA, mixed with PtOEP and DPA in the solid state. (b) A SEM micrograph of AgNA. (c) Emission intensity of the upconverted light when TTA materials are coated on different substrates: (i) quartz, (ii) SiO_2/Ag, and (iii) AgNA/SiO_2/Ag. (d) Power-dependency measurements of the configurations in (c). (a-e) Reproduced and adapted with permission of The Royal Society of Chemistry.[2] (e) Schematics of using AuNP to improve the intensity of a TTA system made from RB and DPBF in solution. (f) Emission intensities of TTA materials with and without AuNP. (e, f) Reproduced adapted with permission of The Royal Society of Chemistry.[3]

The second approach to improving solar technology focuses on improving perovskite solar cells. Chapter 3 elucidates the factors limiting the flexibility of these devices (section 1.4.1), and measures the fatigue resistance of the $MAPbI_3$ perovskite (section 1.4.4). By measuring the fatigue resistance of devices over 2000 bending cycles, it was shown that it is the metal oxide electrode that limits device flexibility. The electrode was replaced with a polymer-based PEDOT electrode, improving the flexibility. In addition, by making both perovskite and organic solar cells using the PEDOT electrode, the flexibility of perovskite and polymer active layers was compared. It was concluded that although the perovskite layer is less flexible than organic polymers, it is more than flexible enough to be used in R2R manufacturing. In the time this work was in preparation for publication, one study showed that cracks in the ITO electrode, and not in the perovskite layer, are responsible for device failure.[7] However, it did not provide an alternative to address the issue, and therefore could not evaluate the flexibility of the perovskite layer itself. Importantly, the device fabricated in this thesis (chapter 3) was the first metal oxide-free perovskite solar cell in the literature.

To improve solar technology, device flexibility is important, and in this regard, the results of chapter 3 of this thesis have played an important role. In a later study, the work function of the HC-PEDOT electrode was modified by polyetherimide, resulting in a better energy alignment with the perovskite and resulting in a PCE of 9.7% on flexible substrates.[8] Another study replaced the HC-PEDOT with graphene and obtained a PCE of 11.5 %.[9] In addition, work using a very similar device configuration to that used in this thesis (PET/PEDOT/perovskite/$PC_{61}BM$) showed that ultrathin perovskite solar cells could be fabricated on a 1.4 μm-thick PET foil (**Figure 6.3a**).[10] Regarding the challenges of different types of solar cell (section 1.1.2), the fabrication of efficient, flexible, and light-weight solar panels is important. The direct bandgap, high extinction coefficient,

and low-temperature fabrication of the perovskite allow PSCs to be both flexible and lightweight, which are potential advantages over silicon. In a comparison drawn between different types of solar cells, perovskite devices had the highest power-to-weight ratio (Figure 6.3b).[10] In order to highlight the light weight of perovskite solar cells, a small prototype airplane was fabricated, which was powered by an ultrathin perovskite solar panel (Figure 6.3c). To improve the stability of this flexible device, a layer of Cr_2O_3, created by the oxidation of Cr in their device fabrication process, was shown to prevent the corrosion of the top electrode. The Cr_2O_3 blocks the migration of iodide ions from the perovskite layer. This is an example of pathways that other researchers have chosen to reach the overall objective of improving solar cell technology.

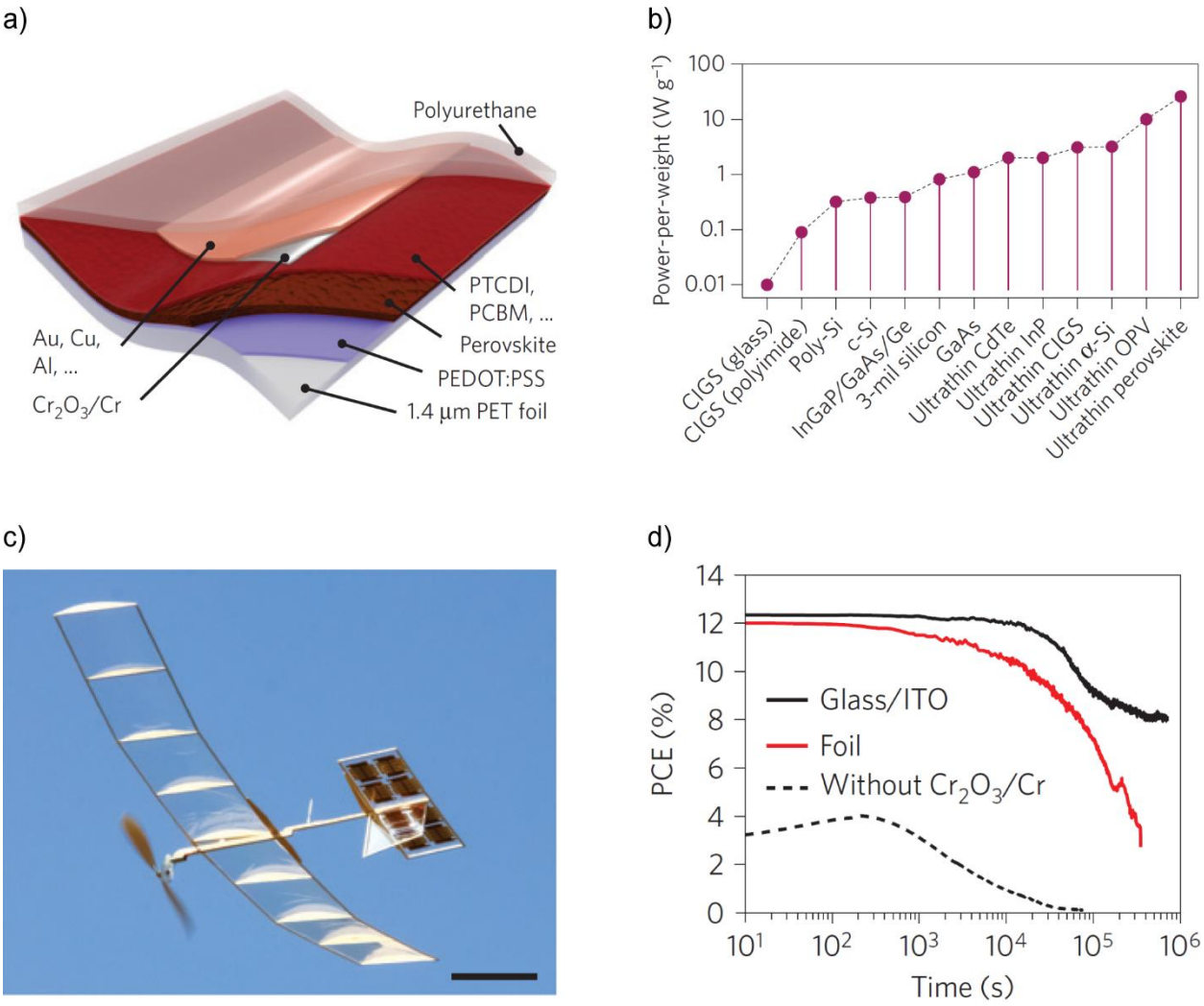

Figure 6.3. A literature example after the publication of the flexible perovskite-device work (chapter 3 of this thesis). (a) Device configuration. (b) A comparison of power per weight for different types of solar cells. (c) A prototype manufacturing of a small airplane powered by ultrathin perovskite solar panel. Scale bar is 10 cm. (d) Monitoring PCE during a stability test done by electric biasing at maximum power in ambient conditions. Devices were fabricated on rigid or flexible substrates and with or without a Cr_2O_3 protective layer. Reprinted by permission from Macmillan Publishers Ltd: Nature Materials, copyright 2015.[10]

In the third approach, a strategy to prevent environmental device degradation was developed (section 1.5.1). A comprehensive study on perovskite stability was conducted, and the effect of each important environmental factor was assessed. Through the fabrication of ABX_3

perovskites with different A-site and X-site dopants, it was shown that there was greater moisture resistance and photochemical stability when the perovskite was doped with FA cations. This superior stability is related to the delocalized positive charge on the FA cation, which reduces the inherent tendency of the perovskite to bind water molecules or react with the superoxide anion. As a result, the MA-rich domains of a $MA_{(1-x)}FA_xPbI_3$ perovskite decompose faster than the FA-rich domains when it is exposed to either a humid environment or to O_2 in the presence of light. This leads to a red shift in the absorption spectrum, since the band edge of the decomposing perovskite shifts closer to that of α-$FAPbI_3$. These results make it possible to compare the effect of changes in perovskite composition on stability.

In the fourth approach, a strategy was formulated that considered both the efficiency requirements (section 1.6.2) and stability-related concerns (section 1.6.3) of perovskite solar cells. Chapter 4's findings on the stability of perovskite films were used to improve the stability of state-of-the-art perovskite solar cells. Chapter 5 demonstrates that $PbBr_2$ and MABr are not necessary additives in $FA_{(1-x)}Cs_xPbI_3$-based perovskite solar cells. Removing these components improved the stability of the devices by eliminating the unstable MA-rich domains and the possibility of halide segregation. In addition, by adding PbI_2 and GAI to the perovskite solution, the density of trap states was decreased in the perovskite layer. This increased the V_{oc} of the devices, one of the few remaining ways of improving state-of-the-art device efficiencies. Since most recent high-performance devices use the $FA_{1-x-y}Cs_xMA_yPbI_{3-y}Br_y$ perovskite, these findings are extremely important for the future research and commercialization of perovskite solar cells.

The findings of all chapters are related to the overall theme of this thesis. To develop solar cell technology, device efficiency, flexibility, and stability can be improved. Chpater 2 deals with plasmon-enhanced upconversion, which has the pottential to be coupled with solar cells, and

increase their photocurrent and efficiency. Chapter 3 discusses the ways to remove the limiting factor of perovskite solar cells and comments on the inherent flexibility of $MAPbI_3$ perovskite. Chapter 4 shows the effect of a variety of cationic and anionic dopants on the stability of perovskite films, and distinguishes the effects of each environmental factor. Chapter 5 demonstrates how to improve of both the efficiency and stability of perovskite solar cells at the same time.

6.2 Outlook and Further Work

The four approaches described in this thesis all have the potential to improve solar cell technology. Plasmon-enhanced TTA is a useful strategy to circumvent the Shockley-Queisser limit of single-junction solar cells. Flexible PSCs have a variety of applications, and their light weight and ease of manufacture can help them compete in the market with silicon solar cells. The stability of PSCs is improving quickly and the efficiency of PSCs might still be further improved. Here, possible future work for each of our approaches is discussed.

Making TTA practical for real applications in solar cells will require further research. Using near-infrared sensitizers, preventing O_2 quenching, applying non-destructive nanoparticle phase transfer methods, and using a lower glass transition temperature host polymer are important strategies in the plasmonic enhancement of TTA. TTA sensitizers usually absorb in the visible region of the solar spectrum.[11-16] This makes them unsuitable for coupling with solar cell active layers possessing absorption edges in the NIR region, such as perovskite solar cells. Although lanthanide-based upconverting systems may be useful for such solar cells, their narrow absorption bands limit the number of photons that can be upconverted.[17-20] Therefore, NIR sensitizers with broader absorption bands are required to have an efficient upconversion process. This can be done

by extending the conjugation length in small molecules or polymers; however, care should be taken not to sacrifice their absorption cross-section or solubility. The other factor is the dependency of TTA on the density of triplet states. This necessitates an O_2-free environment, to prevent quenching of the triplets. Further increasing the TTA quantum yield and providing highly effective encapsulation methods might address this issue. Useful encapsulation materials should have low oxygen transmission rates (OTR), low permeability to water, long-term stability, high stiffness, high optical transmittance (if used on the front side of a device), and be light weight. To create tortuous pathways in encapsulation systems, different materials are coated layer by layer. Ceramic/polymer (such as ZnO/Parylene C) and metal/polymer (such as Al/Parylene C) stacks are commonly used as O_2 barrier multilayers.[21] Cellulose family materials[22] and clay-filled polymer composites[23] have also been used. Generally, polymers are used to make a smooth surface, and inorganics are used as the O_2 barrier. However, these systems encounter long-term problems. Nanoparticle aggregation during the fabrication of polymer composites weakens their barrier properties and decreases their optical transmittance.[24] Although conventional inorganic encapsulating layers, such as SiO_2, show excellent barrier behavior, the formation of pinholes and defects by mechanical deformation have negative effects on the protection of devices against O_2. In this regard, a multilayer coating of graphene oxide/branched polyethylenimine with a thickness of 91 nm was shown to have the same permeability as a 100 nm-thick SiO_2 coating.[24] These examples imply that the ability of encapsulation systems to keep O_2 away from TTA layers can still be evaluated and improved. Regarding the third point, during our phase transfer process, the Ag nanoprisms were corroded at the tips. As a result, their shape changed to nanoplates when they were blended with the TTA materials. This weakens the near-field effect, which is expected to be stronger at sharp nanoprism edges and tips.[25] Therefore, work should be done on non-destructive

phase-transfer processes. Another point is related to the diffusion of TTA chromophores in the solid state. PMMA was used in this thesis as the host polymer. The glass transition temperature of a polymer is an important factor with respect to the diffusion rate of the chromophore in the solid state.[26, 27] It is expected that polymers with lower glass transition temperatures provide a medium for easier diffusion. Therefore, a future study can be conducted on the effect of the glass transition temperature of the host polymer on the efficiency of TTA. Solving the problems associated with the practical use of TTA is an important step toward breaking the Shockley-Quiesser limit and the improvement of solar cell technology.

Flexible perovskite solar cells also require further work. Although our work improved device flexibility by fabricating the first metal oxide-free perovskite solar cell, the hygroscopic properties of the PEDOT electrode may impact the long-term stability of the devices. To improve the stability of these highly-flexible perovskite cells, one strategy is to reduce the tendency of the PEDOT layer to absorb moisture. A commercially-available, water-free, and non-acidic PEDOT formulation was recently used as the hole transport layer in a perovskite solar cell.[28] The conductivity of such a PEDOT layer could be increased, e.g. by doping, to be used as a transparent electrode. Similar to the Cr_2O_3 example described in the previous section (Figure 6.3d),[10] other protective layers can be used with the HC-PEDOT electrodes to improve their stability. Another strategy is to simultaneously improve the flexibility, transparency, and conductivity of other alternative electrodes.[29-34] For this purpose, a thin layer of graphene or carbon nanotubes is transparent and has enormous flexibility. However, work needs to be done to decrease the number of defects in their structure, and to increase their conductivity. In terms of improving the flexibility itself, our work was on the $MAPbI_3$ perovskite made using a single fabrication procedure. Therefore, it remains to be seen whether the perovskite flexibility itself can be improved. One can

address this question by making a change in the perovskite layer, followed by performing fatigue resistance tests on the devices. One possible way to make a change is by carrying out compositional engineering. Then, the effect on the flexibility can be assessed by measuring either the Young's modulus or the Poisson's ratio. For example, flexibility can be improved if the compositional engineering shifts the Poisson's ratio of the perovskite from ~0.30 ($MAPbI_3$) closer to the 0.50 of rubber.[35] The other way to make a change may be by using different fabrication methods, which may alter the physical properties of the perovskite layer. For instance, one can study the effect of larger crystallite sizes and smaller grain boundary areas on the fatigue resistance. Removing the stability issues of flexible perovskite solar cells and further improving their flexibility will further contribute to the overall goal of improving solar cell technology.

To reach the ~25% efficiency and 25 year warranty of silicon solar modules, PSC technology needs to be further improved. Possible pathways to improvement are further decreasing the density of trap states and finding more stable perovskite compositions and more stable interfacial layers. To improve the efficiency of perovskite solar cells, decreasing the density of trap states has been shown to be the only remaining strategy (section 1.6.2).[36-40] To improve the stability, there are many possible modifications that can be made to the device configuration. The studies in chapters 4 and 5 were based on perovskites containing FA, Cs^+, MA, EA and GA as the A-site cations. Now, a variety of different perovskite compositions have been developed by doping with Rb^+ as an A-site cation,[41] or with Ni^{2+}, Co^{2+}, Mn^{2+}, Cu^{2+}, Sr^{2+}, Zn^{2+}, and Ba^{2+} as B-site cations.[42, 43] This has opened new options for improving the stability of perovskite solar cells. Other than providing many options for stability improvement, B-site cation doping is promising, since it can partly address the issue of lead toxicity. Once a relatively good stability is obtained in the perovskite layer, the stability of interfacial layers becomes more important. For instance, when

Spiro-OMeTAD is used as the hole-transport layer, the resulting PSCs have very short device lifetimes. Therefore, the next important step is to improve the stability of the interfacial layers. Finally, when testing the stability of perovskite solar cells, it is very important to investigate the synergetic effects of environmental factors. This may be done by simultaneously exposing them to 85% RH, one sun light intensity, a temperature of 85 ºC, and the electrical bias of the maximum power point. The ultimate goal is to produce a perovskite module that would survive under these accelerated aging test conditions.

In conclusion, assuming that their stability issues can be addressed, the high efficiency, low weight, cost effectiveness, and flexibility of perovskite solar cells make them a promising environmentally friendly alternative to fossil fuels. This thesis developed different pathways to reach this objective, and it is believed that it significantly contributes to the improvement of solar cell technology.

6.3 References

1. S. Baluschev, F. Yu, T. Miteva, S. Ahl, A. Yasuda, G. Nelles, W. Knoll and G. Wegner, *Nano Lett.*, 2005, **5**, 2482-2484.
2. J. K. Park, G. Y. Lee, K. Jung, D.-H. Ko, I. K. Han and H. Ko, *Nanoscale*, 2015, **7**, 12828-12832.
3. X. Cao, B. Hu, R. Ding and P. Zhang, *Phys. Chem. Chem. Phys.*, 2015, **17**, 14479-14483.
4. T. F. Schulze and T. W. Schmidt, *Energy Environ. Sci.*, 2015, **8**, 103-125.
5. L. Frazer, J. K. Gallaher and T. W. Schmidt, *ACS Energy Lett.*, 2017, **2**, 1346-1354.
6. D. M. Wu, A. García-Etxarri, A. Salleo and J. A. Dionne, *J. Phys. Chem. Lett.*, 2014, **5**, 4020-4031.
7. B. J. Kim, D. H. Kim, Y.-Y. Lee, H.-W. Shin, G. S. Han, J. S. Hong, K. Mahmood, T. K. Ahn, Y.-C. Joo, K. S. Hong, N.-G. Park, S. Lee and H. S. Jung, *Energy Environ. Sci.*, 2015, **8**, 916-921.
8. L. Chen, X. Xie, Z. Liu and E.-C. Lee, *J. Mater. Chem. A*, 2017, **5**, 6974-6980.
9. Z. Liu, P. You, C. Xie, G. Tang and F. Yan, *Nano Energy*, 2016, **28**, 151-157.

10. M. Kaltenbrunner, G. Adam, E. D. Glowacki, M. Drack, R. Schwodiauer, L. Leonat, D. H. Apaydin, H. Groiss, M. C. Scharber, M. S. White, N. S. Sariciftci and S. Bauer, *Nat. Mater.*, 2015, **14**, 1032-1039.
11. R. R. Islangulov, D. V. Kozlov and F. N. Castellano, *Chem. Commun.*, 2005, 3776-3778.
12. S. Baluschev, V. Yakutkin, T. Miteva, Y. Avlasevich, S. Chernov, S. Aleshchenkov, G. Nelles, A. Cheprakov, A. Yasuda, K. Müllen and G. Wegner, *Angew. Chem., Int. Ed.*, 2007, **46**, 7693-7696.
13. S. Baluschev, J. Jacob, Y. S. Avlasevich, P. E. Keivanidis, T. Miteva, A. Yasuda, G. Nelles, A. C. Grimsdale, K. Müllen and G. Wegner, *ChemPhysChem*, 2005, **6**, 1250-1253.
14. S. K. Sugunan, C. Greenwald, M. F. Paige and R. P. Steer, *J. Phys. Chem. A*, 2013, **117**, 5419-5427.
15. P. E. Keivanidis, S. Baluschev, T. Miteva, G. Nelles, U. Scherf, A. Yasuda and G. Wegner, *Adv. Mater.*, 2003, **15**, 2095-2098.
16. P. Du and R. Eisenberg, *Chem. Sci.*, 2010, **1**, 502-506.
17. J.-C. Boyer, L. A. Cuccia and J. A. Capobianco, *Nano Lett.*, 2007, **7**, 847-852.
18. F. Wang, Y. Han, C. S. Lim, Y. Lu, J. Wang, J. Xu, H. Chen, C. Zhang, M. Hong and X. Liu, *Nature*, 2010, **463**, 1061-1065.
19. F. Wang and X. Liu, *Chem. Soc. Rev.*, 2009, **38**, 976-989.
20. W. Zou, C. Visser, J. A. Maduro, M. S. Pshenichnikov and J. C. Hummelen, *Nat. Photonics*, 2012, **6**, 560-564.
21. S. P. Subbarao, M. E. Bahlke and I. Kymissis, *IEEE Trans. Electron Devices*, 2010, **57**, 153-156.
22. C. Aulin, E. Karabulut, A. Tran, L. Wågberg and T. Lindström, *ACS Appl. Mater. Int.*, 2013, **5**, 7352-7359.
23. A. Walther, I. Bjurhager, J.-M. Malho, J. Pere, J. Ruokolainen, L. A. Berglund and O. Ikkala, *Nano Lett.*, 2010, **10**, 2742-2748.
24. Y.-H. Yang, L. Bolling, M. A. Priolo and J. C. Grunlan, *Adv. Mater.*, 2013, **25**, 503-508.
25. J. Nelayah, M. Kociak, O. Stephan, N. Geuquet, L. Henrard, F. J. G. de Abajo, I. Pastoriza-Santos, L. M. Liz-Marzan and C. Colliex, *Nano Lett.*, 2010, **10**, 902-907.
26. T. N. Singh-Rachford, J. Lott, C. Weder and F. N. Castellano, *J. Am. Chem. Soc.*, 2009, **131**, 12007-12014.
27. A. Turshatov, D. Busko, N. Kiseleva, S. L. Grage, I. A. Howard and B. S. Richards, *ACS Appl. Mater. Int.*, 2017, **9**, 8280-8286.
28. Y. Hou, H. Zhang, W. Chen, S. Chen, C. O. R. Quiroz, H. Azimi, A. Osvet, G. J. Matt, E. Zeira, J. Seuring, N. Kausch-Busies, W. Lövenich and C. J. Brabec, *Adv. Energy Mater.*, 2015, **5**, 1500543-n/a.
29. K. Ellmer, *Nat. Photonics*, 2012, **6**, 809-817.
30. S. Soltanian, R. Rahmanian, B. Gholamkhass, N. M. Kiasari, F. Ko and P. Servati, *Adv. Energy Mater.*, 2013, **3**, 1332-1337.
31. D. S. Hecht, L. Hu and G. Irvin, *Adv. Mater.*, 2011, **23**, 1482-1513.
32. F. Bonaccorso, Z. Sun, T. Hasan and A. C. Ferrari, *Nat. Photonics*, 2010, **4**, 611-622.
33. S. Seo, M. Min, S. M. Lee and H. Lee, *Nat. Commun.*, 2013, **4**, 1920.
34. D. Chen, H. Zhang, Y. Liu and J. Li, *Energy Environ. Sci.*, 2013, **6**, 1362-1387.
35. J. Feng, *APL Materials*, 2014, **2**, 081801.
36. W. Tress, *Adv. Energy Mater.*, 2017, **7**, 1602358.

37. M. Hadadian, J.-P. Correa-Baena, E. K. Goharshadi, A. Ummadisingu, J.-Y. Seo, J. Luo, S. Gholipour, S. M. Zakeeruddin, M. Saliba, A. Abate, M. Grätzel and A. Hagfeldt, *Adv. Mater.*, 2016, **28**, 8681-8686.
38. D. Yang, X. Zhou, R. Yang, Z. Yang, W. Yu, X. Wang, C. Li, S. Liu and R. P. H. Chang, *Energy Environ. Sci.*, 2016, **9**, 3071-3078.
39. S. M. Jain, Z. Qiu, L. Haggman, M. Mirmohades, M. B. Johansson, T. Edvinsson and G. Boschloo, *Energy Environ. Sci.*, 2016, **9**, 3770-3782.
40. J. T.-W. Wang, Z. Wang, S. Pathak, W. Zhang, D. W. deQuilettes, F. Wisnivesky-Rocca-Rivarola, J. Huang, P. K. Nayak, J. B. Patel, H. A. Mohd Yusof, Y. Vaynzof, R. Zhu, I. Ramirez, J. Zhang, C. Ducati, C. Grovenor, M. B. Johnston, D. S. Ginger, R. J. Nicholas and H. J. Snaith, *Energy Environ. Sci.*, 2016, **9**, 2892-2901.
41. M. Saliba, T. Matsui, K. Domanski, J.-Y. Seo, A. Ummadisingu, S. M. Zakeeruddin, J.-P. Correa-Baena, W. R. Tress, A. Abate, A. Hagfeldt and M. Grätzel, *Science*, 2016, **354**, 206-209.
42. M. T. Klug, A. Osherov, A. A. Haghighirad, S. D. Stranks, P. R. Brown, S. Bai, J. T. W. Wang, X. Dang, V. Bulovic, H. J. Snaith and A. M. Belcher, *Energy Environ. Sci.*, 2017, **10**, 236-246.
43. S.-H. Chan, M.-C. Wu, K.-M. Lee, W.-C. Chen, T.-H. Lin and W.-F. Su, *J. Mater. Chem. A*, 2017, **5**, 18044-18052.